

Electrical Control of Optical Bistability in Silicon Microring Resonators

A THESIS

submitted by

RIDDHI NANDI

for the award of the degree

of

DOCTOR OF PHILOSOPHY



**DEPARTMENT OF ELECTRICAL ENGINEERING.
INDIAN INSTITUTE OF TECHNOLOGY MADRAS.**

Sunday 22nd August, 2021

THESIS CERTIFICATE

This is to certify that the thesis titled **Electrical Control of Optical Bistability in Silicon Microring Resonators**, submitted by **RIDDHI NANDI**, to the Indian Institute of Technology Madras, for the award of the degree of **Doctor of Philosophy**, is a bonafide record of the research work done by her under my supervision. The contents of this thesis, in full or in parts, have not been submitted to any other Institute or University for the award of any degree or diploma.

Prof. Bijoy Krishna Das

Research Guide

Professor

Dept. of Electrical Engineering

IIT-Madras, 600 036

Place: Chennai, India

Date: Sunday 22nd August, 2021

"Research is creating new knowledge"

- Neil Armstrong

Dedicated to my **Family**
for their constant love and support

ACKNOWLEDGEMENTS

PhD thesis is not a job of a single person. There are lot of people associated who have directly or indirectly contributed in the completion of this work. I am really grateful to each and every one who has helped me during this journey.

First I would like to thank my PhD supervisor Prof. Bijoy Krishna Das. His guidance and support at all stages in my PhD term is highly appreciable. His attitude of not giving up on any topic till it is fully understood impresses me a lot. His dedication in his work and encouraging words motivated me a lot to work in this exciting field of silicon photonics.

I would like to thank Prof. Rajib Chakraborty of University of Calcutta, who introduced me to the world of integrated optoelectronics.

I would like to acknowledge the members of my Doctoral Committee, Prof. Shreepad Karmalkar, Dr. Deleep Nair and Prof. Nilesh J Vasa for their valuable comments and suggestions during the review meetings. Time to time discussions with Prof. Karmalkar and Dr. Nair has helped me to plan small experiments in between long fabrication processes.

I would also like to extend my gratitude to Prof. Shayan Mookherjea of UCSD, who visited us during GIAN course in 2017 and as a Vajra Faculty in 2019. The discussions with him were really helpful.

I am also thankful to Prof. Nandita Dasgupta for her fruitful inputs during various fabrication processes. I am grateful to the professors of EE5 and EE3 for the different courses and discussions I had with them.

I would like to acknowledge the Center for NEMS and Nanophotonics (CNNP), IIT Madras for providing world-class fabrication facilities. My sincere gratitude to all the technicians and staff members in the MEMS and Microelectronics Lab for all the technical help provided during fabrication of devices. I would specially like to thank

Ms. Vani for her nonstop emails to vendors to get chemicals and instruments in time. Also I would like to thank Mr. Rajendran, Mr. Prakash, Mr. Joseph and Mr. Sreedhar as they were available round the clock for any help required. My special thanks to Mareeswaran, Venkatesh and Deva for their help with different process instruments.

My heartfelt gratitude to all my fellow labmates in integrated optoelectronics group who made my PhD journey a memorable experience. I would like to thank Dr. Shantanu for his valuable inputs, Dr. Sujith for his military training in fabrication processes. My sincere gratitude to Saket and Meenatchi Sundaram for helping me with fabrication and giving lot of insights and tricks about the different process steps. My heartfelt thanks to Sireesha, Siddharth, Dadavali, Sumi, Ramesh and Sreevatsa for making the lab atmosphere wonderful during the first few years of my PhD. Sumi has been a close friend since she joined our lab. We spent wonderful time both inside and outside lab. Time spent with Sreevatsa in lab during the fabrication and characterization of p-i-n diodes is also noteworthy. I would also extend my gratitude to Ramesh for helping me learn EBL. I would also thank my seniors Dr. Parimal, Rashmi, Vivek, Sakthivel and Seethalakshmi for their guidance and moral support. My gratitude to my fellow labmates presently and in the recent past in Integrated Optoelectronics group, Arnab, Meena, Srinath, Suvarna, Ram Mohan, Ashitosh, Pratyasa, Anushka, Vishnu, Vinoth, Pawan, Pranita, Piyush, Ankan, Sarad, Riddhi Goswami for their help and encouragements and I wish them all the best in their future endeavours. My special thanks to Arnab for helping me with characterization related to non-linear measurements and long discussions regarding our research specially during the COVID-19 pandemic lockdown. I would also like to thank Anushka and Vishnu for helping me with the transient measurements and optimization of fabrication steps.

My friends outside IOLAB needs a special mention. They made my stay in IITM really memorable. Special thanks to Sanjoy, Nikhil, Arvind, Pragyan, Pobitro, Shelly, Anusha, Aditya, Bhadri, Nidhin, Prashant, Sarath, Shon, Manu, Nikhil, Anvar. I am really grateful to each and every one who has helped me directly or indirectly in this journey.

My heartfelt thanks to Dr. Daisaku Ikeda and my Soka family in Chennai who have always been there by my side through thick and thin. Their prayers mean a lot to me.

My deepest gratitude to my parents for constantly supporting me and encouraging me. Their prayers and emotional support has helped me gain strength during the ups and downs of this beautiful journey. I extend my gratitude to my father-in-law and mother-in-law for their support and my brother-in-law for his love. I also thank my close friend, Prama for her motivations and encouragement.

Last but not the least, my loving husband deserves my wholehearted love and gratitude for his constant motivation, patience and support. I am really grateful for him being by my side even in the toughest of times. His constant encouragement helped me to finish this thesis.

Thank you one and all.

ABSTRACT

KEYWORDS: Silicon Photonics, Silicon-on-Insulator, Waveguides, Integrated Optics, Microring resonators, Thermo-optic Switch, Non-linear optics, Optical bistability, Four wave mixing, Optical memory.

Silicon microring resonator is an important component for silicon photonics circuits as it can be used to realise different applications like notch-filter in all-pass configuration, add-drop configuration for channel multiplexer, delay lines in coupled ring configuration, ON-OFF switches and modulators by integrating p-i-n/p-n diodes or resistive heaters, photon-pair source and optical memory in non-linear regime. All of these devices have been demonstrated in SOI platform, but there is lot of research going on in improving the figure of merits for each of them. Photon pair source and optical memory are two major applications of microring resonator in the non-linear domain, i.e. when very high input power is launched into it. But the MRR exhibits optical bistability or hysteresis at high input power along with resonance shift. This poses serious problem for nonlinear four-wave mixing process which leads to the generation of less bright photon-pairs (reduced conversion efficiency). It is desirable to precisely align the laser wavelength along one of the resonances of the MRR to obtain enhanced efficiency. Efforts have been made to improve the efficiency by designing dispersion-free waveguide geometry, integrating p-i-n diodes to operate in reverse bias and withdraw the generated free carriers due to two photon absorption at high input power. Another method of cooling the complete chip to align the laser wavelength with the MRR resonance has also been explored in the recent past. However, there is not much literature to address the optical bistability in on-chip photon-pair generation. Hence, this PhD thesis intends to explore the methods to control the optical bistability electrically. We have proposed integrating of electro-optic phase shifters and thermo-optic phase shifters with the MRR to control the bistability. For demonstration we have designed and fabricated MRR of radius $50\ \mu\text{m}$ on $220\ \text{nm}$ SOI with $2\ \mu\text{m}$ BOX and handle layer thickness of $700\ \mu\text{m}$,

the standard SOI wafers used in silicon photonics foundries.

We first demonstrated all-pass silicon MRRs on 220 nm SOI having a free spectral range of ~ 2 nm, Q-factor of $\sim 50,000$ and extinction of ~ 45 dB at critical coupling wavelength around $\lambda = 1550$ nm. We proposed a technique to integrate p-i-n/p-n diodes using diffusion doping for different device layer thickness. Finally we have demonstrated thermo-optic phase shifters by integrating both metal microheaters as well as doped microheaters on the slab of the rib waveguide MRR which produces a wavelength tunability of ~ 45 pm/mW and ~ 70 pm/mW respectively.

We have shown with the existing theoretical model that the previous history of phase detuning in a silicon MRR determines the effective gain in stimulated four wave mixing process. Using the thermo-optic phase shifter integrated MRRs, we have demonstrated an improved stimulated four wave mixing gain of ~ 11.6 dB while thermo-optically blue-shifting resonances in comparison to that of red-shifting resonances, for a launched pump power of 8.4 mW operating at a slightly off-resonant wavelength λ_p . The proposed technique can be used in designing actively controlled efficient photon sources in a large-scale integrated quantum photonic circuit operating at $\lambda \sim 1550$ nm.

In addition, we have explored the transient measurements of the devices and proposed electrically controlled optical memory using the same. We have presented a theoretical analysis and experimental investigation on thermo-optic switching in silicon microring resonators in presence of two photon absorption, which is unavoidable for nonlinear photonic applications. For a pump laser light operating at a resonant wavelength ($\lambda \sim 1550$ nm) could be thermo-optically switched faster from its lower transmission output to a higher value, but found to be extremely slower in reverse direction as the power level increases. An experimental rise-time was observed to be as small as $\sim 0.6 \mu\text{s}$, whereas the fall-time of $\sim 45 \mu\text{s}$ is obtained for just about 1.15 mW of launched pump power. This study was useful to optimize the operating parameters of a silicon microring resonator for electrically driven thermo-optic memory application.

TABLE OF CONTENTS

ACKNOWLEDGEMENTS	v
ABSTRACT	viii
LIST OF TABLES	xiv
LIST OF FIGURES	xxvi
ABBREVIATIONS	xxvii
NOTATIONS	xxx
1 Introduction	1
1.1 Motivation	1
1.2 Research Objective	13
1.3 Thesis Organization	14
2 Background Theory and Simulation Results	16
2.1 Waveguide Design Parameters	16
2.2 Working Principle of Microring Resonators	19
2.3 Nonlinear Effects in Microring Resonators	22
2.3.1 Bistability: Theory and Modelling	25
2.3.2 Simulation Results	29
2.4 Summary	33
3 Phase-shifter Design and Simulation	34
3.1 Electro-optic Phase Shifters: P-I-N/P-N waveguides	34
3.1.1 Design Parameters and Process Flow	36
3.1.2 Simulation Results: Optical	39
3.1.3 Simulation Results: Electro-optic	41

3.2	Thermo-optic Phase shifters: Doped microheater	49
3.2.1	Design of Doped Microheater Integrated with MRR	49
3.2.2	Simulation Results	51
3.3	Thermo-optic Phase-shifters: Metal microheater	53
3.3.1	Design of Metal Microheater Integrated MRR	53
3.3.2	Simulation Results	55
3.4	Summary	57
4	Device Fabrication and Characterization	59
4.1	P-I-N/P-N Waveguides	59
4.1.1	Device Layout and Fabrication	61
4.1.2	Characterization Results	65
4.2	Doped Microheater with MRR	72
4.2.1	Thermo-optic Detuning Characteristics	75
4.2.2	Transient Response	77
4.3	Metal Microheater with MRRs	78
4.3.1	Passive Characterization of MRRs	86
4.3.2	Extraction of MRR Parameters	87
4.3.3	Thermo-optic Detuning Characteristics	90
4.3.4	Transient Response	94
4.4	Comparison Between Doped and Metal Microheater	95
4.5	Summary	97
5	Experimental Results: Stimulated Four Wave Mixing	99
5.1	Non-linear Phase Measurement	99
5.2	Phase-dependent Transmission Hysteresis	102
5.3	Stimulated Four-Wave Mixing Experiment	104
5.4	Summary	107
6	Transient Analysis	108
6.1	Theory and Simulation	108
6.1.1	High Power Switching: Simulation	113

6.2	Experimental Results	116
6.2.1	Thermo-optic Transient Measurements	117
6.2.2	High Power Switching	118
6.3	Summary	122
7	Conclusion	124
7.1	Thesis Summary	124
7.2	Future scopes	126
A	Additional Information on Fabrication	128
A.1	SOI wafer specifications	128
A.2	Silicon Wafer Cleaning Steps	128
A.3	Spin Coating Parameters	129
A.4	Photolithography Parameters	129
A.5	EBL Column Parameters	130
A.6	Dry Etching Parameters	130
A.7	Phosphorus Diffusion	131
A.8	Boron Diffusion	132
B	DOCTORAL COMMITTEE	134
C	List of Publications Based on Thesis	135

LIST OF TABLES

2.1	Material constants and Waveguide parameters used for a microring resonator bistability simulation.	30
3.1	Calculated confinement factor (Γ) for both TE and TM polarization of the waveguide dimensions chosen for the three device layer thickness $H = 1 \mu\text{m}$, $H = 0.5 \mu\text{m}$ and $H = 0.25 \mu\text{m}$	42
3.2	Calculated junction peak electric field strengths for three different single-mode waveguides designed with device layer thickness of $H = 1 \mu\text{m}$, $H = 0.5 \mu\text{m}$ and $H = 0.25 \mu\text{m}$ for varying δ . The peak electric field strength at 0 V bias (E_0) and -5 V bias (E_{-5}) are compared.	46
3.3	Optimized device parameters for three devices layer thicknesses ($H = 1 \mu\text{m}$, $0.5 \mu\text{m}$, $0.25 \mu\text{m}$) with gap between doping windows $G = 5 \mu\text{m}$	49
3.4	The values of thermal and electrical parameters used for COMSOL Simulation [100, 95]	57
4.1	Sheet resistance (Ω/\square) measured at various stages of diffusion dopings.	70
4.2	Simulated and experimental value of sheet resistance [Ω/\square] after first step of phosphorous diffusion and final step of boron diffusion.	72
4.3	Extracted values of parameters used in the polynomial function to fit ΔT with V_B along with the microheater length (L_H) and resistance (R_H).	92
4.4	Observed and/or extracted parameters of a fabricated device (D_2)	94
A.1	Specifications of SOI wafers used	128
A.2	Spin coating parameters for S1805 (positive tone photoresist) to obtain ~ 500 nm thickness on SOI.	129
A.3	Spin coating parameters for S1813 (positive tone photoresist) to obtain ~ 1200 nm thickness on SOI.	129
A.4	Spin coating parameters for HSQ (negative tone resist) to obtain ~ 100 nm thickness on SOI.	129
A.5	Spin coating parameters for PMMA (A4) (positive tone resist) to obtain ~ 250 nm thickness on SOI.	129
A.6	EBL (Raith 150 TWO) column parameters and patterning parameters used for conventional and FBMS patterning on HSQ resist.	130

A.7	Optimized recipe for dry etching of silicon using ICP-RIE	131
A.8	Optimized recipe for dry etching of silicon-di-oxide using ICP-RIE .	131

LIST OF FIGURES

1.1	Schematic of >50Gb/s WDM optical transceiver based on add-drop silicon photonic microring modulators and all-pass filters. TX1-TX5 represents the transmitter for 5 wavelengths, RX1- RX5 represents the receiver for 5 wavelengths, $\lambda_1 - \lambda_5$ are the 5 wavelengths of the 5 channels which are transmitted through Single Mode Fiber (SMF) into the input-output grating couplers [64].	2
1.2	Schematic of MRR in (a) all-pass configuration, (b) add-drop configuration. R : bending radius of ring, k, k_1, k_2 : cross-coupling coefficient, t, t_1, t_2 : self coupling coefficient in the ring-bus directional coupler region, (c) cross-section of a rib waveguide showing the rib width ‘W’, rib height ‘H’ and slab height ‘h’, (d) cross-section of the directional coupler region showing the gap ‘g’ between two rib waveguides. . .	3
1.3	Typical transmission characteristics of an add-drop silicon MRR. the blue curve shows the transmission spectrum of the drop port and the red curve shows the drop-port spectrum. The free spectral range (FSR) and the extinction ratio of both the through port and the drop port are marked using ER_t and ER_d respectively.	4
1.4	(a) Schematic layout of p-i-n diode integrated silicon micro-ring resonator for modulator operation. R is the MRR radius and V_F is the bias voltage applied to the p-i-n diode. The inset shows the cross-section of the p-i-n diode integrated rib waveguide, (b) the transmission spectrum of the MRR for three values of applied bias voltage. The dashed vertical line shows the position of the probe wavelength used for dynamic modulation measurements. The inset shows the transfer function of the modulator for light with a wavelength of 1573.9 nm [75].	5
1.5	(a) Optical micrograph of MRR of 10 μm bend radius integrated with 500 nm wide metal microheater on top, (b) normalized transmission spectrum of the MRR for different power dissipated in the microheater [79].	6
1.6	Schematic of the experimental set-up used to lock the resonance wavelength and thermally stabilize the MRR output using dithering signals [83].	7
1.7	Schematic of a quantum photonic circuit consisting of microring resonator as the photon-pair source, Mach-Zehnder interferometers for routing, processing and measuring the photons [85].	8

1.8	Schematic showing the generation of entangled photon pair from a high pulsed laser via a silicon MRR along with the experimental setup for high-dimensional quantum state generation and control [88].	9
1.9	(a) Optical power dependent hysteresis curve for a MRR of $5 \mu\text{m}$ radius fabricated on a 250 nm SOI. Markers denote the position of the laser w.r.t to the resonance in the hysteresis curve, (b) transmission spectrum of a MRR for different input optical power [92].	9
1.10	All-optical memory demonstration in a silicon MRR driven by optical bistability around $\lambda \sim 1560 \text{ nm}$. The markers represent the different states in the optical memory corresponding to the positions marked in the hysteresis loop [92].	11
1.11	(a) Schematic of the experimental setup used to generate and detect photon pairs using a MRR of $100 \mu\text{m}$ radius, inset: MRR transmission spectrum showing the position of the pump, signal and idler wavelengths along with zoom view of one of the resonances showing the FWHM, (b) normalized transmission spectrum of the MRR and the photon pair generation rate for different input optical power obtained while cooling and heating the sample temperature [50].	12
2.1	Schematic cross-section of a rib waveguide on SOI, W: rib width, H: rib height, h: slab height.	17
2.2	Calculated values of slab height (h_c) cut-off as function of rib width (W) for $2 \mu\text{m}$ device layer thickness. Area above blue and black lines represents the single mode regions for TM and TE polarization respectively. Bottom and top claddings are considered to be BOX and air, respectively. Calculations are carried out for $\lambda = 1550 \text{ nm}$ [99].	18
2.3	Calculated values of slab height (h) cut-off as function of rib width (W) for 220 nm device layer thickness for TE, TM and HE mode guidance. Bottom and top claddings are considered to be BOX and air, respectively. Calculations are carried out for $\lambda = 1550 \text{ nm}$. The dotted lines demarcate the regions for different modes [100].	18
2.4	Simulated optical mode profile (intensity of the electric field) of the fundamental TE mode for rib waveguide dimensions of (a) $W = 2 \mu\text{m}$, $H = 2 \mu\text{m}$, $h = 1.5 \mu\text{m}$, (b) $W = 420 \text{ nm}$, $H = 220 \text{ nm}$, $h = 150 \text{ nm}$	19
2.5	Schematic of all pass MRR, R: bend radius of MRR, L_{DC} : length of directional coupler, a: single pass transmission coefficient, k : cross-coupling coefficient, t : through-coupling coefficient.	19
2.6	Plot showing the coupling strength ($\kappa [\mu\text{m}^{-1}]$) as a function of slab height and directional coupler (DC) gap (g) for wavelength $\lambda = 1550 \text{ nm}$ on 220 nm SOI.	21

2.7	Simulated transmission spectrum of the designed MRR of bend radius (R) = $50 \mu\text{m}$, $L_{DC} = 5 \mu\text{m}$ for (a) $1545 \text{ nm} \leq \lambda \leq 1555 \text{ nm}$, (b) zoom resonance around $\lambda \sim 1550 \text{ nm}$	21
2.8	Non-linear mechanisms that impact the photon pair generation inside a silicon photonic device when high optical power is launched into it. [108].	23
2.9	Schematic representation of a silicon microring resonator in all-pass configuration. The representative wavelength symbols are shown for the pump laser and generated signal/idler photons via spontaneous four wave mixing process: m stands for the m -th order resonance.	24
2.10	Simulated transmission spectrum of a MRR for different input optical power.	26
2.11	Schematic representation of a microring resonator in all-pass configuration showing the through-coupling coefficient (t) and the cross-coupling coefficient (k) in the bus and ring waveguide directional coupler. P_{in} is the input pump power to the MRR at $z = 0$, and P_{out} is the output power. $A(z)$ is assigned for the field amplitude of circulating light-wave along the ring waveguide.	26
2.12	Schematic representation of a silicon microring resonator in all-pass configuration integrated with a phase-tuning element (ϕ_A). The representative wavelength symbols are shown for the pump laser and generated signal/idler photons via spontaneous four wave mixing process: m stands for the m -th order resonance.	29
2.13	Simulated (a) wavelength dependent transmission spectrum of the MRR along with the position of the off-resonant wavelength, (b) power dependent hysteresis curve obtained from Fig. 2.13(a) by increasing and decreasing the input optical power.	30
2.14	Simulated output power (P_{out} , blue curve) and the cavity power (P_0 , black curve) normalized to input power P_{in} as a function of ϕ_A increasing/decreasing in the MRR for: (a) $P_{in} = 1\text{mW}$, (b) $P_{in} = 4 \text{ mW}$, (c) $P_{in} = 8 \text{ mW}$. Double arrows represent the path with increasing ϕ_A and single arrows for decreasing ϕ_A . The simulation was carried out for parameters given in Table 2.1.	31
2.15	Simulated maximum field enhancement factor (F_0^{max}) and corresponding detuned phase (ϕ_A^{op}) as a function of P_{in} . The solid line represents the forward tuning of ϕ_A and dotted line shows the backward tuning of ϕ_A . The simulation was carried out for parameters given in Table 2.1	32

3.1	Fabrication process flow (see text for process parameters) and schematic cross-sectional views: (a) oxidation for masking during phosphorous diffusion, (b) etching of oxide for phosphorus diffusion window, (c) phosphorous diffusion, (d) oxidation for masking during boron diffusion, (e) etching of oxide for boron diffusion window, (f) boron diffusion, (g) removal of oxide after diffusion, (h) blanket etching to control device layer thickness of H , (i) rib waveguide definition (width W and slab height h optimized for single-mode guidance at $\lambda \sim 1550$ nm) by ICP-RIE using photoresist mask, (j) oxidation for surface passivation, (k) oxide etching for metal contacts, (l) metalization.	35
3.2	Concentration profile along the device layer after all the process steps (before blanket etching) for (a) n-doped region, (b) p-doped region. Point A corresponds to the initial SOI surface, point B is the SOI surface after all the oxidation and diffusion steps (corresponding to Figure 3.1(g)), point C is the silicon device layer and Buried Oxide (BOX) interface and point D is the end of the BOX ($1 \mu\text{m}$ thickness was considered for simulation), (c) net doping concentration across the junction at different device layer thickness ($0.25 \mu\text{m}$, $0.5 \mu\text{m}$, $0.75 \mu\text{m}$ and $1 \mu\text{m}$).	37
3.3	Single-mode cut-off in $W - h$ plane for the guidance of both TE and TM-polarization at $\lambda = 1550$ nm. The color gradient is the measure of confinement strength of the fundamental guided mode underneath the rib width: (a) $H = 1 \mu\text{m}$ (TE), (b) $H = 1 \mu\text{m}$ (TM), (c) $H = 0.5 \mu\text{m}$ (TE), (d) $H = 0.5 \mu\text{m}$ (TM), (e) $H = 0.25 \mu\text{m}$ (TE), (f) $H = 0.25 \mu\text{m}$ (TM).	39
3.4	Simulated electric field distributions (E_x component) for the guidance of TE-polarization in single-mode waveguides ($\lambda = 1550$ nm) with SiO_2 surface cladding: (a) $W = 1 \mu\text{m}$, $H = 1 \mu\text{m}$, and $h = 0.6 \mu\text{m}$; (b) $W = 0.6 \mu\text{m}$, $H = 0.5 \mu\text{m}$, and $h = 0.25 \mu\text{m}$; (c) $W = 0.5 \mu\text{m}$, $H = 0.25 \mu\text{m}$, and $h = 0.1 \mu\text{m}$	40
3.5	Space charge fields (a) for SOI thickness $H = 1 \mu\text{m}$, [(b)-(g)] for rib waveguides integrated with p-n diodes on $H = 1 \mu\text{m}$ for various δ shifts, (h) for SOI thickness $H = 0.5 \mu\text{m}$, [(i)-(n)] for rib waveguides on $H = 0.5 \mu\text{m}$ for various δ shifts, (o) for SOI thickness $H = 0.25 \mu\text{m}$ and [(p)-(u)] for rib waveguides on $H = 0.25 \mu\text{m}$ for various δ shifts, at 0 V bias voltage. The color grading is normalized to a scale of unity field strength.	43
3.6	Change of n_{eff} as a function of reverse bias across waveguide p-n junction diode of reduced geometry with δ (offset from the middle of the gap between doping windows) as a parameter for waveguide with device layer thickness (a) $H = 1 \mu\text{m}$, (b) $H = 0.5 \mu\text{m}$, (c) $H = 0.25 \mu\text{m}$	45
3.7	The calculated (a) change of n_{eff} , (b) optical attenuation, (c) junction capacitance, as a function of reverse bias across the waveguide diodes (p-n junction) designed with device layer thickness $H = 0.25 \mu\text{m}$, and gap between doping windows as a parameter.	47

3.8	Simulated (a) $I - V$ characteristics, (b) change of n_{eff} as a function of forward bias, (c) optical loss as a function of forward bias across a waveguide diode (p-i-n junction) of reduced geometry ($H = 0.25 \mu\text{m}$) with gap (G) between doping windows as a parameter.	48
3.9	Schematic top-view of the slab doped microheater integrated with MRR. The microheater is flared to Aluminium contact pads. Grating coupler (GC) is used for optical interfacing.	49
3.10	Schematic cross-section of the fabrication process flow for doped microheater integrated microring resonator, (a) SOI wafer of device layer $H' = 250 \text{ nm}$, (b) oxidation for masking during boron diffusion, (c) etching of oxide for boron diffusion, (d) boron diffusion and oxide removal, (e) lithography for waveguide diffusion, (f) etching of rib waveguide, (g) oxidation for surface passivation, (h) oxide etching and aluminum metalization for contact pads	50
3.11	Simulated doping concentration of Boron along the depth of SOI wafer, (b) simulated optical loss for different gap between the rib waveguide and the doped micro-heater.	51
3.12	(a) Simulated temperature profile showing the cross-section of the doped microheater, (b) extracted temperature profile for a slice 10 nm below the top of the waveguide slab.	52
3.13	Schematic of (a) design layout showing a set of three identical rib waveguide MRRs (D_1, D_2 and D_3) integrated with identical slab integrated Ti-strip microheaters of three different lengths approximately covering one-quarter, two-quarter, and three-quarter lengths of the MRRs along with input/output grating couplers (GC) for optical interfacing and Al contact pads for electrical interfacing; (b) cross-section view of the directional coupler used for light coupling between the ring and bus waveguides (W - waveguide width, H - waveguide height, h - slab height, g - gap between ring and bus waveguides, BOX - buried oxide); (c) cross-section view of a waveguide-slab-integrated Ti-strip microheater (W_H and t_H are the width and thickness of Ti-strip, respectively, and G is the distance between rib-waveguide and Ti-strip).	53
3.14	(a) Schematic top-view showing the fabrication process steps for microheater integrated MRR: (a) rib waveguide and MRR fabrication, (b) Aluminum patterning and lift-off for contact pads, (c) Titanium patterning and lift-off for microheater.	54

3.15	Simulated 3-D temperature profile extracted from COMSOL Multiphysics of the designed rib waveguide MRRs integrated with slab integrated microheaters: (a) $L_H = 83.5 \mu\text{m}$ (D_1), (b) $L_H = 162 \mu\text{m}$ (D_2), (c) $L_H = 240.5 \mu\text{m}$ (D_3) for 50 mW of electrical power which is assumed to be dissipated uniformly along the waveguide, and (d) ΔT obtained in the waveguide core as a function of dissipated power (mW) for all the three device geometries (D_1 , D_2 and D_3), (e) 2D temperature profile for the cross-section showing the rib waveguide integrated with the Ti metal microheater placed.	56
3.16	Simulated transient response of the Titanium microheaters for device D_1 , D_2 and D_3 for 50 mW of electrical power supplied to the microheaters.	57
4.1	Schematic cross-section depicting the process steps for fabricating p-i-n diodes on $2 \mu\text{m}$ SOI: (a) rib waveguide fabrication, (b) oxidation for masking for phosphorous diffusion, (c) lithography and etching of oxide from diffusion window, (d) phosphorous diffusion, (e) oxidation for masking for boron diffusion, (f) lithography and etching of oxide from diffusion window, (g) boron diffusion, (h) surface passivation, (i) metallization for contact pads	60
4.2	Layout of the waveguide mask used to fabricate the p-i-n waveguides on $2 \mu\text{m}$ SOI.	61
4.3	Layout of the phosphorus diffusion window mask used to fabricate the p-i-n waveguides on $2 \mu\text{m}$ SOI.	62
4.4	Layout of the boron diffusion window mask used to fabricate the p-i-n waveguides on $2 \mu\text{m}$ SOI.	62
4.5	Layout of the contact pads mask used to fabricate the p-i-n waveguides on $2 \mu\text{m}$ SOI.	63
4.6	Confocal micrograph of the $2 \mu\text{m}$ SOI devices fabricated showing the different fabrication steps (a) after phosphorus diffusion, (b) after boron diffusion, (c) after surface passivation, (d) metallization.	64
4.7	SEM image of the fabricated waveguides on $2 \mu\text{m}$ SOI showing the (a) cleaved end-facet, (b) polished end-facet.	65
4.8	Schematic of the lens-coupling set-up used for characterizing the $2 \mu\text{m}$ SOI p-i-n waveguides. PC: Polarization Controller, IC: Input Collimator, L: Lens, P: Polariser, SMU: Source Measure Unit.	66
4.9	Fabry-Perot loss measurements showing the optical output power vs. wavelength for (a) TE polarization, (b) TM polarization.	66
4.10	Measured optical mode profile for (a) TE polarization, (b) TM polarization.	67

4.11	Optical attenuation with the applied current to the p-i-n diodes of doping length $500 \mu\text{m}$ and gap between the doping windows form the rib being varied from (a) $1 \mu\text{m}$, (b) $2 \mu\text{m}$, (c) $3 \mu\text{m}$, (d) $4 \mu\text{m}$	68
4.12	Reverse bias I-V characteristics of the p-i-n waveguides at various power levels for diode length (a) $250 \mu\text{m}$, (b) $500 \mu\text{m}$ and (c) $750 \mu\text{m}$	69
4.13	(a) SEM image of the cleaved end-facet of a rib waveguide with thermally grown surface passivation oxide of thickness $\sim 163 \text{ nm}$, fabricated with initial SOI device layer thickness of $2 \mu\text{m}$, (b) confocal micro-graph showing the top Aluminum metal contact pads of the fabricated diodes of three different lengths ($L = 250 \mu\text{m}$, $500 \mu\text{m}$ and $750 \mu\text{m}$).	70
4.14	(a) $I - V$ characteristics of diodes ($L = 500 \mu\text{m}$) for device layer thickness of $H = 1.5 \mu\text{m}$, $1.0 \mu\text{m}$, and $0.75 \mu\text{m}$ derived from initial device layer thickness of $H_0 = 2 \mu\text{m}$. Inset: SEM image of a fabricated diode with Aluminum contact pads. (b) $I - V$ characteristics of diodes with three different lengths $L = 250 \mu\text{m}$, $500 \mu\text{m}$ and $750 \mu\text{m}$ ($H = 1.5 \mu\text{m}$). (c) $C - V$ characteristics of diodes with three different lengths $L = 250 \mu\text{m}$, $500 \mu\text{m}$ and $750 \mu\text{m}$ ($H = 1.5 \mu\text{m}$).	71
4.15	Schematic cross-section of the fabrication process flow for doped microheater integrated microring resonator, (a) SOI wafer of device layer $H' = 250 \text{ nm}$, (b) oxidation for masking during boron diffusion, (c) etching of oxide for boron diffusion, (d) boron diffusion and oxide removal, (e) lithography for waveguide diffusion, (f) etching of rib waveguide, (g) oxidation for surface passivation, (h) oxide etching and aluminum metalization for contact pads	73
4.16	Mask layout used to fabricate p-doped integrated microheaters. A reference waveguide is followed by four MRRs integrated with doped heater. The gap between the MRR and the microheater is $2 \mu\text{m}$ for the first two structures and $3 \mu\text{m}$ for the next two structures.	73
4.17	SEM image of (a) micro-heater ($W_H = 1\mu\text{m}$) integrated along with MRR at a distance of $2 \mu\text{m}$, (b) zoomed image of the doped microheater integrated MRR, (c) grating coupler, (d) directional coupler.	75
4.18	A schematic illustration of the experimental set-up used for device characterizations: TLS -Tunable Laser Source, PC - Polarization Controller, DUT - Device Under Test, SMU - Source Measurement Unit, FG - Function Generator, PD - Photodetector, DSO - Digital storage oscilloscope, OSA - Optical Spectrum Analyzer. P_{in} is the launched laser power into the MRR and P_{out} is the output from the MRR.	76
4.19	Normalized transmission spectrum of the fabricated MRR for (a) wavelength range of $1520 \text{ nm} < \lambda < 1600 \text{ nm}$, (b) different electrical power of the doped microheater for a resonance around $\lambda \sim 1560 \text{ nm}$	76

4.20	Bar chart showing the thermal tuning efficiency of the different devices fabricated with two variations of gap between the micro-heater and the ring resonator ($G = 2 \mu\text{m}$ and $3 \mu\text{m}$).	77
4.21	Thermo-optic transient response for the slab integrated doped micro-heater for $\Delta V = 5\text{V}$ (5 kHz). An additional bias voltage $V_B = 35\text{V}$ was applied between the microheater contact pads for a launched laser power $P_{in} = 0.2 \text{ mW}$ set to operate at one of the resonant wavelengths.	78
4.22	Schematic cross-section depicting the process steps for fabricating the MRRs: (a) cleaned SOI substrate, (b) HSQ resist coating on the surface, (c) electron beam lithography for patterning of rib waveguide and directional coupler, (d) dry etching (ICPRIE) of rib waveguide and directional coupler.	79
4.23	Mask layout for D_1 set of devices consisting of one reference waveguide and six MRRs integrated with microheater. Device D_1R_1 , D_1R_3 and D_1R_5 have $4 \mu\text{m}$ length of the directional coupler and device D_1R_2 , D_1R_4 and D_1R_6 have $5 \mu\text{m}$ length of the directional coupler.	79
4.24	Mask layout for D_2 set of devices consisting of one reference waveguide and six MRRs integrated with microheater. Device D_2R_1 , D_2R_3 and D_2R_5 have $4 \mu\text{m}$ length of the directional coupler and device D_2R_2 , D_2R_4 and D_2R_6 have $5 \mu\text{m}$ length of the directional coupler.	80
4.25	Mask layout for D_3 set of devices consisting of one reference waveguide and six MRRs integrated with microheater. Device D_3R_1 , D_3R_3 and D_3R_5 have $4 \mu\text{m}$ length of the directional coupler and device D_3R_2 , D_3R_4 and D_3R_6 have $5 \mu\text{m}$ length of the directional coupler.	80
4.26	(a) Confocal micrograph of a fabricated all-pass MRR, SEM image showing zoom image of (b) grating coupler, (c) directional coupler of the fabricated MRR.	82
4.27	Schematic cross-section of the fabrication process flow for Titanium microheater integrated microring resonator, (a) PMMA resist coating, (b) window opening for Aluminium contact pads, (c) Aluminium deposition, (d) Aluminium lift-off, (e) PMMA resist coating, (f) window opening for Titanium microheaters, (g) Titanium deposition, (h) Titanium lift-off.	82
4.28	Microscopic images for lithography of contact pads the fabricated devices (a) D_1 , (b) D_2 , (c) D_3	83
4.29	Microscopic images after Aluminium lift-off of contact pads the fabricated devices (a) D_1 , (b) D_2 , (c) D_3	83
4.30	Microscopic images for lithography of microheaters of the fabricated devices (a) D_1 , (b) D_2 , (c) D_3	84
4.31	Microscopic images after Titanium liftoff of the microheaters of the fabricated devices (a) D_1 , (b) D_2 , (c) D_3	84

4.32	Microscopic images of the complete fabricated devices (MRR integrated with Titanium slab microheater flared to Aluminium contact pad) (a) D_1 , (b) D_2 , (c) D_3	85
4.33	SEM images of the fabricated rib waveguide MRRs integrated with slab integrated microheaters: (a) $L_H = 83.5 \mu\text{m}$ (D_1), (b) $L_H = 162 \mu\text{m}$ (D_2), (c) $L_H = 240.5 \mu\text{m}$ (D_3), (d) zoomed image of the Ti-strip microheater placed $\sim 2.2 \mu\text{m}$ away from the rib waveguide.	86
4.34	Schematic of the characterization set-up. TLS: Tunable Laser Source, OSA: Optical Spectrum Analyzer, PC: Polarization Controller. . . .	87
4.35	Transmission characteristics of reference straight waveguide (red curve) ($W = 420 \text{ nm}$, $H = 220 \text{ nm}$, $h = 150 \text{ nm}$) and a microring resonator ($R = 50 \mu\text{m}$, $L_{DC} = 5 \mu\text{m}$) (blue curve) for $1520 \text{ nm} \leq \lambda \leq 1600 \text{ nm}$. .	87
4.36	Extracted Q-values for each of the resonances from Fig.4.35 for the wavelength range $1520 \text{ nm} \leq \lambda \leq 1580 \text{ nm}$	88
4.37	Zoom transmission of the resonance around $\lambda_r \sim 1550 \text{ nm}$ of Fig.4.35.	88
4.38	Extracted free spectral range (FSR) and group index (n_g) for the MRR from $1520 \text{ nm} \leq \lambda \leq 1570 \text{ nm}$	89
4.39	Self-coupling coefficient t of the ring-bus waveguide coupler as a function of wavelength along with a (wavelength independent) and λ_c extracted from the experimental results shown in Fig. 4.36.	89
4.40	(a) Transmission characteristics of device D_1 for $1520 \text{ nm} \leq \lambda \leq 1600 \text{ nm}$, (b) shift in resonant wavelength ($\Delta\lambda_r$) around $\lambda_r \sim 1550 \text{ nm}$ with the applied voltage.	90
4.41	(a) Transmission characteristics of device D_2 for $1520 \leq \lambda \leq 1600 \text{ nm}$, (b) shift in resonant wavelength ($\Delta\lambda_r$) around $\lambda_r \sim 1550 \text{ nm}$ with the applied voltage.	91
4.42	(a) Transmission characteristics of device D_3 for $1520 \leq \lambda \leq 1600 \text{ nm}$, (b) shift in resonant wavelength ($\Delta\lambda_r$) around $\lambda_r \sim 1550 \text{ nm}$ with the applied voltage.	91
4.43	(a) Shift in resonant wavelengths ($\Delta\lambda_r$) of the MRRs (D_1 , D_2 , D_3) as a function of applied voltage (V_B) between microheater contact pads, (b) experimental rise in waveguide temperatures as a function of applied voltage (V_B) between microheater contact pads (dotted lines how the polynomial fit), (c) experimental rise in waveguide temperatures as a function of applied electrical power for D_1 , D_2 , D_3 , (symbols are experimental data, dotted lines how the COMSOL simulation), (d) extracted line resistance of the three length of microheaters D_1 , D_2 , D_3 for different waveguide temperature.	93
4.44	SEM image of a damaged microheater of D_1 burnt due to passing of high current.	94

4.45	Thermo-optic transient response for the slab integrated Ti metal microheater for $\Delta V = 1V$ (5 kHz). An additional bias voltage $V_B = 6V$ was applied between the microheater contact pads for a launched laser power $P_{in} = 0.2$ mW set to operate at one of the resonant wavelengths.	95
4.46	Comparison of maximum temperature rise in the rib waveguide core for Titanium microheater (D_2) and p-doped microheater of length $162 \mu m$ integrated with MRR w.r.t the power dissipated in the microheater.	96
5.1	Thermo-optic detuning of resonance wavelength ($\Delta \lambda_m$ and estimated linear phase-shift ϕ_A (measured and simulated for $\lambda_m \sim 1550.7$ nm) as a function of applied voltage (V_B) between microheater contact pads.	100
5.2	Scheme of the experimental set-up used for transmission characterization of the device and its active detuning of linear phase ϕ_A by the integrated microheater: TLS -Tunable Laser Source, EDFA - Erbium-Doped Fiber Amplifier, PC - Polarization Controller, DUT - Device Under Test, OSA - Optical Spectrum Analyzer. P_{in} is the launched laser power into the MRR and P_{out} is the output from the MRR.	100
5.3	(a) Transmission characteristics of the MRR for higher input powers (P_{in} varying from 0.22 mW to 11.6 mW), (b) shift in resonance wavelength (λ_m^{NL}) and estimated ϕ_{NL} as a function of P_{in} : scattered symbols are experimental results, dashed and solid lines show simulation results corresponding to $\tau_h = 1 \mu s$ and $1.5 \mu s$, respectively.	101
5.4	Scheme of the experimental set-up used for ϕ_A dependent transmission characterizations at high input powers: TLS -Tunable Laser Source, EDFA - Erbium-Doped Fiber Amplifier, PC - Polarization Controller, DUT - Device Under Test, OSA - Optical Spectrum Analyzer. P_{in} is the launched laser power into the MRR and P_{out} is the output from the MRR.	102
5.5	Wavelength dependent transmission showing off-resonant pump wavelength λ_p ($P_{in} = 8.4$ mW), and resonant wavelengths λ_m and λ_{m+1} .	103
5.6	Transmission hysteresis (normalized) as a function of ϕ_A for $P_{in} = 8.4$ mW ($\lambda_p = 1550.951$ nm): (a) experimental and (b) simulation.	104
5.7	Scheme of the experimental set-up used for stimulated four wave mixing (FWM) measurements: DUT - Device Under Test, OSA - Optical Spectrum Analyzer, FOC - Fiber Optic Coupler, EDFA - Erbium Doped Fiber Amplifier, PC - Polarization Controller. λ_p is the laser wavelength for the pump and λ_s is the laser wavelength for the signal.	105
5.8	Output spectra of stimulated FWM in MRR as observed in the OSA for $P_{in}^p = 8.4$ mW and $P_{in}^s = 0.2$ mW: (a) $\phi_A \sim \phi_A^{op} \uparrow$ (Point 'A' of Fig. 5.6(a)), and (b) $\phi_A \sim \phi_A^{op} \downarrow$ (Point 'B' of Fig. 5.6(a)).	105

5.9	Simulated conversion efficiency as a function of P_{in}^p measured at $\phi_A \sim \phi_A^{op}$. Scattered symbols are experimental, solid and dashed lines are for simulated results.	106
6.1	(a) Change in refractive index, (b) change in loss obtained due to the contribution of Kerr effect, FCD due to TPA, TPM due to TPA and the effective contribution of all the mechanisms for different input optical power (P_{in}) when the laser is pointed at the resonance wavelength for each P_{in}	109
6.2	Device cross-section of a waveguide-slab-integrated Ti-strip microheater used for simulation. W - rib waveguide width, S - gap between rib waveguide and the Ti microheater, W_H - width of the microheater, t_H - thickness of the microheater, BOX - buried oxide.	110
6.3	Flowchart showing the steps used to obtain thermo-optic transient response.	110
6.4	Thermal transient response obtained from the 2D simulation of the rib waveguide-microheater structure cross-section for three different temperature pulse (305K, 310K, 320K) applied to the microheater. . . .	112
6.5	Thermo-optic transient response of the MRR integrated metal microheater for three different temperature pulses (305K, 310K, 320K). The corresponding effective index is shown in the right y-axis.	112
6.6	Simulated normalized thermo-optic transient response of the MRR for different temperature pulses applied in the microheater for (a) $P_{in} = 0.15$ mW, (b) $P_{in} = 2$ mW, (c) $P_{in} = 4$ mW, (d) $P_{in} = 8$ mW.	113
6.7	Simulated thermo-optic transient response for different input laser powers ($P_{in} = 0.25$ mW to 2.8 mW) at $V_B = 15$ V, when the operating laser wavelength is exactly aligned to one of the MRR resonances: (a) $\Delta T = 5$ K; and (b) $\Delta T = -5$ K.	114
6.8	Simulated thermo-optic rise time and fall time w.r.t P_{in} for applied positive and negative temperature swings ($\Delta T = \pm 5$ K).	114
6.9	Normalized transmission spectrum of the MRR when the wavelength is tuned from 1549 nm to 1549.3 nm and vice versa for (a) $P_{in} = 0.15$ mW, (b) $P_{in} = 6$ mW.	115
6.10	Simulation of thermo-optic hysteresis as a function of bias voltage V_B for $P_{in} = 6$ mW.	115
6.11	(a) Applied input switching voltage, (b) optical bistable switching representation by thermo-optic transients derived from Fig. 6.10. . . .	116

6.12	Scheme of the experimental set-up used for device characterizations: TLS -Tunable Laser Source, EDFA - Erbium-Doped Fiber Amplifier, PC - Polarization Controller, SMU - Source Measurement Unit, FG - Function Generator, PD - Photodetector, DSO - Digital storage oscilloscope. P_{in} is the launched laser power into the MRR and P_{out} is the output from the MRR.	117
6.13	Normalized thermo-optic transient response for different switching voltage (ΔV) for (a) $P_{in} = 0.15$ mW, (c) $P_{in} = 1.45$ mW, rise time and fall time for each of the switching voltages for (b) $P_{in} = 0.15$ mW, (d) $P_{in} = 1.45$ mW.	118
6.14	Thermo-optic transient response for different input laser powers ($P_{in} = 0.05$ mW to 1.15 mW) at $V_B = 15$ V, when the operating laser wavelength exactly aligned to one of the MRR resonances: (a) $\Delta V = 2$ V (5 kHz); and (b) $\Delta V = -2$ V (5 kHz).	119
6.15	Thermo-optic rise time and fall time obtained w.r.t the input optical power (P_{in}) launched inside the MRR for two different values of voltage modulation ($\Delta V = \pm 2$ V).	119
6.16	MRR transmission (right y-axis) obtained by applying a ramp signal (left y-axis) of 14V to the microheater within 1 ms for (a) $P_{in} = 0.4$ mW, (b) $P_{in} = 4.5$ mW by placing the laser ~ 215 nm right of the resonance wavelength around $\lambda = 1550$ nm.	120
6.17	Wavelength dependent transmission characteristics for $P_{in} = 0.4$ mW along with the position of the laser (λ_L).	120
6.18	Thermo-optic hysteresis as a function of bias voltage V_B for P_{in} (a) 0.4 mW, (b) 0.6 mW, (c) 1.0 mW, (d) 1.5 mW, (e) 2.1 mW, (f) 2.6 mW, (g) 3.5 mW, (h) 4.0 mW, (i) 4.5 mW . In the hysteresis curves, the black solid lines are obtained by voltage ramping up and red dashed lines by voltage ramping down over a duration of 1 ms.	121
6.19	Voltage hysteresis width (ΔV) obtained experimentally with respect to the input optical power (P_{in}) launched inside the MRR.	122
7.1	Schematic of a quantum photonic circuit used to separate the generated photon pairs.	126
A.1	SEM images of positive photoresist profile of (a) top view of a 2 μ m rib waveguide, (b) cross-section view of the PPR, (c) and (d) zoom view of the PPR side wall roughness	130
A.2	Data sheet for sheet resistance of Phosphorous diffusion [85].	132
A.3	Boron Nitride wafer preparation process for Boron diffusion.	133
A.4	Data sheet for sheet resistance vs time for Boron diffusion.	133

ABBREVIATIONS

Acronyms

BOX	Buried Oxide
CMOS	Complementary Metal Oxide Semiconductor
DC	Directional Coupler
DI	De-ionized (water)
DSO	Digital Storage Oscilloscope
DUT	Device Under Test
EBL	Electron Beam Lithography
ER	Extinction Ratio
FBMS	Fixed Beam Moving Stage
FG	Function Generator
FSR	Free Spectral Range
GC	Grating Coupler
GDS-II	Graphic Database System-II (mask file format)
HSQ	Hydrogen Silsesquioxane
ICPRIE	Inductively Coupled Plasma Reactive Ion Etching
IL	Insertion Loss
OSA	Optical Spectrum Analyzer
PD	Photodetector
PIC	Photonic Integrated Circuit
PMMA	Poly(methyl methacrylate)
MMI	Multi-Mode Interference
MRR	Microring Resonator
MZI	Mach-Zehnder Interferometer
SEM	Scanning Electron Microscope
SMF	Single Mode Fiber
SMU	Source Measure Unit

SOI	Silicon-on-Insulator
SWG	Sub-Wavelength Grating
TE	Transverse Electric (polarization)
TM	Transverse Magnetic (polarization)
WDM	Wavelength Division Multiplexing
SPM	Self Phase Modulation
FCA	Free Carrier Absorption
FCD	Free Carrier Dispersion
TPA	Two Photon Absorption
TPM	Thermo-optic Phase Modulation

Chemical Names

BN	Boron Nitride
CHF₃	Tri-fluoro Methane
HF	Hydrofluoric Acid
HNO₃	Nitric Acid
H₂O	Water
H₂O₂	Hydrogen Peroxide
H₂SO₄	Sulphuric Acid
NH₄OH	Ammonium Hydroxide
POCl₃	Phosphorous Oxychloride
SF₆	Sulfur Hexafluoride
Si	Silicon
SiO₂	Silicon dioxide
TCE	Tri-chloro Ethylene

Units

dB	decibel
dBm	decibel milli-watt
K	Kelvin
μm	micrometer
μW	micro watt

μs	microsecond
mW	milli watt
mbar	milli-bar
ml	milli-litre
mTorr	milli-Torr (of pressure)
nm	nanometer
ns	nanosecond
sccm	standard cubic centimeter per minute

NOTATIONS

\mathbf{n}	Refractive index
\mathbf{n}_{eff}	Effective refractive index
\mathbf{n}_g	Group index
ϵ	Permittivity
λ	Wavelength
β	Propagation constant
β_{TPA}	Two-photon absorption co-efficient
ϕ	EM wave phase
S_H	Thermal sensitivity
Λ	Grating period
H	Silicon device layer thickness
h	Silicon slab thickness
W	Rib waveguide width
t_{BOX}	Buried oxide thickness
L_T	Micro-ring perimeter
L_{DC}	Length of directional coupler
S_b	Bulk sensitivity
R	Average microring radius
t	Through coupling co-efficient of directional coupler
k	Cross coupling co-efficient of directional coupler
a	Single pass transmission coefficient of microring
F_0	Field enhancement factor
P_0	Circulating power inside the microring
P_{in}	Optical power launched into the grating coupler
Γ	Confinement factor of optical mode
τ	Transient response time

CHAPTER 1

Introduction

Silicon Photonics is an enabling platform of the 21st century. Microring resonator (MRR) is one of the important device used for large scale integrated photonic circuits. When a silicon MRR is subjected to operate at higher power levels, its resonance wavelength shifts and it exhibits hysteresis and optical bistability. Optical bistability has been used to demonstrate optical memory and all-optical switching. However, it also poses serious difficulties for most of the non-linear applications like wavelength conversion, four wave mixing, photon pair generation, etc due to the resonance wavelength shift with increased pump power levels. In this thesis, we have shown a mechanism to electrically control the optical bistability of the MRR by integrating a phase-shifter with it and obtain enhanced stimulated four wave mixing. We have also proposed voltage controlled optical memory and present a study on its speed of operation by considering various cases of transient measurements. The devices discussed in this thesis are designed, fabricated and characterized using the in-house facilities available at IIT Madras. In this introductory chapter, we present the motivation for our research through a detailed literature review, which eventually streamlines the objectives of the PhD work. Finally a brief overview on the organization of the remaining chapters of the thesis is included.

1.1 Motivation

The success of Silicon Photonics technology is due to its fabrication compatibility with CMOS process line, operating at 1310 nm and 1550 nm communication wavelength, ability to integrate on-chip modulators, III-V materials for lasers and Germanium for photodetectors which has helped to manufacture wide range of devices in the last two decades [1, 2, 3, 4, 5, 6, 7]. After decades of extensive research on the basic building blocks like low-loss optical waveguides (operating at $\lambda = 1310$ nm, 1550 nm) [8, 9, 10],

sub-wavelength grating structures [11, 12, 13], directional couplers [14, 15, 16], Mach-Zehnder interferometers [17, 18, 19], microring resonators (MRRs) [20, 21, 22] etc, they have been used to demonstrate different devices and functionalities using small circuits like filters [23, 24, 25, 26, 27, 28], switches [29, 30, 31, 32, 33, 34], delay lines [35, 36, 37, 38], modulators [39, 2, 40], add-drop multiplexers [41, 42, 43, 44, 45, 46, 47], photon sources [48, 49, 50, 51] etc. Silicon MRRs have been used to demonstrate functions such as notch filters in all-pass configuration [23, 24, 25, 26, 27, 28], channel multiplexers in add-drop configuration [41, 42, 52, 43, 53, 44, 45, 46, 47, 54, 55], delay lines in coupled ring waveguide configuration [56, 57, 35, 36, 37, 58, 38], ON-OFF switches [59, 60, 61, 62], switching matrix [63], modulators by integrating p-i-n/p-n diodes [39, 2, 40] or resistive microheaters etc [29, 30, 31, 32, 33, 34]. The advancement and the development of the technology over the years has helped the silicon photonics community to demonstrate high speed transceivers which have been commercialized by companies like Intel and Cisco and have made a huge impact on the market. The pluggable transceiver modules are cost-, power- and space-effective devices where the optics and the electronics are packaged together.

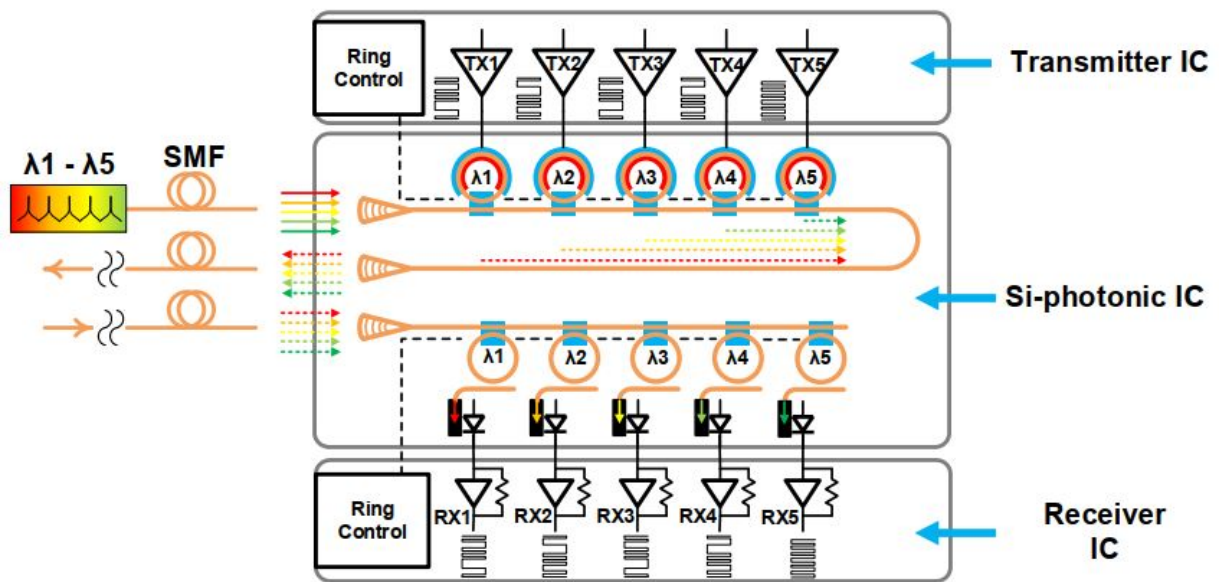


Figure 1.1: Schematic of >50Gb/s WDM optical transceiver based on add-drop silicon photonic microring modulators and all-pass filters. TX1-TX5 represents the transmitter for 5 wavelengths, RX1- RX5 represents the receiver for 5 wavelengths, $\lambda_1 - \lambda_5$ are the 5 wavelengths of the 5 channels which are transmitted through Single Mode Fiber (SMF) into the input-output grating couplers [64].

Fig. 1.1 shows the block diagram of transmitter and receiver section of a transceiver circuit designed with MRRs by HP labs. In the transmitter side the MRRs have been used in all-pass configuration which are integrated with depletion based modulators to obtain resonance wavelength spacing. The data/bit stream modulates the optical signal by the depletion based modulator and is sent to the receiver. In the receiver side a collectively thermally tunable 5-channel add-drop-ring based WDM filter with matching wavelength channel spacing is used to demultiplex the WDM optical signals into separate waveguides. Finally the optical signals are detected by on-chip Germanium photodiodes which are amplified and converted to electrical signals using trans-impedance amplifiers (TIA). This is used to transmit data bits from the transmitter IC to the Receiver IC. Similar work has been reported in transceivers [65] and the tremendous success in the transceiver market has motivated the community to work towards other areas using silicon photonics, like microwave photonics [66, 67, 27, 68], quantum photonics [69, 70, 71, 51], lab-on-chip sensors [72, 73, 74] to name a few.

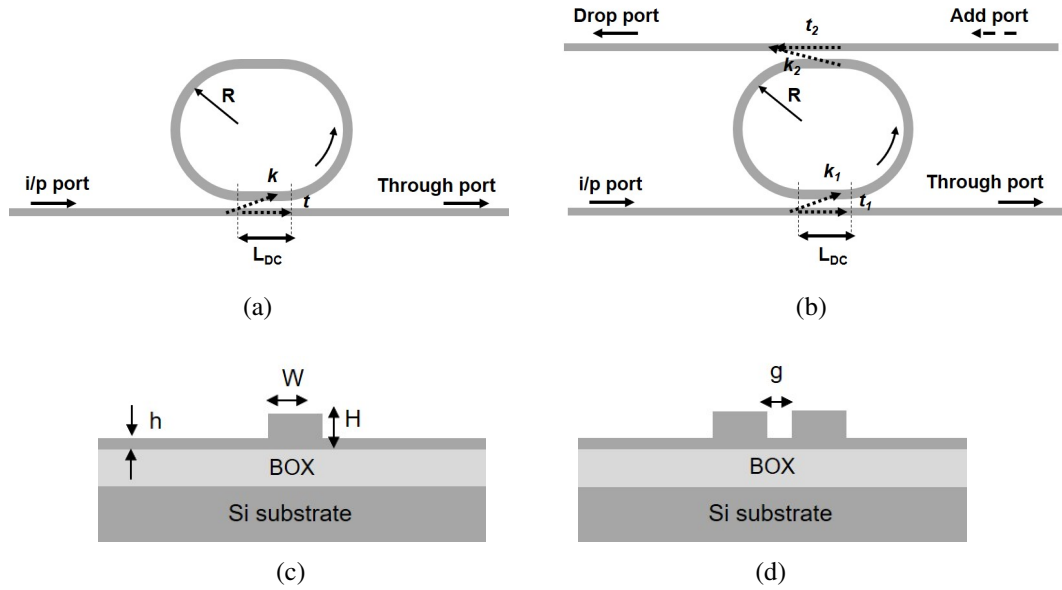


Figure 1.2: Schematic of MRR in (a) all-pass configuration, (b) add-drop configuration. R : bending radius of ring, k, k_1, k_2 : cross-coupling coefficient, t, t_1, t_2 : self coupling coefficient in the ring-bus directional coupler region, (c) cross-section of a rib waveguide showing the rib width ‘ W ’, rib height ‘ H ’ and slab height ‘ h ’, (d) cross-section of the directional coupler region showing the gap ‘ g ’ between two rib waveguides.

The transceiver circuit shown in Fig. 1.1 has used all-pass configuration of MRR in the transmitter side and add-drop configuration of the MRR in the receiver side. The

schematic of both the all-pass as well as add-drop configuration is shown in Fig. 1.2(a) and 1.2(b) respectively. The typical cross-section of the rib waveguide and the directional coupler region is shown in Fig. 1.2(c) and 1.2(d) along with the rib waveguide dimensions (rib width: W , rib height: H and slab height: h) and the directional coupler gap (g). The input port, through port, drop port and add port are marked in the schematic along with the ring radius ' R '. The self-coupling coefficient and the through coupling coefficient are named as ' t ' and ' k ' respectively. A typical transmission characteristics of the add-drop MRR is shown in Fig. 1.3. The blue curve shows the through port transmission spectrum and the red curve shows the drop port transmission. The difference between two successive resonance is the free spectral range (FSR). The extinction ratio obtained in the through port and drop port is marked as ER_t and ER_d respectively. For this simulation a typical rib waveguide geometry is considered where the rib width is 500 nm, slab height is 90 nm and the rib height is 220 nm, supporting single mode TE polarization. The ring radius is 50 μm along with a directional coupler length of 5 μm and the gap between the bus and ring waveguide is 500 nm. The coupling coefficient in this wavelength range is 0.0168 μm^{-1} . The loss of the waveguide considered for simulation is 1.5 dB/cm. The other parameters like group-index, Q-factor, etc will be discussed in Chapter-2.

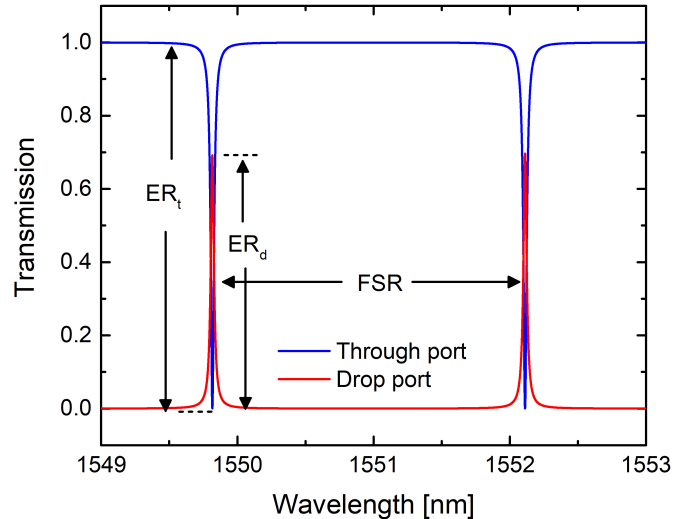


Figure 1.3: Typical transmission characteristics of an add-drop silicon MRR. the blue curve shows the transmission spectrum of the drop port and the red curve shows the drop-port spectrum. The free spectral range (FSR) and the extinction ratio of both the through port and the drop port are marked using ER_t and ER_d respectively.

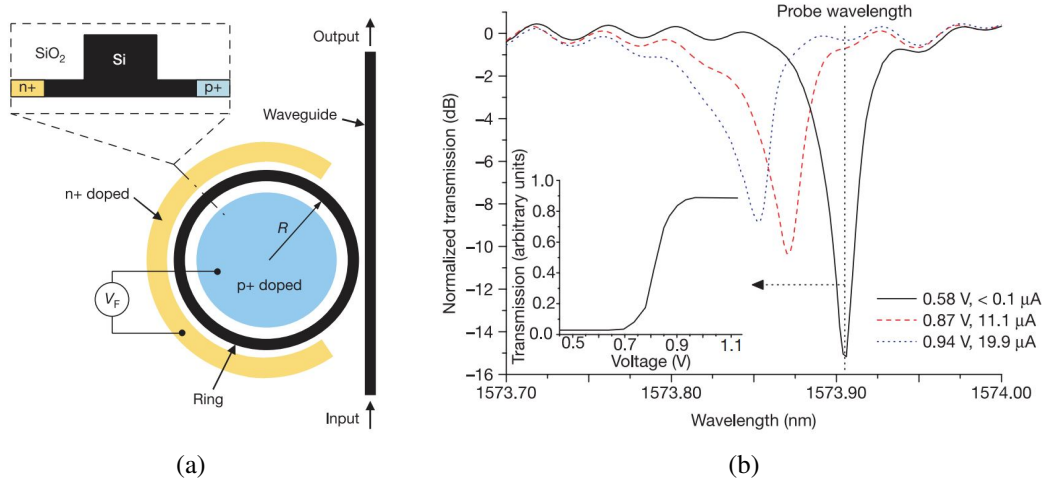


Figure 1.4: (a) Schematic layout of p-i-n diode integrated silicon micro-ring resonator for modulator operation. R is the MRR radius and V_F is the bias voltage applied to the p-i-n diode. The inset shows the cross-section of the p-i-n diode integrated rib waveguide, (b) the transmission spectrum of the MRR for three values of applied bias voltage. The dashed vertical line shows the position of the probe wavelength used for dynamic modulation measurements. The inset shows the transfer function of the modulator for light with a wavelength of 1573.9 nm [75].

As discussed, the transmitter circuit shown in Fig. 1.1 has MRRs integrated with electro-optic phase-shifters in the transmitter side and thermo-optic phase shifters in the receiver side. These are used to actively control their resonance wavelength. For the electro-optic phase shifters, p-i-n/p-n diodes are integrated to obtain the change in phase by the change in carrier concentration due to the applied voltage [76]. The thermo-optic phase shifters are implemented by integrating microheaters to obtain phase change by exploiting the thermo-optic co-efficient of silicon [77].

Many types of designs have been tried to maximize the efficiency, speed of operation, extinction ratio, insertion loss and bandwidth of on-chip modulators using the electro-optic effect. Different modulation techniques have been implemented like ON-OFF switching, RZ, NRZ, PAM4, etc. to improve the data rate. Fig. 1.4(a) shows a schematic of a p-i-n diode integrated silicon MRR [75]. In this work, Xu et al. reports a high-speed electro-optic modulator of 1.5 Gbps achieved in a MRR of $6 \mu\text{m}$ radius. Fig. 1.4(b) shows the transmission characteristics around $\lambda \sim 1573.9 \text{ nm}$, along with the detuning when positive bias voltage is applied to the p-i-n diode. The black curve shows a 15 dB drop in transmission at resonance wavelength. The transmission changes

from low-to-high when 0.87 V is applied. The resonance spectrum blue shifts due to the reduction in the effective index caused by the increase in the electron-hole concentration in the cavity. They observed modulation of more than 5 Gbits^{-1} by using non-RZ (NRZ) signal. The circuit performance is limited by the carrier recombination lifetime as the p-i-n diode is operated in forward bias. Nevertheless, this wavelength selective modulation finds applications in wavelength division multiplexing (WDM) applications and provides high optical bandwidth, as already shown in Fig. 1.1. Further improvement in modulation speed has been achieved and reported by using a pn diode depletion based travelling wave modulator [78].

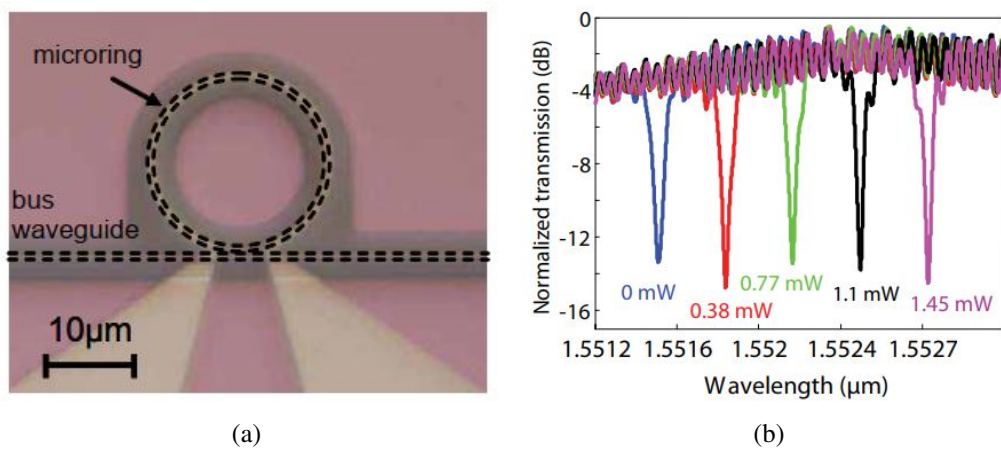


Figure 1.5: (a) Optical micrograph of MRR of $10 \mu\text{m}$ bend radius integrated with 500 nm wide metal microheater on top, (b) normalized transmission spectrum of the MRR for different power dissipated in the microheater [79].

Besides modulators, the MRRs are used for switching applications where the operating speed is slightly less. Hence thermo-optic phase shifters can be integrated. Though they offer slightly slow speed compared to their electro-optic counterpart, they too exhibit low loss which is advantageous to be used in switching matrix applications [80]. A thin metal strip deposited on top of the cladding oxide is used as the microheater. Fig. 1.5(a) shows an all-pass MRR of $10 \mu\text{m}$ radius integrated with a metal microheater of 500 nm width on top of it. The transmission spectrum of the MRR is shown in Fig. 1.5(b). The resonance shifts to longer wavelengths as power dissipation is increased in the microheater. This kind of architecture is also integrated in the receiver end of the transceiver circuit to align the filters to the respective wavelengths (Fig. 1.1).

The main drawback in the operation of silicon MRRs is its thermal instability.

The resonance wavelength shifts due to the fluctuations in the ambient temperatures. Though there has been some research on designing athermal silicon MRRs, but still they have some drawbacks and very critical steps are required to design them [81, 82]. The transceiver circuit shown in Fig. 1.1 has also adopted an electronic feedback control circuit to stabilize the resonant wavelength. There has also been some more research to stabilise MRR output using dithering signals and feedback control [83, 84].

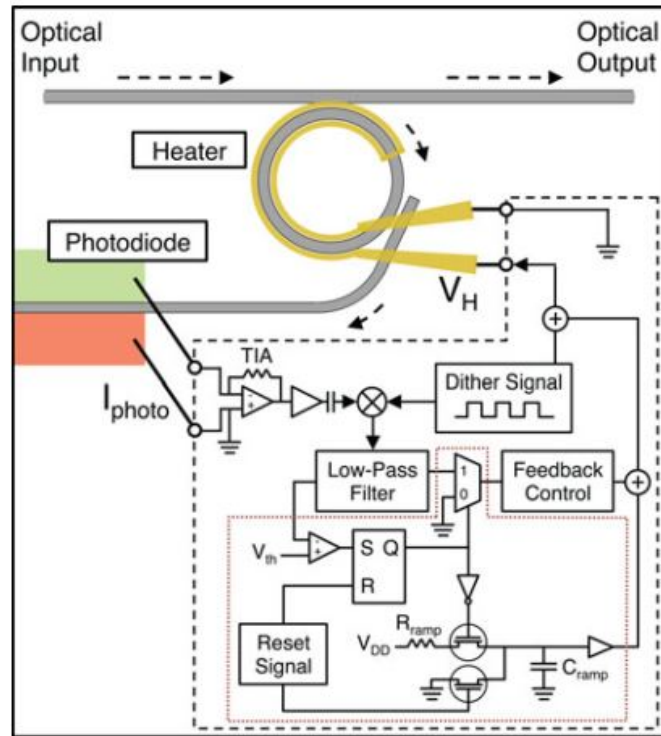


Figure 1.6: Schematic of the experimental set-up used to lock the resonance wavelength and thermally stabilize the MRR output using dithering signals [83].

Fig. 1.6 shows the schematic of the experimental setup used to lock the MRR resonance and stabilize the MRR thermally using a dithering signal. A titanium micro-heater is placed $1 \mu\text{m}$ above the MRR on the top oxide, and a p-i-n based photo diode is integrated in the drop port of the MRR to monitor the optical power dropped into the microring. The off-chip electronics is used for thermal dithering system which is shown by the dashed black line in Fig. 1.6. The optical signal is modulated by the thermal dithering and it generates a photocurrent on the integrated photodiode which is converted to voltage and further amplified by the trans-impedance amplifier (TIA). The amplified signal is multiplied with the dithering signal and finally the ac component is suppressed by the low-pass filter. This generates an anti-symmetric error signal which

can be used to lock the wavelength and thermally stabilize the MRR. This method is useful to stabilise the resonance when the MRR is operating in linear regime, i.e when the optical power launched into it is low, as in the case of transceiver. The wavelength variation and resonance shift is more prominent and obvious when the MRR is subjected to high input power levels which leads to non-linear phenomenon inside the ring. The wavelength shifts to the right with high pump power. Hence, operating the MRRs at a fixed wavelength for quantum photonic circuit applications is challenging.

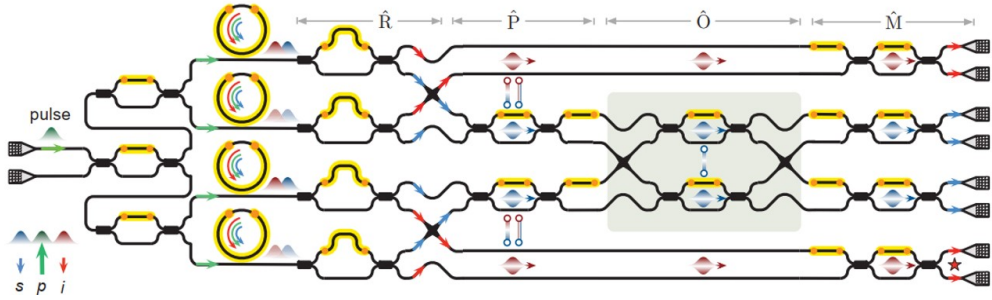


Figure 1.7: Schematic of a quantum photonic circuit consisting of microring resonator as the photon-pair source, Mach-Zehnder interferometers for routing, processing and measuring the photons [85].

MRRs are intensively used in quantum photonic circuits due to its compact cavity structure. Silicon MRRs have been used as photon pair sources in most of the quantum photonics circuits due to its high field enhancement factor [86, 85, 87]. The photon sources are integrated with quantum photonic circuits to realise different functionalities like routing the generated photon pairs, processing them, applying Bell operator and finally measuring the photons separately as shown in Fig. 1.7 [85]. A strong pump pulse is launched at the input and the generation of signal and idler occurs at the output of the MRRs. They are routed using the Mach-Zehnder interferometers (MZI) and waveguide crossings and are finally processed using other MZIs. Finally, balanced MZIs are used before detecting the photons. Hence, it is very crucial to have efficient photon pair sources to finally obtain a reasonable number of photons at the output of the circuit.

Fig. 1.8 shows the schematic of an experimental set-up for generating entangled-photon pairs via spontaneous four wave mixing, using a pulsed laser and an add-drop MRR configuration [88]. A high pump pulse is launched into the MRR and the generation of signal photons and idler photons (entangled photon pair) occur due to the enhancement in the cavity, which is shown by the blue and red colour dots in Fig. 1.8.

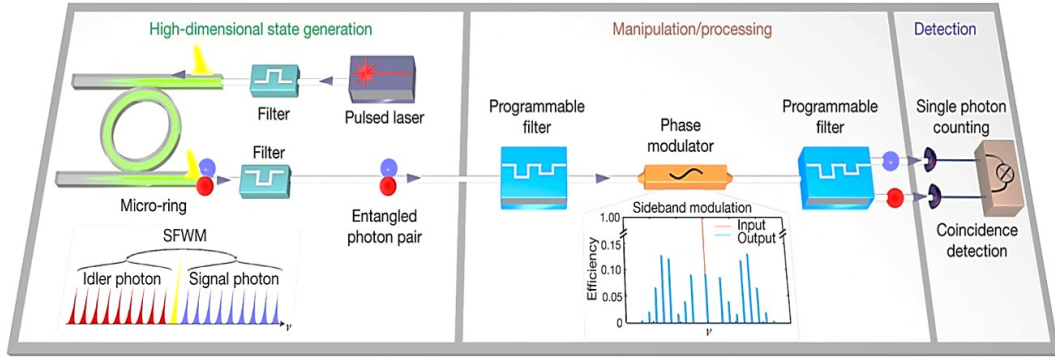


Figure 1.8: Schematic showing the generation of entangled photon pair from a high pulsed laser via a silicon MRR along with the experimental setup for high-dimensional quantum state generation and control [88].

The generated photons are processed using a phase modulator and are detected using single photon detectors. With the advancement of the research in quantum domain, researchers have also tried to enhance the generation of photon pairs by using different techniques like fabricating low dispersive waveguide [89], integrating p-i-n diodes with the waveguides or MRRs and extracting the carriers generated due to high optical power by reverse biasing the diode [90], higher Q-values with critical coupling [91], etc. The main drawback of MRRs while handling high power (non-linear regime) is the inability to operate at a fixed wavelength.

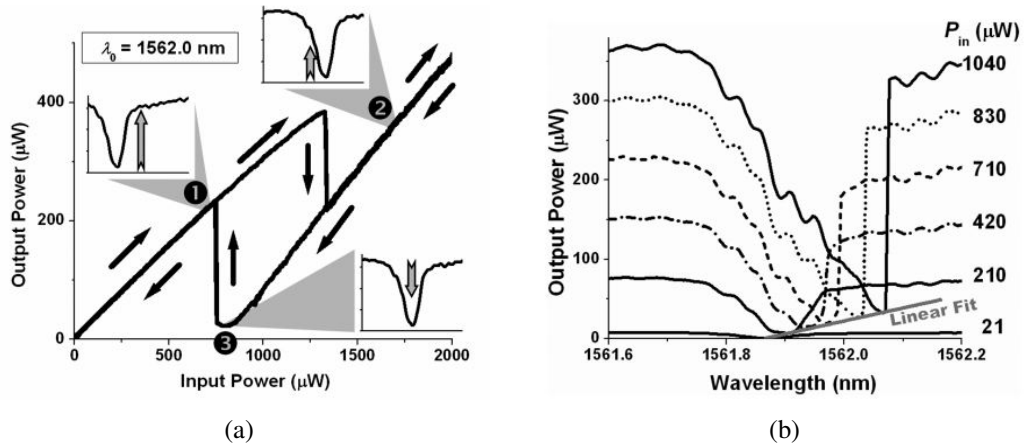


Figure 1.9: (a) Optical power dependent hysteresis curve for a MRR of 5 μm radius fabricated on a 250 nm SOI. Markers denote the position of the laser w.r.t to the resonance in the hysteresis curve, (b) transmission spectrum of a MRR for different input optical power [92].

The third order susceptibility ($\chi^{(3)}$) gives rise to the non-linearity in silicon. The high launched optical power gives rise to different mechanisms inside silicon like Kerr

effect, two-photon absorption (TPA), etc. The heat generated due to the generation of carriers due to TPA is mostly dominant and shifts the resonance wavelength towards the right. This phenomena was reported by Almeida et al. and they demonstrated optical bistability for the first time in silicon MRRs in 2004 [92]. They presented all-optical functionalities like memory and switching by exploiting the thermal non-linear effect in silicon which helps to exhibit bistability at higher input powers. Fig.1.9(a) shows the hysteresis loop obtained in a 5 μm radius MRR fabricated on 250 nm SOI. This has been obtained by tracking the output power when the wavelength is initially fixed few picometers right to the resonance. The inset marked '1' of Fig. 1.9(a) depicts the initial scenario when the power is increased from a low value. With the increase in the optical power the resonance red-shifts, i.e shifts towards higher wavelength due to the non-linear processes occurring, especially the thermo-optic effect being dominant. At a certain input power the resonance dip coincides with the tracking wavelength and produces a dip in the output power. With further increase in the input power, the output keeps on increasing as marked by '2' in the inset of Fig. 1.9(a). Similarly, while decreasing the input power, the resonance coincides with the tracking wavelength at a lower value of input power as shown in the inset marked point '3' of Fig. 1.9(a). This clearly gives rise to hysteresis and shows the presence of bistability at high input optical power. Fig. 1.9(b) shows the transmission spectrum of the MRR around 1560 nm wavelength. As mentioned, the resonance shifts right with the increase in input optical power due to the thermo-optic effect. The bistability property has been used to obtain all-optical memory as shown in Fig. 1.10. With the application of an input optical pulse the output state is changed from high to low or vice versa depending on the position in the hysteresis curve.

However, not much research has been done in the area of stabilizing the red-shifting of the detuned resonances and bistability when operated at high input optical power levels. Recently, Guo et al. [50] demonstrated higher generation of photon pairs in a 100 μm ring radius MRR by locking the resonance with pump wavelength by reducing the sample temperature while operating at high input power. Fig. 1.11(a) shows the experimental setup used to generate photon pair sources using a MRR. The MRR has been placed on a temperature controller for cooling and heating it effectively. The inset shows the MRR transmission spectrum showing the position of the pump, signal and

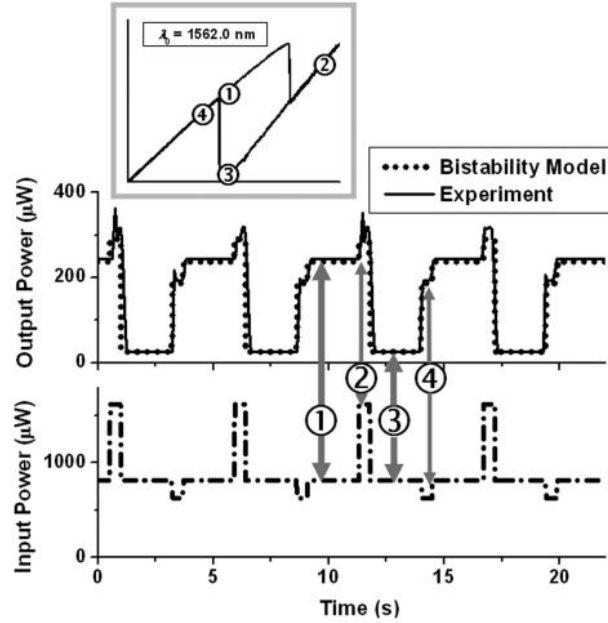
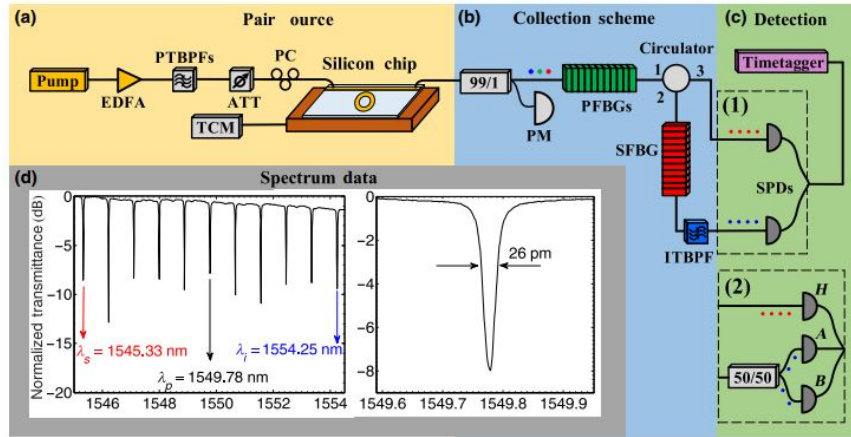


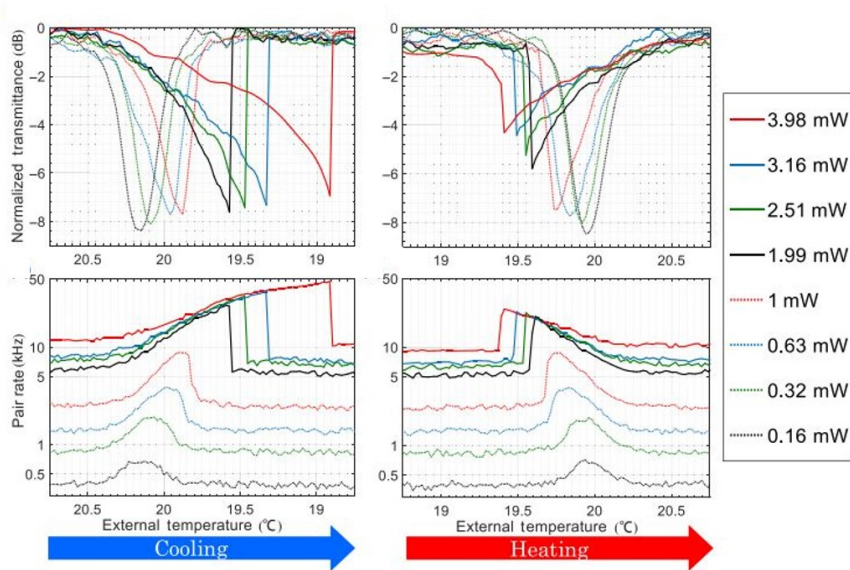
Figure 1.10: All-optical memory demonstration in a silicon MRR driven by optical bistability around $\lambda \sim 1560$ nm. The markers represent the different states in the optical memory corresponding to the positions marked in the hysteresis loop [92].

idler wavelengths and a zoomed resonance at 1550 nm wavelength having FWHM of 26 pm. Fig. 1.11(b) shows the experimental results showing the transmission at different power levels for the sample being heated and cooled. Correspondingly the pair generation rate is measured. It is observed that more number of photons are generated by cooling the substrate. But in this case, the complete sample's temperature is changed to enhance the photon pair generation rate, thus affecting the operation of other devices on the chip. However, there has not been detailed study regarding controlling the bistability to enhance the photon pair generation by actively tuning the MRR. Using this technique to align the pump wavelength with the resonance protects the other devices in the chip from being operated at other temperatures. In this thesis, we study about electrically controlling the bistability to align the pump wavelength with the MRR resonance and demonstrate efficient four wave mixing.

The other parameter for active controlled MRRs is the switching speed. The reconfiguration speed or switching time reported in literature for each of the microheaters of a switching matrix is $\sim 4 \mu\text{s}$ [80]. These microheaters have been mostly deposited on the top oxide. These devices also find application in wavelength multiplexing where the usual response time reported is 10 - 20 μs [62]. As the main application targeted in



(a)



(b)

Figure 1.11: (a) Schematic of the experimental setup used to generate and detect photon pairs using a MRR of $100 \mu\text{m}$ radius, inset: MRR transmission spectrum showing the position of the pump, signal and idler wavelengths along with zoom view of one of the resonances showing the FWHM, (b) normalized transmission spectrum of the MRR and the photon pair generation rate for different input optical power obtained while cooling and heating the sample temperature [50].

these works is wavelength tuning, different methods like etching an undercut have been adopted to reduce the tuning power which instead leads to the increase in the fall time to $\sim 170 \mu\text{s}$ [93, 94]. However with proper design of air trenches, the transient time could be reduced to $6\text{-}9 \mu\text{s}$ when input wavelength was set at resonance [62]. Further reduction in reconfiguration speed ($4 \mu\text{s}$) was obtained by replacing the silicon-di-oxide top cladding with silicon nitride [79]. All these configurations have been demonstrated

by integrating the microheater on top oxide which ideally exhibits high response time. Hence, we have studied slab integrated microheater with MRR which produces comparatively faster response time [95]. Nevertheless, silicon MRR is also attractive for quantum photonic applications as already discussed. However, there has not been much investigation on transient effect in non-linear photonics switching and memory applications. Especially, optical power dependent switching response is especially important for quantum photonic applications where nonlinear $\chi^{(3)}$ process is harnessed for entangled and/or heralded single-photon generation [96, 85], all-optical logic operation via free carrier dispersion effect [97], and all-optical bistable switching by the use of optical pulses [92]. All-optical memory is another attractive application of optical bistability and has been studied by Almeida *et al.* [92]. In this thesis we have also studied the transient response of the MRRs integrated with microheaters. For operating in the non-linear regime, the non-linear physics including Kerr non-linearity and two-photon absorption have been considered to simulate the thermo-optic response. Finally bistable switching and optical memory is proposed towards the end of the work.

1.2 Research Objective

In the literatures discussed above, we observed that compact silicon MRRs are becoming significant for quantum photonic applications, especially for entangled photon pair generation via spontaneous four wave mixing (SFWM) process. This is due to its requirement of lower threshold pump power levels in comparison to that of an alternative option of reasonably longer spiralled photonic wire waveguide (centimeter-long) [70]. However, fixed wavelength operation is challenging at high input power levels in silicon MRRs. In general, the experiments are usually carried out by adjusting/tuning the pump laser wavelength along with the changed power levels [98]. Alternatively, it was proposed for compensation of nonlinear phase-shift by adjusting operating temperatures of the silicon photonics chip as a whole [50]. This is something unacceptable for large-scale photonic integrated circuits in which the MRR based photon sources are to be independently programmed. Hence, we propose a method to control the optical bistability of MRRs using an integrated phase-shifters. Therefore, we set our objective

to study in detail about the working principle of a silicon MRR, physics of nonlinear phase-shifts, and finding a suitable solution such that its optical bistability can be controlled by locally driven electrical signal. To accomplish the objective, we decided to study and design the MRRs having high extinction, Q-value, low-loss, etc followed by fabricating and characterizing them. It was also targeted to develop methods and techniques to reconfigure the MRRs to achieve efficient tunability using electro-optic phase-shifters as well as thermo-optic phase shifters, and finally demonstrating efficient non-linear processes like stimulated four wave mixing and optical memory in silicon MRR by controlling the optical bistability using the integrated phase-shifter. The transient response for the MRR integrated with phase shifter was also decided to be studied for different power levels to demonstrate the impact of switching in quantum photonics circuit. All the devices planned for the study and demonstration were fabricated in IIT Madras using the in-house fabrication facilities (Centre for NEMS and Nanophotonics). The devices were also chosen to operate around the communication wavelength $\lambda \sim 1550$ nm as the characterization equipments were easily available in our Integrated Optoelectronics laboratory.

1.3 Thesis Organization

To execute the research objective, we have first designed a single mode rib waveguide MRR on 220 nm SOI. The non-linear physics behind the operation of MRRs have been considered to establish a model for the optical bistability in silicon MRRs. To actively tune the resonant wavelength, both electro-optic and thermo-optic phase shifters have been studied to be integrated with the MRRs. Using the MRRs integrated with thermo-optic phase-shifters we have demonstrated the phase-controlled optical bistability while operating the MRR in non-linear regime. Finally as an application we have demonstrated efficient stimulated four wave mixing and optical memory. The complete work of this thesis is structured as follows:

Chapter-2 starts with the device design of single mode silicon waveguide for different device layer thickness and MRR design on 220 nm SOI. It further discusses the background theory of the non-linear effects and origin of optical bistability in silicon MRRs.

Detailed simulation study of electrical control of the optical bistability of a MRR integrated with a phase shifter is presented. A model has also been developed for the phase dependent hysteresis which becomes prominent at high input optical power.

Chapter-3 is reserved for the phase-shifter design. Detailed simulation study to integrate p-i-n/p-n diodes using diffusion doping on thicker SOI device layer thickness is presented. The complete fabrication flow and the simulation results are presented for integrating p-i-n/p-n diodes with rib waveguides. Further, microheater design and simulation is performed for the thermo-optic phase shifters. Both metal microheaters and doped microheaters integrated on the slab of the rib waveguides have been studied.

Chapter-4 presents the fabrication and experimental demonstration of the phase-shifters. p-i-n/p-n diode waveguides are fabricated and applications like variable optical attenuators and TPA based photodiodes have been demonstrated on 2 μm SOI. Further the fabrication of p-i-n.p-n diodes for smaller device layer thickness is presented. Next the integration of thermal phase-shifter with the MRR is presented along with the characterization results for both p-doped and metal microheaters. Various parameters of the MRRs have also been extracted and presented.

Chapter-5 demonstrates the electrical control of the optical bistability in the MRR. Phase dependent hysteresis followed by demonstration of stimulated four wave mixing is reported to show the efficiency enhancement in a non-linear process by electrically controlling the hysteresis.

Chapter-6 discusses the transient response of the MRR integrated with microheater. Both simulation and experimental results are presented considering the effect of bistability on the transient response. Electrically controlled optical memory is proposed. Preliminary results of a voltage controlled optical memory is presented.

Chapter-7 marks the conclusion of the thesis. It consists of a brief summary of the research work presented and discussions on the possible work which can be done in the future.

CHAPTER 2

Background Theory and Simulation Results

Microring resonators have been designed, fabricated and characterised to study the optical bistability and mitigate the problem of parking the laser wavelength in the resonance at high power by integrating phase shifters. This chapter deals with the theory and simulation results of the MRR when operated both in linear and nonlinear regime. Simulations on single mode rib waveguide design followed by MRR working principle is presented. The physics of non-linearity in silicon MRRs is highlighted along with the theory of optical bistability in them. The non-linear simulation results are presented for the designed MRRs to observe the phase dependent hysteresis. Finally, a model is developed to control the optical bistability using an external phase-shifter.

2.1 Waveguide Design Parameters

Single mode rib waveguides were designed in different device layer thickness (H) in SOI starting from $2\ \mu\text{m}$ to 220 nm using Lumerical MODE Solutions simulator. The rib height (H), waveguide width (W) and slab height (h) were chosen to ensure sufficient confinement of the optical mode in the rib waveguide as well as guide a single mode of TE polarization. Fig. 2.1 shows the schematic of a rib waveguide in SOI substrate. We have considered higher device layer in our study to incorporate diffusion doping to obtain p-i-n/p-n diodes integrated with the rib waveguide MRRs. The dimensions for the rib waveguide have been considered from the single mode cut-off regions already developed by our laboratory group [99, 100]. Fig.2.2 shows the single-mode cut-off region for both TE and TM modes for different values of rib width ($0\ \text{nm} \leq W \leq 2\ \mu\text{m}$) and slab height ($0\ \text{nm} \leq h \leq 2\ \mu\text{m}$) on $2\ \mu\text{m}$ SOI device layer thickness. Similarly Fig. 2.3 shows the single-mode region along with the different TE/TM higher order modes by varying rib width ($300\ \text{nm} \leq W \leq 700\ \text{nm}$) and slab height ($0\ \text{nm} \leq h \leq 200\ \text{nm}$) on 220 nm SOI. The degree of polarization of the guided optical modes are defined by

comparing the fraction of transverse electric field component along x-direction. It can be expressed as follows [100]:

$$\gamma_x = \frac{\int |E_x|^2 dx dy}{\int (|E_x|^2 + |E_y|^2) dx dy} \quad (2.1)$$

where, E_x and E_y are the transverse electric field components of a guided mode. For $\gamma_x \geq 0.6$, the optical mode is considered as quasi-TE polarized, whereas for $\gamma_x \leq 0.4$ it is considered to be quasi-TM polarized. If the value of γ_x lies in between 0.4 and 0.6 it is termed as hybrid mode (HE) as shown in Fig. 2.3. The calculations of Fig. 2.2 and 2.3 were done using air as the top cladding. These simulations paved the way to decide the rib waveguide dimensions to be used in this thesis work. However, there is slight difference in the single-mode cut-off boundaries when the top cladding is replaced with silicon-di-oxide. The detail dimensions of the different device layer thickness will be discussed along with the integration process of p-i-n/p-n diode in Chapter-3.

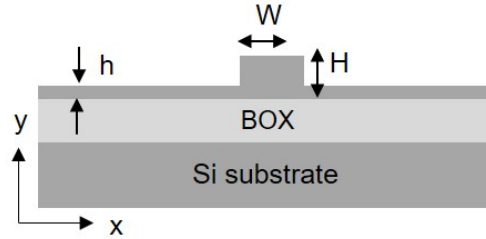


Figure 2.1: Schematic cross-section of a rib waveguide on SOI, W: rib width, H: rib height, h: slab height.

For the demonstration of MRRs, 220 nm SOI was chosen due to its capability to fabricate tighter bends with compact design which will give high field enhancement factor to perform efficient non-linear processes. Fig. 2.4(b) shows the simulated optical mode profile for TE polarization on 220 nm SOI for the waveguide dimensions of $W = 420$ nm, $H = 220$ nm, $h = 150$ nm. The dimensions of the waveguide have been chosen such that it supports single mode TE polarization [100]. The optical mode profile of TE polarization designed on $2 \mu\text{m}$ SOI ($W: 2 \mu\text{m}$, $H: 2 \mu\text{m}$, $h = 1.5 \mu\text{m}$) is also shown in Fig. 2.4(a). $2 \mu\text{m}$ SOI device layer has been considered as a starting device layer to fabricate p-i-n/p-n diodes using diffusion doping to achieve electro-optic phase shifters.

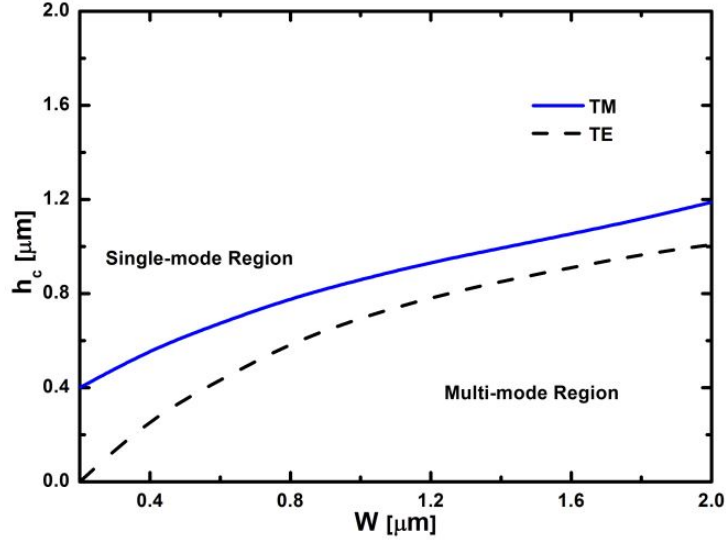


Figure 2.2: Calculated values of slab height (h_c) cut-off as function of rib width (W) for $2 \mu\text{m}$ device layer thickness. Area above blue and black lines represents the single mode regions for TM and TE polarization respectively. Bottom and top claddings are considered to be BOX and air, respectively. Calculations are carried out for $\lambda = 1550 \text{ nm}$ [99].

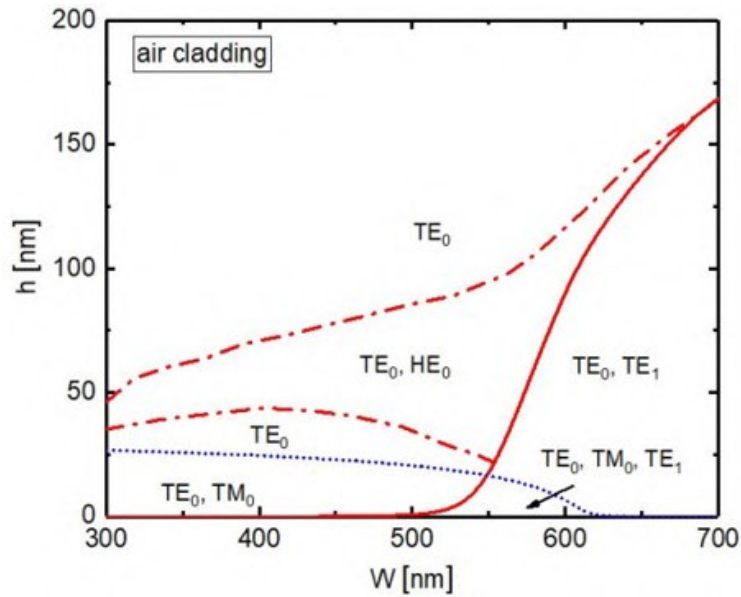


Figure 2.3: Calculated values of slab height (h) cut-off as function of rib width (W) for 220 nm device layer thickness for TE, TM and HE mode guidance. Bottom and top claddings are considered to be BOX and air, respectively. Calculations are carried out for $\lambda = 1550 \text{ nm}$. The dotted lines demarcate the regions for different modes [100].

However lower device layer thickness is used to demonstrate MRRs since they provide compact design and tighter bends.

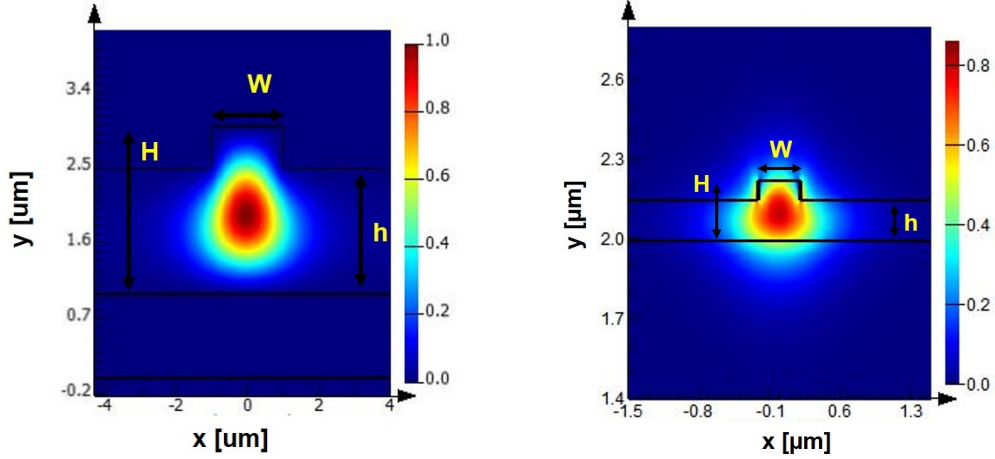


Figure 2.4: Simulated optical mode profile (intensity of the electric field) of the fundamental TE mode for rib waveguide dimensions of (a) $W = 2 \mu\text{m}$, $H = 2 \mu\text{m}$, $h = 1.5 \mu\text{m}$, (b) $W = 420 \text{ nm}$, $H = 220 \text{ nm}$, $h = 150 \text{ nm}$.

2.2 Working Principle of Microring Resonators

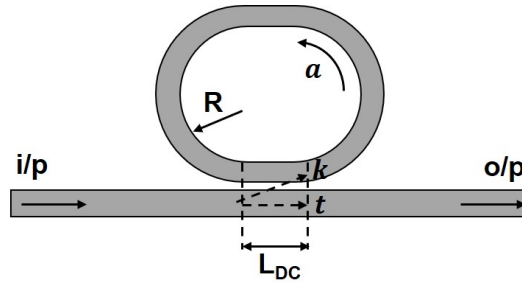


Figure 2.5: Schematic of all pass MRR, R : bend radius of MRR, L_{DC} : length of directional coupler, a : single pass transmission coefficient, k : cross-coupling coefficient, t : through-coupling coefficient.

Silicon MRRs in all-pass configuration as well as add-drop configuration are used for entangled photon-pair generation via four wave mixing process [101, 88]. The working principle of MRRs has been studied in detail in [102]. Here we will discuss the theory of MRRs in all-pass configuration for the completeness of the thesis. The design of the MRR has been made considering the integration of active phase shifters on it's slab. Fig. 2.5 shows the schematic of the race-track all-pass MRR with input and output port marked as 'i/p' and 'o/p' respectively. The average bend radius of the ring resonator is ' R ' ((outer ring radius + inner ring radius)/2) and the directional coupler region where the light couples from the bus waveguide to ring waveguide has a length marked as ' L_{DC} '. ' t ' and ' k ' are the through-coupling and cross-coupling coefficient

respectively in the ring-bus waveguide junction. ‘ a ’ is the single pass transmission coefficient which considers both the bend loss and the propagation loss, which can be expressed as

$$a = \exp\left[\frac{-(\alpha_{bend} \cdot 2\pi R + \alpha_{wg} \cdot L)}{2}\right] \quad (2.2)$$

where, α_{bend} and α_{wg} are the power attenuation coefficients due to bend induced loss and propagation loss respectively. The total perimeter of the MRR is ‘ L_T ’ ($L_T = 2\pi R + 2L_{DC}$). The directional coupler is considered as loss-less ($t^2 + k^2 = 1$) in this case. The total throughput transmission of the MRR can thus be expressed as

$$T = \frac{a^2 - 2at\cos\phi + t^2}{1 - 2at\cos\phi + (at)^2} \quad (2.3)$$

where ϕ is the total phase accumulated in the round trip of the ring and the phase of the directional coupler. At resonance, $\phi = 2m\pi$, where ‘ m ’ is an integer, and the throughput transmission can be expressed as

$$T = \frac{(a - t)^2}{(1 - at)^2} \quad (2.4)$$

The MRR was designed using the single mode design parameters used for 220 nm SOI device layer thickness with 2 μm buried oxide (BOX) and handle layer thickness of 700 μm . The MRR and bus waveguides are designed in all-pass configuration with a silicon rib of width $W = 420$ nm, height $H = 220$ nm, slab height $h = 150$ nm. The input/output access waveguides are integrated with grating couplers (GCs) for interfacing with standard single-mode optical fibers over a broad wavelength range as mentioned in [16]. The gap between the waveguides in the directional coupler region was chosen depending on the coupling strength (κ : Eq. 2.5).

$$\kappa(\lambda) = \pi \frac{\Delta n_{eff}(\lambda)}{\lambda} \quad (2.5)$$

where, $\Delta n(\lambda)$ is the difference of the effective refractive index of the symmetric and anti-symmetric modes of the directional coupler for a particular wavelength of operation (λ). The coupling coefficient can be made completely wavelength independent depending on the application by designing wavelength independent directional cou-

plers [16]. Mode simulations were performed to extract the coupling strength between the two rib waveguides of the directional coupler by varying the slab height and gap as shown in Fig. 2.6. Considering the tolerance in our fabrication process, a parallel section of the DC of length $L_{DC} = 5 \mu\text{m}$ and gap $g = 150 \text{ nm}$ was chosen for the MRR design having waveguide bending radius $50 \mu\text{m}$, to ensure reasonable Q-values and extinction for resonances at $\lambda \sim 1550 \text{ nm}$. The slab height was kept considerably high to integrate the phase-shifters on the slab. For this design, an expected free spectral range (FSR) of resonances is $\sim 2 \text{ nm}$ ($\sim 250 \text{ GHz}$).

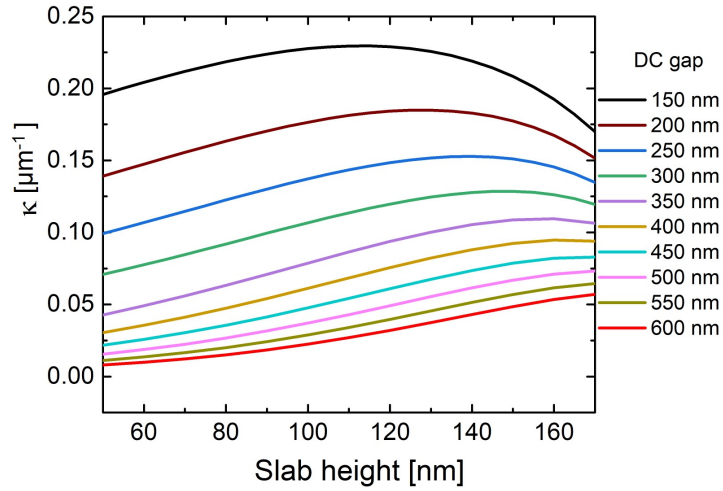


Figure 2.6: Plot showing the coupling strength ($\kappa [\mu\text{m}^{-1}]$) as a function of slab height and directional coupler (DC) gap (g) for wavelength $\lambda = 1550 \text{ nm}$ on 220 nm SOI.

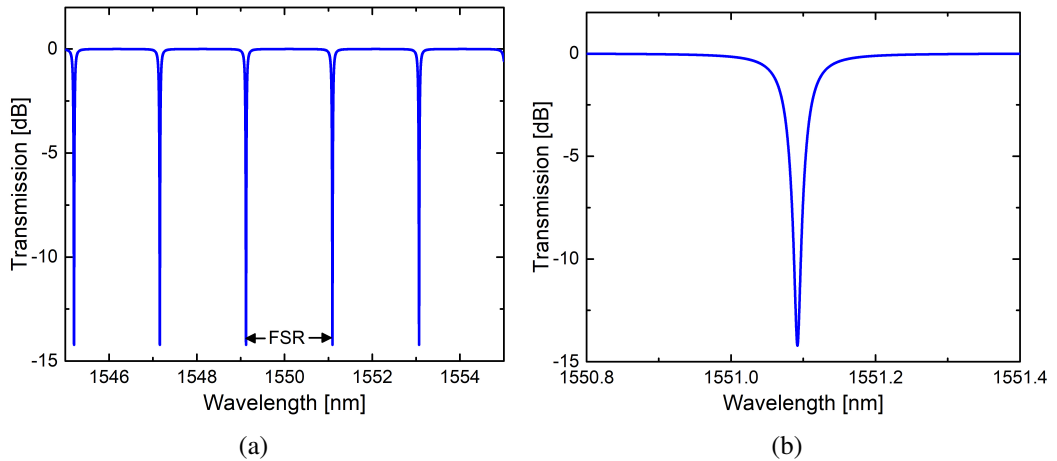


Figure 2.7: Simulated transmission spectrum of the designed MRR of bend radius (R) = $50 \mu\text{m}$, $L_{DC} = 5 \mu\text{m}$ for (a) $1545 \text{ nm} \leq \lambda \leq 1555 \text{ nm}$, (b) zoom resonance around $\lambda \sim 1550 \text{ nm}$.

The simulated transmission spectrum for the MRR with the above mentioned di-

mensions is shown in Fig. 2.7(a), where the separation between two successive resonances is known as Free Spectral Range (FSR), which is expressed as follows [102]:

$$FSR = \frac{\lambda^2}{n_g L} \quad (2.6)$$

where, λ is the operating wavelength, n_g is the group index and L is the perimeter of the microring. Fig. 2.7(b) shows the MRR resonance around 1550 nm wavelength. The Q-value extracted for this resonance is 64000. This structure has been used for further studies by integrating thermo-optic phase shifters. For this simulation we have not considered wavelength dependent coupling coefficient, hence the extinction ratio is same for all the resonance wavelength as shown in Fig. 2.7. Using this theoretical background and design of the MRR we will discuss the different non-linear effects that take place inside Silicon MRRs.

2.3 Nonlinear Effects in Microring Resonators

The nonlinear optical $\chi^{(3)}$ processes in silicon waveguides have been exploited for various CMOS technology compatible integrated photonic functions such as on-chip wavelength conversion [103, 104, 105, 89], all-optical signal processing [39], frequency comb generation [106] and very lately for a large-scale integrated quantum photonics circuit applications [86, 85]. At high optical intensities, the induced polarization in a material exhibits a nonlinear dependence on the electric field. The polarization can be expressed in terms of power series of the electric field.

$$\mathbf{P} = \epsilon_0 \chi^{(1)} \mathbf{E} + \epsilon_0 \chi^{(2)} \mathbf{E}^2 + \epsilon_0 \chi^{(3)} \mathbf{E}^3 + \dots \quad (2.7)$$

where, \mathbf{E} is the electric field, \mathbf{P} is the polarization and χ is the susceptibility. The first order term mainly contributes to the linear process and the higher order terms are generated during non-linear process, i.e. at high optical intensities. Silicon being a centrosymmetric crystal, $\chi^{(2)}$ is generally zero, and the $\chi^{(3)}$ processes ideally contributes for the non-linearity in silicon. The refractive indices also change with the non-linearity. The intensity-dependent refractive index can be expressed in terms of linear refractive

index (n_0) and non-linear refractive index (n_2)

$$n = n_0 + n_2 I \quad (2.8)$$

This n_2 contributes to the Kerr non-linearity for silicon. n_2 is related to $\chi^{(3)}$ as follows:

$$n_2 = \frac{D\chi^{(3)}}{4n_0^2\epsilon_0 c} \quad (2.9)$$

where, D is the degenerate factor whose value is ‘3’ for self-phase modulation (SPM) and ‘6’ for cross-phase modulation (XPM) [107].

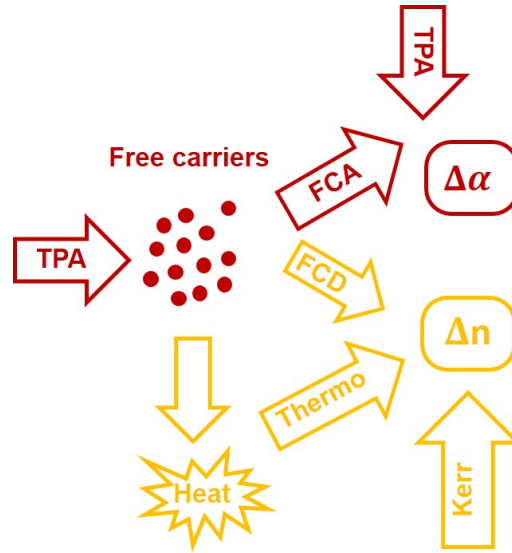


Figure 2.8: Non-linear mechanisms that impact the photon pair generation inside a silicon photonic device when high optical power is launched into it. [108].

Two-photon absorption (TPA) is another non-linear mechanism which is dominant in silicon at high optical power [109, 110]. This mechanism has also been exploited to demonstrate different functionalities like TPA based photodetector [111], Raman laser [112] etc. During the two-photon absorption process, since the total energy of two photons of $\lambda \sim 1550$ nm ($E = \frac{hc}{\lambda} = 0.8$ eV) is higher than the silicon bandgap ($E_g(\text{Si}) = 1.12$ eV), they are absorbed to transit electrons from ground state to higher energy levels. This results in the generation of free carriers. The free carriers are either absorbed by free carrier absorption (FCA) or dispersed by free carrier dispersion (FCD). Heat energy is also produced during this dissipation process as silicon is an indirect band-gap semiconductor which gives rise to thermal phase modulation (TPM).

The complete non-linear processes are illustrated using the schematic in Fig. 2.8. The absorption processes (TPA and FCA) translate to loss and the Kerr non-linearity, the FCD and the thermal effect contribute to the change in the refractive index which finally translates to phase. The contribution from the TPM and FCD can be expressed in a simplified manner as following using n_2' and n_2'' respectively (for $\lambda_p \sim 1550$ nm) [113]:

$$n_2' = \left(\frac{dn_{eff}}{dT} \right)_{\lambda_p} \cdot \left(\frac{\beta\tau_h}{\rho C} \right) \quad (2.10)$$

$$n_2'' = -8.2 \times 10^{-16} \cdot \lambda_p^2 \cdot \left(\frac{\beta\tau_e}{2E_p} \right) \quad (2.11)$$

where τ_h is the thermal relaxation time, ρ is the mass density and C is the specific heat capacity of waveguide core, $\left(\frac{dn_{eff}}{dT} \right)_{\lambda_p}$ is the effective thermo-optic co-efficient for the guided mode at λ_p and β is the two-photon absorption coefficient.

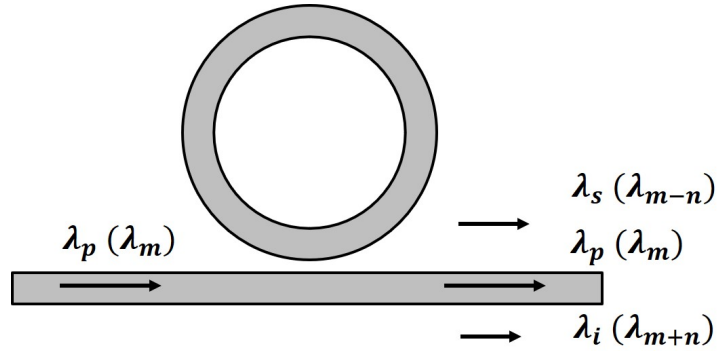


Figure 2.9: Schematic representation of a silicon microring resonator in all-pass configuration. The representative wavelength symbols are shown for the pump laser and generated signal/idler photons via spontaneous four wave mixing process: m stands for the m -th order resonance.

A silicon microring resonator (MRR) designed with photonic wire waveguide is an attractive device in silicon based CMOS compatible quantum photonics technology. Low-loss waveguide, tightly confined guided modes, compact footprint and optical field enhancement around resonances are the key factors making silicon MRR so attractive, especially for generating entangled photon pairs via spontaneous four wave mixing (FWM) process [114]. Fig. 2.9 shows a MRR in all-pass configuration where a pump laser of wavelength λ_p is matched to m -th order resonance (λ_m) and the correlated photon pairs (idler and signal) are generated at neighbouring resonances at λ_{m+n} and λ_{m-n} , respectively, where $n = 1, 2, 3, \dots$

2.3.1 Bistability: Theory and Modelling

Spontaneous FWM or stimulated FWM in silicon via $\chi^{(3)}$ process requires intense pump power for the non-linearity to set in. Compact MRR with a suitably designed waveguide core in SOI substrate is an excellent device to enhance the field strength of a pump laser light for the spontaneous emission of correlated photon pairs (signal and idler); all operating at different resonance wavelengths satisfying energy and momentum conservation. It has been shown that the average power of all photons $P_{\bar{N}}$, generated via spontaneous FWM process is proportional to the sixth power of field enhancement factor F_0 inside a MRR ($P_{\bar{N}} \propto F_0^6$) [115]. In case of stimulated FWM, a relatively weaker signal laser is added along with the pump laser and intense idler photons are generated; evolution of pump-, signal-, and idler intensities are classically evaluated by solving nonlinear coupled wave equations [116]. However, there are many bottlenecks to overcome for an efficient FWM process in silicon MRRs. Besides self-phase modulation due to nonlinear Kerr effect, the TPA at communication wavelengths ($\lambda \sim 1550$ nm) and subsequent free carrier induced plasma dispersion (absorption and reduction in refractive index) are the major cause of concern for stabilizing pump field strength exactly at a given resonance wavelength. The resonance shifts towards higher wavelengths with the increase in input pump power as shown in Fig 2.10. Though these have been studied in detail by several researchers [117, 118, 119], we would like to revisit here in the light of controlling bistability of pump field strength inside the MRR via external phase detuning using an integrated phase shifter. Our aim here is to study the bistable hysteresis of the MRR as a function of applied phase (ϕ_A : actively controlled by an integrated microheater or by a p-i-n waveguide phase-shifter) and enabling it for compensating unwanted pump power dependent nonlinear phase-shift ϕ_{NL} .

To estimate ϕ_{NL} as a function of the input pump power P_{in} , operating at an arbitrary wavelength λ_p , we consider a silicon MRR of radius R in all-pass configuration as shown in Fig. 2.11 for which t and k are the through- and cross-coupling coefficients in the bus- and ring waveguide directional coupler (DC). For simplicity, we have assumed loss-less DC in this case such that $t^2 + k^2 = 1$. Further in steady-state, we have the

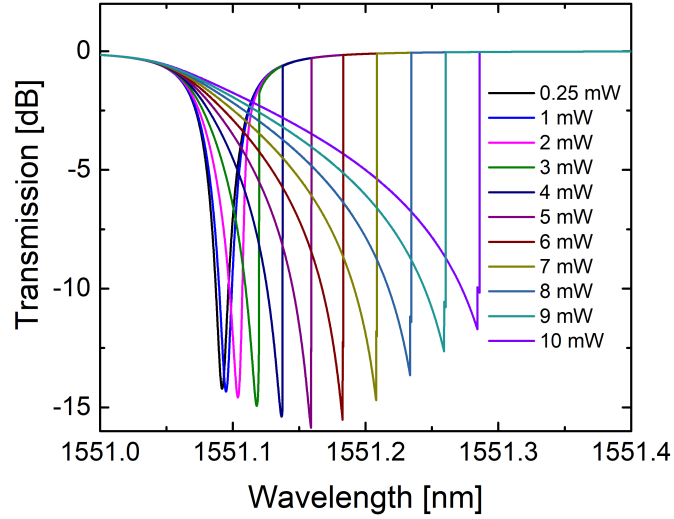


Figure 2.10: Simulated transmission spectrum of a MRR for different input optical power.

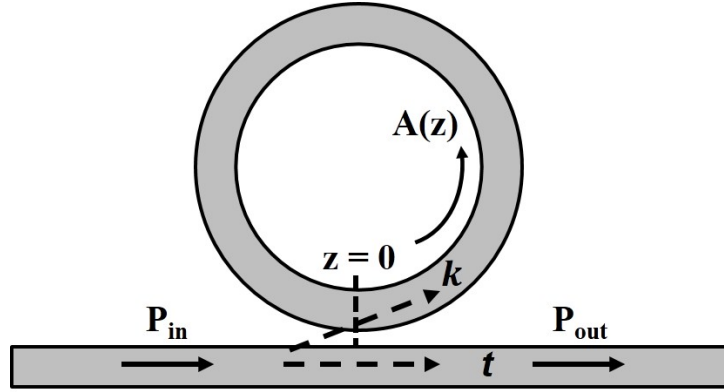


Figure 2.11: Schematic representation of a microring resonator in all-pass configuration showing the through-coupling coefficient (t) and the cross-coupling coefficient (k) in the bus and ring waveguide directional coupler. P_{in} is the input pump power to the MRR at $z = 0$, and P_{out} is the output power. $A(z)$ is assigned for the field amplitude of circulating light-wave along the ring waveguide.

following boundary conditions [119]:

$$A_0 = -jk\sqrt{P_{in}} + tA_0e^{-j(\phi_{rt}-j\alpha_{rt})} \quad (2.12)$$

$$E_{out} = -jkA_0e^{-j(\phi_{rt}-j\alpha_{rt})} + t\sqrt{P_{in}} \quad (2.13)$$

where the pump field amplitude $A(z = 0) = A_0$, the round-trip loss and phase in the ring are defined by α_{rt} (in Np) and ϕ_{rt} (in rad.), respectively. Thus for a given launched power P_{in} , the circulating power inside the ring waveguide is $P_0 = |A_0|^2$ and

transmitted power is $P_{out} = |E_{out}|^2$. In a nonlinear regime, i.e. for a larger circulating pump power $P_0 = |A_0|^2$, α_{rt} and ϕ_{rt} can be decomposed into linear and nonlinear components:

$$\alpha_{rt} = \alpha_0 + \alpha_{NL} \quad (2.14)$$

$$\phi_{rt} = \phi_0 + \phi_{NL} \quad (2.15)$$

with loss parameter $\alpha_0 = \alpha \cdot L$ and round-trip phase parameter $\phi_0 = \frac{2\pi}{\lambda_p} \cdot (n_{eff}L)$, where α is the waveguide loss co-efficient (Np/m), n_{eff} is effective index of the guided mode and $L = 2\pi R$ is the ring waveguide perimeter. Both α_0 and ϕ_0 are independent of circulating power P_0 .

The nonlinear loss parameter α_{NL} depends on TPA process and TPA induced free carrier absorption (FCA) process, both are dependent on P_0 as follows [120]:

$$\alpha_{NL} = \alpha(TPA) + \alpha(FCA) \quad (2.16)$$

From the detail theoretical analyses given by [113], we can model α_{NL} as following:

$$\alpha_{NL} = \alpha_1 P_0 + \alpha_2 P_0^2 \quad (2.17)$$

with

$$\alpha_1 = \beta \cdot \left[\frac{1 - e^{-\alpha_{rt}}}{\alpha_{rt}} \right] \left(\frac{L}{A_{eff}} \right) \quad (2.18)$$

$$\alpha_2 = \frac{\beta \sigma_e \tau_e}{2E_p} \cdot \left[\frac{1 - e^{-2\alpha_{rt}}}{2\alpha_{rt}} \right] \left(\frac{L}{A_{eff}^2} \right) \quad (2.19)$$

where β is the two-photon absorption co-efficient, $2E_p$ is the energy of two pump photons, σ_e is free carrier absorption co-efficient, τ_e is the free carrier life-time and A_{eff} is the effective area of the waveguide cross-section. It must be noted that the factor in parenthesis in both Eqns. 2.18 and 2.19 depends on waveguide geometry and device footprint. Again, the nonlinear phase ϕ_{NL} is a combined result of self-phase modulation (SPM) due to Kerr effect, free carrier dispersion (FCD) followed by TPA, and thermo-optic phase modulation (TPM) due to free carrier relaxation:

$$\phi_{NL} = \phi(SPM) + \phi(FCD) + \phi(TPM) \quad (2.20)$$

Similar to α_{NL} , we can also simplify ϕ_{NL} as:

$$\phi_{NL} = \delta_1 P_0 + \delta_2 P_0^2 \quad (2.21)$$

with

$$\delta_1 = \frac{2\pi}{\lambda_p} \left[n_2 \cdot \frac{1 - e^{-\alpha_{rt}}}{\alpha_{rt}} \right] \left(\frac{L}{A_{eff}} \right) \quad (2.22)$$

$$\delta_2 = \frac{2\pi}{\lambda_p} \left[(n_2' + n_2'') \cdot \frac{1 - e^{-2\alpha_{rt}}}{2\alpha_{rt}} \right] \left(\frac{L}{A_{eff}^2} \right) \quad (2.23)$$

In Eqn. 2.22, the nonlinear Kerr co-efficient n_2 contributes to SPM, whereas in Eqn. 2.23, n_2' and n_2'' contribute to TPM and FCD, respectively as expressed earlier in Eq. 2.10 and 2.11.

Thus by inserting the complete expressions of α_{rt} and ϕ_{rt} , we can numerically solve the transcendental Eqns. 2.12 and 2.13 in order to obtain circulating power P_0 and transmitted power P_{out} for a given input power P_{in} operating at wavelengths λ_p tuned around a resonance wavelength λ_m (corresponding to $\phi_0 = 2m\pi$, $m = 1, 2, 3, \dots$). Because of quadratic presence of P_0 in the coupled analytical expressions of ϕ_{rt} and α_{rt} , multi-valued solutions exist. It has been shown experimentally that the bistable solutions of P_0 and P_{out} exist and could be obtained depending on the history of input power levels of P_{in} , i.e., increasing or decreasing [92, 97]. However, since the field enhancement factor $F_0 = \frac{|A_0|}{\sqrt{P_{in}}} = \sqrt{\frac{P_0}{P_{in}}}$ is crucial at a given input power level of P_{in} for maximizing correlated photon pair generation, we have investigated bistability as a function of actively controlled phase ϕ_A as shown in Fig. 2.12. Eqns. 2.12 and 2.13 can be solved numerically by considering P_{in} as a parameter and variable ϕ_{rt} as following:

$$\phi_{rt} = \phi_0(\lambda_p) + \phi_{NL}(P_{in}, \lambda_p) + \phi_A(\lambda_p) \quad (2.24)$$

Nevertheless, from the analytical model discussed here predicts that the field enhancement factor can be stabilized and/or maximized to a value of F_0^{max} for a given P_{in} and $\lambda_p \neq \lambda_m$, simply by detuning ϕ_A to a desired value of ϕ_A^{op} such that $\phi_0(\lambda_p) + \phi_{NL}(P_{in}, \lambda_p) + \phi_A^{op}(\lambda_p) = 2m\pi$. Since ϕ_{NL} changes with P_{in} , one can adjust the ϕ_A accordingly by integrating an active phase-shifter in the MRR without compromising on λ_p . We have discussed this in detail by numerical simulations in the following section.

2.3.2 Simulation Results

Fig. 2.12 shows design layout of the device for numerical simulation. The device was designed on a silicon-on-insulator (SOI) substrate with a device layer thickness of 220 nm, buried oxide (BOX) layer thickness of $2 \mu\text{m}$, and handle layer thickness of $700 \mu\text{m}$ using the parameters described in Section-2.1. The bending radius of MRR is considered to be $50 \mu\text{m}$, with a straight coupling section of $5 \mu\text{m}$ to ensure sufficient coupling from the bus to the ring waveguide. An external phase-shifter (ϕ_A) has been integrated to control the non-linear phase (ϕ_{NL}). The calculated device parameters (using Lumerical full vectorial mode solver) and other important physical parameters/constants used for the numerical simulations are given in Table 2.1. We have considered resonance wavelength $\lambda_m = 1549.12 \text{ nm}$ ($m = 549$) and $\lambda_p = 1549.32 \text{ nm}$ satisfying to a value of $\phi_0(\lambda_p) - \phi_0(\lambda_m) = -0.2\pi$ (corresponding to $FSR/10$) for simulating P_0/P_{in} and P_{out}/P_{in} hysteresis curves as a function of ϕ_A ; keeping in mind it can be increased or decreased by integrating a microheater or a p-i-n diode.

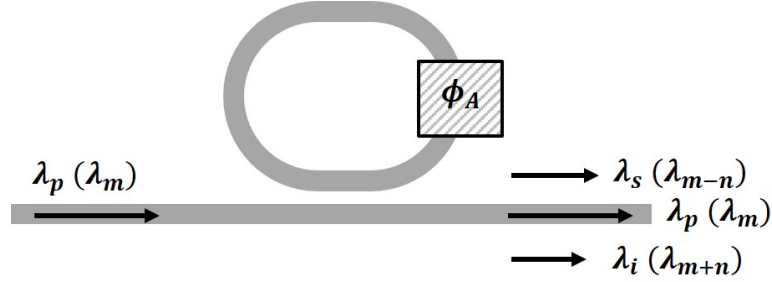
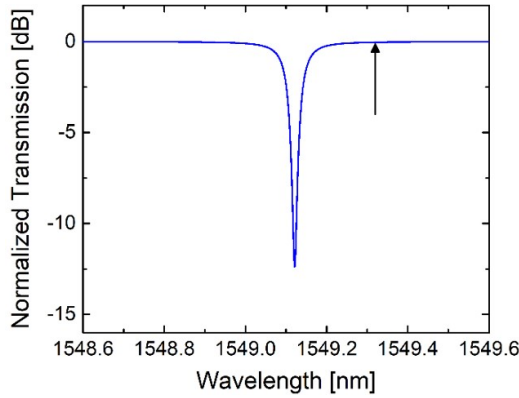


Figure 2.12: Schematic representation of a silicon microring resonator in all-pass configuration integrated with a phase-tuning element (ϕ_A). The representative wavelength symbols are shown for the pump laser and generated signal/idler photons via spontaneous four wave mixing process: m stands for the m -th order resonance.

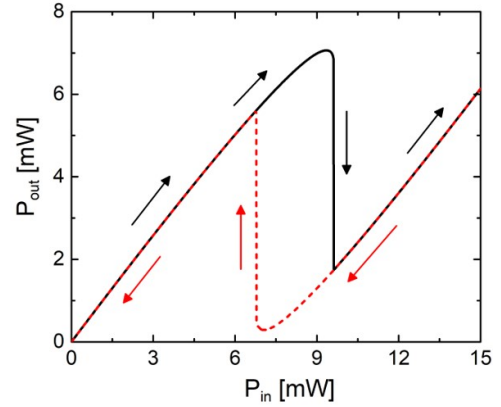
The simulation for power dependent hysteresis was performed first followed by the phase dependent hysteresis. Fig. 2.13(a) shows the MRR resonance around 1550 nm wavelength along with the position of the off-resonant pump wavelength placed $\sim 200 \text{ pm}$ right to study the power dependent hysteresis. The resonance shifts right with the increase of the input power, due to the generation of heat as a result of all the non-linear processes. A dip in the output power is observed when the probe wavelength matches with the resonance wavelength in the forward path while increasing the optical power as

Table 2.1: Material constants and Waveguide parameters used for a microring resonator bistability simulation.

Parameters	Value	Remark
L	324 μm	Race Track Design ($R = 50 \mu\text{m}$)
α	5 dB/cm	Experimental Observation
k^2	0.04	Estimated for a loss-less DC
t^2	0.96	Estimated for a loss-less DC
A_{eff}	0.25 μm^2	Calculated ($\lambda = 1550 \text{ nm}$)
n_{eff}	2.623	Calculated ($\lambda = 1550 \text{ nm}$)
n_g	3.764	Calculated ($\lambda \sim 1550 \text{ nm}$)
FSR	2 nm	Calculated ($\lambda = 1550 \text{ nm}$)
Q-Value	6.4×10^4	Calculated ($\lambda = 1550 \text{ nm}$)
λ_m	1549.12 nm	Calculated ($m = 549$)
λ_p	1549.32 nm	$\phi_0(\lambda_p) - \phi_0(\lambda_m) \approx -0.2\pi$
$\frac{dn_{eff}}{dT}$	$1.8 \times 10^{-4} K^{-1}$	Calculated ($\lambda = 1550 \text{ nm}$)
n_2	$6 \times 10^{-18} m^2/W$	[118]
β	$6.7 \times 10^{-12} m/W$	[120]
σ_e	$1.97 \times 10^{-21} m^2$	[120]
τ_e	1 ns	[113]
τ_h	1 μs	[113]
C	705 J/kg.K	[113]
ρ	$2.3 \times 10^3 \text{ kg.m}^{-3}$	[113]



(a)



(b)

Figure 2.13: Simulated (a) wavelength dependent transmission spectrum of the MRR along with the position of the off-resonant wavelength, (b) power dependent hysteresis curve obtained from Fig. 2.13(a) by increasing and decreasing the input optical power.

shown by the black solid curve in Fig. 2.13(b). During the reverse process of reducing the optical power, the probe wavelength matches with the resonance wavelength at a lower value of input power as shown by the red dotted lines in Fig. 2.13(b), thus giv-

ing rise to the power dependent optical hysteresis. Following this simulation we have studied the applied phase dependent hysteresis by tuning the phase externally.

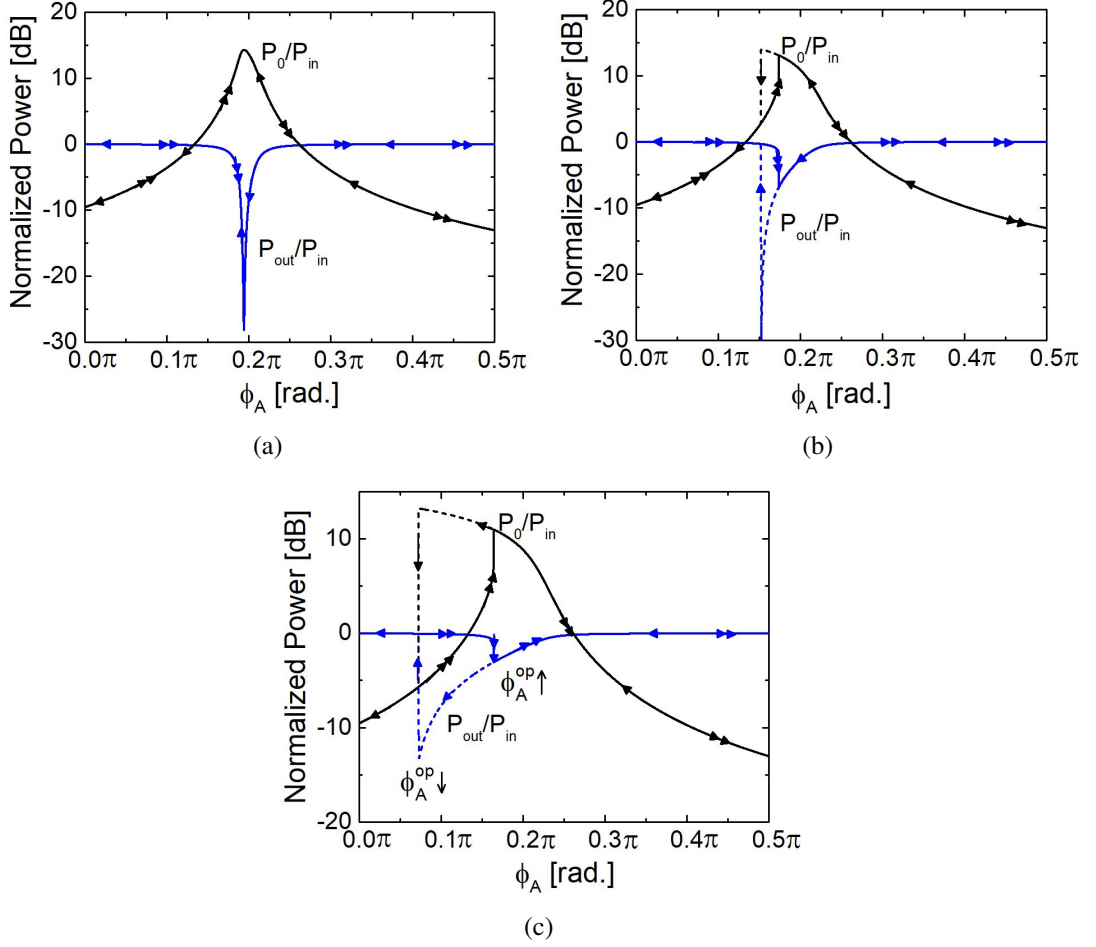


Figure 2.14: Simulated output power (P_{out} , blue curve) and the cavity power (P_0 , black curve) normalized to input power P_{in} as a function of ϕ_A increasing/decreasing in the MRR for: (a) $P_{in} = 1\text{ mW}$, (b) $P_{in} = 4\text{ mW}$, (c) $P_{in} = 8\text{ mW}$. Double arrows represent the path with increasing ϕ_A and single arrows for decreasing ϕ_A . The simulation was carried out for parameters given in Table 2.1.

Fig. 2.14 shows the hysteresis curves for three different pump power levels viz. $P_{in} = 1\text{ mW}$, 4 mW and 8 mW with respect to the applied phase (ϕ_A). As expected, no hysteresis is observed for a lower pump power level ($P_{in} = 1\text{ mW}$) when ϕ_{NL} is negligibly small as evident from Fig. 2.14(a). In this case, P_0/P_{in} is maximum and P_{out}/P_{in} minimum at $\phi_A \approx 0.2\pi = \phi_0(\lambda_p) - \phi_0(\lambda_m)$; both while its increasing and decreasing. However, at higher power levels, ϕ_{NL} dominates and maxima/minima occur at different ϕ_A values exhibiting clear hysteresis in ϕ_A as shown in Figs. 2.14(b) and 2.14(c) corresponding to $P_{in} = 4\text{ mW}$ and 8 mW , respectively. More importantly, stronger maxima

and minima appear while decreasing ϕ_A compared to those of increasing ϕ_A . Moreover, P_0/P_{in} decreases at resonances with the increase of P_{in} as a direct consequence of increase in α_{NL} . It must also be noted that while decreasing ϕ_A in a strongly nonlinear regime (see for example Fig. 2.14(c)), the value of P_0/P_{in} slowly increases to the maximum and drops suddenly ensuring the pump wavelength completely out of the resonance envelope. Therefore, one can be assured that relatively more stable and efficient nonlinear process is possible by adjusting a suitable value of ϕ_0 (or positioning pump wavelength λ_p slightly higher than the designated resonance wavelength λ_m) and subsequently bringing down ϕ_A from a higher value.

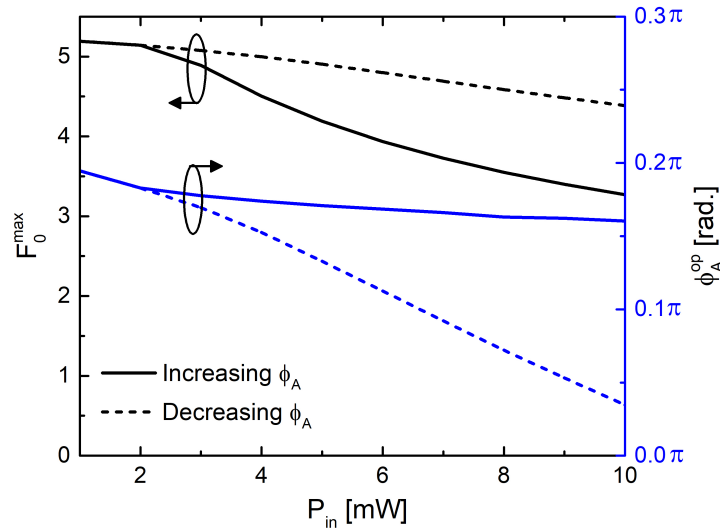


Figure 2.15: Simulated maximum field enhancement factor (F_0^{max}) and corresponding detuned phase (ϕ_A^{op}) as a function of P_{in} . The solid line represents the forward tuning of ϕ_A and dotted line shows the backward tuning of ϕ_A . The simulation was carried out for parameters given in Table 2.1

By defining maximum field enhancement factor as $F_0^{max} = \sqrt{\frac{P_o}{P_{in}}}$ for $\phi_A = \phi_A^{op}$, we have plotted F_0^{max}, ϕ_A^{op} vs. P_{in} in case of ϕ_A increasing (decreasing) from a lower (higher) value to a higher (lower) value and they are plotted in Fig. 2.15. Again according to our expectation, values of F_0^{max} are found to be same at lower pump powers ($P_{in} < 2$ mW) but widened apart for higher pump levels when compared between ϕ_A increasing and decreasing to ϕ_A^{op} . The important point here is that F_0^{max} decreases with P_{in} but it is always advantageous for settling corresponding ϕ_A^{op} by reducing ϕ_A from a higher value. This ϕ_A can be obtained by integrating a electro-optic phase shifter or a thermo-optic phase-shifter which we will discuss in Chapter-3.

2.4 Summary

In this chapter, we started with the design of single mode rib waveguides and further discussed the theory, design and simulation of all-pass MRRs on 220 nm SOI. We have then studied the background theory of optical bistability and its origin in silicon waveguides. The non-linear processes like Kerr nonlinearity, TPA, FCA, FCD have been considered to establish the theoretical model for optical bistability in silicon. Further, we have studied using simulations the resonance shift at high input power for MRRs and have formulated a method to mitigate the problem of parking the laser wavelength in the MRR resonance at high power by integrating a phase shifter and controlling the phase with it. We have performed all the simulations on a 50 μm radius MRR designed on 220 nm SOI to establish the theory. Simulation studies show that hysteresis exists after a certain value of input power and widens with the increase in the optical power, also the extinction ratio decreases due to the non-linear losses being prominent at high input power. Importantly we have concluded that though the field enhancement factor reduces with the input optical power, still it is higher when the pump wavelength is aligned to the resonance by reducing the applied phase (ϕ_A) from a higher value. Thus, the pump wavelength can be aligned with the resonance by reducing the applied phase from the external phase tuner. Using this theoretical background, we will next discuss in Chapter-3 the design of two different types of phase-shifters which can be integrated with the MRRs to tune the phase, along with the simulation results.

CHAPTER 3

Phase-shifter Design and Simulation

Phase-shifters are essential to be integrated with MRRs not only for wavelength detuning, but also for phase adjustments during nonlinear photonics processes as we already discussed in Chapter-2. In this chapter we have investigated and designed both p-i-n/p-n waveguide based electro-optic phase-shifters as well as doped and metal microheater integrated thermo-optic phase-shifters. The design parameters along with the simulation results are discussed such that the devices can be fabricated using the in-house fabrication facilities available at IIT Madras. Section- 3.1 deals with the design and simulation results to integrate p-i-n/p-n phase shifters using diffusion doping on SOI substrates. The doped microheater based thermo-optic phase shifters are presented in Section 3.2 followed by the metal microheater based thermo-optic phase shifters in Section 3.3. Finally, the chapter is summarized in Section 3.4.

3.1 Electro-optic Phase Shifters: P-I-N/P-N waveguides

The p-i-n/p-n waveguide junction diodes are considered to be important components for silicon photonics applications such as variable optical attenuator [121], on-chip Raman laser [112], two-photon absorption based photodetector [122], modulator [123, 124], and high-speed energy efficient transceiver circuits [125]. For all these applications, the junction diodes are mostly used to control the free carrier concentrations (holes and electrons) in the waveguide and hence properties of guided optical modes via plasma dispersion effect [76]. Typically, p-type and n-type doping regions are defined suitably across the waveguide by ion implantation method. The rib waveguide cross-sectional geometry is usually predefined to obtain desired overlaps between guided modes and injected/depleted free carrier concentration profiles. For depletion based modulator designs, the desired p-n junction profiles (e.g. U-shaped) are achieved by controlling the

ion implantation parameters/conditions such as energy of implanted ions, angular positioning of waveguide substrate w.r.t. incoming ion flux etc. [126, 127, 128, 129]. For

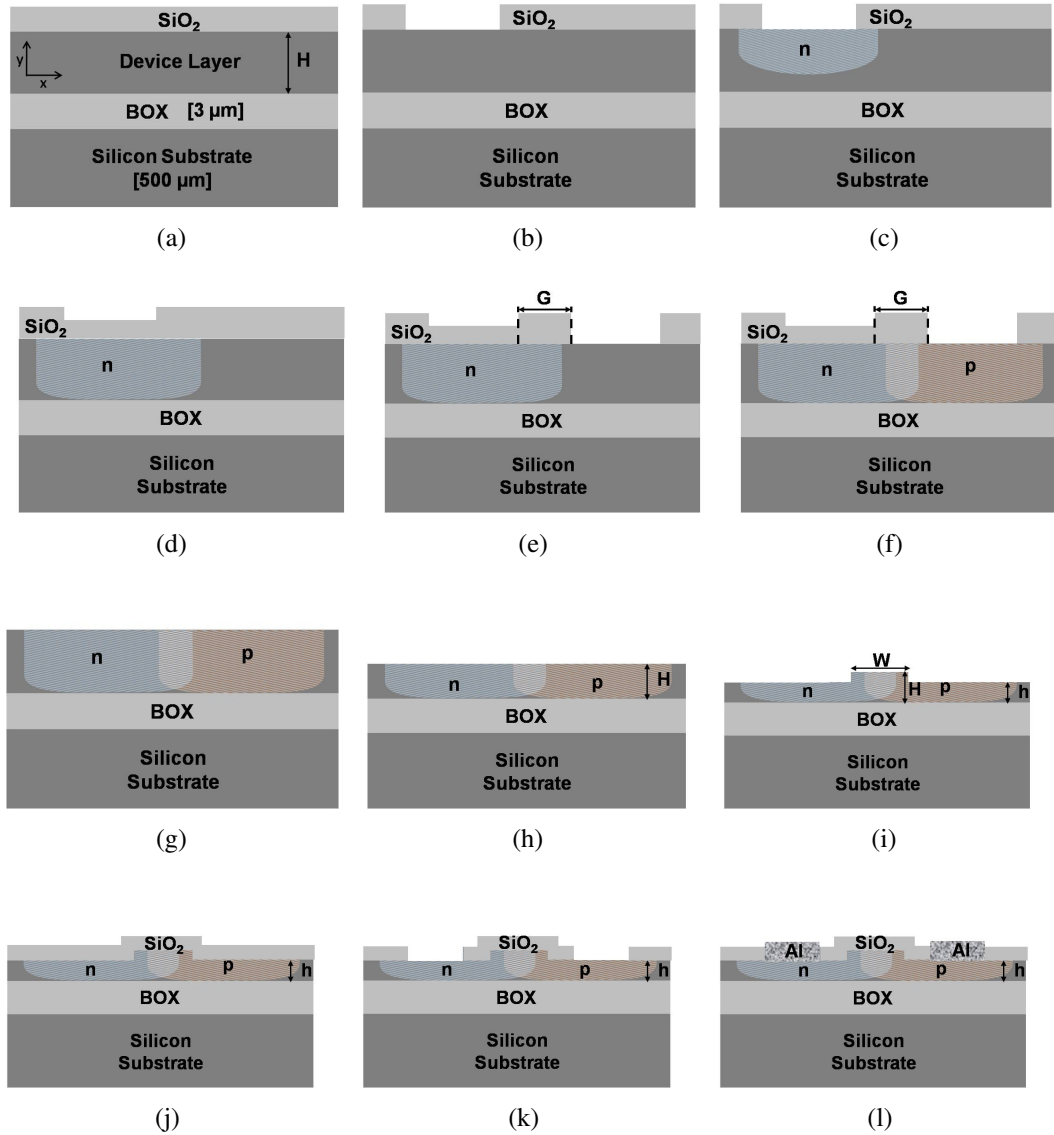


Figure 3.1: Fabrication process flow (see text for process parameters) and schematic cross-sectional views: (a) oxidation for masking during phosphorous diffusion, (b) etching of oxide for phosphorus diffusion window, (c) phosphorous diffusion, (d) oxidation for masking during boron diffusion, (e) etching of oxide for boron diffusion window, (f) boron diffusion, (g) removal of oxide after diffusion, (h) blanket etching to control device layer thickness of H , (i) rib waveguide definition (width W and slab height h optimized for single-mode guidance at $\lambda \sim 1550$ nm) by ICP-RIE using photoresist mask, (j) oxidation for surface passivation, (k) oxide etching for metal contacts, (l) metalization.

our work, to control the nonlinear phase by an integrated phase-shifter we have presented the design to integrate a p-i-n/p-n diode with the rib waveguide using diffusion

doping. As we have limitations on fabrication processes for doping, we have used diffusion doping on higher device layer thickness and reduced the dimensions to achieve the final smaller device layer. The fabrication steps to achieve p-i-n/p-n diodes using diffusion doping for different device layer thickness are shown in Fig. 3.1. We have also shown the possibility to engineer a predefined diffusion doped junction profile by controlling the device layer thickness (H), waveguide parameters (rib width : W and slab height : h) and position w.r.t. the doping windows in the following subsections. Thus the proposed approach provides additional freedom for the design of application specific waveguide parameters [130, 131, 22].

3.1.1 Design Parameters and Process Flow

The fabrication process steps of the proposed scalable SOI waveguide with laterally integrated p-i-n/p-n diodes is described in this section. Initially, a desired junction diode is formed by diffusing n-type and p-type dopants on a lightly p-type doped ($\sim 10^{14} \text{ cm}^{-3}$) SOI substrate with a thicker device layer ($H_0 > 1 \mu\text{m}$). Synopsys Taurus TSUPREM4 software [132] has been used to optimize the process parameters like oxide growth for hard mask, diffusion time t , temperature T and ambiance inside the furnace. The sequential fabrication steps and optimized process parameters in detail are as the following:

First, an oxide layer thickness of $\sim 600 \text{ nm}$ is grown by thermal oxidation process at $T = 1000^\circ\text{C}$ (dry : wet : dry oxidation for 20 : 110 : 20 minutes followed by 20 minutes annealing in N_2 ambiance) to be used as mask during phosphorous diffusion (n-type doping). Standard photolithography followed by oxide etching defines the window for phosphorus diffusion. This diffusion process is carried out at $T = 900^\circ\text{C}$ for $t = 3 \text{ hrs}$, resulting into a Gaussian dopant profile with a junction depth of $\sim 0.5 \mu\text{m}$ and a surface concentration of $\sim 3 \times 10^{20} \text{ cm}^{-3}$. Afterwards, an additional oxide layer thickness of $\sim 300 \text{ nm}$ is grown and subsequent photolithography, oxide etching were carried out to define the boron diffusion window. Boron diffusion (p-type doping) is performed at $T = 1100^\circ\text{C}$ for $t = 2 \text{ hrs}$, which is then followed by a final drive-in step in N_2 ambiance at $T = 900^\circ\text{C}$ for $t = 1 \text{ hr}$.

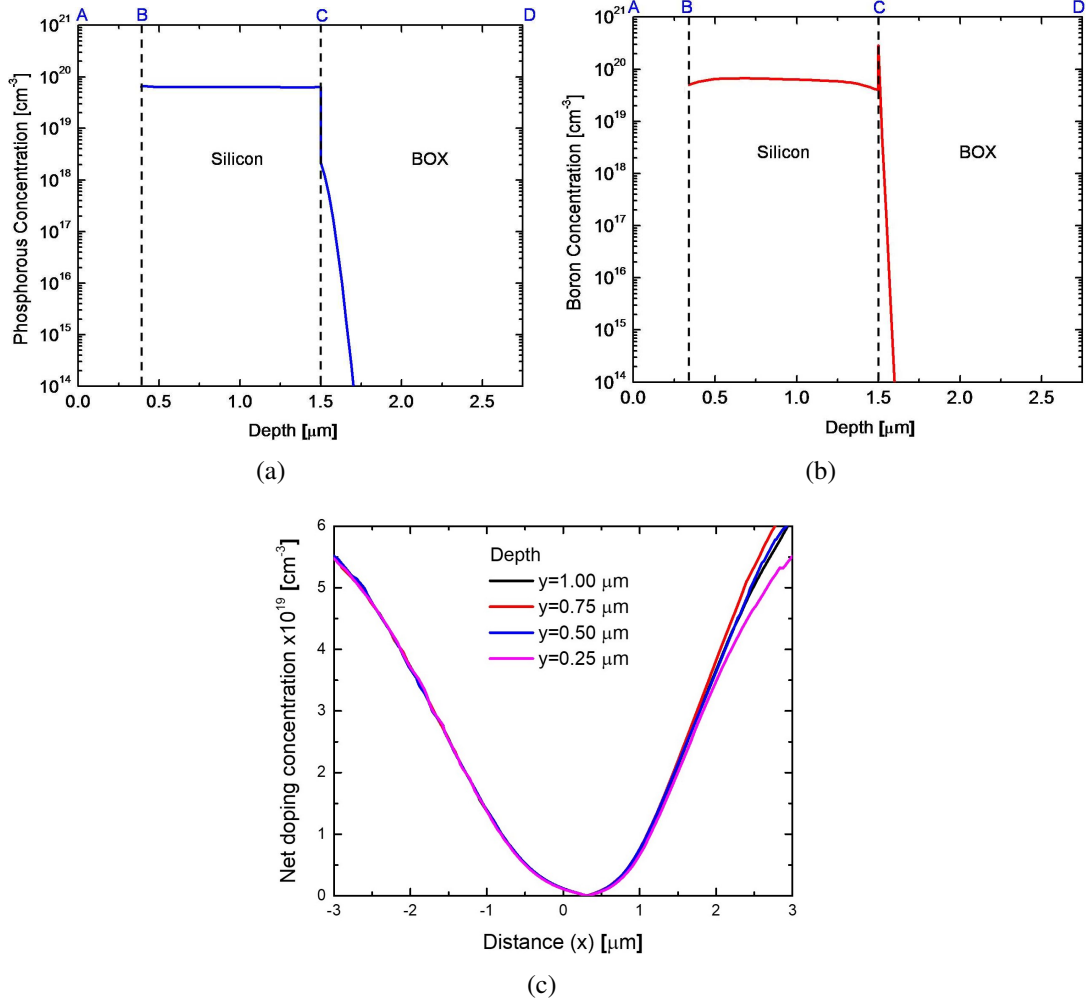


Figure 3.2: Concentration profile along the device layer after all the process steps (before blanket etching) for (a) n-doped region, (b) p-doped region. Point A corresponds to the initial SOI surface, point B is the SOI surface after all the oxidation and diffusion steps (corresponding to Figure 3.1(g)), point C is the silicon device layer and Buried Oxide (BOX) interface and point D is the end of the BOX (1 μm thickness was considered for simulation), (c) net doping concentration across the junction at different device layer thickness (0.25 μm , 0.5 μm , 0.75 μm and 1 μm).

The fabrication process flow described above provides nearly uniform doping concentrations up to the BOX layer for both p-type and n-type dopants and the gradient in the lateral direction is controlled by the gap G between the doping windows. The concentration profiles are extracted from the process simulation performed. A nearly step-type concentration profile with surface concentration of $\sim 9 \times 10^{19} \text{ cm}^{-3}$ and $\sim 5 \times 10^{19} \text{ cm}^{-3}$ is obtained in both the ‘n’ and ‘p’ - doped regions respectively as shown in Figures 3.2(a) and 3.2(b). Point A in Figures 3.2(a) and 3.2(b) is marked as

the top surface of the initial $H_0 = 1.5 \mu\text{m}$. As a result of the thermal oxidation steps (as in Figure 3.1(a) and 3.1(d)) silicon has been consumed and the effective height reduces from point A to point B. Point C marks the interface between the end of silicon device layer end and the buried oxide layer (BOX). Point D marks the end of the BOX ($1 \mu\text{m}$ thickness was considered for simulation). Dopant concentration profile along the horizontal slices are also extracted. Figure 3.2(c) shows the net doping concentration along the horizontal direction for device layer thickness of $1 \mu\text{m}$, $0.75 \mu\text{m}$, $0.5 \mu\text{m}$, and $0.25 \mu\text{m}$. It is observed that the neutral concentration point (junction) has a lateral shift from exact mid-point of the gap (G) between doping windows (right of $x = 0 \mu\text{m}$ on Figure 3.2(c)), which can be understood from the fact that the doping concentration in n-region is slightly more than that of p-region.

Once the ‘p’ and ‘n’ -regions are defined as discussed above, the wafer/substrate is ready to be etched to any desired device layer thickness H ($\leq 1.1 \mu\text{m}$, for a given $H_0 = 1.5 \mu\text{m}$) by using standard inductively-coupled plasma reactive ion etching (ICP-RIE). A blanket ICP-RIE with standardized recipe is necessary to control the device layer thickness without any degradation of surface quality. An appropriate lithography process and subsequent dry etching (ICP-RIE) are performed to define the waveguide along the center line (or shifted laterally by δ , if necessary) between doping windows. Here the gap (G) between the p-type and n-type doping windows (hence the actual position of the junction), value of δ , waveguide parameters W , H , and h decide the junction profile under the rib waveguide; they are studied in detail using a device simulator and discussed in the following sections. Once the waveguide is defined, final steps of fabrication, i.e. surface passivation (thermal oxide $\sim 200 \text{ nm}$) and metalization (to obtain the metal contacts or vias) are carried out. So far we have discussed the junction profiles for an initial device layer thickness of $H_0 = 1.5 \mu\text{m}$. However, the same diffusion parameters can also be used for higher initial device layer thicknesses (e.g., $H_0 = 2 \mu\text{m}$), but with a slight modification of junction profile.

3.1.2 Simulation Results: Optical

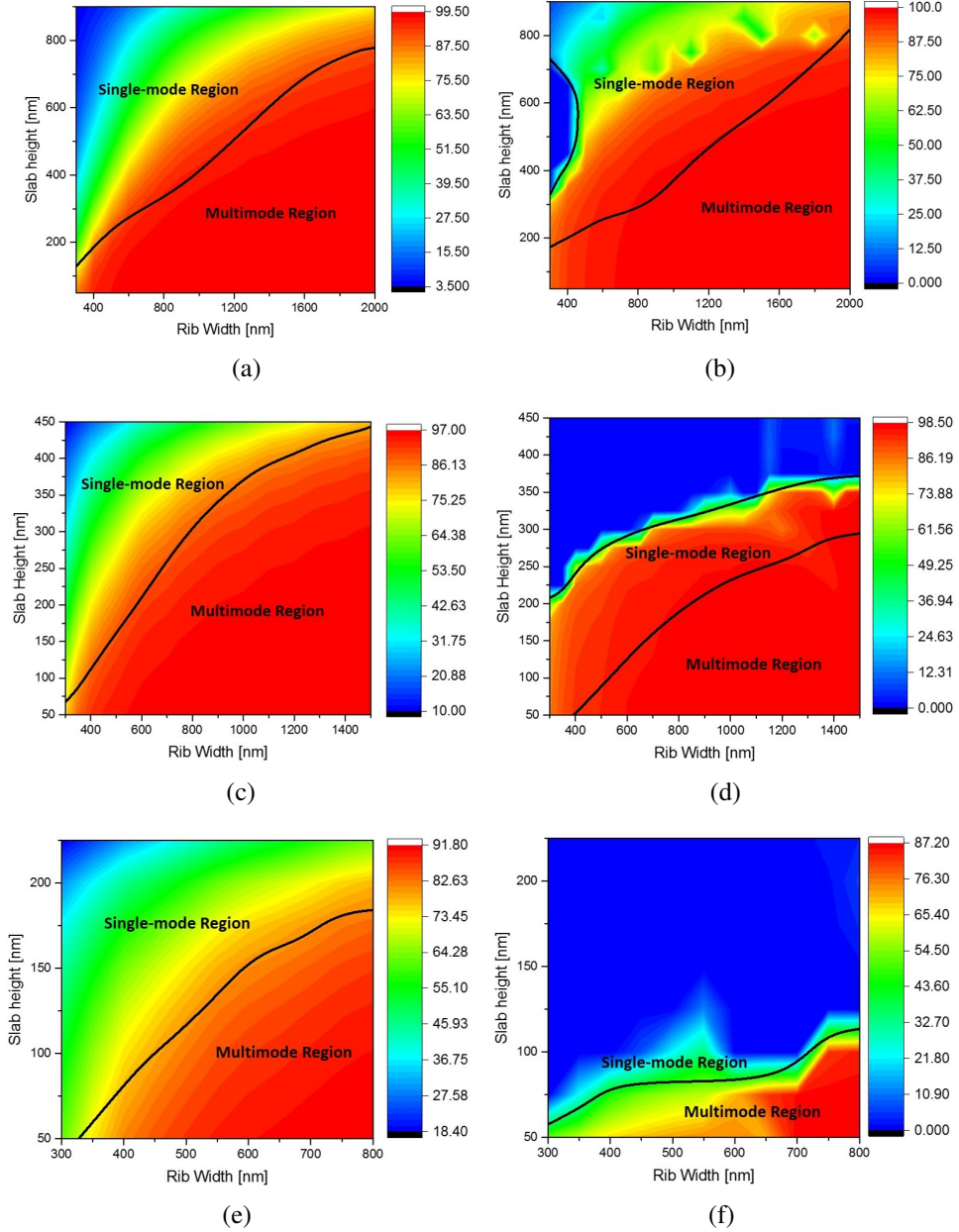


Figure 3.3: Single-mode cut-off in $W - h$ plane for the guidance of both TE and TM-polarization at $\lambda = 1550 \text{ nm}$. The color gradient is the measure of confinement strength of the fundamental guided mode underneath the rib width: (a) $H = 1 \mu\text{m}$ (TE), (b) $H = 1 \mu\text{m}$ (TM), (c) $H = 0.5 \mu\text{m}$ (TE), (d) $H = 0.5 \mu\text{m}$ (TM), (e) $H = 0.25 \mu\text{m}$ (TE), (f) $H = 0.25 \mu\text{m}$ (TM).

We have studied the electro-optic properties of three different single-mode waveguide designs integrated with p-i-n/p-n junctions as described earlier. For that we have chosen three different device layers viz., $H = 1 \mu\text{m}$, $0.5 \mu\text{m}$ and $0.25 \mu\text{m}$, respectively. The waveguide widths W and slab heights h are optimized by simulating the single-

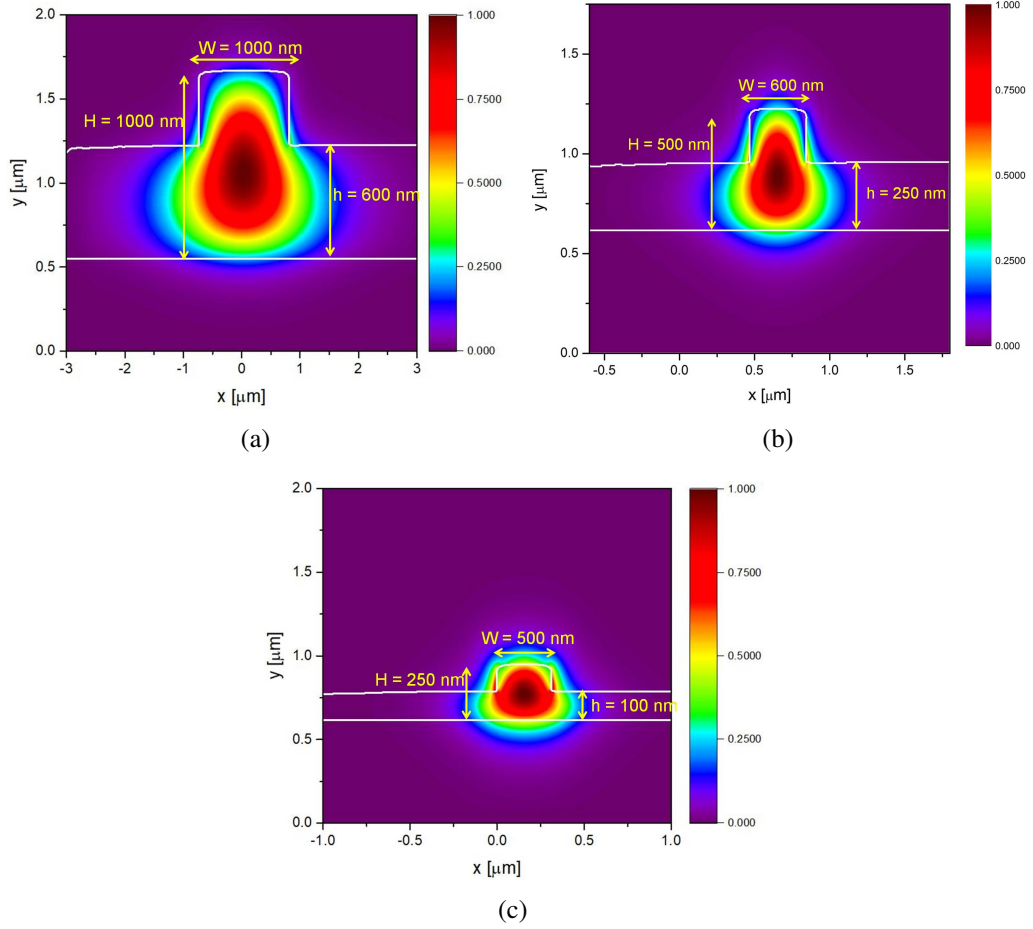


Figure 3.4: Simulated electric field distributions (E_x component) for the guidance of TE-polarization in single-mode waveguides ($\lambda = 1550$ nm) with SiO_2 surface cladding: (a) $W = 1 \mu\text{m}$, $H = 1 \mu\text{m}$, and $h = 0.6 \mu\text{m}$; (b) $W = 0.6 \mu\text{m}$, $H = 0.5 \mu\text{m}$, and $h = 0.25 \mu\text{m}$; (c) $W = 0.5 \mu\text{m}$, $H = 0.25 \mu\text{m}$, and $h = 0.1 \mu\text{m}$.

mode cut-off regions for each of the device layer thicknesses, using Lumerical MODE Solution [133]. Figs. 3.3(a) - 3.3(f) shows the contour plots for all the three device layer thickness for rib-width (W) vs. slab height (h), respectively. The color gradient shows the power confinement factor (Γ) for the fundamental mode ($\lambda = 1550$ nm, TE and TM-polarization) under the rib waveguide cross-section. It is defined as the fraction of power of the guided mode propagating within rib height ($y_1 \leq y \leq y_2$) and width

($x_1 \leq x \leq x_2$) and can be expressed as:

$$\Gamma = \frac{\int_{x_1}^{x_2} \int_{y_1}^{y_2} (\vec{\mathcal{E}} \times \vec{\mathcal{H}}^*)_z dx dy}{\int_{-\infty}^{\infty} \int_{-\infty}^{\infty} (\vec{\mathcal{E}} \times \vec{\mathcal{H}}^*)_z dx dy} \quad (3.1)$$

where $\vec{\mathcal{E}}$ and $\vec{\mathcal{H}}$ are electric and magnetic field components of the guided fundamental mode. The Γ values and single-mode guiding cut-offs are calculated with top cladding as SiO₂ (surface passivated), using Lumerical MODE Solutions [133]. The Γ value of a given rib waveguide is one of the deciding factors to optimize the gap (G) between doping windows depending on active device operations (e.g. VOA, Raman amplifier, phase-shifter etc.).

The chosen set of waveguide parameters of $\{W, H, h\} = \{1.0 \mu m, 1.0 \mu m, 0.6 \mu m\}$, $\{0.6 \mu m, 0.5 \mu m, 0.25 \mu m\}$, $\{0.5 \mu m, 0.25 \mu m, 0.1 \mu m\}$, are found supporting only the fundamental modes (verified for the guidance in TE-polarization at $\lambda = 1550$ nm) and corresponding electric field distribution for E_x components are shown in Figure 3.4. The estimated modal confinements are 0.85, 0.86 and 0.76, respectively. It must be noted that the single-mode waveguide designs with $H = 1 \mu m$ and $0.5 \mu m$ support both TE and TM-modes, whereas that for $H = 0.25 \mu m$ supports only the TE-mode. A combination of waveguide parameters (W, H, h) has to be chosen carefully to ensure that the confinement factor is nearly equal for both the polarization in order to obtain polarization independent behavior as mentioned in Table 3.1.

3.1.3 Simulation Results: Electro-optic

As mentioned earlier, the gap (G) between the doping windows and positioning the rib waveguide (δ -shift) plays an important role in dictating bias dependent electro-optic effect (plasma dispersion effect). The value of G was varied from $1 \mu m$ to $10 \mu m$ in steps of $1 \mu m$, to obtain both p-n and p-i-n junction diodes. Once the process parameters were optimized using Synopsys Taurus TSUPREM4 software for these device dimensions, electrical and optical simulations were performed using Lumerical DEVICE [134] and

Table 3.1: Calculated confinement factor (Γ) for both TE and TM polarization of the waveguide dimensions chosen for the three device layer thickness $H = 1 \mu\text{m}$, $H = 0.5 \mu\text{m}$ and $H = 0.25 \mu\text{m}$.

Waveguide geometry	Pol.	Γ [%]
H = 1 μm , W = 1 μm , h = 0.6 μm	TE	92
	TM	96
H = 0.5 μm , W = 0.6 μm , h = 0.25 μm	TE	86
	TM	93
H = 0.25 μm , W = 0.5 μm , h = 0.1 μm	TE	76
	TM	-

MODE Solutions [133]. The doping profile of the simulated structure in TSUPREM was imported to DEVICE simulator, which was then used to obtain electrical properties. The I-V/C-V characteristics, free carrier concentration profiles and the electric field profiles across junction were simulated.

The electric field profiles of the junction for various device layer thicknesses (obtained by the surface etching) were simulated starting from $H_0 = 1.5 \mu\text{m}$ as the initial thickness. Figures 3.5(a), 3.5(h), and 3.5(o) show the simulated 2D space charge field profile for $H = 1.0 \mu\text{m}$, $0.5 \mu\text{m}$ and $0.25 \mu\text{m}$, respectively. These device layer thicknesses were assumed to be obtained after blanket etching of the surface of initial device layer thickness $H_0 = 1.5 \mu\text{m}$ with diffusion doped diodes. For each of these simulations shown in Figure 3.5, the gap (G) between the doped regions was kept at $5 \mu\text{m}$ to form p-n junction within rib region for a maximum overlap with the guided mode. The simulation results for 2D space charge field distribution also confirm that the shape of depletion region for each of the cases is not exactly straight. Moreover, the device layer thickness in n-type doping window region is slightly reduced than the rest because of additional oxide layer grown for masking during p-type doping. However, this hardly influences if the rib waveguide is designed with a higher value of Γ and located right near the metallurgical junction. Further, it is interesting to note that though the shape of depletion region is slightly modified, the peak space-charge field remains nearly constant as the device layer thickness reduces by surface etching.

Once the device layer is etched and reduced to the desired thickness ($1 \mu\text{m}$, $0.5 \mu\text{m}$,

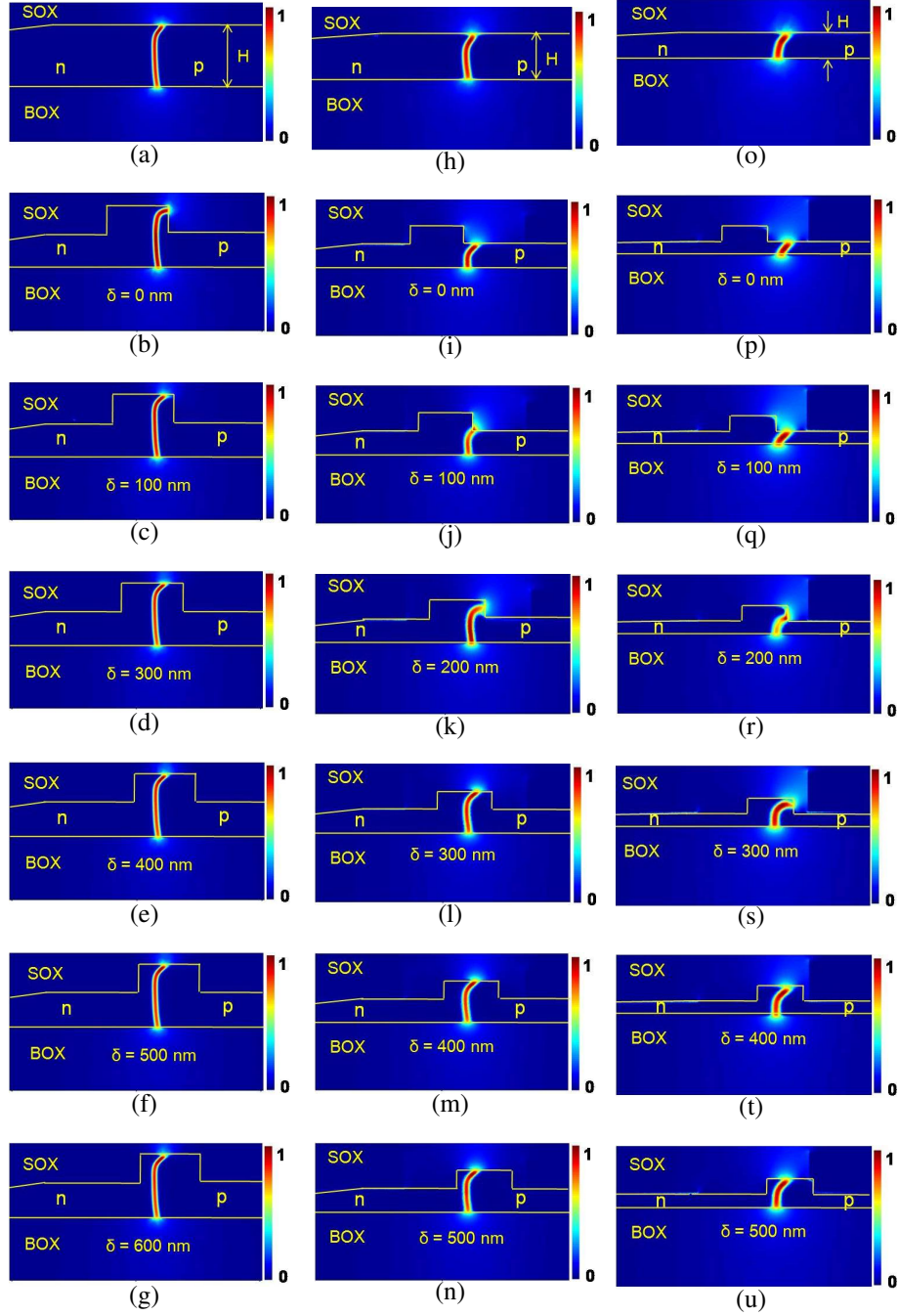


Figure 3.5: Space charge fields (a) for SOI thickness $H = 1 \mu\text{m}$, [(b)-(g)] for rib waveguides integrated with p-n diodes on $H = 1 \mu\text{m}$ for various δ shifts, (h) for SOI thickness $H = 0.5 \mu\text{m}$, [(i)-(n)] for rib waveguides on $H = 0.5 \mu\text{m}$ for various δ shifts, (o) for SOI thickness $H = 0.25 \mu\text{m}$ and [(p)-(u)] for rib waveguides on $H = 0.25 \mu\text{m}$ for various δ shifts, at 0 V bias voltage. The color grading is normalized to a scale of unity field strength.

0.25 μm), the respective designs of single-mode rib waveguides are defined. Figures 3.5(b), 3.5(i), and 3.5(p) show the space charge field strength for a single mode rib waveguides with parameters $\{W, H, h\} = \{1.0 \mu\text{m}, 1.0 \mu\text{m}, 0.6 \mu\text{m}\}$, $\{0.6 \mu\text{m}, 0.5 \mu\text{m},$

0.25 μm }, {0.5 μm , 0.25 μm , 0.1 μm }, respectively, which are defined exactly at the center between p- and n-type doping windows. It is evident that the depletion region is pushed towards p-type doping window because of slightly higher n-type dopant concentrations. However, the depletion region is desired to overlap well with the guided mode for its efficient electro-optic control of the guided modes. A qualitative understanding of electro-optic effects in silicon waveguide is helpful to interpret the simulation results. The free electron concentration ($\Delta N_e(x, y)$) and hole concentration ($\Delta N_h(x, y)$) in the waveguide are controlled by the applied bias voltage (V) across the diffusion doped p-i-n/p-n junction as proposed. It is well-known that free carriers cause complex dielectric constant change in the waveguide. The real part contributes to refractive index change (Δn) and imaginary part causes additional attenuation coefficient ($\Delta\alpha$). They are expressed using Soref's empirical model (for $\lambda = 1550$ nm) [76]:

$$\Delta n(x, y) = -[8.8 \times 10^{-22} \Delta N_e(x, y) + 8.5 \times 10^{-18} \{\Delta N_h(x, y)\}^{0.8}] \quad (3.2)$$

$$\Delta\alpha(x, y) = [8.5 \times 10^{-18} \Delta N_e(x, y) + 6.0 \times 10^{-18} \Delta N_h(x, y)] \quad (3.3)$$

where $\Delta N_e(x, y)$ and $\Delta N_h(x, y)$ are expressed in cm^{-3} ; $\Delta\alpha(x, y)$ is in cm^{-1} . Applying perturbation theory [135], the changes in effective the refractive index and attenuation coefficient for a guided mode can be expressed as:

$$\Delta n_{eff} = \frac{\int \int \vec{\mathcal{E}}^*(x, y) \cdot \Delta n(x, y) \vec{\mathcal{E}}(x, y) dx dy}{\int \int |\vec{\mathcal{E}}(x, y)|^2 dx dy} \quad (3.4)$$

$$\Delta\alpha_{eff} = \frac{\int \int \vec{\mathcal{E}}^*(x, y) \cdot \Delta\alpha(x, y) \vec{\mathcal{E}}(x, y) dx dy}{\int \int |\vec{\mathcal{E}}(x, y)|^2 dx dy} \quad (3.5)$$

where $\vec{\mathcal{E}}(x, y)$ is the electric field profile of the guided mode. Thus it is evident that the positioning of waveguide w.r.t. junction location is crucial for designing phase modulator and/or variable optical attenuator (VOA). First, we have studied the junction profiles by shifting the waveguide laterally (δ) in steps, w.r.t. the center of doping windows separated by 5 μm (see Figure 3.5). Thus we could find the optimized values

of δ corresponding to largest overlap between guided mode and junction profile.

For our simulation studies on single-mode rib waveguides (three designs as discussed earlier) with laterally diffused p-n junctions, we have shifted the rib position at steps of 100 nm towards the p-doping region (right) and compared the results to check for their respective optimum positions (δ_{opt}). Figures 3.5(i) to 3.5(n) show the shifting of rib for $H = 0.5 \mu\text{m}$ and Figure 3.5(p) to 3.5(u) is for $H = 0.25 \mu\text{m}$. The shifting of rib position for $H = 1 \mu\text{m}$ is required slightly more as the rib width for this dimension waveguides are higher compared to the waveguides defined on $0.5 \mu\text{m}$ or $0.25 \mu\text{m}$.

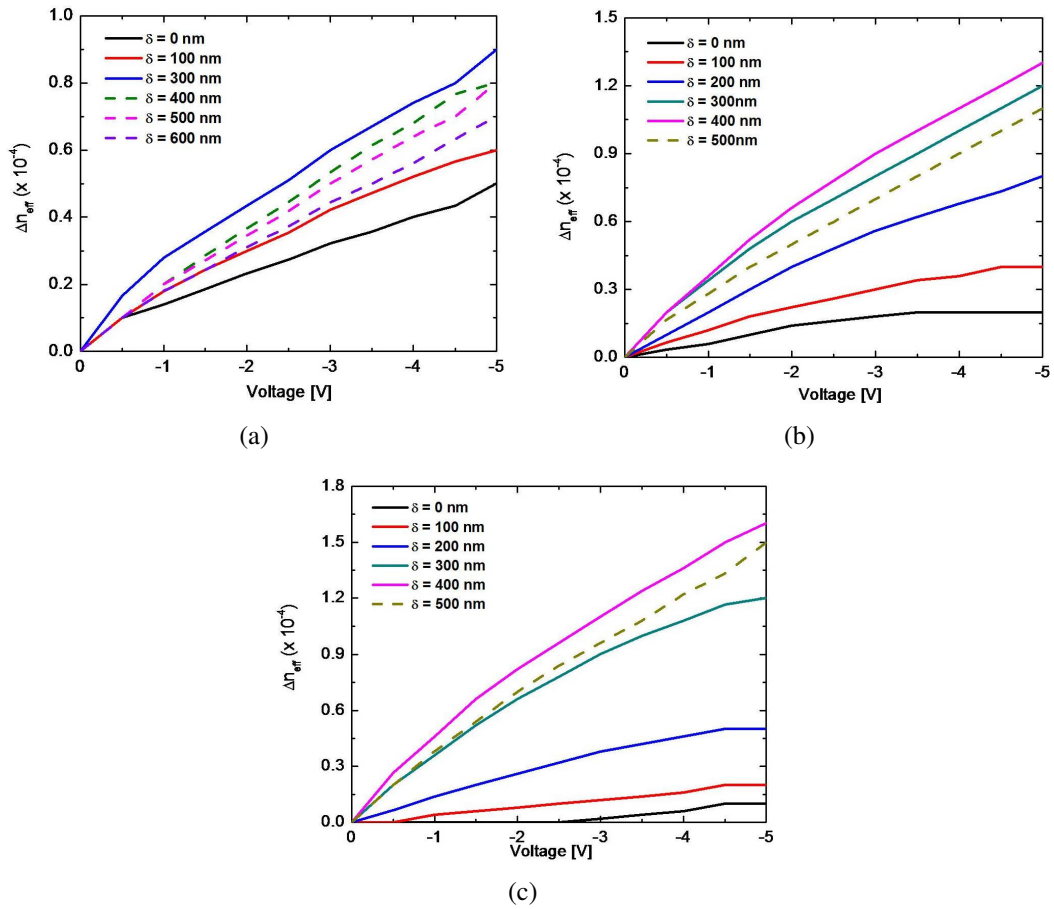


Figure 3.6: Change of n_{eff} as a function of reverse bias across waveguide p-n junction diode of reduced geometry with δ (offset from the middle of the gap between doping windows) as a parameter for waveguide with device layer thickness (a) $H = 1 \mu\text{m}$, (b) $H = 0.5 \mu\text{m}$, (c) $H = 0.25 \mu\text{m}$.

To optimize the rib waveguide position, we calculated the Δn_{eff} as a function of applied bias (up to -5 V) using Lumerical MODE Solution and they are plotted in Figure 3.6. It is observed from Figure 3.6(a), that for $H = 1 \mu\text{m}$ the maximum Δn_{eff} is obtained

for $\delta \sim 300$ nm. For $\delta > 300$ nm, the value of Δn_{eff} decreases as shown with the dashed lines. It is further evident in Figure 3.6(b) and 3.6(c) that the values of Δn_{eff} are maximum for $\delta \sim 400$ nm. Thus the positioning of waveguide w.r.t. the doping windows plays an important role in optimizing the figures of merit of silicon waveguide based electro-optic devices.

Table 3.2: Calculated junction peak electric field strengths for three different single-mode waveguides designed with device layer thickness of $H = 1 \mu\text{m}$, $H = 0.5 \mu\text{m}$ and $H = 0.25 \mu\text{m}$ for varying δ . The peak electric field strength at 0 V bias (E_0) and -5 V bias (E_{-5}) are compared.

δ [nm]	H = 1 μm		H = 0.5 μm		H = 0.25 μm	
	W = 1 μm , h = 0.6 μm		W = 0.6 μm , h = 0.25 μm		W = 0.5 μm , h = 0.1 μm	
	E_0 [V. μm^{-1}]	E_{-5} [V. μm^{-1}]	E_0 [V. μm^{-1}]	E_{-5} [V. μm^{-1}]	E_0 [V. μm^{-1}]	E_{-5} [V. μm^{-1}]
0	10.2	38.3	10.2	35.7	10.3	34.1
100	11.2	39.8	11.3	41.7	9.3	31.1
200	11.9	41.7	9.74	36.2	12.3	47.3
300	12.0	41.8	11.5	38.7	10.3	34.9
400	12.0	41.9	11.9	40.1	11.3	38.1
500	12.0	41.9	11.8	39.4	11.4	39.0
600	12.0	41.8	-	-	-	-

It must be noted that the doping profiles and the reverse bias operation should be adjusted such that the field strength does not exceed the breakdown field strength of $E_{bd} \sim 40 \text{ V.}\mu\text{m}^{-1}$ for silicon crystal [76]. The calculated values of peak electric field strengths E_0 (at 0 V bias) and E_{-5} (at -5 V bias) across the junction are given in Table 3.2, for three representative single-mode waveguides with δ values varying from 0 to 600 nm (as described earlier). The results suggest that an optimum value of δ between 300 nm to 400 nm can be used safely for a reverse bias voltage not exceeding -5 V in case of all the three single-mode waveguide dimensions.

We have also studied device performances by varying G from 2 μm to 10 μm in steps of 1 μm to compare refractive index changes, loss figures, and junction capacitances - they are shown in Figures 3.7(a), 3.7(b), and 3.7(c), respectively, for the waveguide fabricated with $H = 250$ nm. It is observed from the simulation results that till $G = 6 \mu\text{m}$, the diode behaves like p-n junction, whereas for $G > 6 \mu\text{m}$, it is p-i-n junction diodes. As observed from Figure 3.7(a) the change in effective index of the optical mode reduces as the gap increases. But it should also be noted that the optical loss is very high for lower gaps. From the Figure 3.7(a) and 3.7(b) we can say that a gap (G)

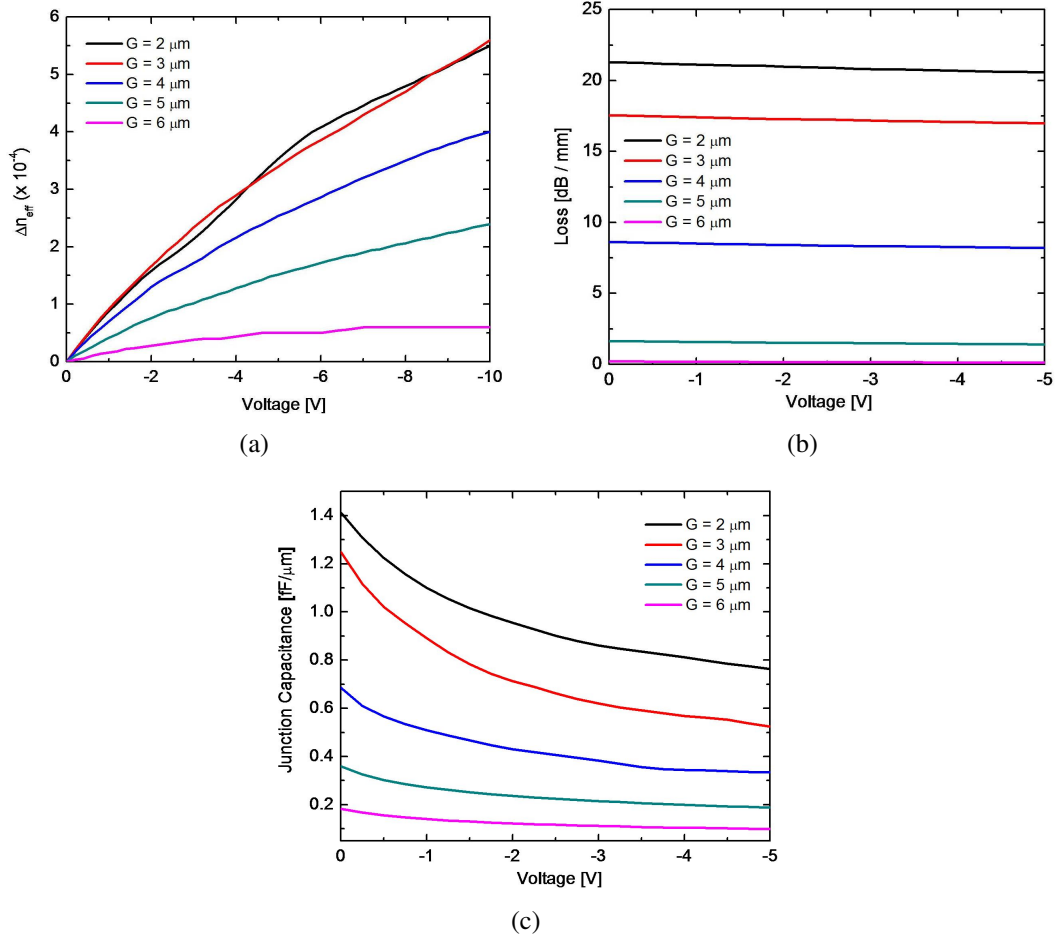


Figure 3.7: The calculated (a) change of n_{eff} , (b) optical attenuation, (c) junction capacitance, as a function of reverse bias across the waveguide diodes (p-n junction) designed with device layer thickness $H = 0.25 \mu\text{m}$, and gap between doping windows as a parameter.

of $6 \mu\text{m}$ between the doping windows will give low loss but also low Δn_{eff} . So a gap (G) around $5 \mu\text{m}$ between the doping windows will be the optimum, taking both the factors into consideration. Some figures of merit like the confinement factor, optimal offset of the rib waveguide (δ), junction capacitance (C_j), length of the doping region for a π phase change (L_π) and $V_\pi L_\pi$ corresponding to $G = 5 \mu\text{m}$ are given in Table 3.3.

It is evident from Figure 3.7(a) that for $G = 6 \mu\text{m}$, the effect of reverse bias causes little change in refractive index of the guided mode. However, we can design waveguides with p-i-n junction for $G \geq 6 \mu\text{m}$ to operate in forward bias for applications like low-speed switches, VOAs, etc. Figure 3.8 shows the electro-optic characteristics of the diode under forward bias junction for gaps varying from 7 to $10 \mu\text{m}$. It is clear that a gap of $7 \mu\text{m}$ forms a narrow intrinsic region leading to more refractive index

change because of very good overlap between carriers and optical mode. However, the imaginary refractive index change adds more optical insertion loss even under no bias. It may also be noted that larger gap can reduce the insertion loss but suffer the disadvantage of low speed and higher power consumption for a given refractive index modulation. The change in refractive index of $\sim 2 \times 10^{-3}$ and attenuation of $\sim 3.5 \text{ dB mm}^{-1}$ are achieved at a forward bias of 1.2 V for the doping window gaps of $\geq 8 \mu\text{m}$. These design flow shows the technique to integrate electro-optic phase shifters with rib waveguides for different device layer thickness using diffusion doping, and finally reduce it to photonic wire waveguide dimensions.

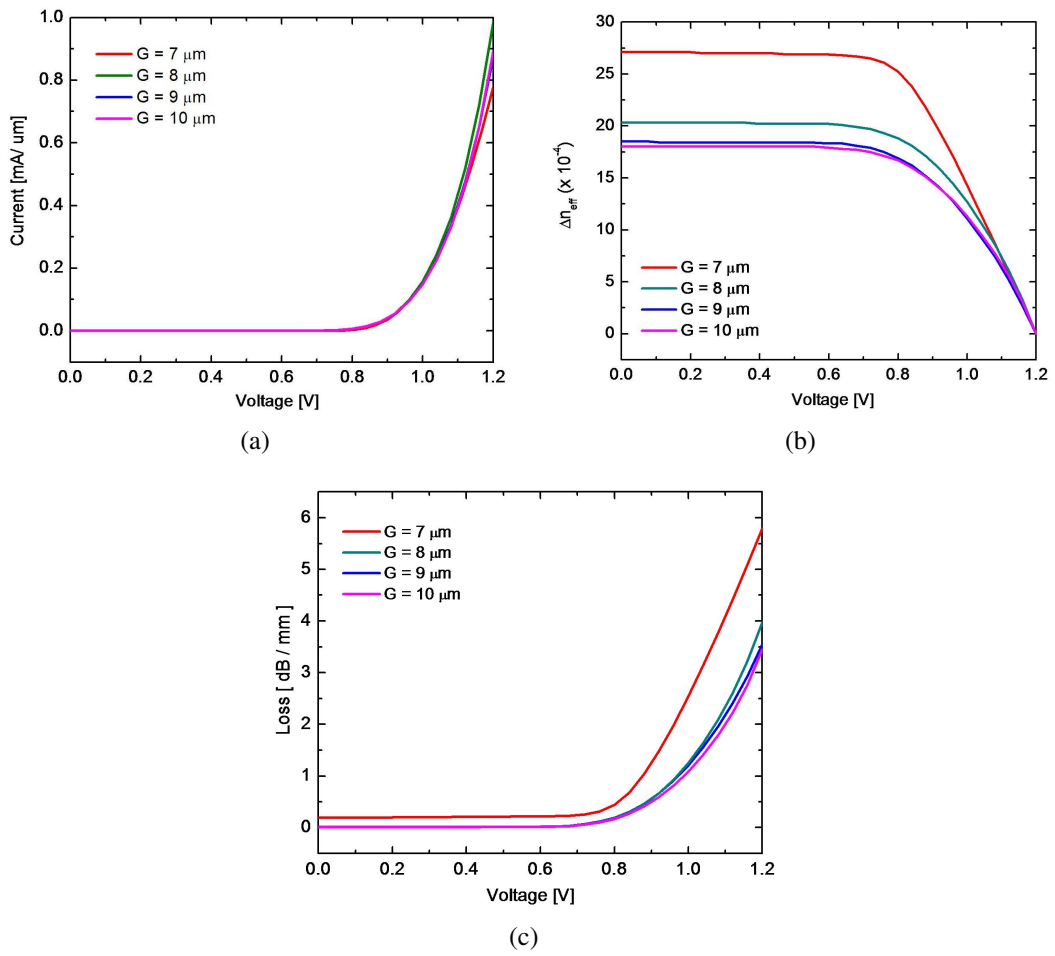


Figure 3.8: Simulated (a) $I - V$ characteristics, (b) change of n_{eff} as a function of forward bias, (c) optical loss as a function of forward bias across a waveguide diode (p-i-n junction) of reduced geometry ($H = 0.25 \mu\text{m}$) with gap (G) between doping windows as a parameter.

Table 3.3: Optimized device parameters for three devices layer thicknesses ($H = 1 \mu\text{m}$, $0.5 \mu\text{m}$, $0.25 \mu\text{m}$) with gap between doping windows $G = 5 \mu\text{m}$.

Optimized parameters	$H = 1.0 \mu\text{m}$, $W = 1.0 \mu\text{m}$, $h = 0.6 \mu\text{m}$	$H = 0.5 \mu\text{m}$, $W = 0.6 \mu\text{m}$, $h = 0.25 \mu\text{m}$	$H = 0.25 \mu\text{m}$, $W = 0.5 \mu\text{m}$, $h = 0.1 \mu\text{m}$
Confinement Factor	0.85	0.86	0.76
$\delta_{opt}[nm]$	~ 300	~ 400	~ 400
$C_j[\text{fF}.\mu\text{m}^{-1}]$ at $V = 0 \text{ V}$	6.3	0.58	0.36
$L_\pi[mm]$ at $V = -5 \text{ V}$	8.6	5.9	4.8
$V_\pi L_\pi[V - cm]$ at $V = -1 \text{ V}$	2.7	2.1	1.6

3.2 Thermo-optic Phase shifters: Doped microheater

Conventionally, p-n/p-i-n diodes are integrated with the ring waveguides for high-speed modulation/switching operations using plasma dispersion effect. Nevertheless, due to the low-loss offered by thermo-optic phase shifter, its finds attractive applications like reconfiguration of operating wavelength [93, 79], mitigating fabrication errors and thermal stabilization [83, 84]. The microheaters integrated with the MRR are mostly reported to be deposited on the top oxide cladding [79, 52]. Even though they provide higher wavelength tunability, their main drawback is on the transient response [95]. Hence we study the MRR tunability as well as response time by integrating microheaters on the slab of the MRR. We present both p-doped microheaters as well as metal microheater integrated on the slab of the MRR.

3.2.1 Design of Doped Microheater Integrated with MRR

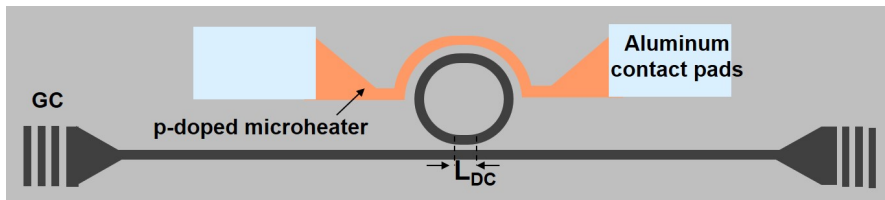


Figure 3.9: Schematic top-view of the slab doped microheater integrated with MRR. The microheater is flared to Aluminium contact pads. Grating coupler (GC) is used for optical interfacing.

A slab integrated doped heater is desirable over thin metallic strip microheaters, as it can be fabricated along with the p-n/p-i-n diodes, hence reducing additional process steps of metal deposition. Fig. 3.9 shows the schematic top-view of the MRR integrated with p-doped microheater on the slab of the waveguide. We have designed the thermo-optically tunable microring resonator (all-pass configuration) using p-type diffusion doped microheater in SOI substrate with a starting device layer thickness (H') of 250 nm. As previously mentioned, the fabrication limitation of doping using ion-implantation had made us develop the technology to diffuse the dopants in a thicker device layer and reduce it to low device layer thickness. Here, we have chosen 250 nm SOI device layer as the starting thickness and for the microheater, as only one type of dopant is required, we have optimized the process parameters such that the final device layer reduces to ~ 220 nm after all the high temperature oxidation and diffusion processes.

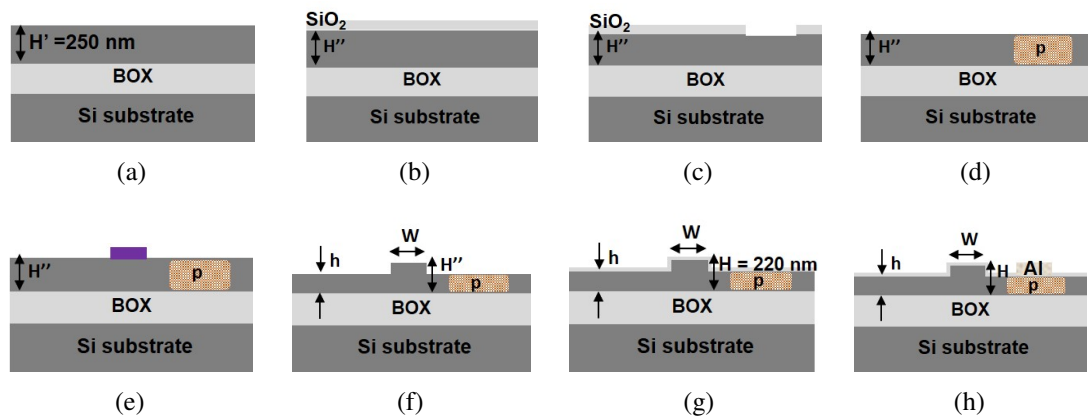


Figure 3.10: Schematic cross-section of the fabrication process flow for doped microheater integrated microring resonator, (a) SOI wafer of device layer $H' = 250$ nm, (b) oxidation for masking during boron diffusion, (c) etching of oxide for boron diffusion, (d) boron diffusion and oxide removal, (e) lithography for waveguide diffusion, (f) etching of rib waveguide, (g) oxidation for surface passivation, (h) oxide etching and aluminum metalization for contact pads .

Fig. 3.10 shows the complete process steps schematically. A thin oxide was grown to act as mask for the diffusion process. Lithography followed by oxide etching, opened the window for diffusion doping for the doped microheater. Boron was chosen due to its high diffusivity, thus reducing the diffusion time and also preventing the wafer from exposure to high temperature- oxygen ambience. The rib waveguides were fabricated

after the diffusion so that a thicker device layer was available for the diffusion process which gives precise control on the dopant concentration. Final step of surface passivation and metallization completed the MRR integrated with p-doped microheater. The complete process of boron diffusion followed by waveguide definition and metallization was simulated in TSUPREM4 process simulator.

3.2.2 Simulation Results

The process simulation was performed considering a 250 nm SOI substrate. Dry oxidation at 900°C was used for the masking layer for the diffusion process. Lithography followed by dry etching of SiO₂ from the diffusion window was followed by Boron diffusion. The temperature of Boron diffusion was considered to be 1100°C from the data sheet specifications of the Boron Nitride wafers used for fabrication. The peak dopant concentration of $\sim 3 \times 10^{18} \text{ cm}^{-3}$ was obtained after all the process steps of surface passivation and metallization. A thin layer of silicon-di-oxide was grown using dry oxidation for the surface passivation. The doping profile along the depth of the SOI was extracted and plotted in Fig. 3.11(a). The vertical dotted lines demarcate the silicon slab from the BOX layer in Fig. 3.11(a). The concentration profile shows a nearly constant concentration in the slab region.

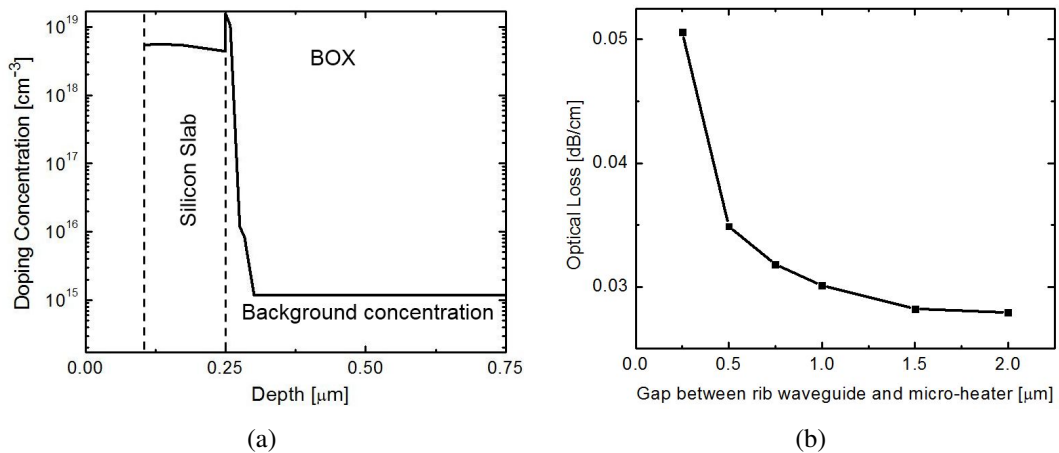
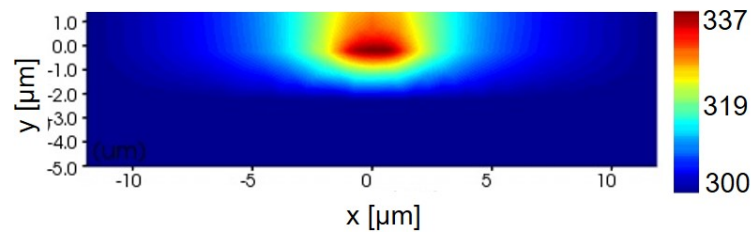


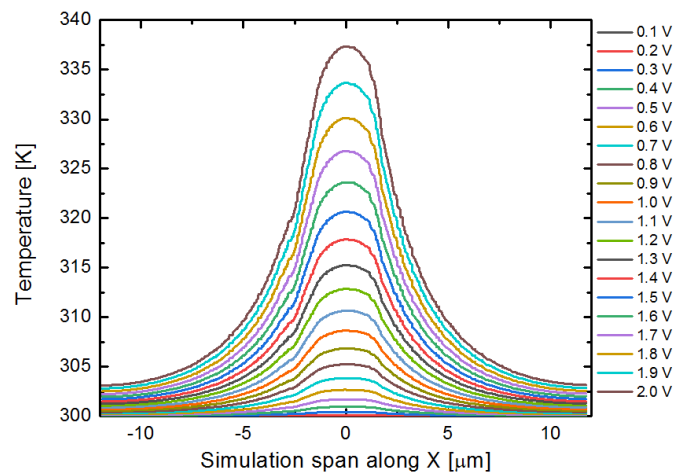
Figure 3.11: Simulated doping concentration of Boron along the depth of SOI wafer, (b) simulated optical loss for different gap between the rib waveguide and the doped micro-heater.

The 2D concentration profile for the complete structure was imported to Lumerical

DEVICE simulator to study the electrical characteristics. The concentration profile was extended in the other direction to form a 3D structure having microheater length of $10\ \mu\text{m}$. The length of the total structure was restricted due to the computation time and memory. The 2D heat profile of the device for an applied bias of 2V is shown in Fig. 3.12(a). The temperature profile was further extracted along a slice (for a fixed ‘y’) 10 nm below the waveguide slab. The extracted temperature along the slice for different voltage values are plotted in Fig. 3.12(b). Convective boundary condition of $5\ \text{W/m}^2\text{K}$ flow has been considered in the top surface for the silicon-di-oxide:air interface. Finally the total heat profile was imported to Lumerical MODE Solution to calculate the optical loss and optimize the separation between the MRR and the doping window. It is observed that closer the MRR is to the doped heater, more is the optical loss due to absorption. The loss obtained for $2\ \mu\text{m}$ gap is $0.02\ \text{dB/cm}$ as shown in Fig. 3.11(b), which can be considered for fabrication.



(a)



(b)

Figure 3.12: (a) Simulated temperature profile showing the cross-section of the doped microheater, (b) extracted temperature profile for a slice 10 nm below the top of the waveguide slab.

3.3 Thermo-optic Phase-shifters: Metal microheater

The other way to integrate microheaters with the MRRs is by using metal strips. This subsection deals with the design and simulation of Titanium microheater integrated with MRR.

3.3.1 Design of Metal Microheater Integrated MRR

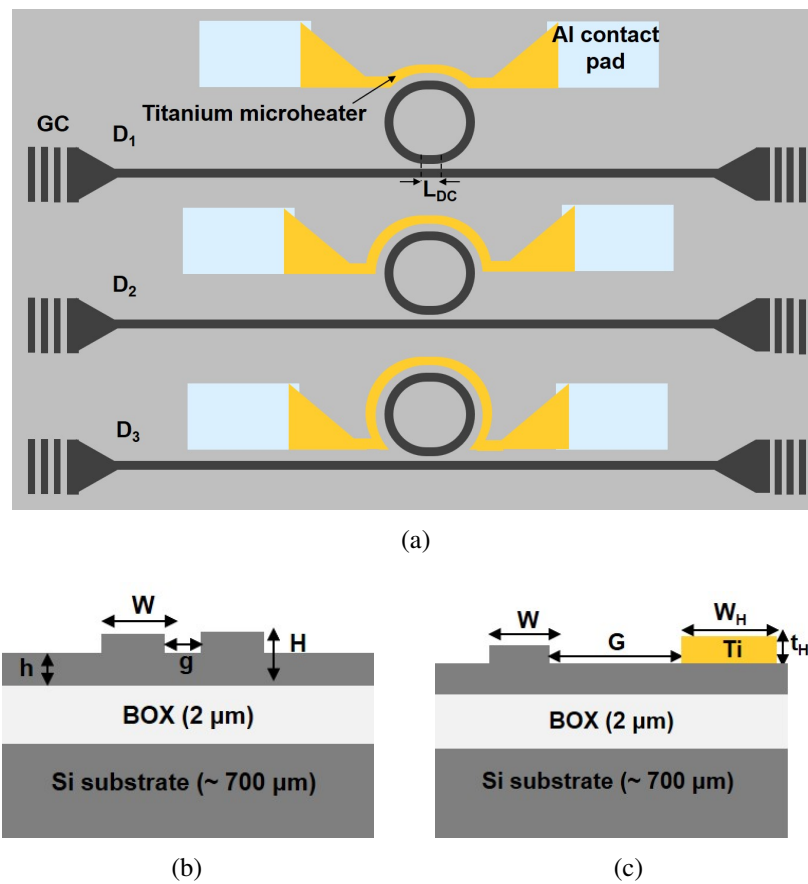


Figure 3.13: Schematic of (a) design layout showing a set of three identical rib waveguide MRRs (D_1 , D_2 and D_3) integrated with identical slab integrated Ti-strip microheaters of three different lengths approximately covering one-quarter, two-quarter, and three-quarter lengths of the MRRs along with input/output grating couplers (GC) for optical interfacing and Al contact pads for electrical interfacing; (b) cross-section view of the directional coupler used for light coupling between the ring and bus waveguides (W - waveguide width, H - waveguide height, h - slab height, g - gap between ring and bus waveguides, BOX - buried oxide); (c) cross-section view of a waveguide-slab-integrated Ti-strip microheater (W_H and t_H are the width and thickness of Ti-strip, respectively, and G is the distance between rib-waveguide and Ti-strip).

Fig. 3.13(a) shows the design layout of devices fabricated for experimental investigations. Three different lengths of phase shifters ($L_H = 83.5 \mu\text{m}$, $162 \mu\text{m}$ and $240.5 \mu\text{m}$) are integrated in three identical rib waveguide MRRs (D_1 , D_2 and D_3) in all-pass configuration.

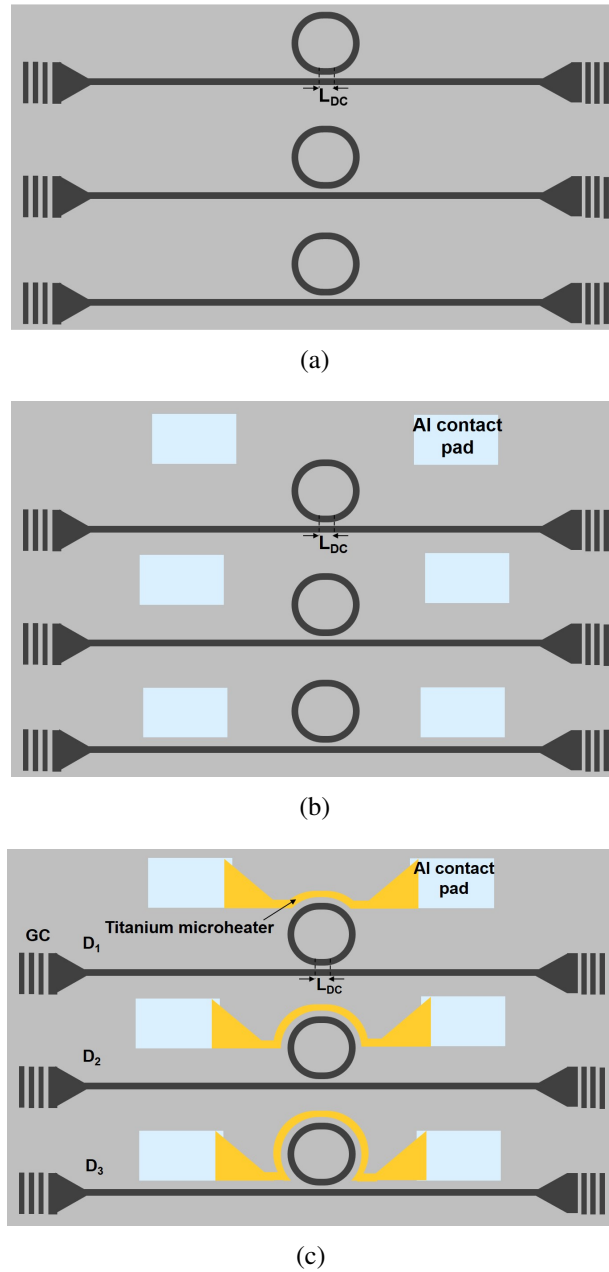


Figure 3.14: (a) Schematic top-view showing the fabrication process steps for microheater integrated MRR: (a) rib waveguide and MRR fabrication, (b) Aluminum patterning and lift-off for contact pads, (c) Titanium patterning and lift-off for microheater.

The same design of single-mode rib waveguide (width $W = 420 \text{ nm}$, height $H = 220 \text{ nm}$, slab height $h = 150 \text{ nm}$), supporting only the fundamental TE-mode operating

in optical telecommunication band ($\lambda \sim 1550$ nm) has been used for bus and ring waveguides. The cross-section views of ring-bus directional coupler (DC) and slab integrated microheater waveguide phase-shifter have been shown schematically in Figs. 3.13(b) and 3.13(c), respectively. The Ti-strip (resistive microheaters) of targeted width $W_H = 1 \mu\text{m}$ and thickness $t_H = 100$ nm are considered to be placed at a distance of $2 \mu\text{m}$ (G) from the waveguides to avoid attenuation loss of guided light. All the three microheaters have identical flarings leading to the Al contact pads of dimensions $100 \mu\text{m} \times 150 \mu\text{m}$ (thickness ~ 200 nm); this is to reduce Joule heating outside the effective length of a microheater [136].

Fig. 3.14 shows the fabrication steps to integrate the Titanium microheater with the MRRs. In the first step the rib waveguides are defined and dry etched. In the second step the Aluminium contact pads are fabricated using subsequent lithography and lift-off processes. Finally the Titanium microheaters are deposited using similar lithography and lift-off processes. The fabrication results will be discussed in the next chapter.

3.3.2 Simulation Results

The devices with the exact dimensions of the MRR and the metal microheater were simulated using COMSOL Multiphysics to estimate the heat spread and the temperature rise in the waveguide core (w.r.t background temperature = 300 K) with the power dissipated. A buried oxide (BOX) layer of $2 \mu\text{m}$ and a handle layer of $10 \mu\text{m}$ is considered in the simulation. The values of various thermal and electrical parameters like specific heat capacity, thermal conductivity, electrical conductivity, thermo-optic coefficients for silicon, silicon-di-oxide and Ti has been chosen similar to [95, 100] and is tabulated in Table 3.4. Fig. 3.15(a) - 3.15(c) shows the temperature profile along the ring waveguide for a dissipated power of 50 mW. The rise in temperature obtained in the waveguide core (ΔT) due to the application of various power levels (in mW) for all the three microheater lengths (D_1 , D_2 and D_3) have been extracted and plotted in Fig. 3.15(d). The temperature rise is highest for D_1 due to its shortest length and scales proportionally for the other two lengths of microheaters. Fig. 3.15(e) shows the 2D temperature profile extracted from the 3D simulation of D_3 for an applied power of 20

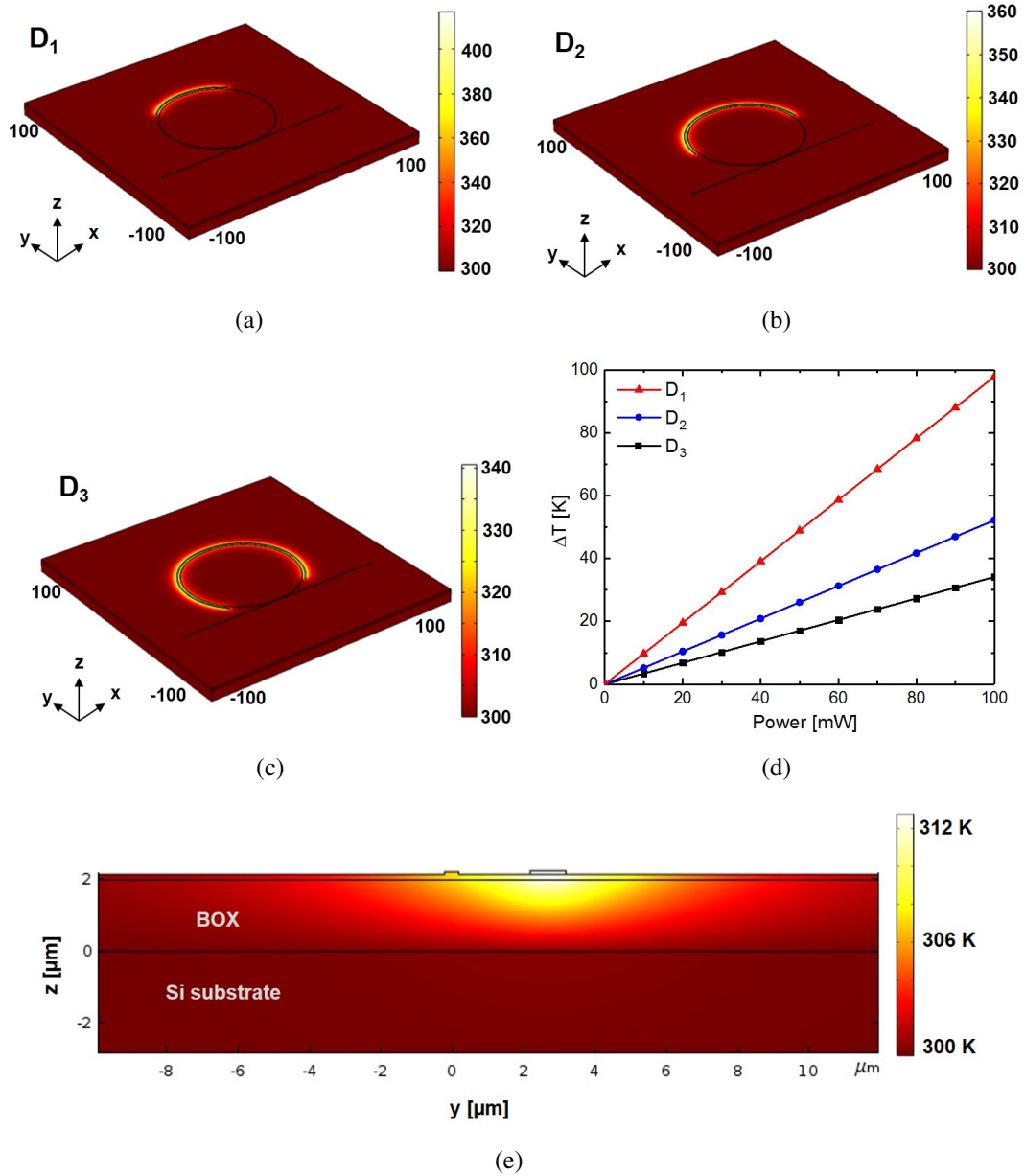


Figure 3.15: Simulated 3-D temperature profile extracted from COMSOL Multiphysics of the designed rib waveguide MRRs integrated with slab integrated microheaters: (a) $L_H = 83.5 \mu\text{m}$ (D_1), (b) $L_H = 162 \mu\text{m}$ (D_2), (c) $L_H = 240.5 \mu\text{m}$ (D_3) for 50 mW of electrical power which is assumed to be dissipated uniformly along the waveguide, and (d) ΔT obtained in the waveguide core as a function of dissipated power (mW) for all the three device geometries (D_1 , D_2 and D_3), (e) 2D temperature profile for the cross-section showing the rib waveguide integrated with the Ti metal microheater placed.

mW to the heater. This figure helps us to visualize the heat spread from the microheater to the rib waveguide.

The transient response of the devices were studied using COMSOL Multiphysics.

Table 3.4: The values of thermal and electrical parameters used for COMSOL Simulation [100, 95]

Material Properties	Silicon	Silicon-di-oxide	Titanium
Specific heat capacity [J/kg.K]	700	730	544
Density [kg/m ³]	2329	2200	4506
Thermal conductivity [W/m.K]	15-140	1.4	21.9
Electrical conductivity [S/m]	8.7	10 ⁻¹⁵	2.6 × 10 ⁶
Thermal expansion coefficient [1/K]	2.6 × 10 ⁻⁶	0.5 × 10 ⁻⁶	8.6 × 10 ⁻⁶
Refractive Index (at λ = 1550 nm)	3.4447	1.444	3.6848 + j4.6088

Fig. 3.16 shows the simulated transient response of all the three devices D_1 , D_2 and D_3 . The rise time and fall time obtained for the devices (rise and fall between 10% to 90 % of the maximum value) were $\sim 4 \mu\text{s}$. This design was used to further fabricate the devices and characterise them.

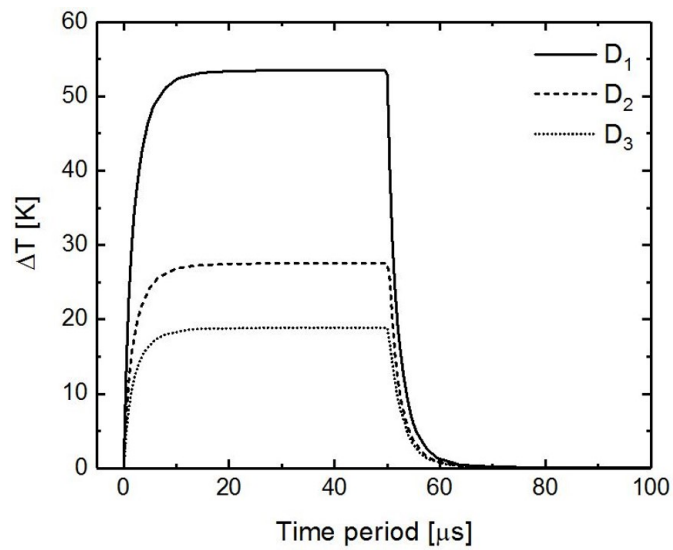


Figure 3.16: Simulated transient response of the Titanium microheaters for device D_1 , D_2 and D_3 for 50 mW of electrical power supplied to the microheaters.

3.4 Summary

In summary, the design of both electro-optic and thermo-optic phase-shifters have been studied. A technique to fabricate p-i-n/p-n diodes using diffusion doping for different device layer thickness was proposed, such that the diffusion is performed at a higher

device layer and finally reduced to photonic wire dimension. Detailed simulation studies were performed to optimize diffusion parameters and waveguide geometry for three different device layer thickness viz. $1\ \mu\text{m}$, $0.5\ \mu\text{m}$ and $0.25\ \mu\text{m}$. The waveguide parameters were chosen by considering single mode guidance and maximum confinement of the optical mode in the rib waveguide to ensure maximum change in the effective index. Next, thermo-optic phase shifters were designed. Slab integrated doped microheaters as well as metal microheaters with MRRs were studied. The complete process simulation for optimizing the steps of p-doped microheater was performed in TSUPREM4 simulator and the concentration profile was exported to Lumerical DEVICE to perform the electrical simulations and obtain the temperature rise in the rib waveguide core. Then the temperature profile was exported to Lumerical MODE to estimate the optical loss and optimize the separation of the microheater from the MRR. For the metal microheater, thermal simulations were performed using COMSOL Multiphysics to estimate the temperature in the rib waveguide core for different applied electrical power in the metal microheater. Also the transient response of the devices were simulated to estimate the response time. These designed devices were used for fabrication and characterization to finally demonstrate the electrical control of the optical bistability of the MRRs. The fabrication and characterization results will be discussed in Chapter-4, followed by the electrical control of the bistability in Chapter-5.

CHAPTER 4

Device Fabrication and Characterization

The phase-shifters and the microring resonators that were designed in Chapter-3 were fabricated using the in-house facilities available at the Centre for NEMS and Nanophotonics (CNNP), IIT Madras. The MRR and phase-shifter fabrication along with the characterization results will be presented in this chapter. Electro-optic phase shifters were attempted to be fabricated using diffusion doping starting from a higher device layer thickness. Variable optical attenuators and two-photon absorption based photodiodes are reported using the p-i-n diodes on $2\ \mu\text{m}$ SOI. Further the attempt to integrate the diodes on a lower SOI device layer thickness will be presented. The preliminary fabrication and characterization results will be discussed in Section 4.1 for the p-i-n/p-n diodes. Fabrication challenges faced during the process of reducing the device layer thickness and reducing to photonic wire dimensions will also be explained. In Section 4.2 we will discuss the fabrication and characterization results of MRRs integrated with p-doped microheaters. Section 4.3 discusses about the integration of metal microheaters on the MRRs along with the various parameter extraction of MRRs and basic characterization results. A comparison between p-doped microheater and the Titanium microheater is presented in Section 4.4. Finally, a brief summary is presented on the overall device fabrication and the characterization results obtained.

4.1 P-I-N/P-N Waveguides

The fabrication of the electro-optic phase-shifters were done according to process flow mentioned in Chapter-3. Prior to that p-i-n waveguide phase shifters were fabricated on $2\ \mu\text{m}$ SOI using the process flow already reported by our lab members [137, 138]. This process flow is slightly different than the method adopted to obtain p-i-n/p-n diodes for lower SOI device layer thickness. Fig. 4.1 shows the fabrication process steps to integrate p-i-n diode using diffusion doping on $2\ \mu\text{m}$ SOI. The rib waveguide is defined and

etched first using photolithography. Growing of masking oxide, followed by definition of phosphorous diffusion window is performed next. Once the phosphorous diffusion is performed, similar masking oxide is grown for boron diffusion. Lithography followed by oxide etching from the diffusion windows makes the sample ready for boron diffusion. After boron diffusion is complete, the masking oxide is removed completely and a fresh oxide layer is grown for surface passivation. Finally metallization is done for the contact pads.

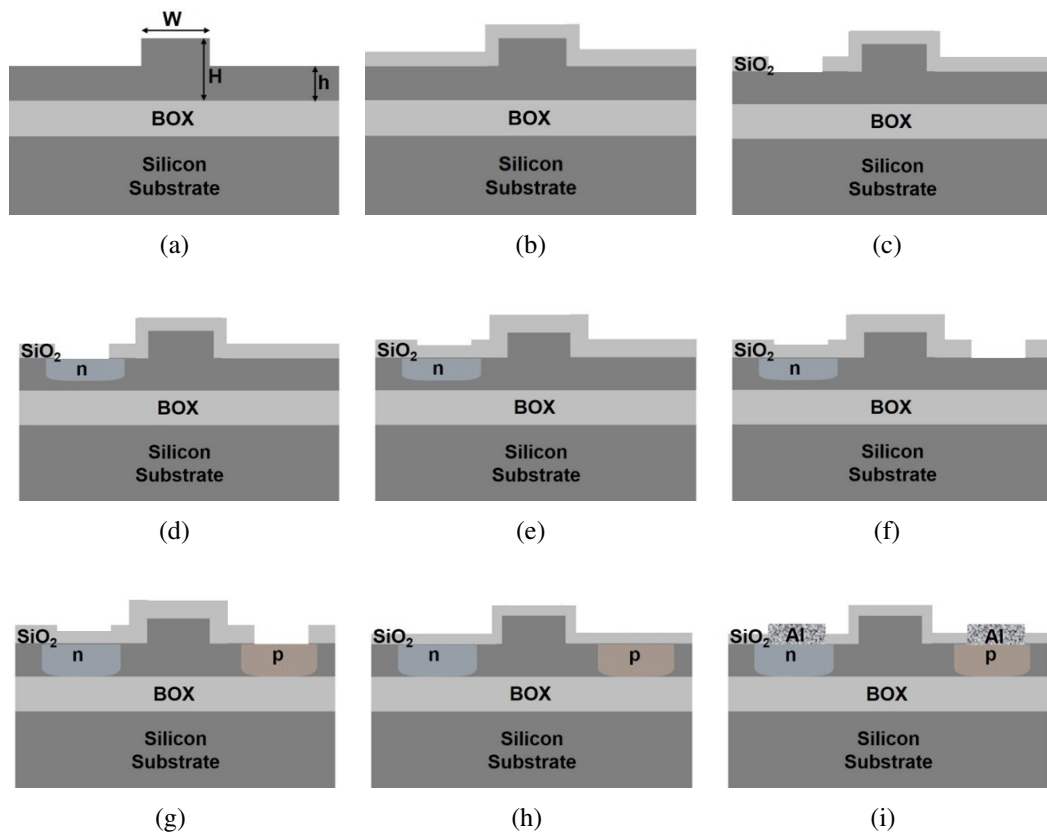


Figure 4.1: Schematic cross-section depicting the process steps for fabricating p-i-n diodes on $2 \mu\text{m}$ SOI: (a) rib waveguide fabrication, (b) oxidation for masking for phosphorous diffusion, (c) lithography and etching of oxide from diffusion window, (d) phosphorous diffusion, (e) oxidation for masking for boron diffusion, (f) lithography and etching of oxide from diffusion window, (g) boron diffusion, (h) surface passivation, (i) metallization for contact pads .

4.1.1 Device Layout and Fabrication

The photolithography masks were fabricated first for demonstrating the p-i-n waveguides on $2\ \mu\text{m}$ SOI. Fig. 4.2-4.5 show the mask layouts used to develop the mask plates used for photolithography. Fig. 4.2 shows the mask for the rib waveguides which were 2 cm long. The phosphorous and boron diffusion windows were opened using the masks shown in Fig. 4.3 and 4.4. The mask layout for the contact pads is shown Fig. 4.5. Three different length of diodes ($250\ \mu\text{m}$, $500\ \mu\text{m}$ and $750\ \mu\text{m}$) were considered for the study. The gap between the doping windows and the rib waveguide was varied from $1\ \mu\text{m}$ to $4\ \mu\text{m}$.

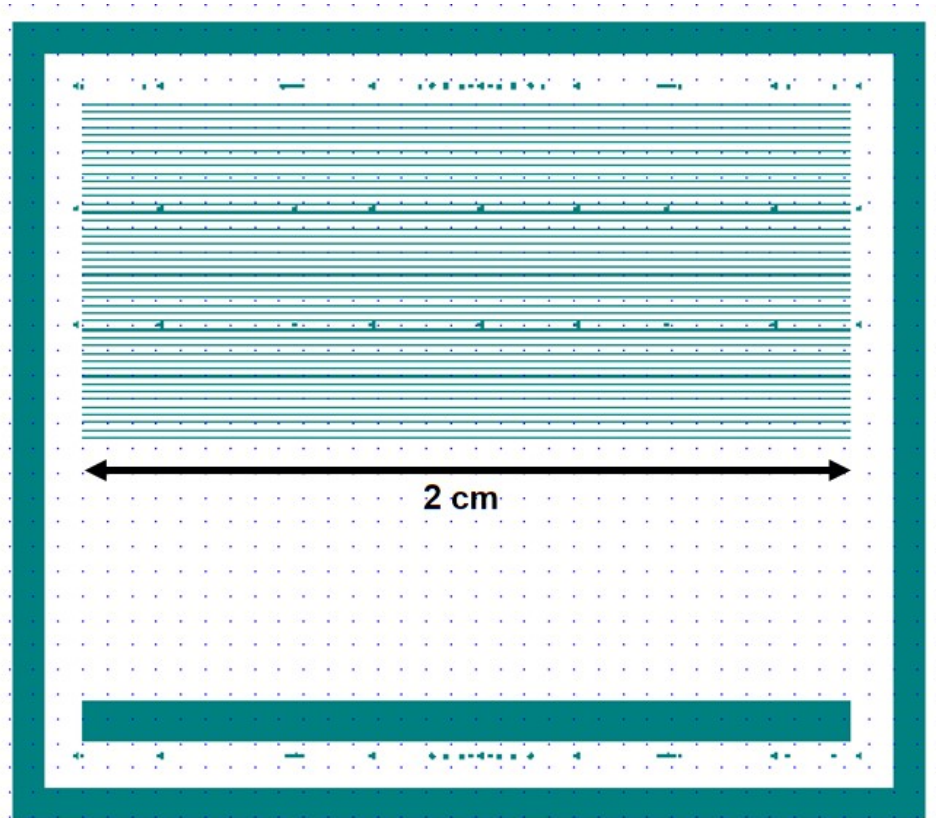


Figure 4.2: Layout of the waveguide mask used to fabricate the p-i-n waveguides on $2\ \mu\text{m}$ SOI.

Initially, p-type SOI wafers of $2\ \mu\text{m}$ device layer thickness with background concentration of $\sim 10^{14}\ \text{cm}^{-3}$ were cleaned using standard silicon cleaning techniques (Appendix A.2). Since photolithography, oxidation, diffusion and metallization are the main steps which can handle batch processing, we have considered three samples in one run. Positive photoresist S1805 was used to define the waveguides of width $2\ \mu\text{m}$ using

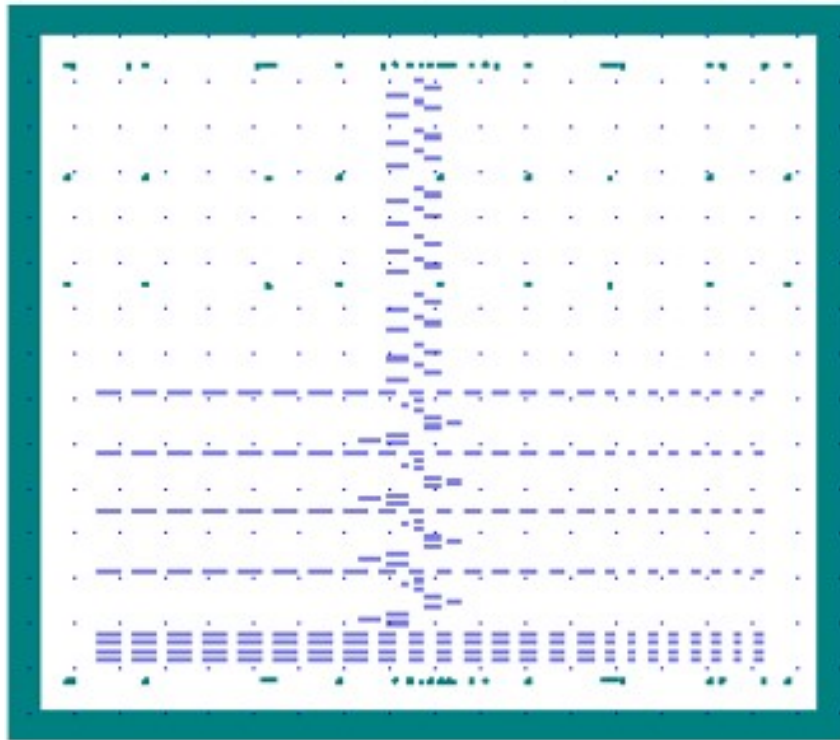


Figure 4.3: Layout of the phosphorus diffusion window mask used to fabricate the p-i-n waveguides on $2\ \mu\text{m}$ SOI.

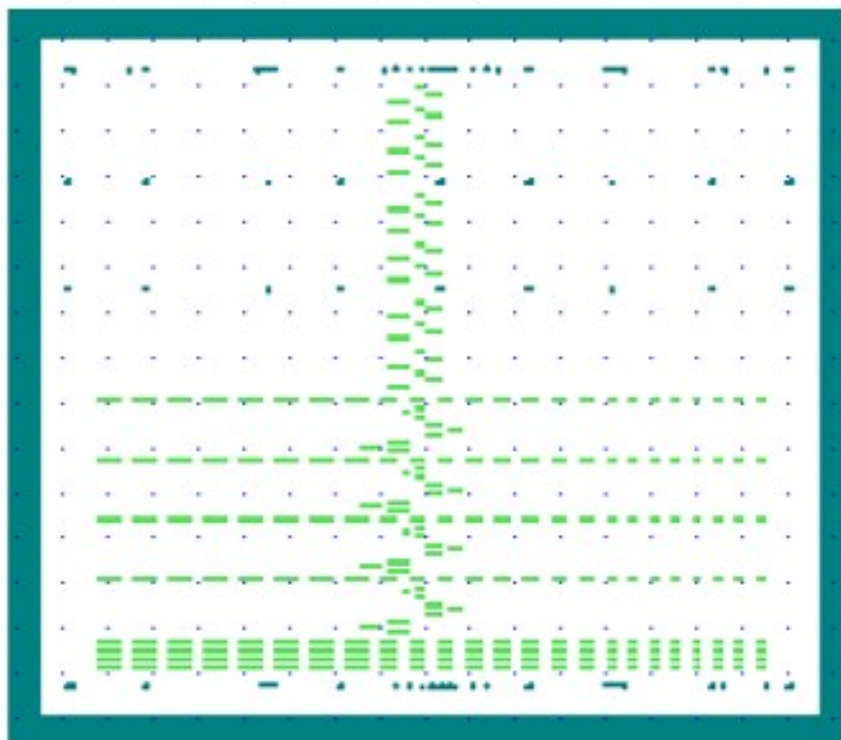


Figure 4.4: Layout of the boron diffusion window mask used to fabricate the p-i-n waveguides on $2\ \mu\text{m}$ SOI.

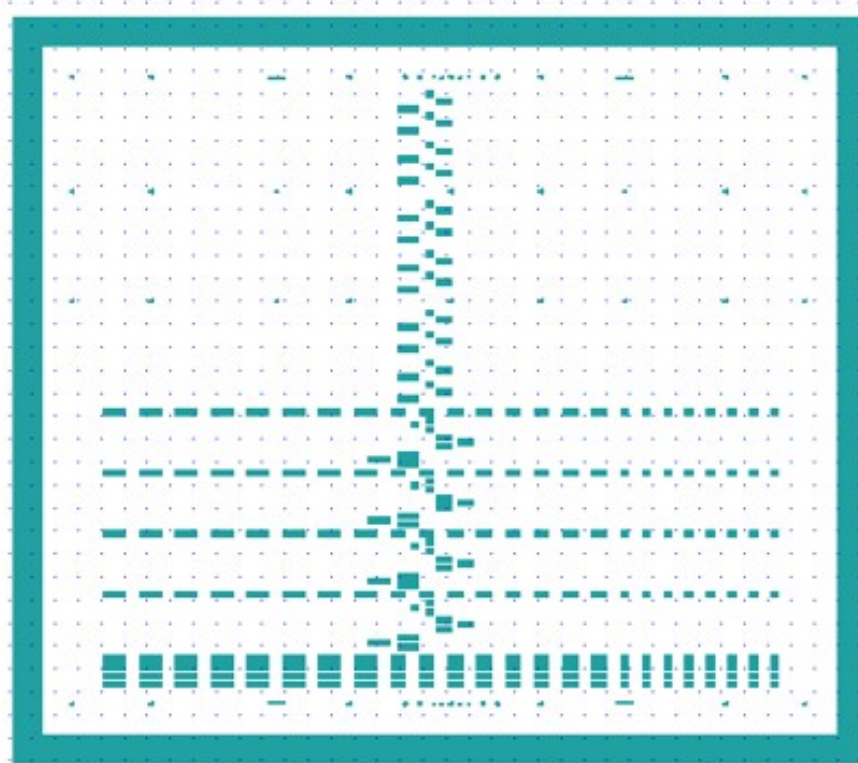


Figure 4.5: Layout of the contact pads mask used to fabricate the p-i-n waveguides on $2 \mu\text{m}$ SOI.

the mask shown in Fig. 4.2. Details of the spin-coating parameters are given in Appendix A.3. The samples were hard-baked to be etched using ICPRIE. SF_6 and CHF_3 gases were used to etch silicon for ~ 500 nm and obtain a single mode rib waveguide whose simulated mode profile was shown in Chapter 2. Thermal oxidation (dry : wet : dry : anneal :: 20 : 120 : 20 : 20 mins) at $T = 1000^\circ\text{C}$ was done on the cleaned samples to achieve a thickness of ~ 600 nm which acted as a masking oxide during phosphorous diffusion. A standard photolithography (i-line, $\lambda = 365$ nm, positive photoresist: S1813) using the mask shown in Fig 4.3, followed by dry oxide etching (ICP-RIE, CHF_3 : Ar chemistry) was carried out to open the phosphorous diffusion window. Phosphorus-oxy-chloride (POCl_3) was used as the liquid source of diffusion to dope the n-type junction. The diffusion was carried out for 2 hrs at 800°C . After removing phosphosilicate glass (PSG) in Buffered HF solution, the samples were again oxidized (dry : wet : dry : anneal :: 20 : 50 : 20 : 20 mins at 1000°C) to grow masking layer (~ 300 nm) for boron diffusion. Another photolithography step using the mask shown in Fig. 4.4 and subsequent oxide etching was carried out to open the boron diffusion window. Boron Nitride (BN1100) wafers were used as the solid source of diffusion to form

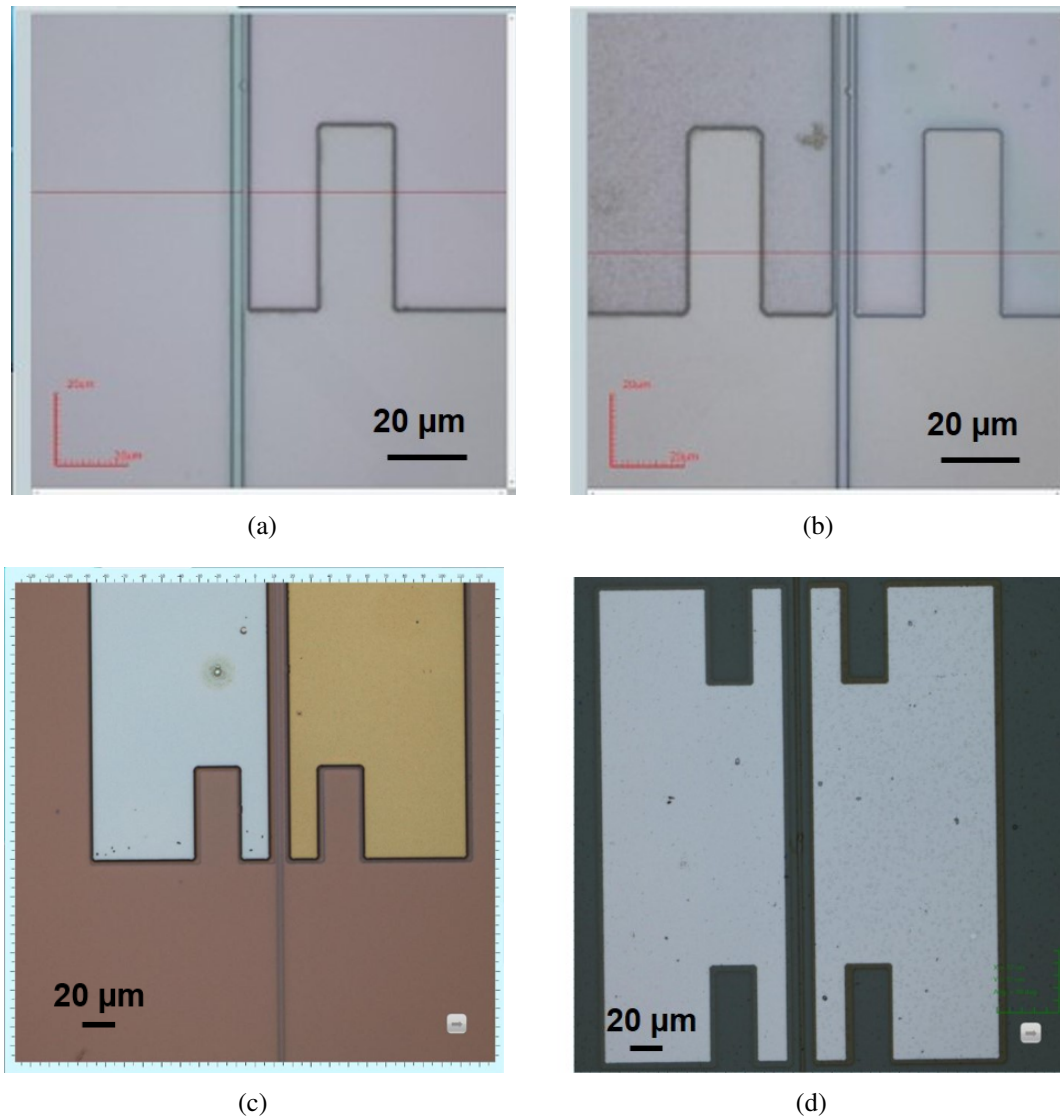


Figure 4.6: Confocal micrograph of the $2\ \mu\text{m}$ SOI devices fabricated showing the different fabrication steps (a) after phosphorus diffusion, (b) after boron diffusion, (c) after surface passivation, (d) metallization.

the p-type junction. The process was carried out at 1100°C for 20 mins. After removing the complete masking oxide, a fresh layer of silicon-di-oxide was grown to passivate the silicon surface. Final step of photolithography was performed using S1813 positive photoresist and the mask plate having the layout shown in Fig. 4.5 followed by removal of oxide from the doping windows. Aluminium was deposited on the sample surface using thermal evaporation and lift-off was performed using Acetone to obtain the metal contact pads. Sheet resistances were measured after every diffusion steps. $14\ \Omega/\square$ and $9\ \Omega/\square$ values of sheet resistance was obtained for the n-doped and p-doped regions respectively which closely matches with the simulation results obtained from TSUPREM

process simulations.

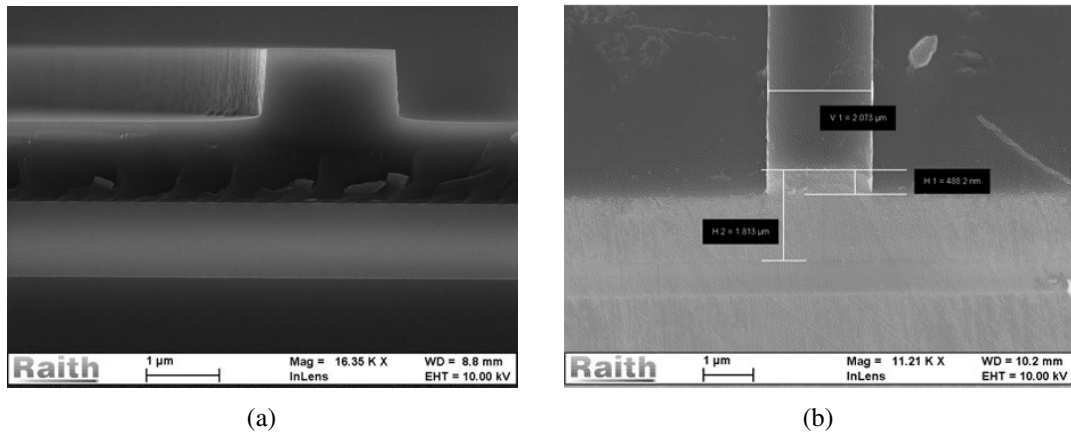


Figure 4.7: SEM image of the fabricated waveguides on $2\ \mu\text{m}$ SOI showing the (a) cleaved end-facet, (b) polished end-facet.

Figs. 4.6(a) and 4.6(b) show the confocal micrograph of the fabricated devices with the phosphorous doping window and boron doping window along with the straight waveguide respectively. The image of the sample after surface passivation oxide is shown in Fig.4.6(c). The final device, p-i-n diode integrated waveguide along with the metal contact pads is shown in Fig. 4.6(d). The samples were cleaved and the waveguide end facets were polished to prepare them for characterization. Figs. 4.7(a) and 4.7(b) show the SEM images of the cleaved end-facet and polished end facet of the fabricated waveguide respectively.

4.1.2 Characterization Results

The polished waveguides fabricated on $2\ \mu\text{m}$ SOI were characterized using the free-space coupling setup shown in Fig. 4.8. The laser light was passed through the polarization controller (PC) to the input collimator lens which collimates the light. The collimated light beam is passed through a polarizer and an input lens in used to focus the beam into the input facet of the rib waveguide. The output light from the waveguide is collected by the output lens and is sent to a power meter using a polarizer. A computer is connected to the power meter to obtain the wavelength sweep data. For biasing the p-i-n diodes a source measure unit (SMU) is connected as shown in the schematic in Fig. 4.8. The polished waveguides were characterized using the Fabry-Perot loss

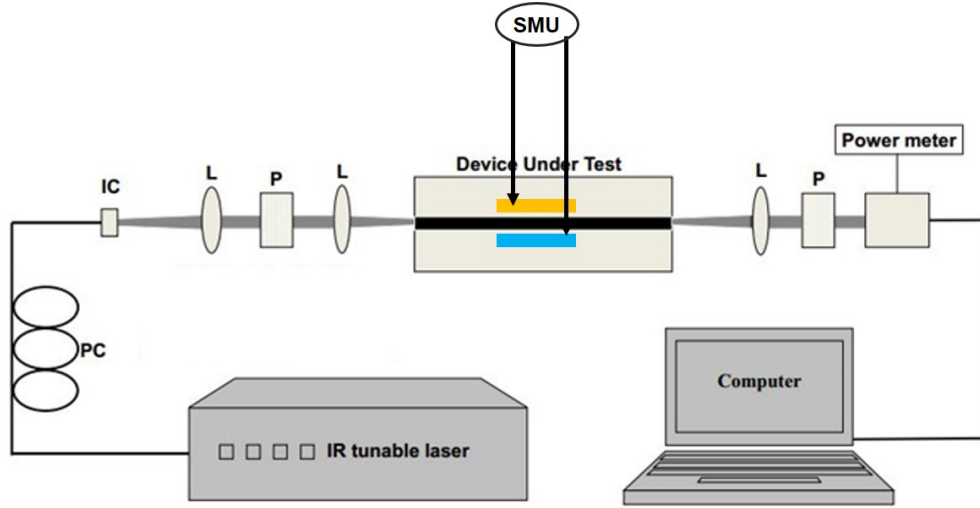


Figure 4.8: Schematic of the lens-coupling set-up used for characterizing the 2 μm SOI p-i-n waveguides. PC: Polarization Controller, IC: Input Collimator, L: Lens, P: Polariser, SMU: Source Measure Unit.

measurement method and the wavelength sweep data of the optical output power from the waveguide is shown in Fig. 4.9(a) and 4.9(b) for TE and TM modes respectively.

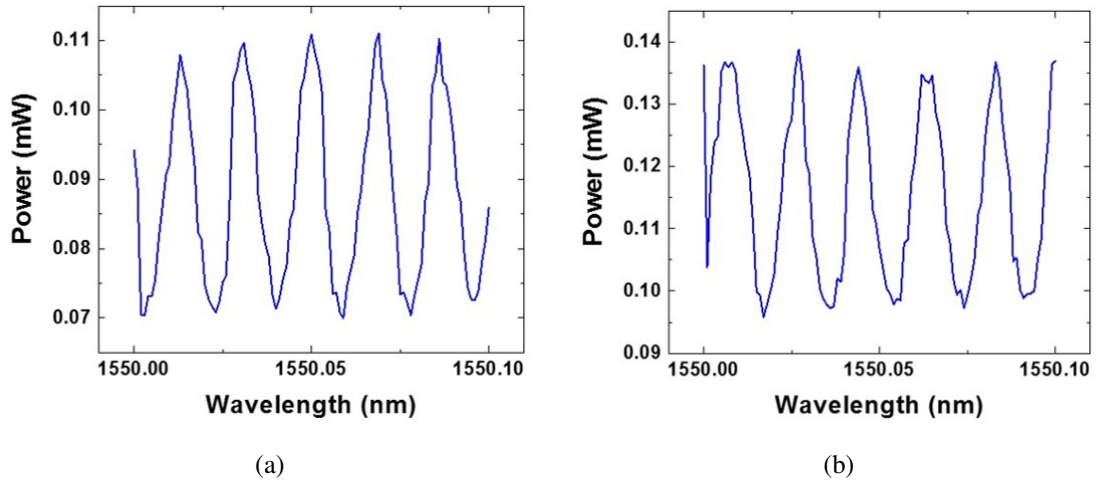


Figure 4.9: Fabry-Perot loss measurements showing the optical output power vs. wavelength for (a) TE polarization, (b) TM polarization.

The waveguide loss was measured using the following equation [99]:

$$\alpha[\text{dB}/\text{length}] = -\frac{4.34}{L} \ln\left[\frac{1}{R} \frac{\sqrt{\zeta} - 1}{\sqrt{\zeta} + 1}\right] \quad (4.1)$$

where, $\zeta = \frac{I_{max}}{I_{min}}$, I_{max} and I_{min} being the maximum and minimum output power for two consecutive peak and dip in the waveguide response. L is the total length of the waveguide and R is the reflectivity at the silicon-air interface through which the laser

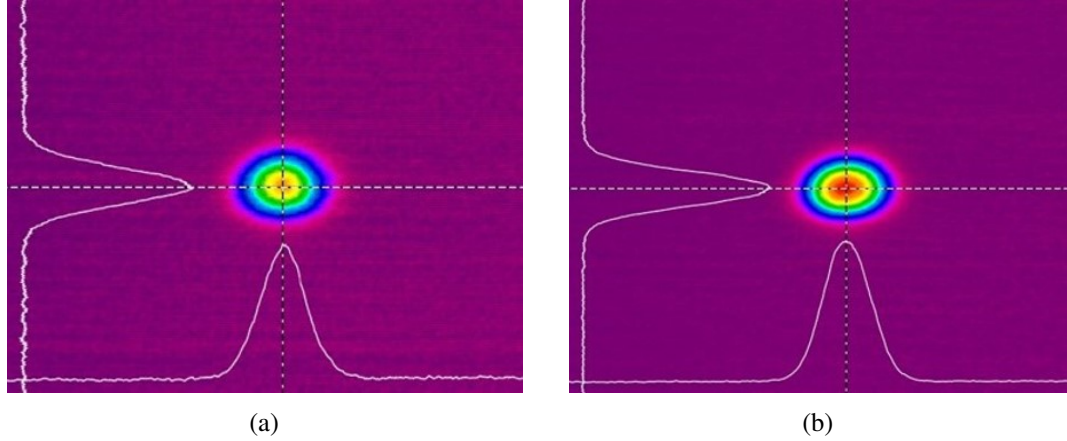


Figure 4.10: Measured optical mode profile for (a) TE polarization, (b) TM polarization.

beam is launched into the waveguide. The waveguide loss was measured for both TE and TM polarizations were found to be 1.85 dB/cm and 1.9 dB/cm. The measured optical mode profiles for TE and TM modes are also shown in Fig. 4.10(a) and 4.10(b) respectively. The mode size obtained were $5 \mu\text{m} \times 3.5 \mu\text{m}$ and $4.8 \mu\text{m} \times 3.5 \mu\text{m}$ for the TE and TM modes respectively. These values are slight higher than those obtained using Lumerical MODE simulations. These modes were measured using infra-red cameras from Newport.

The passive measurements of the devices were followed by the active measurements of the p-i-n waveguides. Two different applications were studied: variable optical attenuator (VOA) and two-photon absorption based photodetector (PD). Fig. 4.11 shows the optical attenuation for both the TE and TM polarizations obtained for the $500 \mu\text{m}$ length of the diodes integrated with the rib waveguides for the gaps varying from $1 \mu\text{m}$ to $4 \mu\text{m}$. With the application of forward bias current, the carriers are injected into the intrinsic rib waveguide region and absorbs the optical light that passes through it. Hence, attenuation is obtained in these devices with the increase in the bias. For a particular bias current, the attenuation reduces with the increase in the distance of the doped region from the rib waveguide. For the devices fabricated a maximum attenuation of ~ 10 dB is achieved for 100 mA of input bias current. The VOA characteristics also show that the devices were polarization independent, as similar amount of attenuation was obtained for both TE and TM modes.

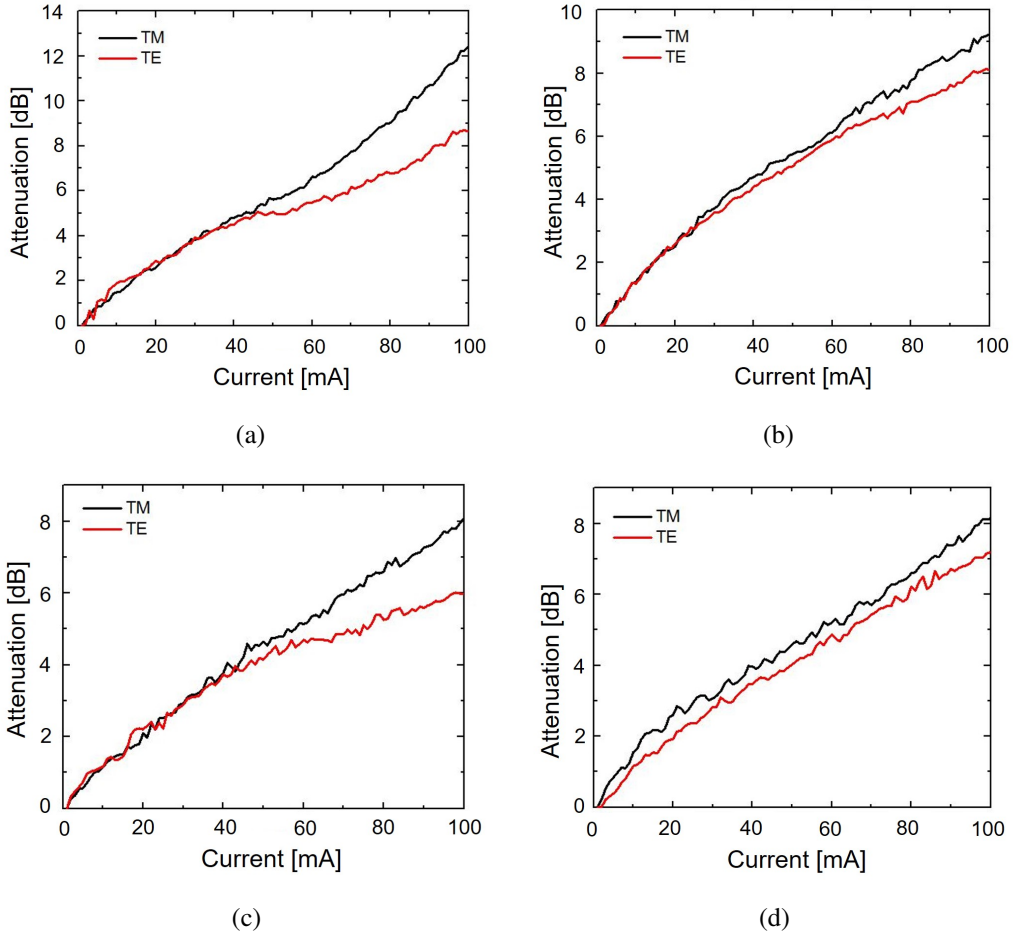


Figure 4.11: Optical attenuation with the applied current to the p-i-n diodes of doping length $500 \mu\text{m}$ and gap between the doping windows from the rib being varied from (a) $1 \mu\text{m}$, (b) $2 \mu\text{m}$, (c) $3 \mu\text{m}$, (d) $4 \mu\text{m}$.

The same devices were used to study the photodetector response using the two-photon absorption based mechanism, by operating the devices in reverse bias. Fig .4.12 shows the reverse bias I-V characteristics of three different length diodes ($250 \mu\text{m}$, $500 \mu\text{m}$ and $750 \mu\text{m}$) having a gap of $2 \mu\text{m}$ between the rib waveguide and the doping window, when subjected to different levels of input optical power. It is observed that the photocurrent increases with the increase in optical power, as the generation of carriers follow a quadratic behaviour with the coupled optical power [137]. It is also observed that the amount of photocurrent is more for higher lengths of diodes, which is due to more carrier generation for longer interaction length.

The fabrication and characterization of the p-i-n waveguide VOAs and the PDs helped to continue the fabrication of the p-i-n/p-n waveguide phase-shifters for dif-

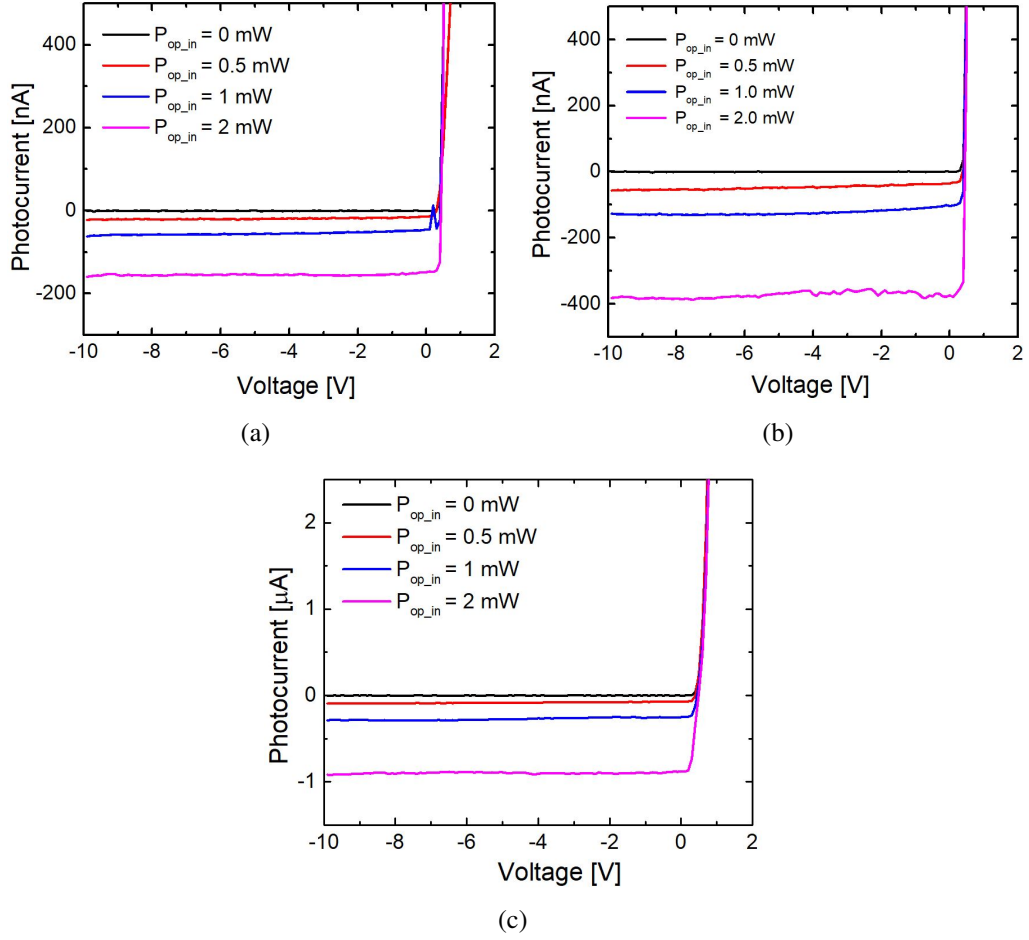


Figure 4.12: Reverse bias I-V characteristics of the p-i-n waveguides at various power levels for diode length (a) 250 μ m, (b) 500 μ m and (c) 750 μ m.

ferent device layer thickness as mentioned in Chapter-3. The proposed waveguide phase-shifter designs with p-n and p-i-n diodes were attempted to be fabricated with the optimized process parameters discussed in Chapter-3. The mask layout shown in Fig. 4.2 - 4.5 were used to fabricate the diodes starting from a higher device layer thickness. The optimised process steps mentioned in Chapter 3 was followed where the diodes were fabricated first followed by the rib waveguides. The steps of photolithography, oxidation, diffusion and metallization used were similar to that of VOA fabrication, except for the difference in the diffusion time. As the 2 μ m SOI needs to be diffused first to obtain the p-i-n/p-n diode, longer duration of diffusion was performed, using the diffusion parameters optimized in Chapter-3. The phosphorous diffusion was for 3 hours at 900°C and boron diffusion was for 2 hours at 1100° as contrary to the low diffusion times mentioned in the previous section. A final drive-in step in nitrogen ambience was performed at 900°C for 1 hr. The sheet resistance [Ω/\square] was measured

after every diffusion step and finally after the drive-in step. These values are tabulated in Table 4.1. Thermal evaporation of Aluminum followed by lift-off was done to get the metal contact pads. Figure 4.13(b) shows the confocal micro-graph of the metal contact pads of diodes having doping length of $250\ \mu\text{m}$, $500\ \mu\text{m}$ and $750\ \mu\text{m}$ of varying gaps (G). SEM image of the cleaved cross-section with thin layer of oxide on top of the waveguide fabricated with $2\text{-}\mu\text{m}$ -SOI is shown in Figure 4.13(a).

Table 4.1: Sheet resistance (Ω/\square) measured at various stages of diffusion dopings.

Steps	'n'-type	'p'-type
After phosphorous diffusion	13.7	-
After boron diffusion	15.2	9.1
After drive-in	16.1	10.2

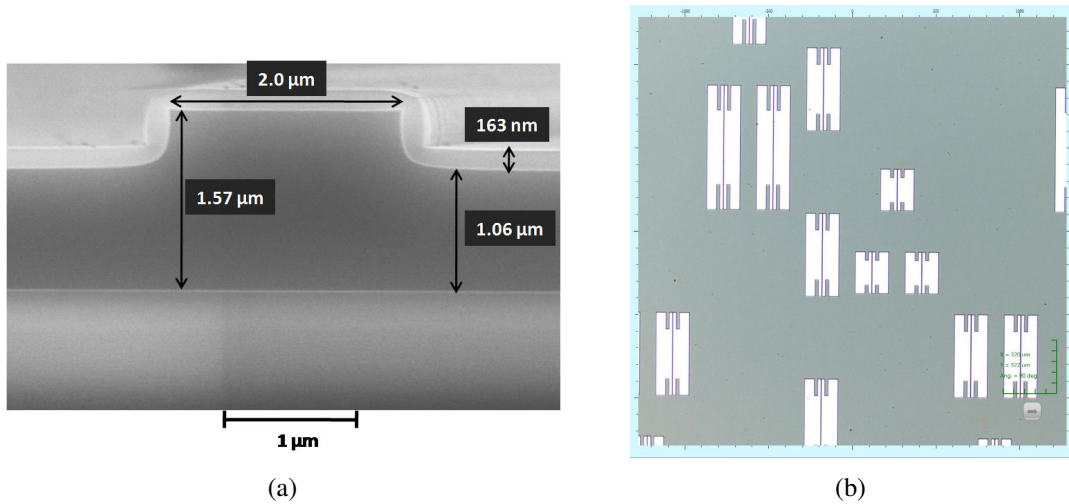


Figure 4.13: (a) SEM image of the cleaved end-facet of a rib waveguide with thermally grown surface passivation oxide of thickness $\sim 163\ \text{nm}$, fabricated with initial SOI device layer thickness of $2\ \mu\text{m}$, (b) confocal micro-graph showing the top Aluminum metal contact pads of the fabricated diodes of three different lengths ($L = 250\ \mu\text{m}$, $500\ \mu\text{m}$ and $750\ \mu\text{m}$).

The I-V characteristics shown in Figure 4.14(a) are corresponding to initial device layer thickness of $2\ \mu\text{m}$ reduced to $\sim 1.5\ \mu\text{m}$ (after all the oxidation steps), and subsequent surface etched device layer thicknesses of $1.0\ \mu\text{m}$ and $0.75\ \mu\text{m}$, respectively. Figure 4.14(b) shows the measured I-V characteristics for diodes with the three different doping lengths. Their corresponding C-V measurements are shown in Figure 4.14(c).

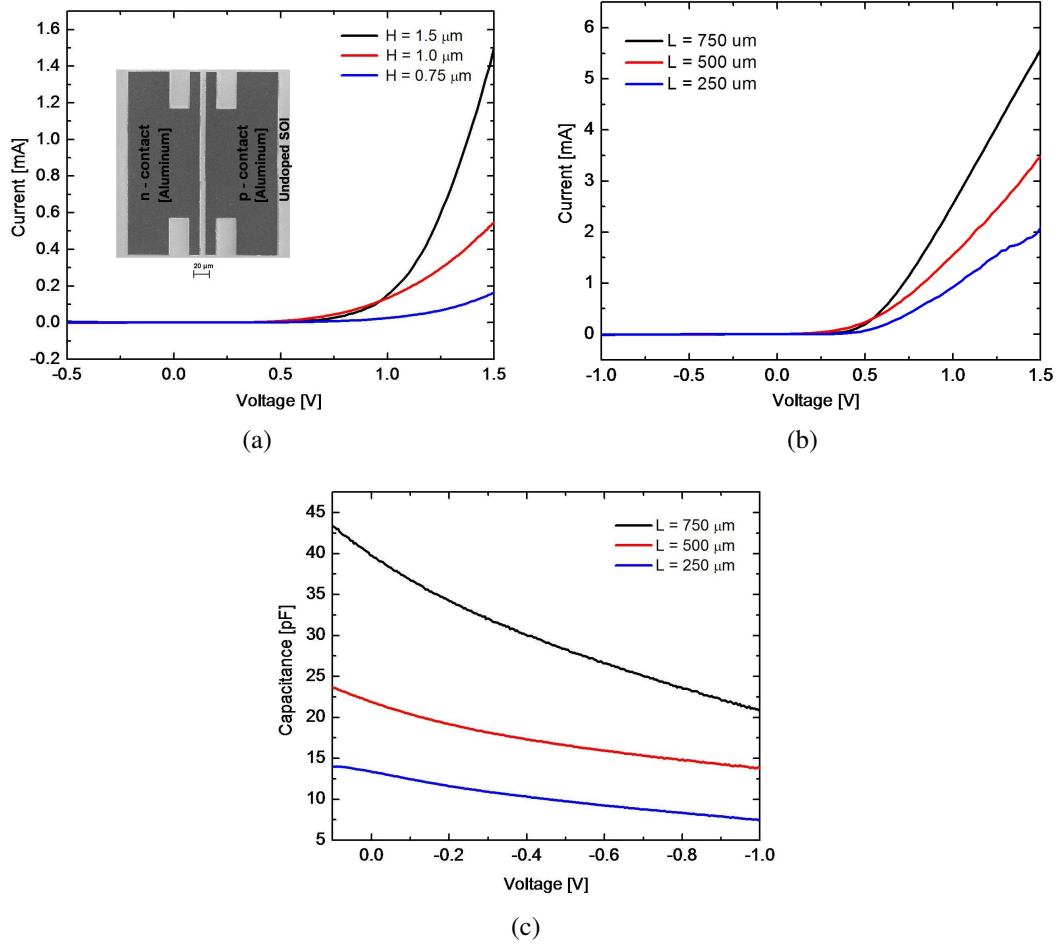


Figure 4.14: (a) $I - V$ characteristics of diodes ($L = 500 \mu\text{m}$) for device layer thickness of $H = 1.5 \mu\text{m}$, $1.0 \mu\text{m}$, and $0.75 \mu\text{m}$ derived from initial device layer thickness of $H_0 = 2 \mu\text{m}$. Inset: SEM image of a fabricated diode with Aluminum contact pads. (b) $I - V$ characteristics of diodes with three different lengths $L = 250 \mu\text{m}$, $500 \mu\text{m}$ and $750 \mu\text{m}$ ($H = 1.5 \mu\text{m}$). (c) $C - V$ characteristics of diodes with three different lengths $L = 250 \mu\text{m}$, $500 \mu\text{m}$ and $750 \mu\text{m}$ ($H = 1.5 \mu\text{m}$).

The forward current at 1.5 V bias is measured to be $\sim 1.8 \text{ mA}$, $\sim 3 \text{ mA}$ and $\sim 5 \text{ mA}$ for diodes of $250 \mu\text{m}$, $500 \mu\text{m}$ and $750 \mu\text{m}$ of doping lengths respectively. The junction capacitance at 0 V for each of them is $\sim 13 \text{ pF}$, $\sim 23 \text{ pF}$ and $\sim 40 \text{ pF}$ respectively. These results are consistent with the predicted theoretical simulations. However, more experimental results are required for close comparisons and accurate modeling.

The I-V characteristics of the diodes were not as expected for device layer lower than $0.75 \mu\text{m}$. Repeated fabrication of samples showed similar behaviour of the diodes as the device layer kept on reducing. Hence, to figure out the exact problem we measured the sheet resistances after every etching step. Table 4.2 shows the values of the

Table 4.2: Simulated and experimental value of sheet resistance [Ω/\square] after first step of phosphorous diffusion and final step of boron diffusion.

SOI thickness (H) [μm]	Phosphorous Diffusion		Boron Diffusion	
	Simulated	Experimental	Simulated	Experimental
1.25	13	14.35	13	11.11
1.00	47	50.01	16	12.38
0.75	159	147.2	19	15.7
0.5	444	390.69	27	23.94
0.25	1259	1313.06	46	47.69

sheet resistances obtained after every etching step along with the predicted value from TSUPREM process simulation. Even though there was not much difference in the values of sheet resistance obtained from experiment and the simulated values, still there was persistent problem with the functioning of the diodes. We expect that the high temperature process of surface passivation (dry oxidation at 900°C) at lower device layer thickness might have affected the diode operation. Also the rate of oxidation varies for p-doped region and n-doped region. Hence, there is a possibility of non-uniform SOI thickness at the diodes, which prevented us to get normal operation of them. Therefore, we could not demonstrate the electro-optic phase-shifters integrated with the MRRs for 220 nm SOI device layer thickness. Nevertheless, it was a good learning process to integrate p-i-n/p-n diode waveguide phase shifters for active control, and gave us an idea to fabricate p-doped microheater directly on 250 nm SOI and reduce it to 220 nm SOI after all the processes.

4.2 Doped Microheater with MRR

As discussed in Chapter-3 about the two kinds of microheaters viz., Titanium microheaters and p-doped microheaters. The p-doped microheaters were also fabricated and characterized using in-house facilities. The fabrication of doped microheater integrated microring resonator was performed taking into consideration the designed parameters and the fabrication flow discussed schematically in Chapter-3 (Fig. 3.10). For a quick

reference, the simulation flow is shown in Fig. 4.15.

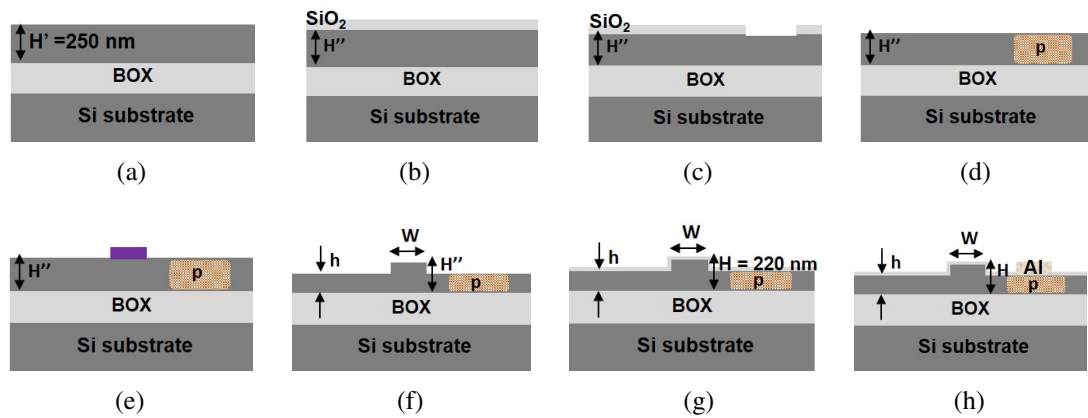


Figure 4.15: Schematic cross-section of the fabrication process flow for doped microheater integrated microring resonator, (a) SOI wafer of device layer $H' = 250$ nm, (b) oxidation for masking during boron diffusion, (c) etching of oxide for boron diffusion, (d) boron diffusion and oxide removal, (e) lithography for waveguide diffusion, (f) etching of rib waveguide, (g) oxidation for surface passivation, (h) oxide etching and aluminum metalization for contact pads .

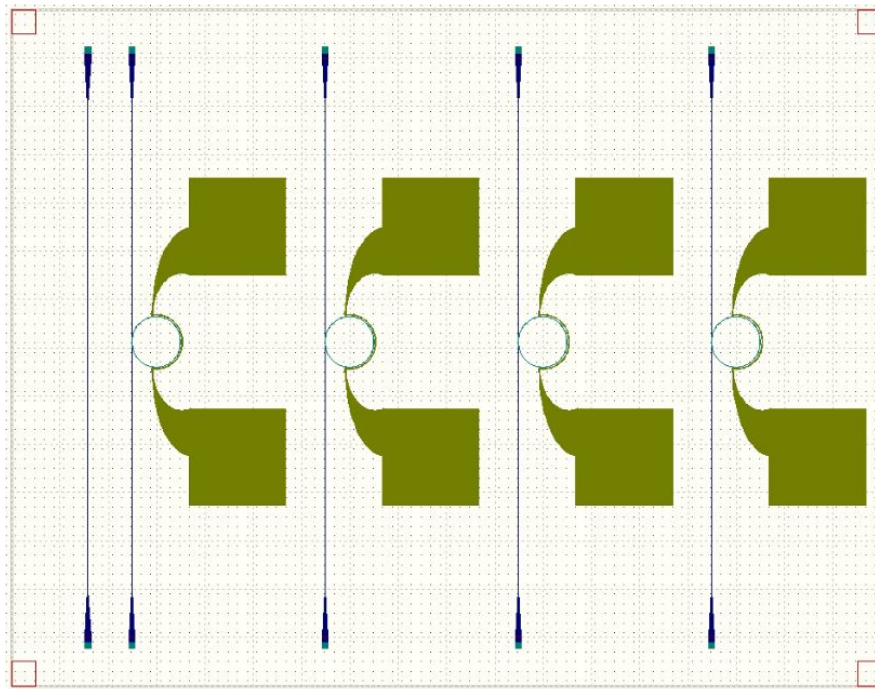


Figure 4.16: Mask layout used to fabricate p-doped integrated microheaters. A reference waveguide is followed by four MRRs integrated with doped heater. The gap between the MRR and the microheater is $2 \mu\text{m}$ for the first two structures and $3 \mu\text{m}$ for the next two structures.

The mask layout used to fabricate the devices is shown in Fig. 4.16. A reference waveguide is placed along with four MRRs in one set of devices. The first two MRRs

have the microheaters placed $2\ \mu\text{m}$ away from them, while the third and fourth MRRs have the microheaters at a distance of $3\ \mu\text{m}$. Two sets of these devices were fabricated on the final sample. A few steps of optimization was also done for the fabrication of the microheaters. A 250 nm SOI sample was cleaned using standard silicon wafer cleaning procedure. The sample was oxidised at 900°C using dry oxidation for 40 mins. A 45 nm thick silicon-di-oxide layer was grown for hard mask during p-type (boron) diffusion doping. The sample was dehydrated at 150°C before spin-coating positive e-beam resist PMMA. Electron-beam lithography was used to do lithography for the diffusion window (microheater as well as the contact pads). Details of spin-coating and electron-beam lithography parameters are given in Appendix A.5. Following the lithography step, oxide etching was performed using standard ICPRIE recipe (see Appendix A.8). The sample was cleaned in acetone to remove the residual resist before loading the sample into the diffusion furnace. Boron diffusion was performed at 1100°C for 5 mins to fabricate the doped microheater. The borosilicate glass (BSG) formed during the diffusion process was softened by low-temperature oxidation (LTO) process and removed using aqueous HF solution. The measured sheet resistance was $\sim 12\ \Omega/\square$ which was similar to the value obtained using TSUPREM4 process simulation. The sample was further dehydrated and prepared for the lithography of the waveguides. Negative tone e-beam resist HSQ was spun on the sample using standard procedure. The waveguides, MRRs and the grating couplers were etched 70 nm using standard ICPRIE silicon etching. The residual HSQ was removed using aqueous HF solution. The second dry oxidation step was performed for surface passivation. A 20 nm thick SiO_2 was grown. Finally the device layer thickness reduces to $H = 220\ \text{nm}$ after all the oxidation steps, and the rib waveguide dimensions also were similar to the one designed in Chapter-3. The last step of lithography for the contact pads was performed on the sample using PMMA resist. The sample was prepared following the usual steps of dehydration, spin-coating, lithography and development. Thermal evaporation of Aluminium was done to deposit the metal. Aluminium lift-off in acetone was performed to obtain the final device.

Fig. 4.17 shows the SEM images of the fabricated device. The MRR with the doped microheater with the Aluminium contact pads is shown in Fig. 4.17(a). Fig. 4.17(b) shows the zoom image of the p-doped microheater of $1\ \mu\text{m}$ width placed $2\ \mu\text{m}$ away

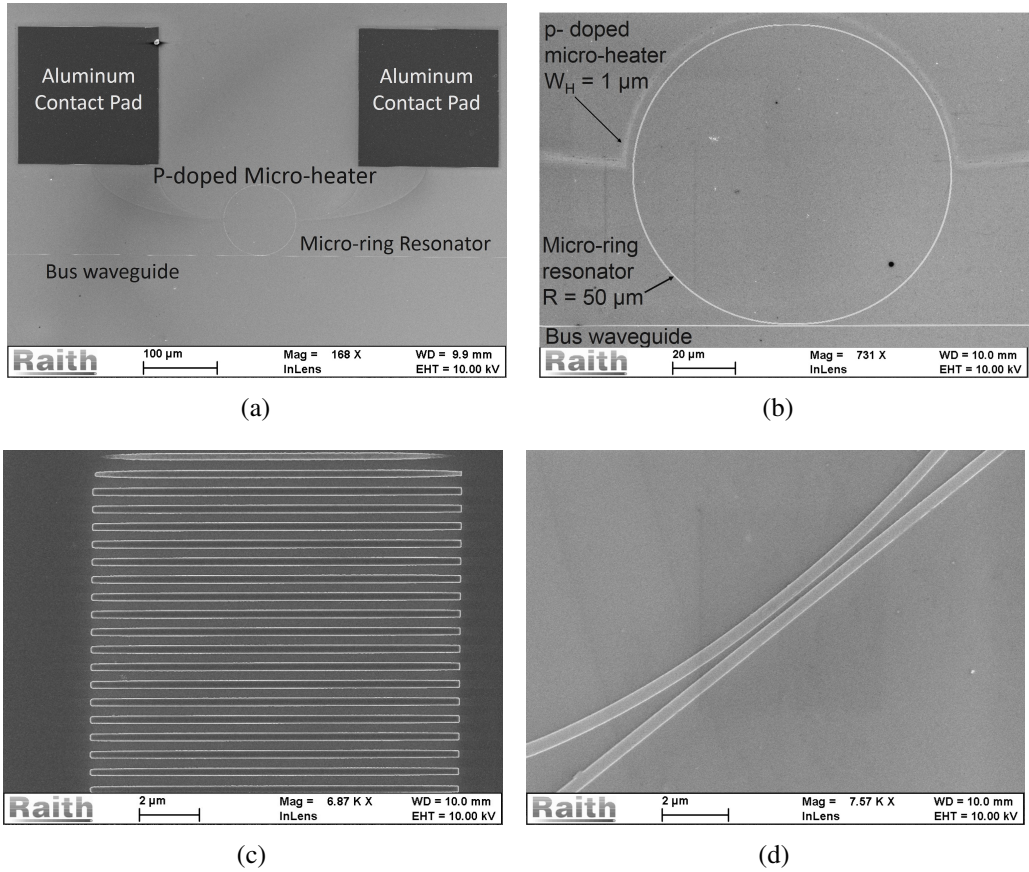


Figure 4.17: SEM image of (a) micro-heater ($W_H = 1\mu\text{m}$) integrated along with MRR at a distance of $2\mu\text{m}$, (b) zoomed image of the doped microheater integrated MRR, (c) grating coupler, (d) directional coupler.

from the MRR of $50\mu\text{m}$ radius. The zoomed image of the grating coupler and the directional coupler is shown in Fig. 4.17(c) and 4.17(d) respectively. The sample had two variations of devices where the gap between the MRR and the microheater was kept as $2\mu\text{m}$ and $3\mu\text{m}$.

4.2.1 Thermo-optic Detuning Characteristics

The fabricated devices were characterized using the characterization setup whose schematic is shown in (Fig.4.18). Grating coupler setup was used to launch light into the MRRs from the tunable laser source (TLS) for the passive characterization. For the active characterization, a source measure unit (SMU) was connected in series with a function generator (FG) for biasing the microheater through electrical probes. The transmission characteristics was observed in the optical spectrum analyser (OSA) and the transient

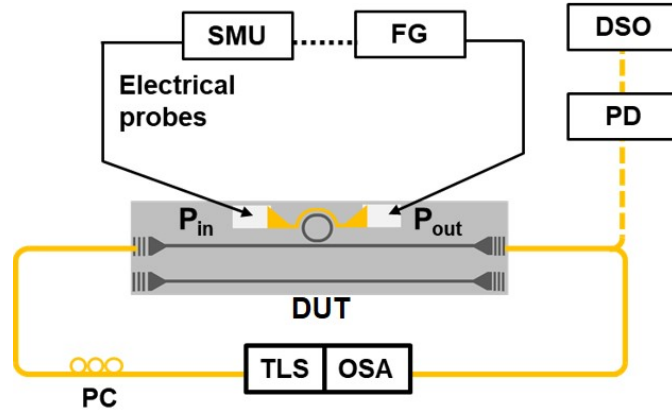


Figure 4.18: A schematic illustration of the experimental set-up used for device characterizations: TLS -Tunable Laser Source, PC - Polarization Controller, DUT - Device Under Test, SMU - Source Measurement Unit, FG - Function Generator, PD - Photodetector, DSO - Digital storage oscilloscope, OSA - Optical Spectrum Analyzer. P_{in} is the launched laser power into the MRR and P_{out} is the output from the MRR.

measurements were observed in the digital storage oscilloscope (DSO) via a photodetector (PD).

The transmission was measured for reference straight waveguide and the MRR. The normalized transmission spectrum of the MRR is shown in Fig.4.19(a).

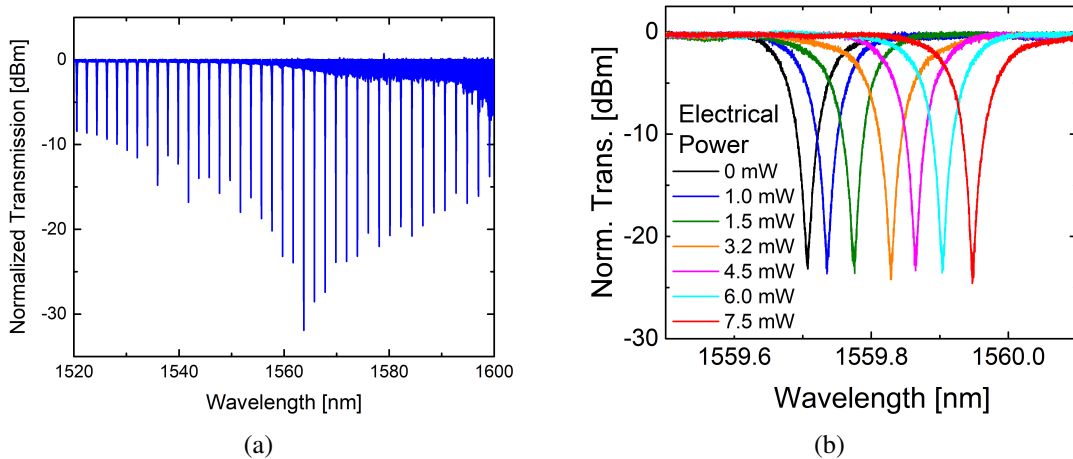


Figure 4.19: Normalized transmission spectrum of the fabricated MRR for (a) wavelength range of $1520 \text{ nm} < \lambda < 1600 \text{ nm}$, (b) different electrical power of the doped microheater for a resonance around $\lambda \sim 1560 \text{ nm}$.

The free-spectral range (FSR) obtained was 1.92 nm with Q-factor of $\sim 35,000$. The noise in the transmission spectrum towards the higher wavelength is due to the grating coupler response. The top surface passivation oxide has slightly changed the response

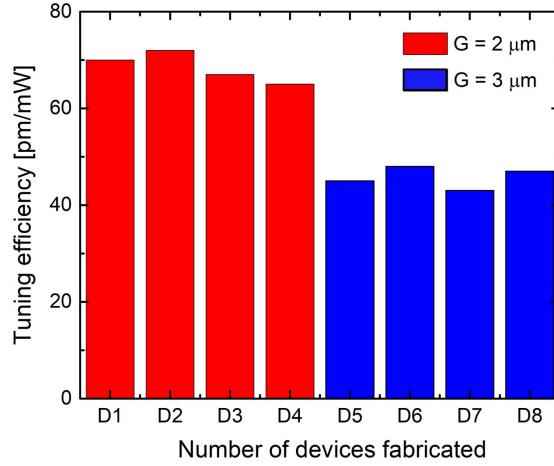


Figure 4.20: Bar chart showing the thermal tuning efficiency of the different devices fabricated with two variations of gap between the micro-heater and the ring resonator ($G = 2 \mu\text{m}$ and $3 \mu\text{m}$).

of the grating couplers. The line resistance of the p-doped microheater was slightly high ($\sim 250 \text{ k}\Omega$) signifying the doping concentration reduced after the rib waveguide was etched. Hence the voltage required to drive the microheaters was high. The measured electro-optic wavelength tunability was $\sim 72 \text{ pm/mW}$ as depicted in Fig. 4.19(b). This value is slightly low compared to as reported in [95] due to low effective heat transfer to the rib because of high contact resistance and also slightly higher slab height than the earlier reported results. This can be further reduced by optimizing the doping concentration and also the slab thickness. Fig. 4.20 shows the tuning efficiency obtained in all the devices fabricated in the sample. Total of 4 devices of $2 \mu\text{m}$ gap between the MRR and microheater was present which showed an average tuning efficiency of $\sim 70 \text{ pm/mW}$. The devices with $3 \mu\text{m}$ gap showed an average tuning efficiency of $\sim 45 \text{ pm/mW}$.

4.2.2 Transient Response

The transient measurements were performed to get the estimation of the switching time of the microheaters. The voltage dependent detuning characteristics was used to decide the modulation voltage strength and to ensure that ON-OFF switching occurs within the linear region of the resonance curve. A bias voltage of 35V was applied in the microheater contact pads. A switching voltage of 5V (5 kHz) was applied in series

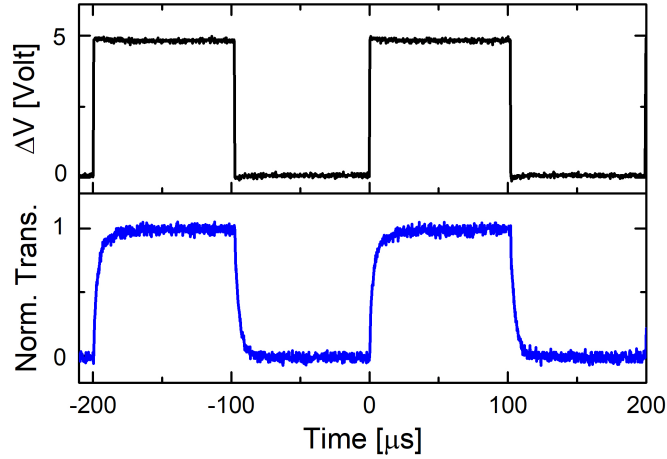


Figure 4.21: Thermo-optic transient response for the slab integrated doped microheater for $\Delta V = 5V$ (5 kHz). An additional bias voltage $V_B = 35V$ was applied between the microheater contact pads for a launched laser power $P_{in} = 0.2$ mW set to operate at one of the resonant wavelengths.

with the bias voltage as shown in the circuit of Fig. 4.18. The thermo-optic transient response is shown in Fig. 4.21 along with the input switching voltage. The rise time and fall time obtained is $4.45 \mu s$ and $4.63 \mu s$ respectively. As the resistance of the doped microheaters were slightly high, the voltage required is also on the higher side.

4.3 Metal Microheater with MRRs

The metal microheater integrated MRRs was fabricated using the designed dimensions and process flow discussed in Chapter-3. The rib waveguide and MRR was etched first followed by the deposition of the metal for contact pads and microheater unlike the doped microheater. A sample was prepared to fabricate only the MRRs along with reference waveguides using the optimized parameters. The all-pass MRRs was fabricated using electron-beam lithography and dry etching using the designed parameters ($W = 420$ nm, $h = 150$ nm, $g = 150$ nm) on 220 nm SOI. Fig. 4.22 shows the schematic cross-section of the process steps to fabricate a passive silicon MRR. Fig. 4.22(a) shows the cross-section of a cleaned SOI wafer, which is followed by the spin-coating of the negative tone electron beam resist HSQ in Fig. 4.22(b). Fig. 4.22(c) shows the cross-section of the SOI after the complete process of electron-beam patterning and developing for a rib waveguide and a directional coupler. Final cross-section after etching the waveguide

and directional coupler and stripping the excess resist is shown in Fig. 4.22(d).

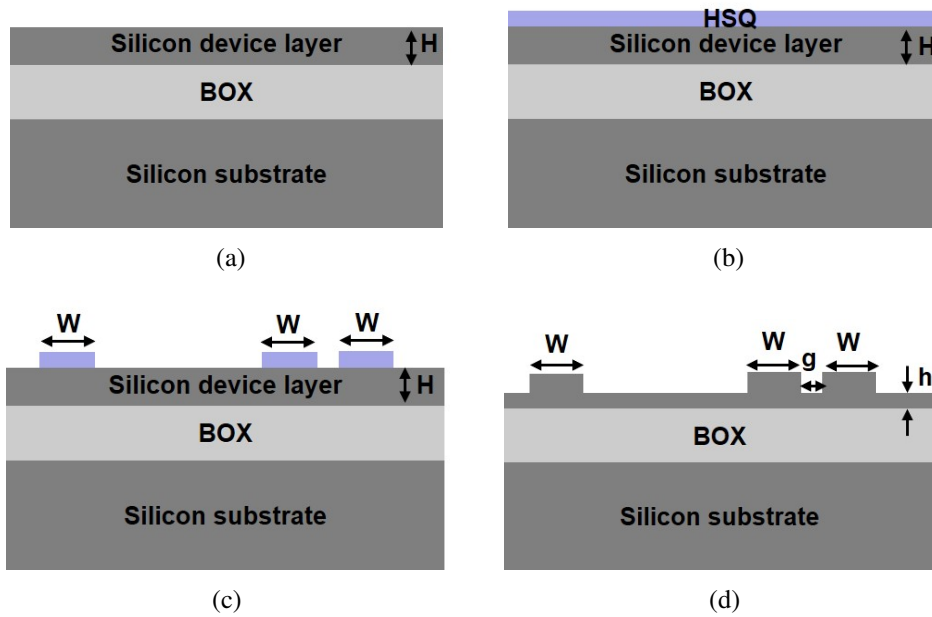


Figure 4.22: Schematic cross-section depicting the process steps for fabricating the MRRs: (a) cleaned SOI substrate, (b) HSQ resist coating on the surface, (c) electron beam lithography for patterning of rib waveguide and directional coupler, (d) dry etching (ICPRIE) of rib waveguide and directional coupler.

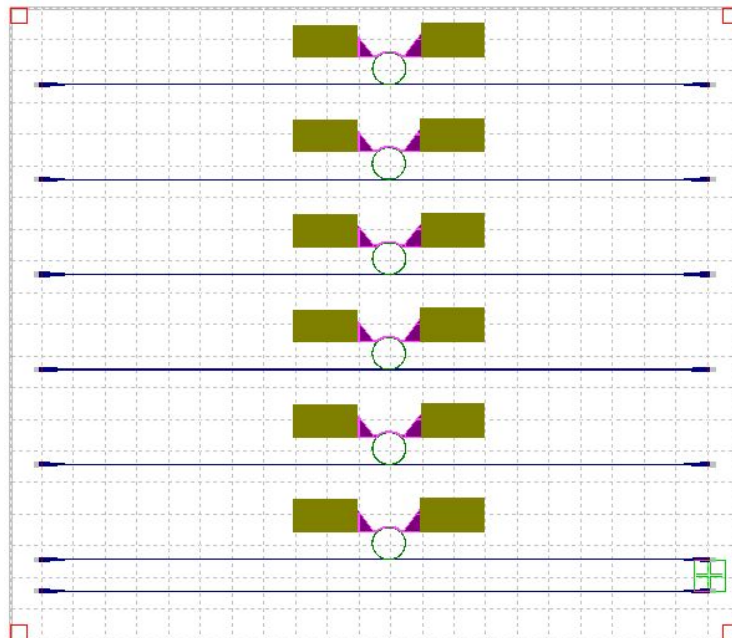


Figure 4.23: Mask layout for D_1 set of devices consisting of one reference waveguide and six MRRs integrated with microheater. Device D_1R_1 , D_1R_3 and D_1R_5 have $4 \mu\text{m}$ length of the directional coupler and device D_1R_2 , D_1R_4 and D_1R_6 have $5 \mu\text{m}$ length of the directional coupler.

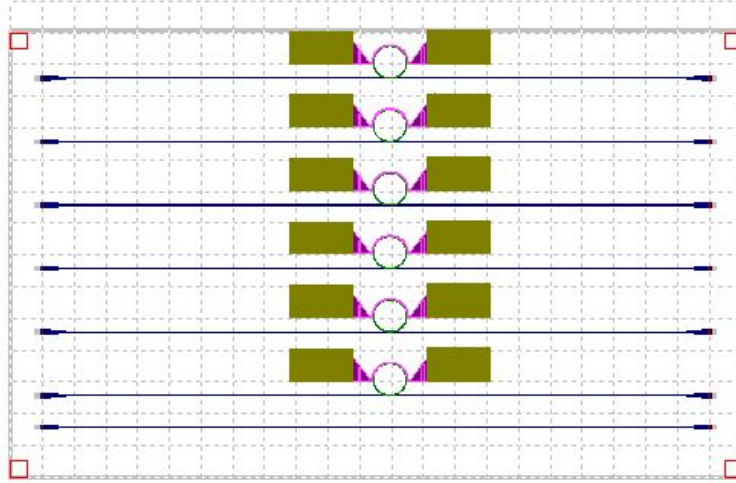


Figure 4.24: Mask layout for D_2 set of devices consisting of one reference waveguide and six MRRs integrated with microheater. Device D_2R_1 , D_2R_3 and D_2R_5 have $4 \mu\text{m}$ length of the directional coupler and device D_2R_2 , D_2R_4 and D_2R_6 have $5 \mu\text{m}$ length of the directional coupler.

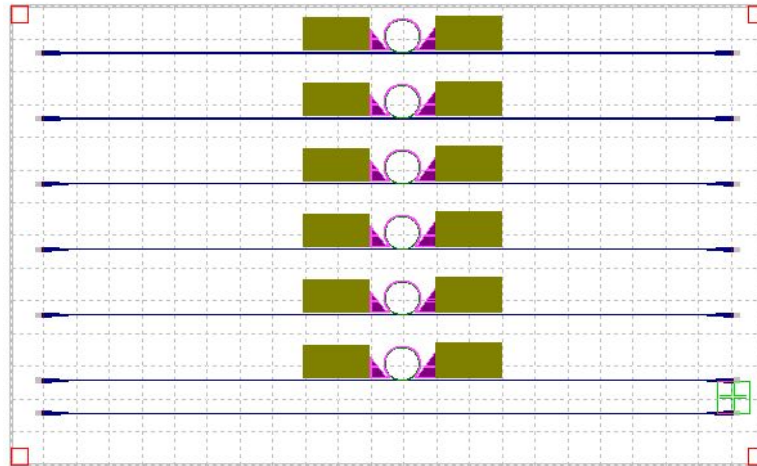


Figure 4.25: Mask layout for D_3 set of devices consisting of one reference waveguide and six MRRs integrated with microheater. Device D_3R_1 , D_3R_3 and D_3R_5 have $4 \mu\text{m}$ length of the directional coupler and device D_3R_2 , D_3R_4 and D_3R_6 have $5 \mu\text{m}$ length of the directional coupler.

The mask layout of the devices fabricated are shown in Fig. 4.23 - 4.25. There were three sets of devices for D_1 , D_2 and D_3 on the sample. Each set consists of one reference waveguide and six MRRs names as $R - 1$ to R_6 . The length of the directional coupler was chosen to be $4 \mu\text{m}$ and $5 \mu\text{m}$ for the alternate MRRs. This was decided after taking into consideration any fabrication errors due to proximity effect in the directional coupler region. The dotted lines show the $100 \mu\text{m} \times 100 \mu\text{m}$ write-field used during the electron-beam lithography.

A 220 nm SOI sample was cleaned using standard silicon wafer cleaning procedure to remove organic and inorganic impurities. The detailed steps of silicon wafer cleaning is given in Appendix A.2. The cleaned SOI sample was dehydrated at 180°C for 10 minutes on a hotplate. The sample was cooled for 5 minutes before spin coating it with negative electron-beam resist HSQ (Hydrogen silsesquioxane). The spin coating parameters are tabulated in details Table. A.4 (Appendix A.3). The HSQ coated SOI sample was soft baked at 180°C for 2 minutes. This was followed by patterning of the device structures using electron-beam lithography (EBL). The column parameters of the EBL patterning is tabulated in Table A.6 (Appendix A.5). After the patterning was completed, the sample was developed using commercial developer MF-319 for ~ 7 minutes. Further, hard bake was performed at 300°C for 2 minutes. The sample was then etched using ICPRIE. An optimized Fluorine based recipe (Table A.7) was used to etch the silicon device layer by ~ 70 nm. CHF_3 gas was used to passivate the side walls to obtain vertical side walls and SF_6 gas was used to etch silicon. The complete etching process involves two chemical steps of gas phase reaction and surface reaction as shown in Eq. 4.2 and 4.3 respectively. The total etching step lasted for 13 seconds to achieve the required etch depth of ~ 70 nm.

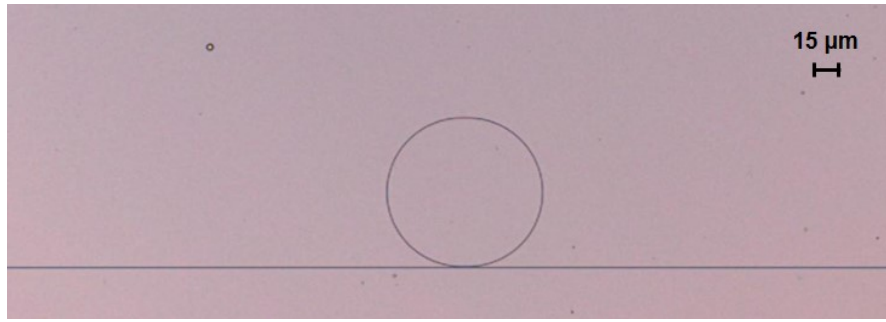
Gas phase reaction:



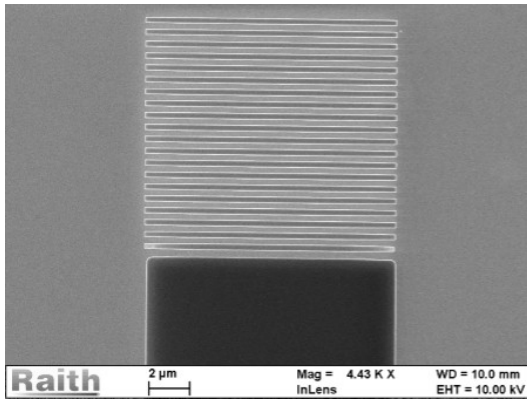
Surface reaction:



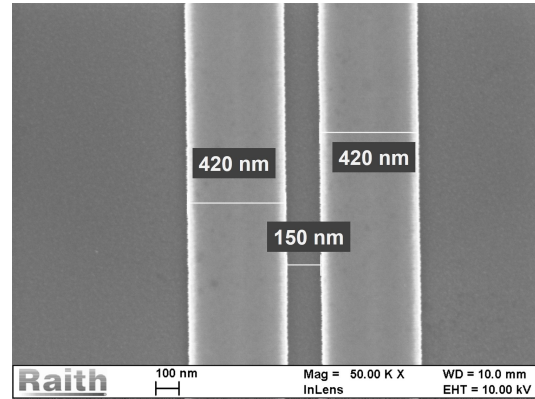
Fig. 4.26(a) shows the confocal micrograph of the fabricated all-pass MRR. The zoomed SEM image of the grating coupler region and the directional coupler region is shown in Fig. 4.26(b) and 4.26(c) respectively. The metal microheaters were fabricated once the passive rib waveguides were fabricated. Al contact pads and Ti microheaters were fabricated, respectively, as already discussed in the previous chapter using the Fig. 3.14. Both were defined again by e-beam lithography (using positive-tone e-beam resist PMMA), metallization and subsequent lift-off processes. The fabrication steps are explained using schematic cross-section as shown in Fig. 4.27. The following part of this section discusses the process steps in details along with the images obtained



(a)



(b)



(c)

Figure 4.26: (a) Confocal micrograph of a fabricated all-pass MRR, SEM image showing zoom image of (b) grating coupler, (c) directional coupler of the fabricated MRR.

during fabrication steps.

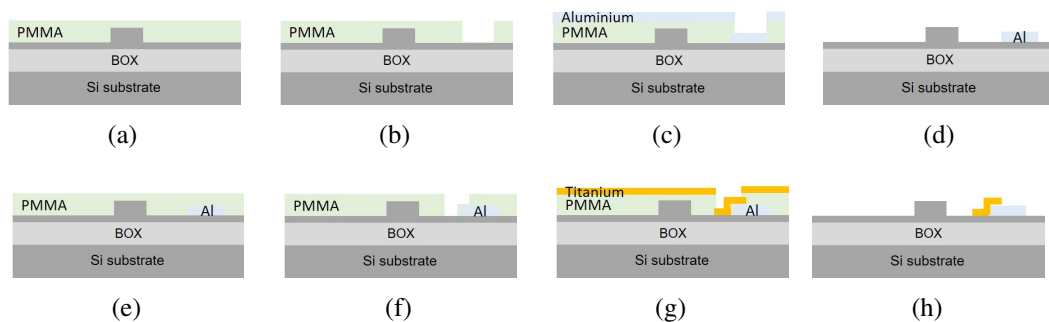


Figure 4.27: Schematic cross-section of the fabrication process flow for Titanium microheater integrated microring resonator, (a) PMMA resist coating, (b) window opening for Aluminium contact pads, (c) Aluminium deposition, (d) Aluminium lift-off, (e) PMMA resist coating, (f) window opening for Titanium microheaters, (g) Titanium deposition, (h) Titanium lift-off .

The detailed fabrication process of integrating microheaters in the slab of rib waveguides for thermo-optic phase-shifters may be found elsewhere [13, 95, 136]. But for

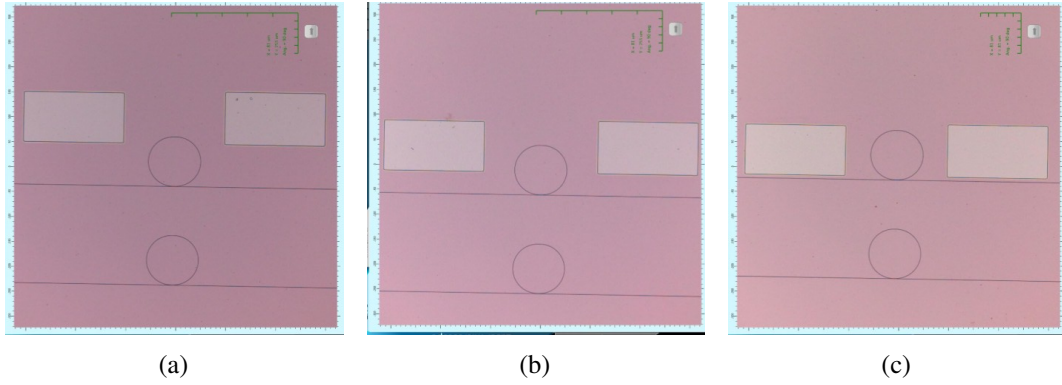


Figure 4.28: Microscopic images for lithography of contact pads the fabricated devices (a) D_1 , (b) D_2 , (c) D_3 .

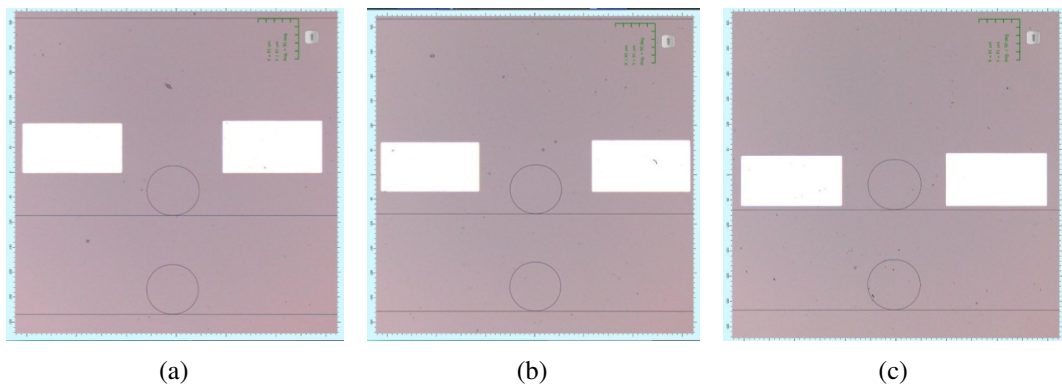


Figure 4.29: Microscopic images after Aluminium lift-off of contact pads the fabricated devices (a) D_1 , (b) D_2 , (c) D_3 .

completeness of the thesis, the complete process steps along with optical micrographs and SEM images of the fabricated devices are discussed here. The 220 nm SOI sample was cleaned as per the standard silicon wafer cleaning procedure. The first step of fabricating the rib waveguide with the grating couplers is same as mentioned in Section 4.1.1. The sample was cleaned in hydrofluoric acid (HF) to remove the HSQ remains after dry etching of the waveguides. The sample was dehydrated at 180 °C for 10 minutes on a hotplate. A positive tone e-beam resist PMMA (A8) was spin coated on the surface to pattern the contact pads. The spin-coating parameters are given in Appendix A.3. A thickness of ~ 250 nm of the resist is obtained after spin-coating. The sample was pre-baked at 150 °C for 2 minutes before patterning using electron-beam lithography. Fig. 4.28 shows the microscopic images of the devices D_1 , D_2 and D_3 after the patterning for the contact pads. Further, Aluminium was deposited using thermal evaporation. Next the contact pads were fabricated using lift-off of Aluminium in Acetone.

Fig. 4.29 shows the microscopic images of D_1 , D_2 and D_3 after the Aluminium contact pads were fabricated. The final mask was for fabricating the Titanium microheater as explained in the fabrication process flow. Similar steps of dehydration of the sample, followed by spin coating of PMMA (A8) was used to prepare the sample for its final lithography step.

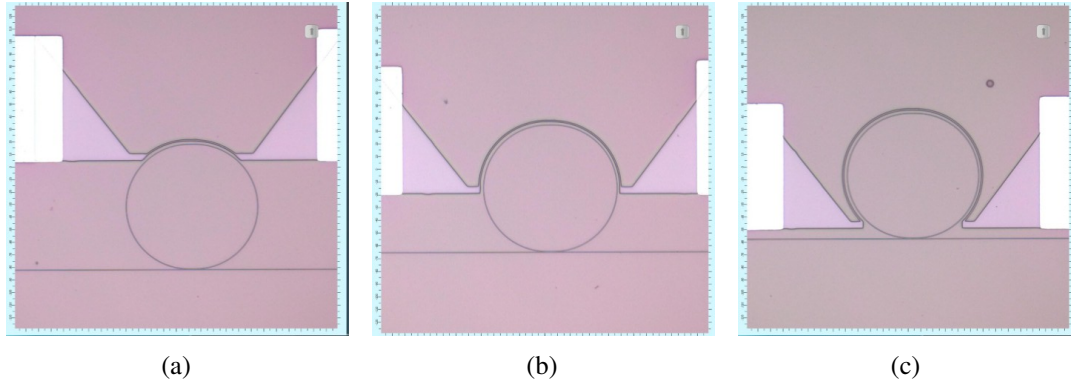


Figure 4.30: Microscopic images for lithography of microheaters of the fabricated devices (a) D_1 , (b) D_2 , (c) D_3 .

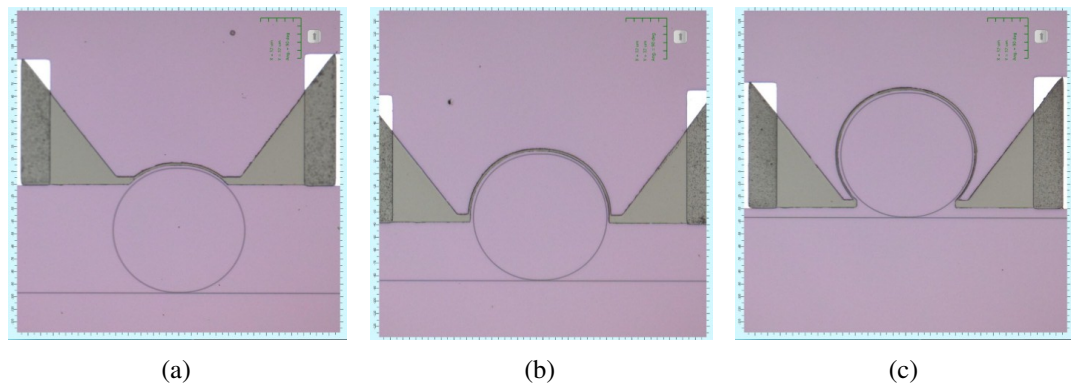
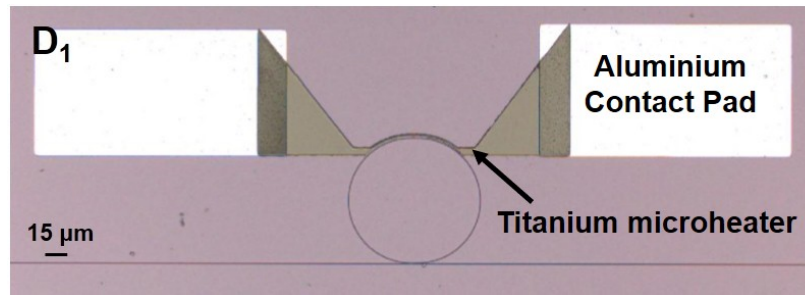
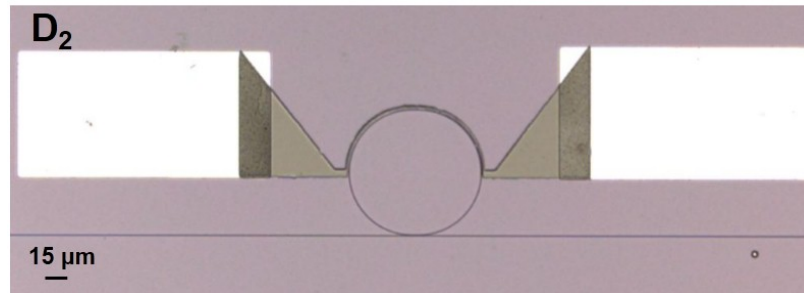


Figure 4.31: Microscopic images after Titanium liftoff of the microheaters of the fabricated devices (a) D_1 , (b) D_2 , (c) D_3 .

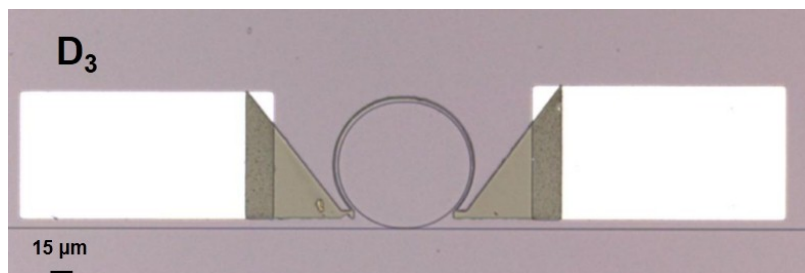
Fig. 4.30 shows the patterned structures for the microheater for D_1 , D_2 and D_3 which were at $2 \mu\text{m}$ separation from the optical waveguide. Electron-beam evaporation was used to deposit 100 nm thickness of Titanium for the metal microheaters. At last lift-off of Titanium was performed to obtain the Titanium microheater integrated on the slab of the MRR. Fig. 4.31 shows the Titanium microheater integrated MRR. The complete devices D_1 , D_2 and D_3 , i.e the Titanium microheater along with the Aluminium contact pads integrated with the MRR is shown in Fig. 4.32. Fig.4.33 show the SEM images also show the three different devices D_1 , D_2 and D_3 along with the zoomed



(a)



(b)



(c)

Figure 4.32: Microscopic images of the complete fabricated devices (MRR integrated with Titanium slab microheater flared to Aluminium contact pad) (a) D_1 , (b) D_2 , (c) D_3 .

region of the optical waveguide-microheater region. It must be noted that the dimensions of fabricated device are slightly deviated from the design parameters but they are acceptable for experimental demonstration. The above images of the microheater integrated MRR fabrication are obtained from the final run performed. There were multiple runs done to optimise the dose for the electron-beam writing, metal lift-off processes and alignment of the MRR with the microheater. Since the lithography was performed using electron-beam, batch processing of samples were not feasible due to the longer patterning time required. Hence, one sample was fabricated after the other during the optimization processes also.

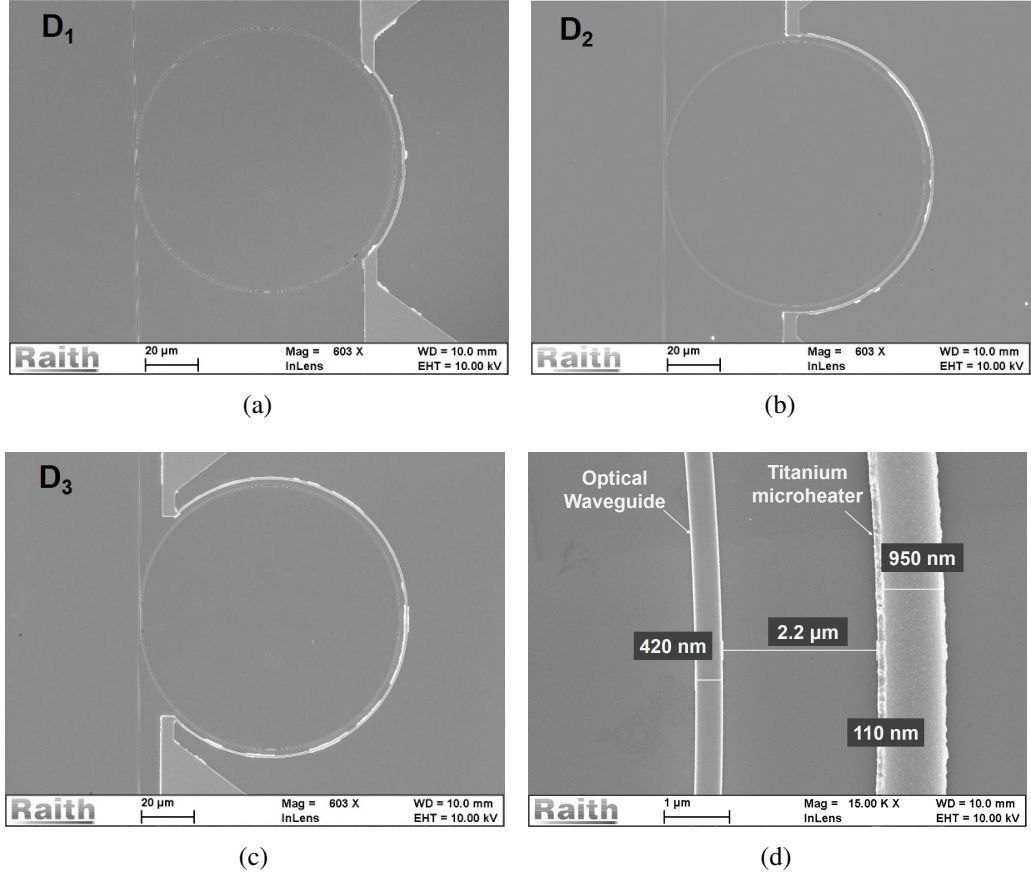


Figure 4.33: SEM images of the fabricated rib waveguide MRRs integrated with slab integrated microheaters: (a) $L_H = 83.5 \mu\text{m}$ (D_1), (b) $L_H = 162 \mu\text{m}$ (D_2), (c) $L_H = 240.5 \mu\text{m}$ (D_3), (d) zoomed image of the Ti-strip microheater placed $\sim 2.2 \mu\text{m}$ away from the rib waveguide.

4.3.1 Passive Characterization of MRRs

The passive transmission characteristics of all MRRs were obtained using a combination of fast tunable narrow linewidth laser and high resolution optical spectrum analyser (Apex OSA with a resolution bandwidth of 0.8 pm). The schematic of the characterization set-up used is shown in Fig. 4.34. The transmission characteristics of a fabricated MRR with the designed parameters i.e. $W = 420 \text{ nm}$, $H = 220 \text{ nm}$, $h = 150 \text{ nm}$, $R = 50 \mu\text{m}$, $L_{DC} = 5 \mu\text{m}$ along with the response of a reference straight waveguide (red curve) in the wavelength range $1520 \text{ nm} \leq \lambda \leq 1600 \text{ nm}$ (C+L band) when -5.6 dBm optical power is launched into the input grating coupler is shown in Fig. 4.35. The upper envelope of the MRR transmission matches with the reference waveguide spectrum, indicating negligible insertion loss of the MRR. The wavelength dependency of the output spectrum is due to the bandwidth limitations of the input/output grating couplers [139].

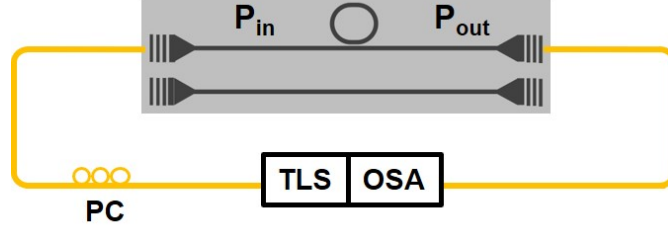


Figure 4.34: Schematic of the characterization set-up. TLS: Tunable Laser Source, OSA: Optical Spectrum Analyzer, PC: Polarization Controller.

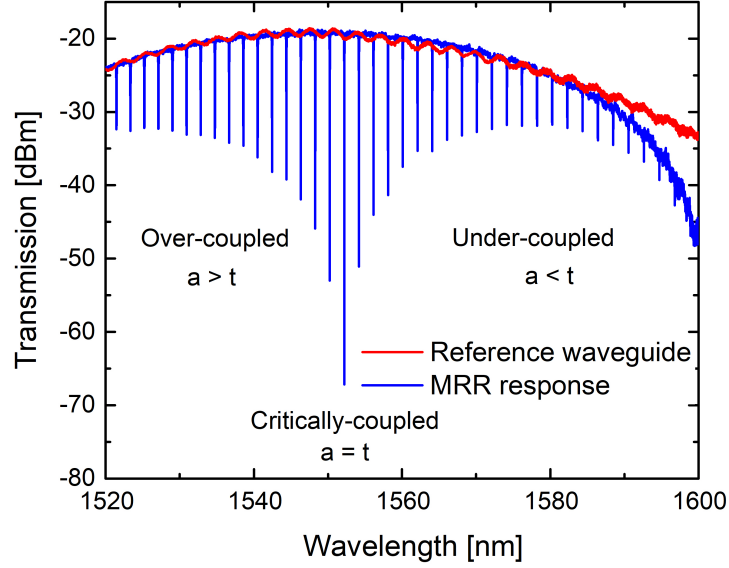


Figure 4.35: Transmission characteristics of reference straight waveguide (red curve) ($W = 420$ nm, $H = 220$ nm, $h = 150$ nm) and a microring resonator ($R = 50$ μm , $L_{DC} = 5$ μm) (blue curve) for 1520 nm $\leq \lambda \leq 1600$ nm.

4.3.2 Extraction of MRR Parameters

Different parameters of the MRR were extracted from the measured transmission characteristics shown in Fig. 4.35. The extracted Q -values of each of the resonances within the wavelength range of 1520 nm $\leq \lambda \leq 1580$ nm are plotted in Fig. 4.36. We have restricted the extraction to 1580 nm wavelength due to the noisy response of the grating couplers beyond $\lambda = 1580$ nm. The Q -values were extracted using Eq. 4.4

$$Q = \frac{\lambda_r}{\Delta\lambda} \quad (4.4)$$

where, λ_r is the value of the resonance wavelength and $\Delta\lambda$ is the 3-dB bandwidth or FWHM (Full Width at Half Maxima) of the resonance from the maximum transmission as shown in Fig. 4.37.

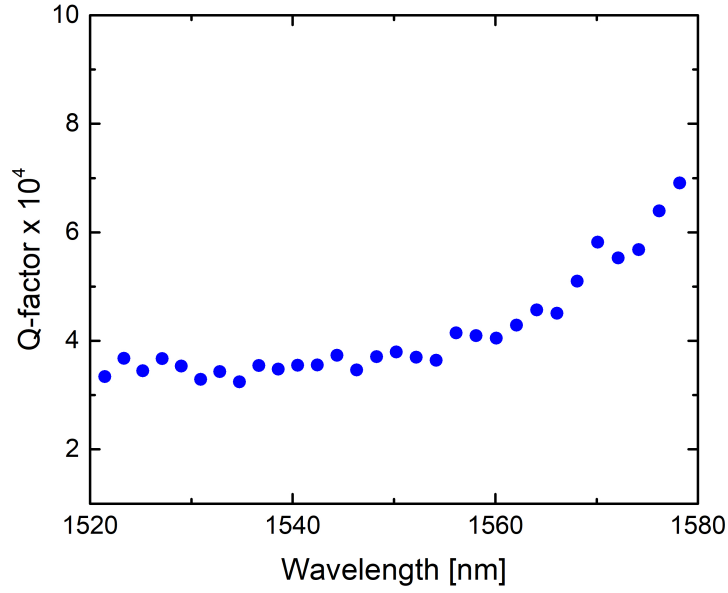


Figure 4.36: Extracted Q-values for each of the resonances from Fig.4.35 for the wavelength range $1520 \text{ nm} \leq \lambda \leq 1580 \text{ nm}$.

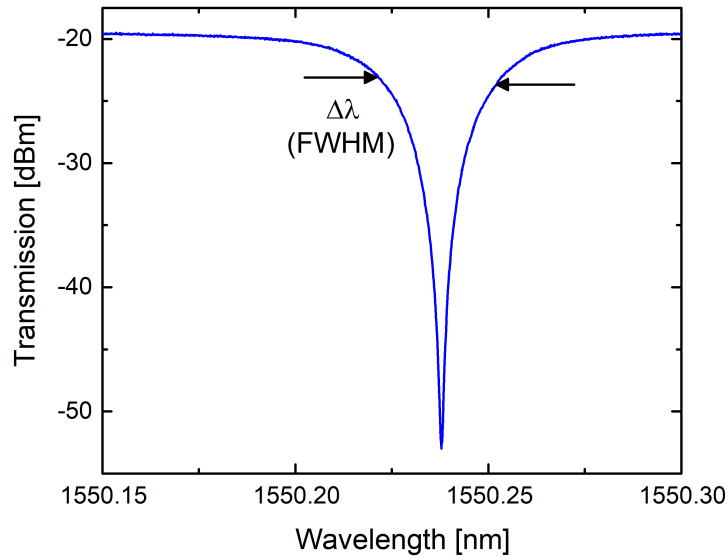


Figure 4.37: Zoom transmission of the resonance around $\lambda_r \sim 1550 \text{ nm}$ of Fig.4.35.

Extinction and Q-values are mainly attributed to the wavelength dependent coupling of ring-bus waveguide directional coupler. For a given round-trip loss factor a in the MRR and self-coupling coefficient t in the coupler, the transmission at any resonant wavelength $T(\lambda_r)$ and corresponding Q-values are given by:

$$T(\lambda_r) = \left[\frac{a - t(\lambda_r)}{1 - at(\lambda_r)} \right]^2 \quad (4.5)$$

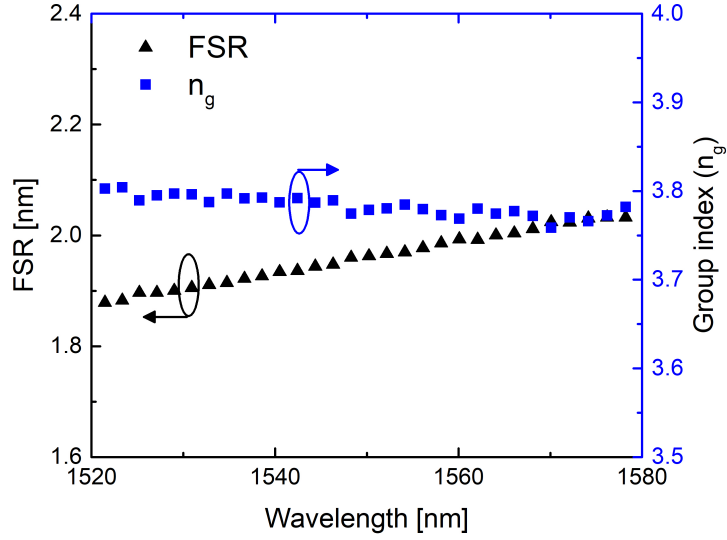


Figure 4.38: Extracted free spectral range (FSR) and group index (n_g) for the MRR from $1520 \text{ nm} \leq \lambda \leq 1570 \text{ nm}$.

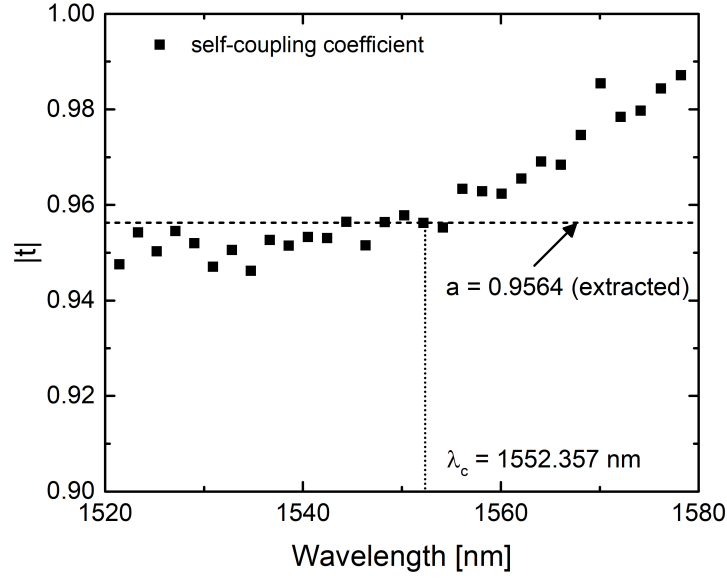


Figure 4.39: Self-coupling coefficient t of the ring-bus waveguide coupler as a function of wavelength along with a (wavelength independent) and λ_c extracted from the experimental results shown in Fig. 4.36.

$$Q(\lambda_r) = \frac{\pi L n_g(\lambda_r) \sqrt{at(\lambda_r)}}{\lambda_r [1 - at(\lambda_r)]} \quad (4.6)$$

In the above equations, we have assumed a is constant over the given wavelength range, $n_g(\lambda_r)$ is the group index of the guided mode at resonance wavelengths λ_r , L is the perimeter length of MRR, and the self-coupling coefficient $t(\lambda_r) = \sqrt{1 - k^2(\lambda_r)}$, where $k(\lambda_r)$ is the cross-coupling coefficient at λ_r (considering loss-less directional coupler) [102]. Thus the maximum extinction (or minimum transmission) occurs for

$a = t(\lambda_r \sim \lambda_c)$, where λ_c is known as the critically coupled wavelength [139]. By extracting group indices around resonant wavelengths from the measured free spectral range $FSR \sim \frac{\lambda_r^2}{n_g(\lambda_r)L}$ (Fig. 4.38), we could evaluate $t(\lambda_r)$ and the result is given in Fig. 4.39 along with the value of $a = 0.9564$, evaluated for $\lambda_r \sim \lambda_c = 1552.357$ nm. We observed little variations in the values of λ_c (± 5 nm) when compared with experimental results of all the fabricated MRRs with same radii ($R = 50$ μm) and with same coupler lengths ($L_{DC} = 5$ μm). This may be attributed to the variations in gap ‘ g ’ between ring-bus waveguides resulting from the drifts and/or proximity errors during e-beam lithography. Nevertheless, it is evident that Q-values are higher for the resonant wavelengths satisfying under-coupled condition, i.e., for $a < t$. The Q-value for all the fabricated rings lie between 42000 - 55000 for $\lambda \sim 1550$ nm.

4.3.3 Thermo-optic Detuning Characteristics

The fabricated MRRs integrated with Titanium metal microheaters were characterised using the same experimental setup as shown schematically in Fig. 4.18.

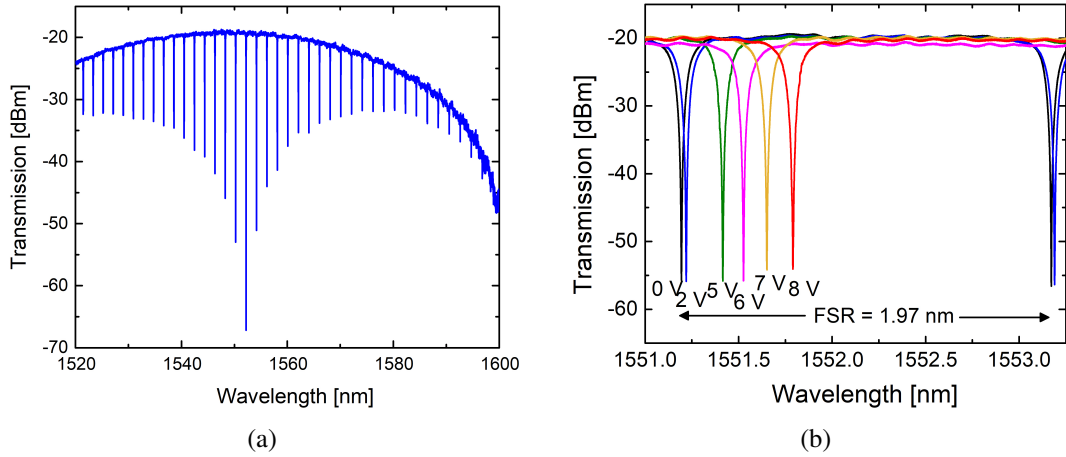


Figure 4.40: (a) Transmission characteristics of device D_1 for $1520 \text{ nm} \leq \lambda \leq 1600$ nm, (b) shift in resonant wavelength ($\Delta\lambda_r$) around $\lambda_r \sim 1550$ nm with the applied voltage.

Fig. 4.40(a), 4.41(a) and 4.42(a) shows the transmission spectrum of the devices D_1 , D_2 and D_3 respectively. The critically coupled wavelength lies in between $1550 \text{ nm} < \lambda < 1560$ nm exhibiting a maximum extinction of 40 dB to 50 dB. Fig. 4.40(b), 4.41(b) and 4.42(b) show the corresponding thermo-optic detuning of resonant wavelengths for

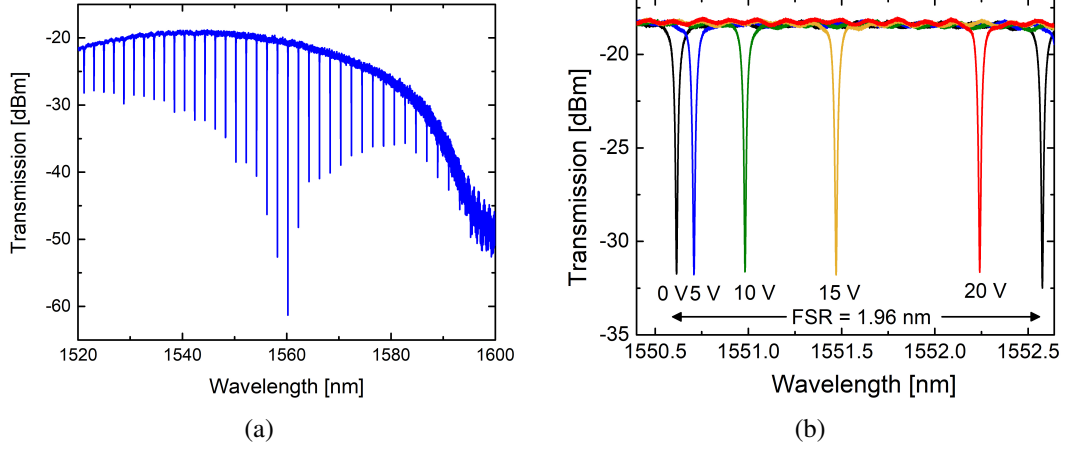


Figure 4.41: (a) Transmission characteristics of device D_2 for $1520 \leq \lambda \leq 1600$ nm, (b) shift in resonant wavelength ($\Delta\lambda_r$) around $\lambda_r \sim 1550$ nm with the applied voltage.

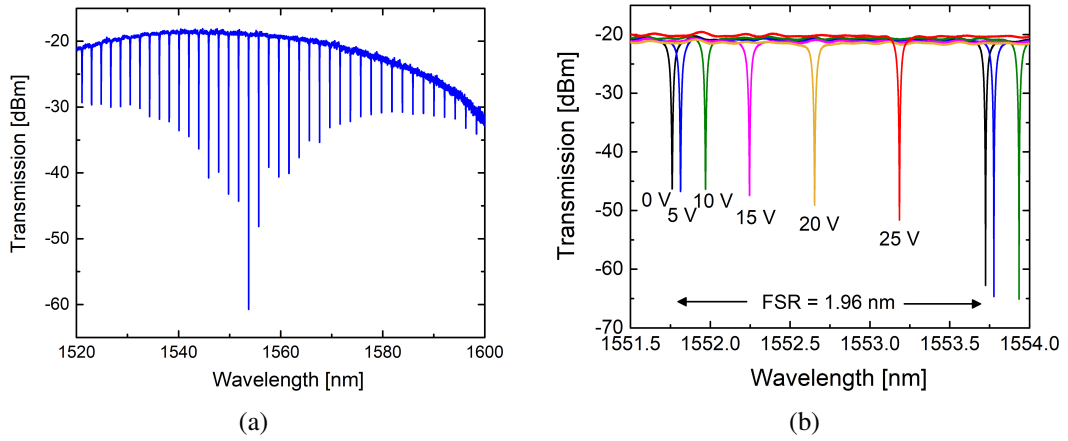


Figure 4.42: (a) Transmission characteristics of device D_3 for $1520 \leq \lambda \leq 1600$ nm, (b) shift in resonant wavelength ($\Delta\lambda_r$) around $\lambda_r \sim 1550$ nm with the applied voltage.

all the three devices D_1 , D_2 and D_3 as a function of bias voltage V_B applied between microheater contact pads.

Fig. 4.43(a) compares the resonance wavelength shift for all the three devices w.r.t the voltage applied to the individual devices. From this wavelength tuning characteristics, the rise in waveguide temperature (ΔT) can be evaluated using following analytical equation (also see Fig. 4.43(b)):

$$\Delta T = \frac{1}{L_H} \left[\frac{L_R n_g(\lambda_r)}{\lambda_r} \cdot \left(\frac{dn_{eff}}{dT} \right)^{-1} \right] \Delta \lambda_r \quad (4.7)$$

where $\Delta\lambda_r$ is the observed shift for a given order of resonant wavelength λ_r and $\frac{dn_{eff}}{dT}$ ($\sim 1.79 \times 10^{-4} \text{ K}^{-1}$)[139] is the thermo-optic coefficient of the guided fundamental mode with its effective index n_{eff} . Thus shorter the length of waveguide phase-shifter L_H , higher is the temperature rise (ΔT) required for a given wavelength detuning of $\Delta\lambda_r$. Accordingly, we estimate the values of $\frac{\Delta\lambda_r}{\Delta T}$ as 19 pm/K, 38 pm/K, and 55 pm/K for devices D_1 , D_2 , and D_3 , respectively. Using Fig. 4.43(a) and Eq. 4.7, we have generated ΔT vs. V_B curves for all the three devices as shown in Fig. 4.43(b). The extracted ΔT values are fitted with a polynomial function of V_B :

$$\Delta T = k_1 V_B^2 + k_2 V_B^3 \quad (4.8)$$

where k_1 and k_2 are found to be non-zero positive constants; they can be extracted independently for each device (depend on shape and footprint of the microheater). The measured resistance for the three different length of microheaters along with the extracted values of k_1 and k_2 are tabulated in Table 4.3.

Table 4.3: Extracted values of parameters used in the polynomial function to fit ΔT with V_B along with the microheater length (L_H) and resistance (R_H).

Device #	L_H [μm]	R_H [$\text{k}\Omega$]	k_1 [$\text{K}\cdot\text{V}^{-2}$]	k_2 [$\text{K}\cdot\text{V}^{-3}$]
D_1	83.5	2.6	0.3131	0.01389
D_2	162.0	6.7	0.0997	0.00028
D_3	240.5	10.5	0.0206	0.00058

The symbols in Fig. 4.43(c) show the experimental values of temperature rise in the waveguide core for the amount of power dissipated for all the three microheaters. It is compared with the simulation data (dashed line) obtained using COMSOL Multiphysics. The figure shows close match of the experimental data with the simulated values. The microheater resistances were also measured while increasing the temperature for all the three lengths of microheaters (Fig. 4.43(d)). There is not much variation observed for the resistance values for the devices.

The value of the current flowing through the microheaters was restricted to $< 4 \text{ mA}$ to prevent the microheaters from being burnt and damaged. Fig. 4.44 shows the SEM image of a burnt/damaged microheater due to excessive current flow through it. Finally, Table 4.4 compares the extracted parameters along with some measured dimensions

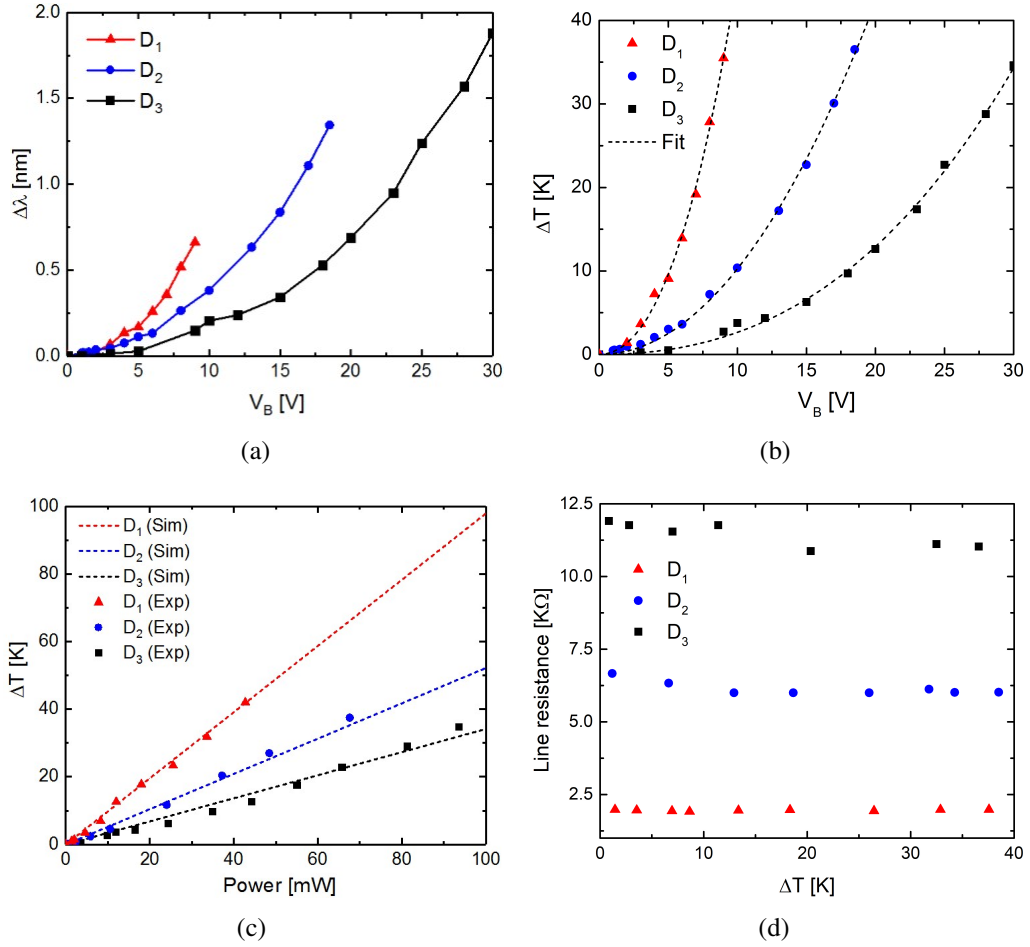


Figure 4.43: (a) Shift in resonant wavelengths ($\Delta\lambda_r$) of the MRRs (D_1 , D_2 , D_3) as a function of applied voltage (V_B) between microheater contact pads, (b) experimental rise in waveguide temperatures as a function of applied voltage (V_B) between microheater contact pads (dotted lines how the polynomial fit), (c) experimental rise in waveguide temperatures as a function of applied electrical power for D_1 , D_2 , D_3 , (symbols are experimental data, dotted lines how the COMSOL simulation), (d) extracted line resistance of the three length of microheaters D_1 , D_2 , D_3 for different waveguide temperature.

(with possible measurement errors) of a fabricated device D_2 for a resonance wavelength around $\lambda_m \sim 1550$ nm. Importantly, the variation of the resistance value for all the microheaters was ± 0.5 $k\Omega$ for D_1 , ± 1 $k\Omega$ for D_2 and ± 2 $k\Omega$ for D_3 . Hence the tuning efficiency of the MRRs integrated with the same length of microheater did not vary much for the devices fabricated on the sample.

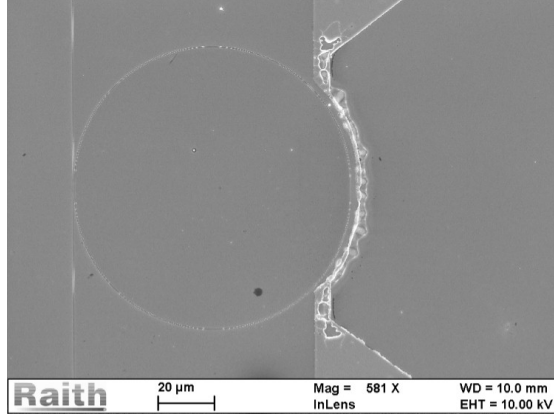


Figure 4.44: SEM image of a damaged microheater of D_1 burnt due to passing of high current.

Table 4.4: Observed and/or extracted parameters of a fabricated device (D_2)

Parameters	Value	Remark
W	420 ± 10 nm	Lithographic Error
g	150 ± 10 nm	Lithographic Error
G	2.0 ± 0.1 μm	Alignment Error
R_H	~ 7 $\text{K}\Omega$	Measured from V-I characteristics
λ_c	~ 1564.7 nm	Observed Value
Q-value	52000	Extracted for a res. $\sim \lambda_c$
Q-value	45000	Extracted for a res. $\lambda_m \sim 1550$ nm
α	6.12 dB/cm	Extracted for $\lambda \sim \lambda_c$
FSR	1.98 nm	Observed at $\lambda \sim 1550$ nm
n_g	3.78	Extracted at $\lambda \sim 1550$ nm
n_{eff}	2.64	Extracted at $\lambda \sim 1550$ nm
k^2	0.06	Extracted for $\lambda \sim 1550$ nm
t^2	0.94	Extracted for $\lambda \sim 1550$ nm
Coupling Loss	6.5 dB	Per GC Facet

4.3.4 Transient Response

The voltage dependent resonance detuning characteristics shown in Fig. 4.43(a) has been used to study further the switching response. A square wave voltage signal with 5 kHz repetition rate were used to study the thermo-optic response times. The square wave voltage modulation depths of ΔV_s has been used for devices D_1 , D_2 and D_3 , respectively to ensure uniform ON-OFF switching extinction of ~ 10 dB for operating the laser wavelength fixed at the resonance wavelengths of the respective MRRs. Fig. 4.45 shows the transient response obtained from device D_2 for a 1V square voltage wave applied along with 6V DC bias for an input optical power of 0.2 mW. The blue curve in Fig. 4.45 shows the transient response of the MRR. The rise time and the fall

time obtained is $\sim 3.3 \mu\text{s}$ and $3.45 \mu\text{s}$ respectively.

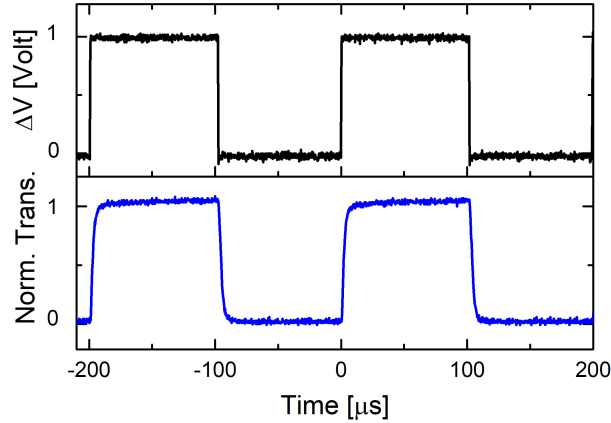


Figure 4.45: Thermo-optic transient response for the slab integrated Ti metal microheater for $\Delta V = 1\text{V}$ (5 kHz). An additional bias voltage $V_B = 6\text{V}$ was applied between the microheater contact pads for a launched laser power $P_{in} = 0.2 \text{ mW}$ set to operate at one of the resonant wavelengths.

4.4 Comparison Between Doped and Metal Microheater

The results from the above sections give us a clear picture about the two kinds of microheater presented in this thesis. From the experimental results point of view, the MRRs integrated with the doped microheater exhibited lower Q-value (avg. - 32000) as compared to the metal counterparts (avg. - 48000). Though the ring dimensions obtained were nearly same, the process steps varied for both of them. Also a thin layer of silicon-dioxide was present for the p-doped microheater, which might have lead to lowering of the Q-value.

The other parameter for comparison for both the microheaters is their resistance. As discussed in the doped microheater section, the resistance obtained was much higher probably due to the etching of the rib waveguide after the diffusion process, thus losing the maximum dopant concentration region. The p-doped microheaters showed a resistance of $\sim 250 \text{ k}\Omega$, whereas the metal microheater of comparable length had resistance of $\sim 7 \text{ k}\Omega$.

The detuning characteristics for both the metal microheater (D_2) and the doped microheater is shown in Fig. 4.46. This graph shows the maximum temperature rise in the rib waveguide w.r.t the electrical power dissipated in the microheater for device

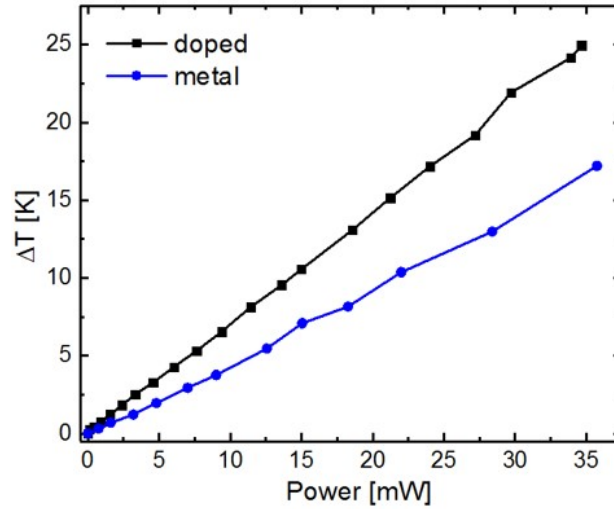


Figure 4.46: Comparison of maximum temperature rise in the rib waveguide core for Titanium microheater (D_2) and p-doped microheater of length $162 \mu\text{m}$ integrated with MRR w.r.t the power dissipated in the microheater.

configuration D_2 of the metal heater and the p-doped heater. Both the microheaters cover half of the MRR perimeter. It is observed that the doped microheaters perform better than its metal counterparts. The doped microheaters exhibited $\sim 72 \text{ pm/mW}$ whereas the metal microheaters exhibited $\sim 45 \text{ pm/mW}$ wavelength detuning. This is due to the fact that the doping is directly in the slab, whereas the metal microheater is placed on top of the slab. Hence the power requirement is higher in case of metal microheaters as it needs to heat the slab as well.

Another parameter of comparison for both the metal and doped microheaters is their switching speed. For a switching extinction of $\sim 8 - 10 \text{ dB}$ (operating within the resonance bandwidth), both the microheaters exhibited nearly comparable speed of $3 - 4 \mu\text{s}$. Nevertheless, the switching speed can be further reduced for the doped microheater by optimising the doping concentration.

Hence the type of microheater to be used completely depends on the targeted application. The doped microheater are mostly integrated in the slab of the rib waveguides while the metal microheaters can be integrated on top of the upper cladding oxide. Hence for tighter bends, metal heaters are preferable. But the doped heaters provide better tuning efficiency. However, the loss incurred due to doping the slab should also be taken into account depending of the application. The experimental response obtained in our work also shows the thermal tuning efficiency is better for the doped microheater.

But for switching applications where the switching speed plays an important role, microheaters having faster response time needs to be used. For our work we have integrated the metal microheater on top of the slab, so that we can compare it with a similar geometry of the doped heater.

4.5 Summary

In summary, the fabrication of p-i-n/p-n diode waveguide phase-shifter fabrication and characterization was presented. Starting from a $2\mu\text{m}$ SOI device layer thickness, p-i-n diodes were fabricated first to study the waveguide loss, VOA performance in reverse bias and PD behaviour in reverse bias. As the dimensions of waveguides were slightly bigger ($2\mu\text{m}$), polarization independent behaviour was observed. The waveguide loss for both the TE and TM mode was nearly same (1.85 - 1.9 dB/cm). The VOAs also showed similar attenuation for TE and TM mode (10 dB for 100 mA of current). The p-i-n diodes when operated in reverse bias showed the photodetector behaviour, and we could observe increase in photocurrent with higher optical power. Also the longer diodes had higher values of photocurrent. The demonstration of p-i-n/p-n diode for lower device layer thickness was attempted. But there was not much promising results of the diode current for device layer thickness below 750 nm.

In the second part of the chapter, we discussed the fabrication and characterization of the thermo-optic phase shifters. First the p-doped microheaters were fabricated and characterized. But the resistance of the p-doped heaters were slightly higher than predicted. This requires further doping optimization. Nevertheless, they exhibited wavelength tuning efficiency of $\sim 72\text{ pm/mW}$ and switching time $\sim 4.5\ \mu\text{s}$. For the MRRs with metal microheaters, a detailed study on the MRR characterization was performed first. Different device parameters like free-spectral range (FSR), group-index (n_g), quality factor (Q-factor) and coupling coefficients were extracted from the passive characterization results. Using the passive MRRs, thermo-optic phase shifters were integrated on the slab of the MRRs. Three different lengths of Titanium microheaters were fabricated and characterized. The detuning characteristics for all the three geometries were measured followed by transient measurements. The switching time obtained was ~ 3

μs for the MRRs integrated with Titanium microheaters. Finally a comparative study of both the microheaters is presented. Using the metal microheater integrated MRRs, we have demonstrated the non-linear experiments in the next chapter. As the MRRs with the titanium microheaters exhibited better Quality factor compared to the p-doped MRRs, we have used them to study the electrical control of optical bistability.

CHAPTER 5

Experimental Results: Stimulated Four Wave Mixing

The MRRs integrated with electro-optic phase-shifters were used to demonstrate the electrically controlled optical bistability. The D_2 devices (MRRs integrated with Titanium metal microheaters encompassing half its perimeter) that were fabricated and characterized has been used for the experimental demonstration of bistability control in this chapter. This chapter presents the non-linear phase obtained from the non-linear transmission at first. The phase dependent transmission hysteresis is presented in Section 5.2, followed by the experimental results of stimulated four wave mixing in Section 5.3. Finally the experimental results are compared with the theoretical model developed and is summarized.

5.1 Non-linear Phase Measurement

The thermo-optic detuning was performed by sourcing bias voltage (V_B) to the microheater contact pads from the voltage source as discussed in Section-4.3.1. The induced phase change ϕ_A is calculated using following equation:

$$\phi_A = \left[\frac{2\pi}{\lambda_m^2} n_g(\lambda_m) L \right] \cdot \Delta\lambda_m \quad (5.1)$$

where we have used $\lambda_m = 1550.736$ nm ($m = 552$). There can be slight uncertainty in the value of ‘m’ since the n_{eff} is considered from simulation. The experimental thermo-optic detuning characteristics is found to be comparable to that of theoretical results; thermo-optic phase-shifts were calculated by simulating 3D temperature profiles as a function of microheater bias voltage V_B using 3D heat transfer module in COMSOL Multiphysics platform as discussed in Section 3.2.2. Fig. 5.1 shows the extracted value of the linear phase shift (ϕ_A) obtained from the resonance wavelength shift obtained from the bias voltage (V_B).

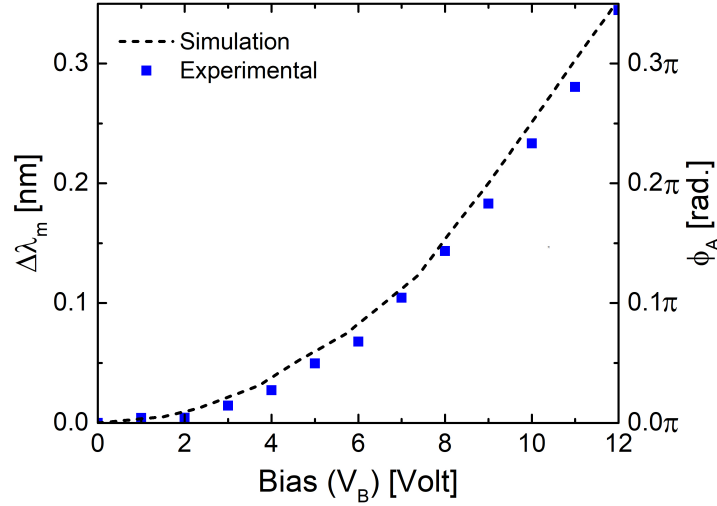


Figure 5.1: Thermo-optic detuning of resonance wavelength ($\Delta\lambda_m$ and estimated linear phase-shift ϕ_A (measured and simulated for $\lambda_m \sim 1550.7$ nm) as a function of applied voltage (V_B) between microheater contact pads.

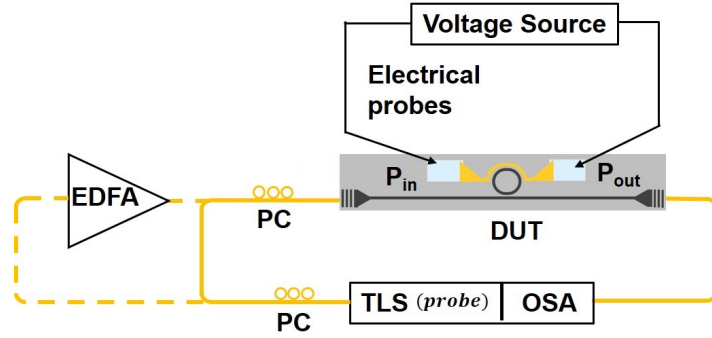
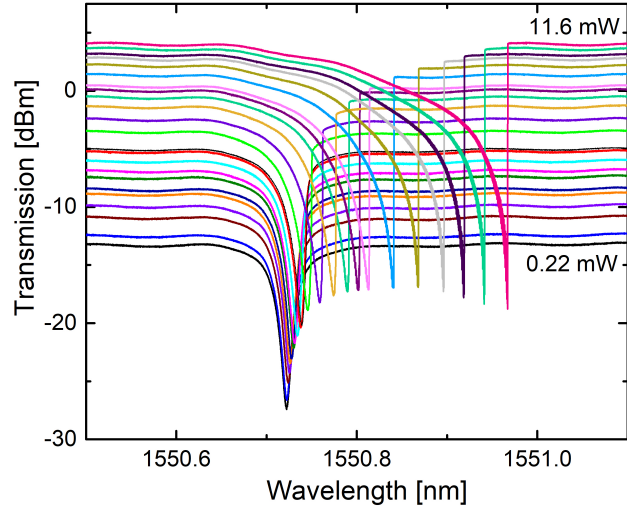
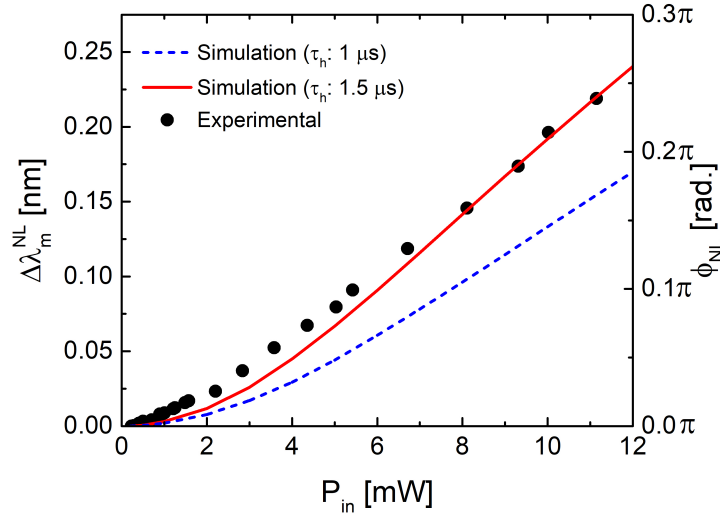


Figure 5.2: Scheme of the experimental set-up used for transmission characterization of the device and its active detuning of linear phase ϕ_A by the integrated microheater: TLS -Tunable Laser Source, EDFA - Erbium-Doped Fiber Amplifier, PC - Polarization Controller, DUT - Device Under Test, OSA - Optical Spectrum Analyzer. P_{in} is the launched laser power into the MRR and P_{out} is the output from the MRR.

To extract ϕ_{NL} , we obtained transmission characteristics of the MRR at higher input power levels. For this experiment, the probe tunable laser source was connected to an erbium doped fiber amplifier (EDFA) as shown in Fig. 5.2. The transmitted spectra around m -th order resonance measured at the OSA are shown in Fig. 5.3(a) for different P_{in} (deduced by subtracting input grating coupler loss from the launched power). As the value of P_{in} increases, the resonance is red-shifted because of increase in ϕ_{NL} and a sharp transition occurs from minimum to maximum because of bistability. From the observed resonance shifts $\Delta\lambda_m^{NL}$, we evaluated values of ϕ_{NL} using Eqn. 5.1 and they are plotted as a function P_{in} as shown in Fig. 5.3(b). We have compared these results



(a)



(b)

Figure 5.3: (a) Transmission characteristics of the MRR for higher input powers (P_{in} varying from 0.22 mW to 11.6 mW), (b) shift in resonance wavelength (λ_m^{NL}) and estimated ϕ_{NL} as a function of P_{in} : scattered symbols are experimental results, dashed and solid lines show simulation results corresponding to $\tau_h = 1 \mu\text{s}$ and $1.5 \mu\text{s}$, respectively.

with theoretical model discussed in Chapter-2 and using extracted parameters given in Table 4.4. The deviation in experimental results may be attributed to the additional heat generation resulting out of free carrier absorption and scattering losses. A fraction of lost laser power due to these processes possibly contributes towards temperature rise in the waveguide core depending on its geometry and ambience. Other important sources of this deviation may be due to the assumptions of relaxation time constants $\tau_e = 1 \text{ ns}$ and $\tau_h = 1 \mu\text{s}$ (see Table 2.1) for our device. However, we find a reasonably good match

of the experimental data with the model by just changing the value of thermal relaxation time constant τ_h (in the model) from $1 \mu\text{s}$ to $1.5 \mu\text{s}$, at least for $P_{in} \geq 8 \text{ mW}$.

5.2 Phase-dependent Transmission Hysteresis

The phase dependent hysteresis was experimentally demonstrated by using the set-up shown in Fig. 5.4. Transmission hysteresis of the MRR was obtained at higher input powers as a function of ϕ_A . The values of ϕ_A is estimated from the experimental curve shown in Fig. 5.1. For convenience, the pump laser wavelength ($\lambda_p = 1550.951 \text{ nm}$) was set slightly higher than m -th resonance wavelength ($\lambda_m = 1550.736 \text{ nm}$) of the MRR, such that $2m\pi - \phi_0(\lambda_p) \approx 0.22\pi$. Joint transmission characteristics of probe TLS and pump laser ($P_{in} = 8.4 \text{ mW}$) measured by the OSA for $\phi_A = 0$ are shown in Fig. 5.5. The device under test (DUT) was left at room temperature and a thermal drift of resonance wavelength was found to be $< 5 \text{ pm}$ observed during the entire process of experiment.

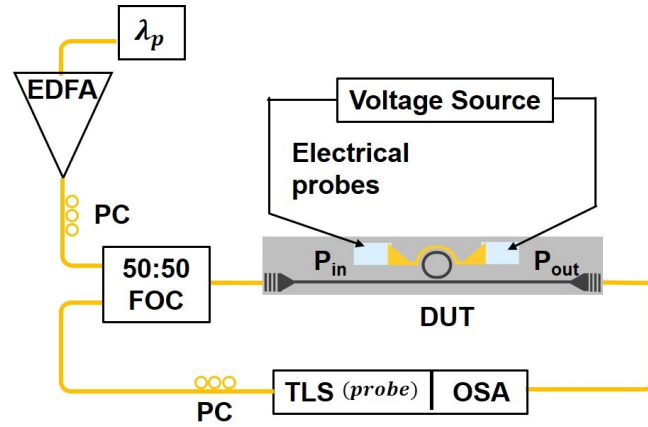


Figure 5.4: Scheme of the experimental set-up used for ϕ_A dependent transmission characterizations at high input powers: TLS - Tunable Laser Source, EDFA - Erbium-Doped Fiber Amplifier, PC - Polarization Controller, DUT - Device Under Test, OSA - Optical Spectrum Analyzer. P_{in} is the launched laser power into the MRR and P_{out} is the output from the MRR .

Fig. 5.6(a) shows the experimental transmitted pump laser output (P_{out}) as a function of ϕ_A increasing as well as decreasing. As expected, we clearly observe a hysteresis loop between forward and reverse paths. In forward path, the minimum transmission occurs at $\phi_A \approx 0.15\pi$ with an extinction of about 3 dB (marked as A), whereas

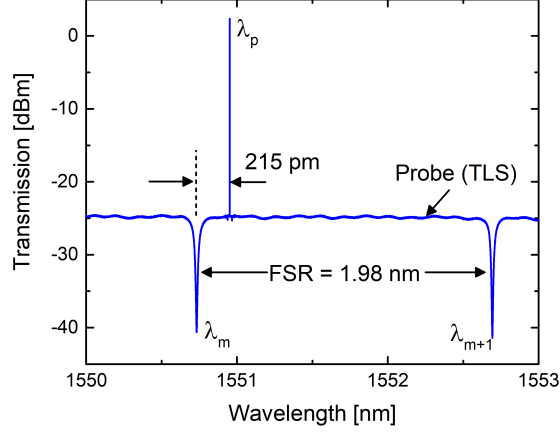


Figure 5.5: Wavelength dependent transmission showing off-resonant pump wavelength λ_p ($P_{in} = 8.4$ mW), and resonant wavelengths λ_m and λ_{m+1} .

their corresponding values are $\sim 0.07\pi$ and ~ 16 dB, respectively for the reverse path (marked as B). This experimental observation can be compared with simulation results shown in Fig. 5.6(b), which was carried out with extracted parameters discussed in Chapter-3 and other constants from Table 2.1, but with $\tau_h = 1.5$ μ s. In simulation curves, A' and B' are designated as the transmission minima in forward and reverse directions, respectively. The maximum pump extinctions in both forward and reverse directions are matching closely with experimental results. However, while we observe $\phi_A(B) \approx \phi_A(B')$, $\phi_A(A')$ is found to be slightly higher than $\phi_A(A)$. This is attributed to the measurement error as we observe point A is more unstable than point B during the experiment. Nevertheless, the most important observation in this experiment is that $\phi_A(B) + \phi_{NL} \approx 2m\pi - \phi_0(\lambda_p) = 0.22\pi$, satisfying perfect resonance condition and minimum transmission (minimum P_{out}) as discussed in Chapter-2.

From the above experimental observations supported by mathematical modeling and simulations, it is now confirmed that the higher and stable field enhancement inside the MRR can be achieved by detuning its phase ϕ_A from a higher value to the operating value of $\phi_A^{op} \downarrow$, such that the following condition is fulfilled for m -th order resonance:

$$\phi_A^{op} \downarrow = 2m\pi - \phi_0(\lambda_p) - \phi_{NL}(\lambda_p) \quad (5.2)$$

when $\lambda_m < \lambda_p < \lambda_{m+1}$. On the other hand, a relatively weaker and unstable field enhancement can be achieved by detuning the phase from a lower value ($\phi_A = 0$) to an operating value of $\phi_A^{op} \uparrow > \phi_A^{op} \downarrow$. From our experimental results shown in Fig.

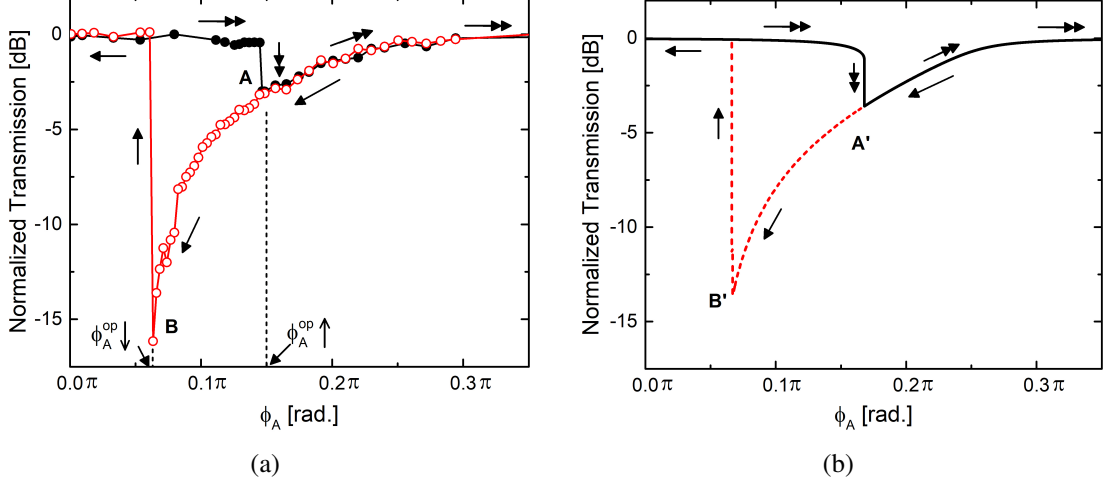


Figure 5.6: Transmission hysteresis (normalized) as a function of ϕ_A for $P_{in} = 8.4$ mW ($\lambda_p = 1550.951$ nm): (a) experimental and (b) simulation.

5.6(a), we observed the values of $\phi_A^{op} \downarrow$ and $\phi_A^{op} \uparrow$ are approximately 0.07π and 0.15π , respectively. We have also observed that the hysteresis curve widened as the value of P_{in} increases.

5.3 Stimulated Four-Wave Mixing Experiment

The hysteresis curves obtained in Section 5.2, it is obvious that the field enhancement inside the MRR at $\phi_A = \phi_A^{op} \downarrow$ is significantly higher than that at $\phi_A = \phi_A^{op} \uparrow$. This has been further re-confirmed by carrying out stimulated FWM experiment using an experimental set-up as shown schematically in Fig. 5.8. This set-up is almost same as Fig. 5.4, except the probe TLS replaced by a relatively high power signal laser operating at wavelength λ_s such that $\lambda_p - \lambda_s = FSR$ or $\phi_0(\lambda_s) - \phi_0(\lambda_p) = 2\pi$. Thus it is ensured that when detuning of ϕ_A helps m -th resonance to match λ_p , $(m - 1)$ -th resonance matches with λ_s (assuming dispersion is negligibly small for a wavelength range of one FSR). Stimulated FWM occurs in presence of a stronger pump and signal fields inside MRR cavity which results into the generation of idler field at λ_i satisfying energy and momentum conservation as discussed in the Chapter - 2.

In Figs. 5.8(a) and 5.8(b), the transmitted stimulated FWM spectra have been shown corresponding to $\phi_A^{op} \uparrow$ and $\phi_A^{op} \downarrow$, respectively, for an input pump power $P_{in}^p = 8.4$ mW

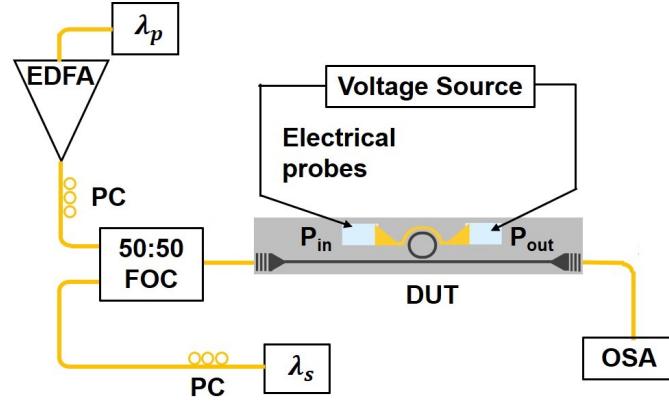


Figure 5.7: Scheme of the experimental set-up used for stimulated four wave mixing (FWM) measurements: DUT - Device Under Test, OSA - Optical Spectrum Analyzer, FOC - Fiber Optic Coupler, EDFA - Erbium Doped Fiber Amplifier, PC - Polarization Controller. λ_p is the laser wavelength for the pump and λ_s is the laser wavelength for the signal.

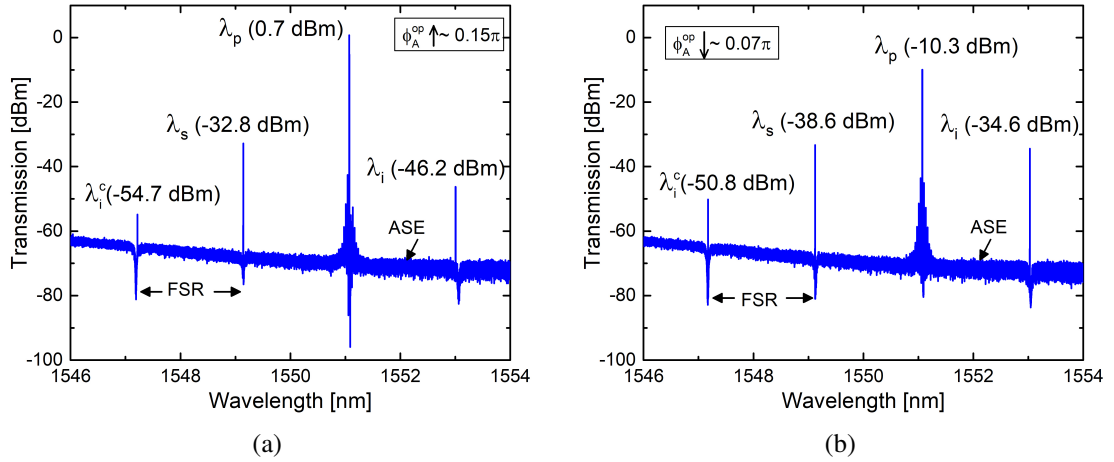


Figure 5.8: Output spectra of stimulated FWM in MRR as observed in the OSA for $P_{in}^p = 8.4$ mW and $P_{in}^s = 0.2$ mW: (a) $\phi_A \sim \phi_A^{op} \uparrow$ (Point 'A' of Fig. 5.6(a)), and (b) $\phi_A \sim \phi_A^{op} \downarrow$ (Point 'B' of Fig. 5.6(a)).

and relatively small input signal power $P_{in}^s = 0.2$ mW. In both cases, we observe the generations of idler (of wavelength λ_i) and conjugate idler (of wavelength λ_i^c) at $(m + 1)$ -th and $(m - 2)$ -th resonances, respectively. Because of the presence of amplified spontaneous emission (ASE) from the EDFA, we could observe the signature of corresponding resonances. It is evident that though λ_s , λ_p , and λ_i could be matched well to successive resonance orders $(m - 1, m$ and $m + 1)$, the conjugate signal at λ_i^c was slightly off-centered to the resonance order of $m - 2$. This may be attributed to the presence of group index dispersion in the waveguide.

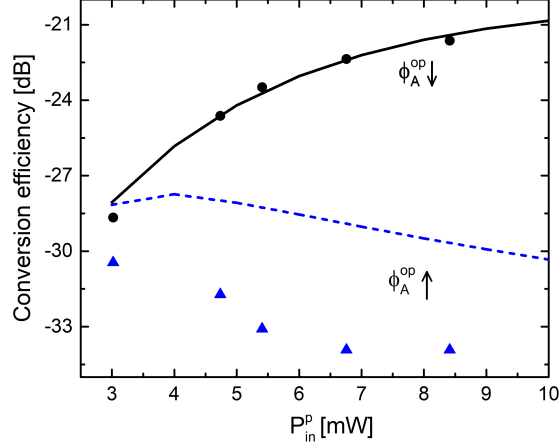


Figure 5.9: Simulated conversion efficiency as a function of P_{in}^p measured at $\phi_A \sim \phi_A^{op}$. Scattered symbols are experimental, solid and dashed lines are for simulated results.

Nevertheless, just keeping our focus on generated idler at λ_i we noticed a stronger and stable output power when operated near $\phi_A = \phi_A^{op} \downarrow$ than that operating near $\phi_A = \phi_A^{op} \uparrow$ as we expected. By noting down the experimental observations of output idler power P_{out}^i as a function of input pump power P_{in}^p operating at corresponding $\phi_A^{op} \downarrow$ and $\phi_A^{op} \uparrow$; we have calculated conversion efficiency $\eta = \frac{P_{out}^i}{P_{in}^p}$ for both cases and they are plotted in Fig. 5.9. These experimental results are also compared with theory by solving the analytical expression given by Turner et al. [89]:

$$\eta = \left[\frac{2\pi n_2}{\lambda A_{eff}} \cdot P_{in}^p \left(\frac{1 - e^{-\alpha_{rt}}}{\alpha_{rt}} \right) L \right]^2 F_{0,p}^4 F_{0,s}^2 F_{0,i}^2 \quad (5.3)$$

where field enhancement factors for pump ($F_{0,p}$), signal ($F_{0,s}$) and idler ($F_{0,i}$) are assumed same corresponding to input pump power P_{in}^p . While the experimental observations are found to be closely matching with the theory for $\phi_A^{op} \downarrow$, they are apparently far below the theoretical results when measured for $\phi_A^{op} \uparrow$. This is because of difficulty in parking pump and signal laser wavelengths exactly at their respective resonances for $\phi_A = \phi_A^{op} \uparrow$; all the experimental readings were taken by setting ϕ_A slightly higher than $\phi_A^{op} \uparrow$ just for trend indication.

5.4 Summary

In this chapter we have investigated the performance of a silicon microring resonator in terms of its bistability effect on four wave mixing process. Since the reason for bistability is identified as nonlinear phase change ϕ_{NL} , we have extracted the non-linear phase from the fabricated MRR by launching high optical input power. Phase dependent hysteresis has also been obtained experimentally and finally stimulated four wave mixing was carried out in the fabricated MRRs integrated with metal microheaters in the slab for its phase detuning. It has been further shown experimentally that the generated idler is relatively stable and stronger while the phase is detuned from a higher value to the resonance condition for any given input pump/signal power levels. For an input pump power of 8.4 mW and input signal power of 0.2 mW, the generated idler is found to be 11.6 dB stronger in case of reverse phase detuning than that of forward phase detuning. We believe this is an important investigation/finding for microring resonator based nonlinear silicon photonics devices, especially for actively controlled photon sources potentially be used in large-scale integrated quantum photonic circuits. In the following chapter we will discuss the effect of high optical power on switching response of the MRRs.

CHAPTER 6

Transient Analysis

In the previous chapter, we demonstrated stimulated four wave mixing by controlling the optical bistability using a microheater integrated with the MRR. In this chapter, the thermo-optic transient response has been studied while operating the MRR in the linear region as well as non-linear regime. The thermo-optic rise/fall time as well as the optical rise/fall time has been studied for complete ON-OFF switching. Simulation results has been shown in details followed by experimental results. Finally, towards the end of the chapter, we have investigated on the electrical control of optical bistability for non-linear photonics switching/memory applications in silicon MRR design suitably integrated with a CMOS compatible resistive microheater (the MRR integrated with metal microheater). A small electrical pulse for a microsecond duration across the microheater has been used to trigger bistable switching for a continuous-wave laser launched at the input while operating around one of the resonances. It has been supported further by the demonstration of voltage controlled thermo-optic hysteresis curves in the transmission characteristics of MRRs operating above a launched threshold power (nonlinear regime).

6.1 Theory and Simulation

In Chapter-6, we showed how the optical bistability in a MRR resonator could be electrically controlled for achieving an efficient gain in four-wave mixing process. Non-linear self-phase modulation (SPM) and two-photon absorption (TPA) were considered for theoretical model and experimental validation. They are considered here again to investigate optical power dependent thermo-optic transient response for switching applications. As discussed in chapter-2 the nonlinear refractive index change experienced by a guided mode can be decomposed into three distinct processes:

$$\Delta n_{NL} = \Delta n_{SPM} + \Delta n_{FCD} + \Delta n_{TPM} \quad (6.1)$$

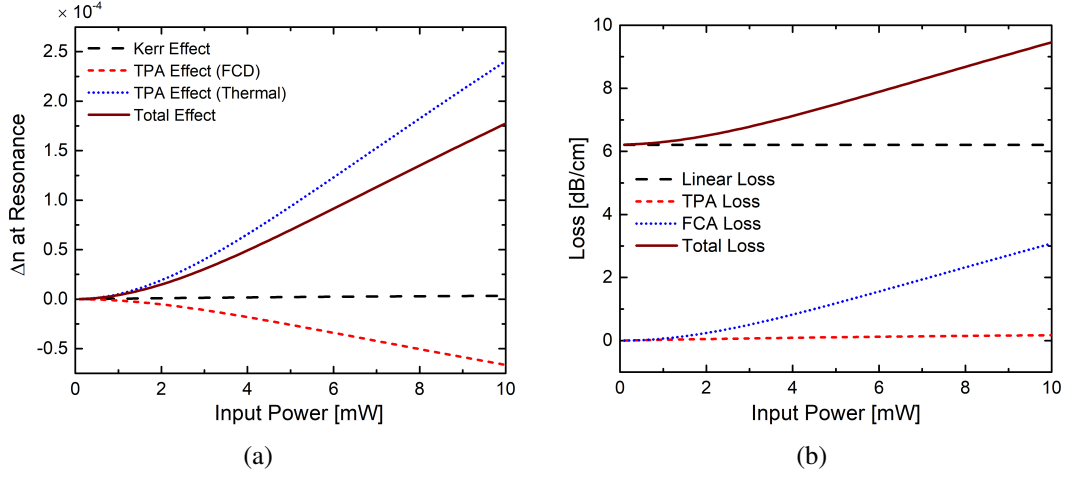


Figure 6.1: (a) Change in refractive index, (b) change in loss obtained due to the contribution of Kerr effect, FCD due to TPA, TPM due to TPA and the effective contribution of all the mechanisms for different input optical power (P_{in}) when the laser is pointed at the resonance wavelength for each P_{in} .

The contribution of the process can be explained by Figures 6.1(a) and 6.1(b). These contributions are crucial to quantify its effect on switching response of the MRRs when operating at higher power levels. Resonance wavelength shift with the increase in input optical power has been considered in our calculations. For each value of P_{in} the corresponding values of Δn is calculated at resonance (λ_r). Due to the presence of loss in the waveguide, the nonlinear effect is not uniform across the perimeter of the MRR. Therefore, the average value of the n_{eff} change is obtained using the following equation:

$$\Delta n_{avg} = \frac{\lambda}{2\pi L_T} \Delta \phi_{rt} \quad (6.2)$$

where, L_T is the perimeter of the MRR of 50 μm radius having a directional coupler length of 5 μm ($L_T = 324 \mu m$), as designed in Chapter-2. The propagation loss considered is 6.12 dB/cm as measured in Chapter-4. From the plots, it is observed that the increase in Kerr nonlinearity (n_2) with P_{in} is negligibly small. The free carriers generated due to TPA reduce the refractive index while the thermal contribution due to TPA causes an increase in the refractive index change [113]. Hence the overall refractive index change is positive as shown by the solid line in Fig.6.1(a). Similarly the loss contributions have been plotted at resonance with the increase in the input power in Fig. 6.1(b). The contribution from the TPA loss is insignificant. The FCA loss increases with the power which impacts the total loss. All these calculations are done when the

resonance is tuned from a lower wavelength.

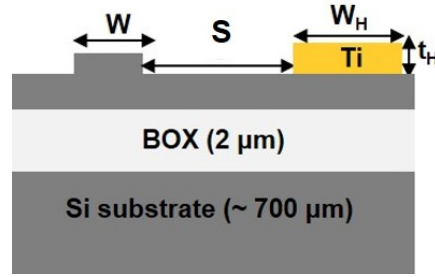


Figure 6.2: Device cross-section of a waveguide-slab-integrated Ti-strip microheater used for simulation. W - rib waveguide width, S - gap between rib waveguide and the Ti microheater, W_H - width of the microheater, t_H - thickness of the microheater, BOX - buried oxide.

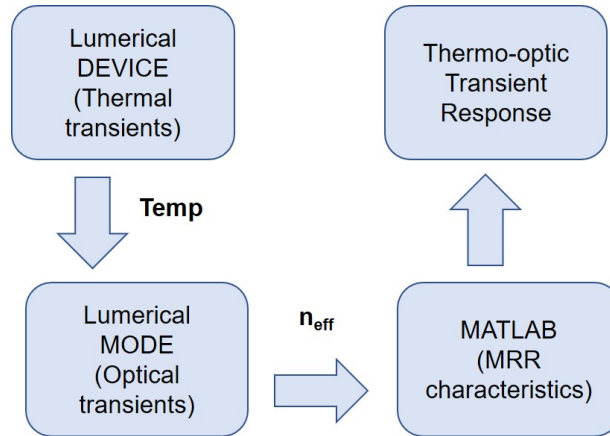


Figure 6.3: Flowchart showing the steps used to obtain thermo-optic transient response.

To study the transient response we have considered the 2D device cross-section of the rib waveguide integrated with Titanium metal microheater as shown in Fig. 6.2 (similar to the fabricated device D_2). Lumerical DEVICE and MODE solutions have been used for the thermal and thermo-optic simulations respectively. The steps used for simulating the thermo-optic transients is shown using the flowchart in Fig. 6.3. A 2D device structure (cross-section of the rib waveguide-microheater geometry) was constructed in Lumerical DEVICE to obtain the temperature response time. A temperature pulse was applied to the microheater and the time needed for the temperature to stabilise in the rib waveguide was recorded. The standard values of material constants for thermal conductivity, specific heat capacity, density etc were used [95]. The temperature transient profile was imported to Lumerical MODE solutions and the change in effective index of the optical mode due to the temperature was extracted. The effective index change was fed to the MRR transfer function and the normalized MRR

output was calculated using MATLAB and finally the thermo-optic transient response was obtained.

We first studied the transient response of the MRR for complete ON-OFF switching in the absence of non-linear effects. To understand the microheater behaviour, instead of using a voltage source to bias it, we have directly applied temperature pulses of different amplitude in the microheater. This assumption has been made considering the fact that the microheater reaches the steady state instantaneously when voltage is applied [140]. Hence the time needed for the temperature to stabilise in the rib waveguide was recorded for the temperature pulse applied to the microheater. Fig. 6.4 shows the temperature rise and fall in the rib waveguide core due to the temperature pulse applied in the microheater (305K, 310K and 320K). The stabilized temperature obtained in the rib waveguide is 301.9K, 303.8K and 307.2K respectively for the above mentioned three temperature values. The thermal rise time and fall time obtained is nearly same from this simulation which is $\sim 2.3 \mu\text{s}$. The time period used for simulation is $40 \mu\text{s}$ to reduce the computation time. The rise time and fall time obtained from Lumerical DEVICE simulation is lower than the values obtained from COMSOL Multiphysics even after having same geometry and similar boundary conditions. This can be probably due to the different numerical methods and different meshing structures used in both the simulators. The experimental values reported in Chapter-4 matches well with the simulated values from COMSOL. Even though the values from Lumerical DEVICE is much lower than the actual values, we continued with this values, since the final objective here is to extract the change in the n_{eff} of the optical mode and observe the transient time when the MRR is subjected to high input optical power.

The temperature transient profile was imported to Lumerical MODE solutions as discussed in the algorithm and the change in effective index of the optical mode due to the temperature was extracted. The effective index change was fed to the MRR transfer function and the normalized MRR output for the three different temperature pulse is plotted in Fig. 6.5 for launched input power of 0.15 mW. The right y-axis shows the values of the effective index (n_{eff}) obtained from Lumerical MODE solution corresponding to the temperature transients. It is observed that as the temperature increases, the rise time reduces and the fall time increases. This is due to the fact that higher

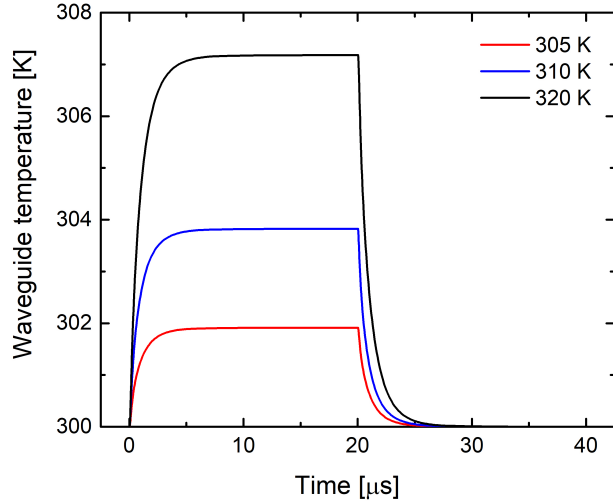


Figure 6.4: Thermal transient response obtained from the 2D simulation of the rib waveguide-microheater structure cross-section for three different temperature pulse (305K, 310K, 320K) applied to the microheater.

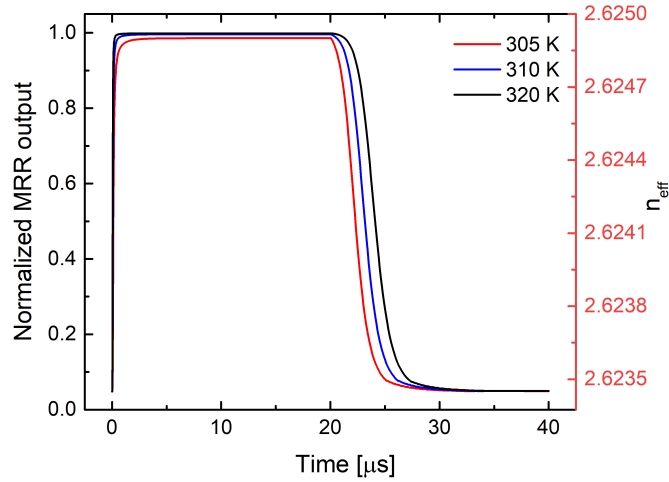


Figure 6.5: Thermo-optic transient response of the MRR integrated metal microheater for three different temperature pulses (305K, 310K, 320K). The corresponding effective index is shown in the right y-axis.

temperature makes the resonator go out of resonance fast. This is similar to using an overdrive voltage to reduce the rise time [79, 141]. Similarly, due to the heat generated it takes more time to cool down, thus increasing the fall time. This behavioural trend is observed irrespective of the input launched power. Fig. 6.6 shows the simulations that were performed with increased optical powers of 2 mW, 4 mW and 8 mW. The figures show that $\Delta T \geq 5K$ is required to be applied to the microheater for complete ON-OFF switching from the resonance wavelength.

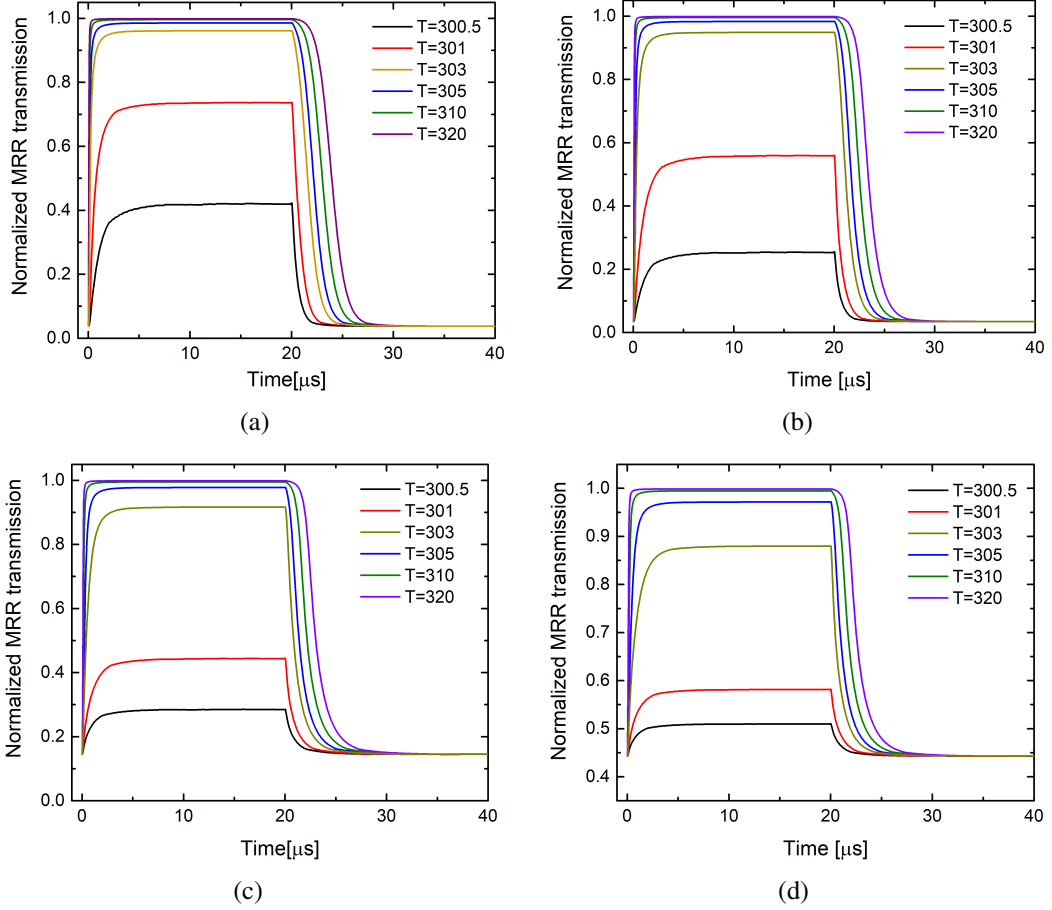


Figure 6.6: Simulated normalized thermo-optic transient response of the MRR for different temperature pulses applied in the microheater for (a) $P_{in} = 0.15$ mW, (b) $P_{in} = 2$ mW, (c) $P_{in} = 4$ mW, (d) $P_{in} = 8$ mW.

6.1.1 High Power Switching: Simulation

Further, simulations were performed by increasing the input power launched into the MRR. The microheater was kept at 320K to enable temperature modulation to be applied in both the directions. When the laser is kept at resonance, a modulation temperature of 5K in both positive and negative direction is chosen to ensure the laser is completely out of resonance in the respective direction. Fig. 6.7(a) and 6.7(b) shows the normalized MRR output for positive (320K - 325K) and negative (320K - 315K) temperature modulation when different levels of input power are launched into the MRR. For each cases the laser was aligned with the resonance by tuning the wavelength from higher values. The rise time and fall time for both the temperature modulation is shown in Fig. 6.8. In the positive temperature swing, the rise time and fall time remains almost constant for all the power levels, though the fall time was higher than the individual rise

time. But in the negative temperature swing the fall time increases significantly with the input power. This is due to the fact that in the rising path and the falling path the laser observes two different behaviours of the cavity because of bistability.

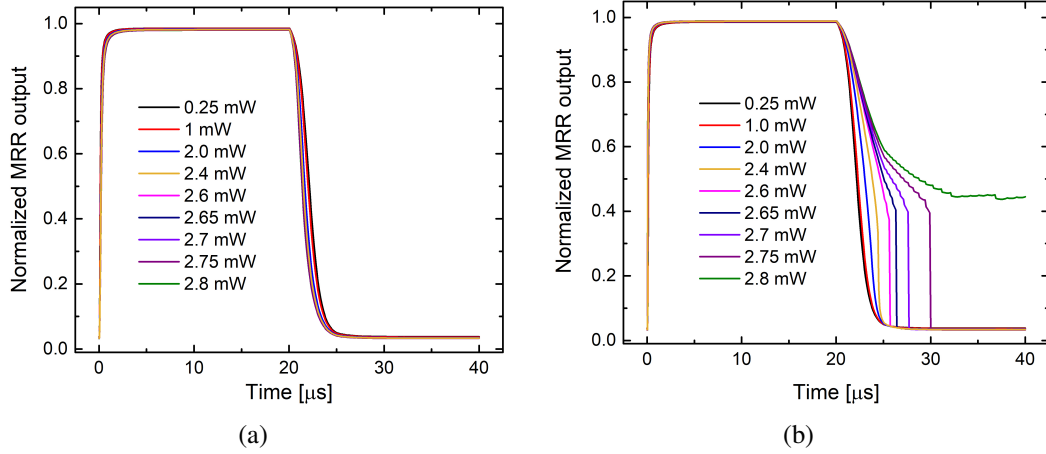


Figure 6.7: Simulated thermo-optic transient response for different input laser powers ($P_{in} = 0.25$ mW to 2.8 mW) at $V_B = 15$ V, when the operating laser wavelength is exactly aligned to one of the MRR resonances: (a) $\Delta T = 5$ K; and (b) $\Delta T = -5$ K.

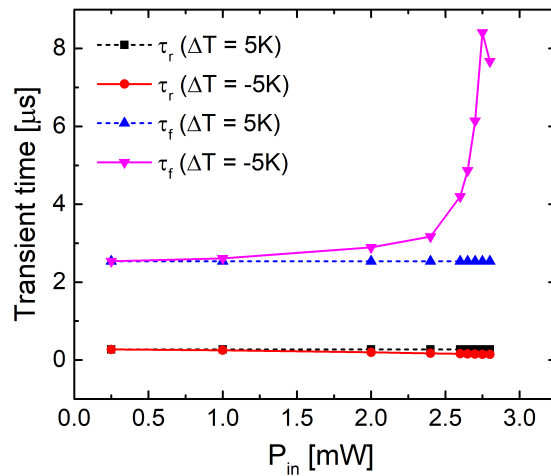


Figure 6.8: Simulated thermo-optic rise time and fall time w.r.t P_{in} for applied positive and negative temperature swings ($\Delta T = \pm 5$ K).

To understand this behaviour better, we have simulated the transmission spectrum for different values of input power. Fig. 6.9(a) shows the normalized transmission spectrum when the input power is in the linear regime ($P_{in} = 0.15$ mW) and Fig. 6.9(b) is the normalized transmission spectrum for high input power where non-linearity is present ($P_{in} = 6$ mW). A clear opened hysteresis is observed in high power / non-linear regime. Taking into account the wavelength dependent hysteresis for $P_{in} = 6$ mW, we

plotted the voltage dependent hysteresis at the same optical power as shown in Fig. 6.10. We have used this behaviour to further explain the electrically controlled optical memory application.

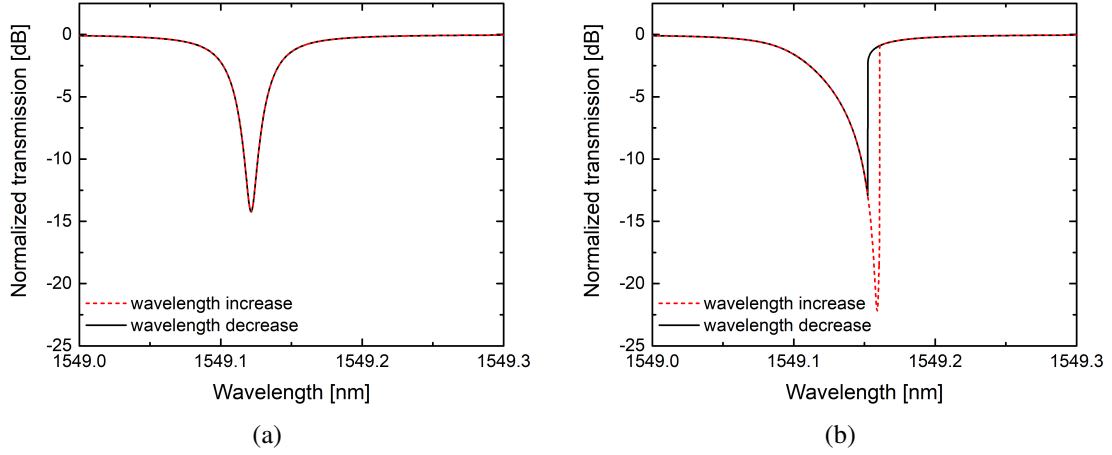


Figure 6.9: Normalized transmission spectrum of the MRR when the wavelength is tuned from 1549 nm to 1549.3 nm and vice versa for (a) $P_{in} = 0.15$ mW, (b) $P_{in} = 6$ mW.

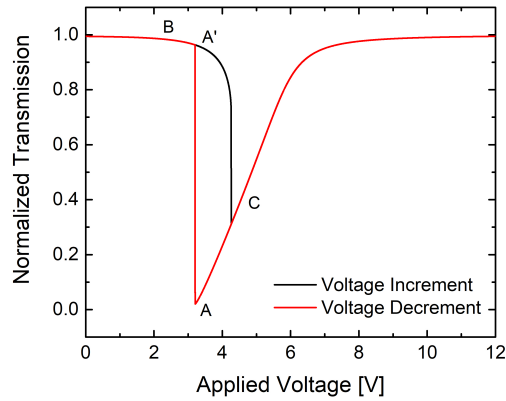


Figure 6.10: Simulation of thermo-optic hysteresis as a function of bias voltage V_B for $P_{in} = 6$ mW.

Based on the thermo-optic response time and the optical hysteresis obtained, we propose optical memory which can be electrically controlled. In Fig. 6.10, the points A, B, C, A' are used to explain the optical memory action for $P_{in} = 6$ mW. According to the hysteresis curve, if a dc bias of $V_B = 3.5$ V is applied, then the laser transmission settles at A which is very close but little above the minimum value. With a settled laser transmission A, if a microsecond voltage pulse of $\Delta V_p = -1.25$ V is triggered across the microheater, one can obtain higher transmission A' via B. Subsequently by applying another voltage pulse of $\Delta V_p = +1.25$ V, the transmission is settled back to lower level

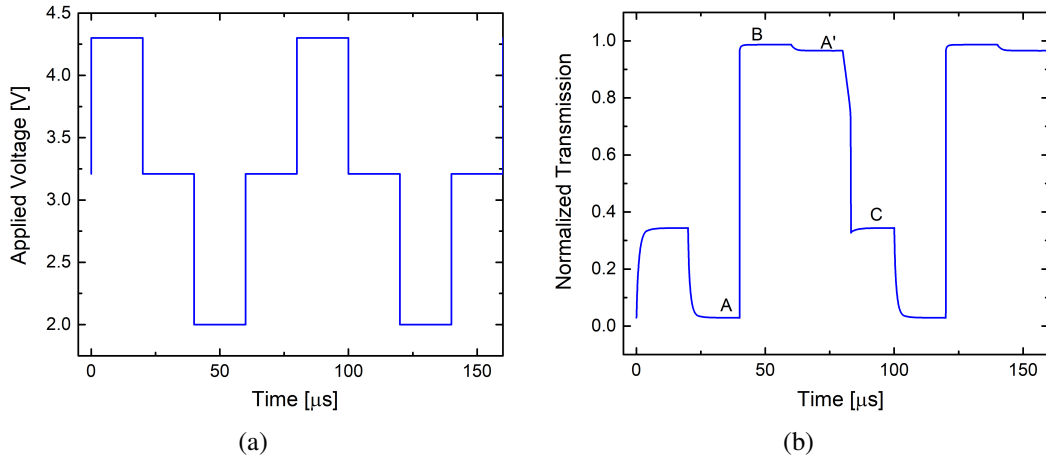


Figure 6.11: (a) Applied input switching voltage, (b) optical bistable switching representation by thermo-optic transients derived from Fig. 6.10.

A via A'CA path. Thus electrical voltage pulse driven thermo-optic bistable switching cycle can be achieved by ABA'CA path as shown schematically in Fig. 6.11(b). Hence the state BA' is acting as the optical memory whose state can be changed by the application of voltage to the microheater. It must be noted that by setting a λ_L value closer to resonance dip at a given value of P_{in} , one can reduce the required dc bias. Lowering the required dc bias V_B is crucial as it causes continuous dissipation of electrical power for bistable memory application. Since the least required negative voltage pulse ΔV_p for switching from A to A' (via B) can be as small as < 0.5 V, one can easily reduce the constant dc bias to an acceptable +0.5V. Thus the constant dc power dissipation can be as little as $\sim 36 \mu\text{W}$ ($P_H^{dc} = V_B^2/R_H$) estimated from our device characteristics.

6.2 Experimental Results

The transient measurements were performed on the device D_2 (MRR integrated with the metal microheater encompassing half of the perimeter of the ring) using the grating coupler set-up. Additionally, a function generator (FG) was connected in series with the source measure unit (SMU) to supply the modulation voltage along with the DC bias. For the high power measurements input laser source was connected to an erbium doped fiber amplifier (EDFA) as discussed in Chapter-5. The schematic of the experimental setup for transient measurements is shown in Fig. 6.12. The output was observed in the

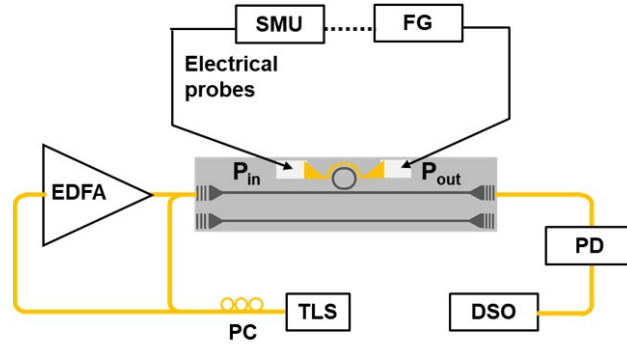


Figure 6.12: Scheme of the experimental set-up used for device characterizations: TLS -Tunable Laser Source, EDFA - Erbium-Doped Fiber Amplifier, PC - Polarization Controller, SMU - Source Measurement Unit, FG - Function Generator, PD - Photodiode, DSO - Digital storage oscilloscope. P_{in} is the launched laser power into the MRR and P_{out} is the output from the MRR.

digital storage oscilloscope (DSO) through a photodiode (PD).

6.2.1 Thermo-optic Transient Measurements

Thermo-optic switching was studied for different modulation voltages. Fig. 6.13(a) is the thermo-optic ON-OFF switching responses corresponding to ΔV varying from 0.3V to 4.0V for an input power (P_{in}) of 0.15 mW launched into the MRR with the operating resonant wavelength $\lambda_r = 1551.5$ nm. The rise time (τ_r) and fall time (τ_f) were nearly same for $\Delta V < 0.8$ V, but τ_r reduced with the increase in ΔV and the value of τ_f increased as clearly shown in Fig. 6.13(b). This is because the incident laser wavelength did not go off-tuned from the resonance bandwidth for $\Delta V < 0.8$ V, whereas as the ΔV kept on increasing the incident laser wavelength was completely off-tuned. For $\Delta V = 4$ V, τ_r was ~ 250 ns and τ_f was ~ 18 μ s. The obtained trend is similar to the simulation results. For a higher value of input power (P_{in}) of 1.45 mW, similar experimental results were obtained as the τ_r became ~ 200 ns and the τ_f reached 27 μ s on the application of $\Delta V = 6$ V as shown in Fig. 6.13(c) and 6.13(d). This proves that for any given power when the modulation voltage is increased beyond a certain value (i.e. complete ON-OFF from the resonance bandwidth for the laser wavelength) the rise time reduces and fall time increases. As explained before we contribute this to the similar behaviour of using an overdrive voltage/pulse to reduce the rise time. Since the

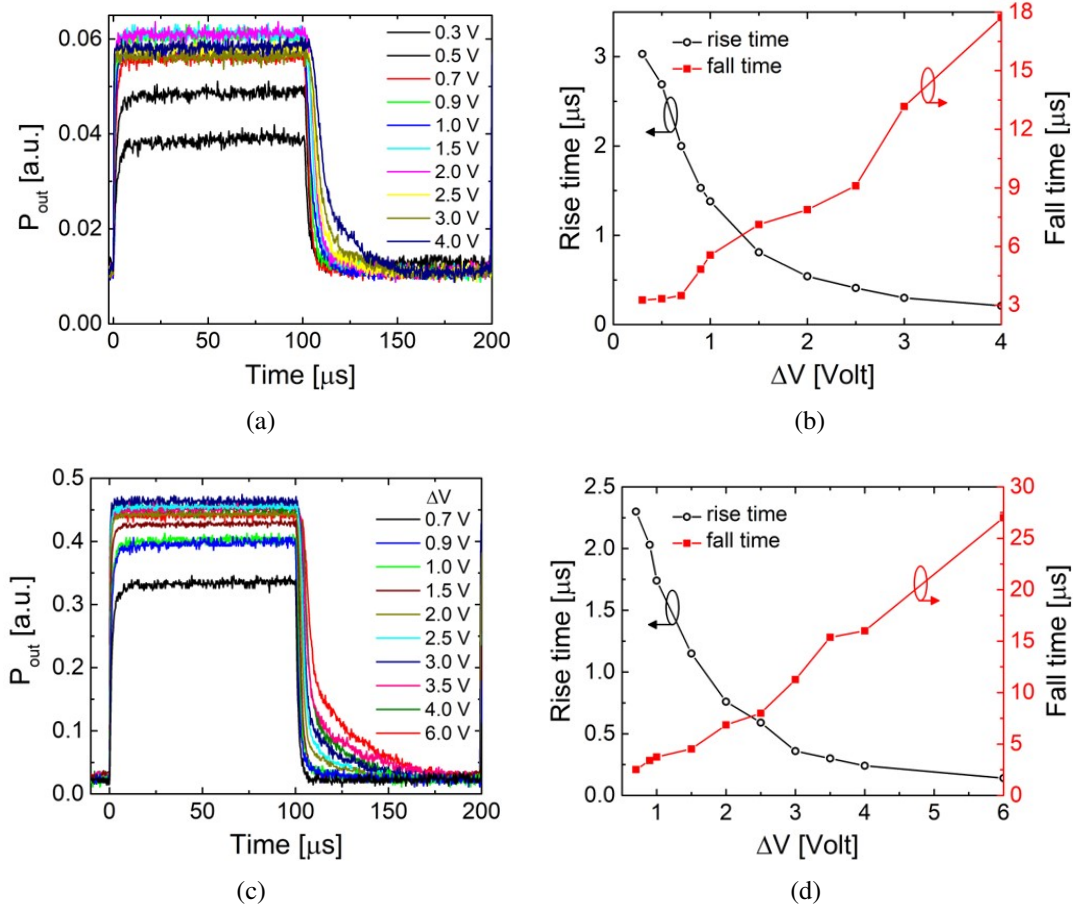


Figure 6.13: Normalized thermo-optic transient response for different switching voltage (ΔV) for (a) $P_{in} = 0.15$ mW, (c) $P_{in} = 1.45$ mW, rise time and fall time for each of the switching voltages for (b) $P_{in} = 0.15$ mW, (d) $P_{in} = 1.45$ mW.

modulation voltage is not removed in our case, it translates to heating up of the MRR and producing a high fall time.

6.2.2 High Power Switching

The above measurements were performed with a positive modulation voltage (ΔV). The asymmetric thermo-optic transient response was obtained for higher ΔV where the laser wavelength went completely out of the resonance bandwidth. Further, we performed experiments with negative modulation voltage for different levels of input optical power. $\Delta V = \pm 2V$ was chosen for this experiment, keeping the bias at 15V. This is chosen because $\frac{d\lambda_r}{dV_B}$ is found to be a nearly constant value of ~ 95 pm/V around the bias voltage $V_B = 15V (\pm 2V)$ (See Fig. 4.43(a) of Chapter-3). Though the values

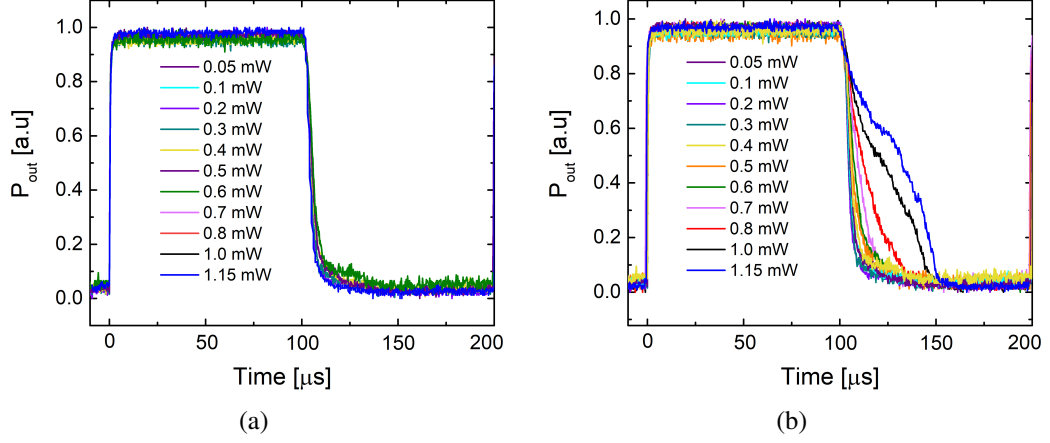


Figure 6.14: Thermo-optic transient response for different input laser powers ($P_{in} = 0.05$ mW to 1.15 mW) at $V_B = 15V$, when the operating laser wavelength exactly aligned to one of the MRR resonances: (a) $\Delta V = 2V$ (5 kHz); and (b) $\Delta V = -2V$ (5 kHz).

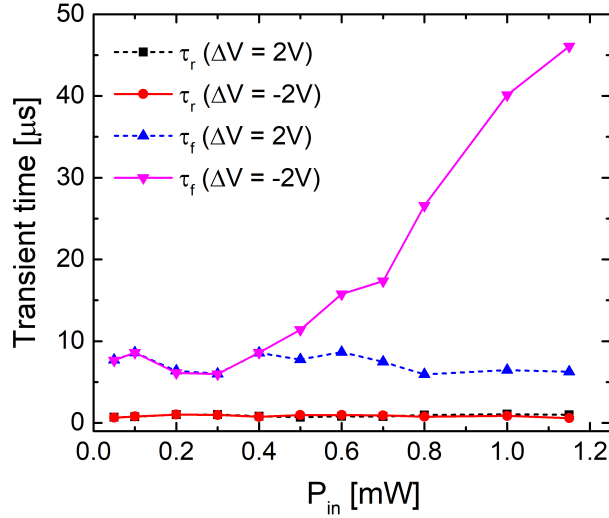


Figure 6.15: Thermo-optic rise time and fall time obtained w.r.t the input optical power (P_{in}) launched inside the MRR for two different values of voltage modulation ($\Delta V = \pm 2V$).

of τ_f do not change significantly as P_{in} increases for $\Delta V = +2V$, we observed a stark increase in case of $\Delta V = -2V$ as shown in Fig. 6.14. The measurements show a $\tau_r \sim 600$ ns and $\tau_f \sim 7 \mu$ s for $\Delta V = 2V$; while for $\Delta V = -2V$, τ_r remains at ~ 600 ns while τ_f becomes $\sim 45 \mu$ s when the launched power is 1.15 mW. The consolidated values of the rise time (τ_r) and fall time (τ_f) for different input power levels is plotted in Fig. 6.15, when the applied bias voltage was 15V and the modulation voltage was $\pm 2V$. We contribute this to the nonlinear refractive index modulation ($\Delta n \propto$ optical intensity), which is well-known for silicon waveguides as explained in the previous

sections. Thus we now firmly attribute this behaviour as a consequence of thermo-optic hysteresis/bistability in microring resonator induced by nonlinear effect at higher field intensities inside the cavity. Though these values of rise time and fall time are different from the simulated values shown in Fig. 6.11, still the trend of the experimental results match well with the trend obtained in simulation.

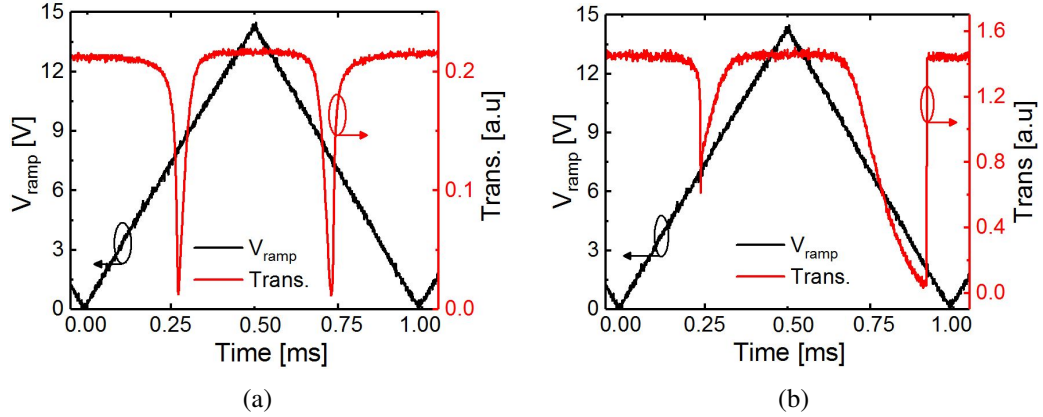


Figure 6.16: MRR transmission (right y-axis) obtained by applying a ramp signal (left y-axis) of 14V to the microheater within 1 ms for (a) $P_{in} = 0.4$ mW, (b) $P_{in} = 4.5$ mW by placing the laser ~ 215 nm right of the resonance wavelength around $\lambda = 1550$ nm.

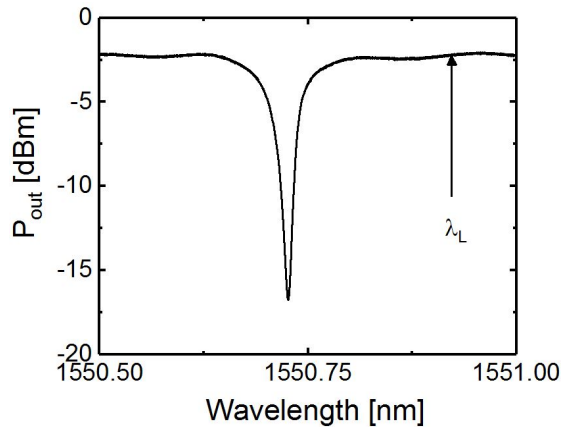


Figure 6.17: Wavelength dependent transmission characteristics for $P_{in} = 0.4$ mW along with the position of the laser (λ_L).

As explained in the previous section, the observed asymmetric transient response at higher input laser powers (P_{in}) motivated us to investigate further for the memory effect (hysteresis) in thermo-optic detuning of resonance wavelength at higher launched power levels (nonlinear regime). To study thermo-optic hysteresis, we used a voltage ramp-up from 0 to 14V (ΔT from 0 to 20K) and subsequent ramp-down over a duration of 1 ms.

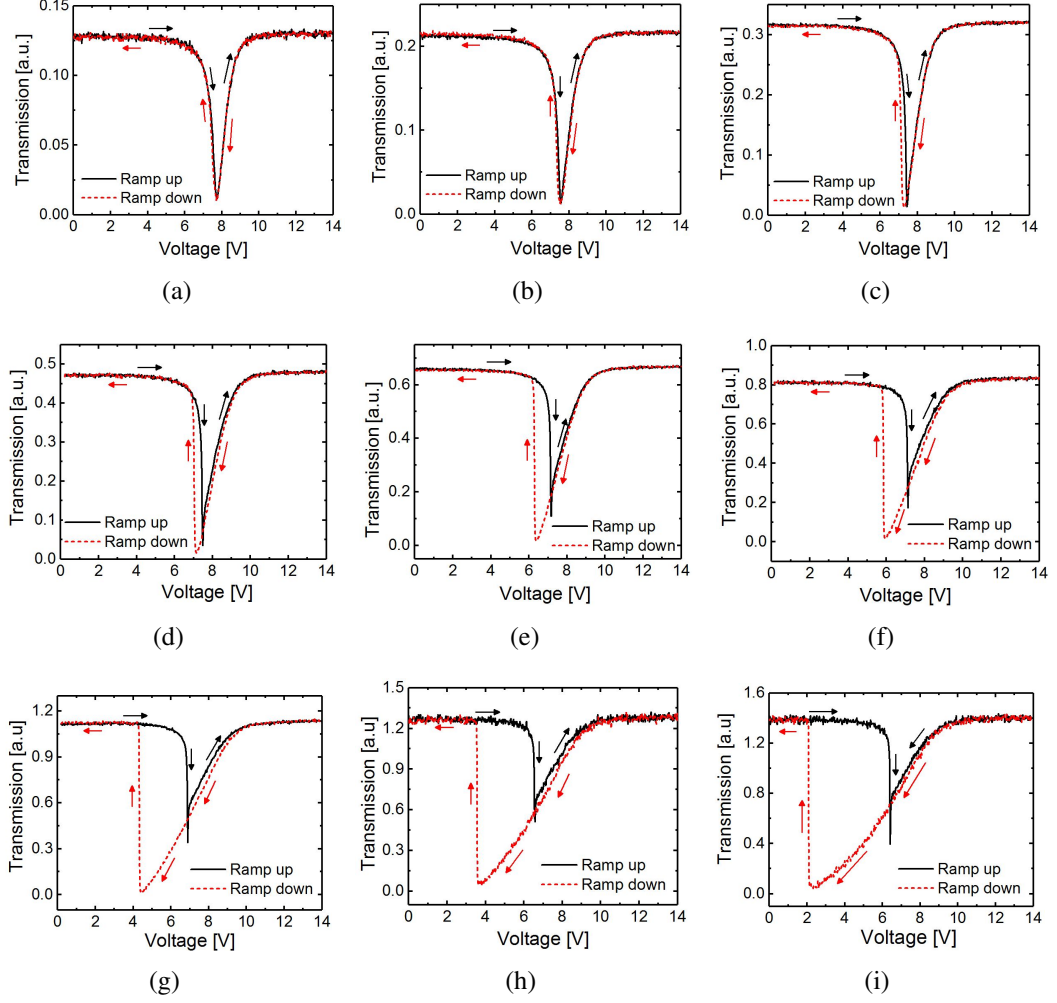


Figure 6.18: Thermo-optic hysteresis as a function of bias voltage V_B for P_{in} (a) 0.4 mW, (b) 0.6 mW, (c) 1.0 mW, (d) 1.5 mW, (e) 2.1 mW, (f) 2.6 mW, (g) 3.5 mW, (h) 4.0 mW, (i) 4.5 mW . In the hysteresis curves, the black solid lines are obtained by voltage ramping up and red dashed lines by voltage ramping down over a duration of 1 ms.

Fig. 6.16 shows the input ramp signal (black curve) along with the MRR transmission obtained (red curve) for two levels of input power ($P_{in} = 0.4$ mW and 4.5 mW). The ramp signal was sourced from the function generator (FG) connected in series with the source measure unit (SMU). During this experiment, the laser wavelength λ_L was carefully positioned sufficiently right to a resonant wavelength λ_r ($\lambda_L - \lambda_r \sim 215$ pm), keeping in mind that the resonance gets red-shifted at higher launched power levels. Fig. 6.17 shows the transmission characteristics for input power (P_{in}) of 0.4 mW along with relative position of λ_L .

The thermo-optic hysteresis curves obtained in Fig. 6.18 are actually extracted from

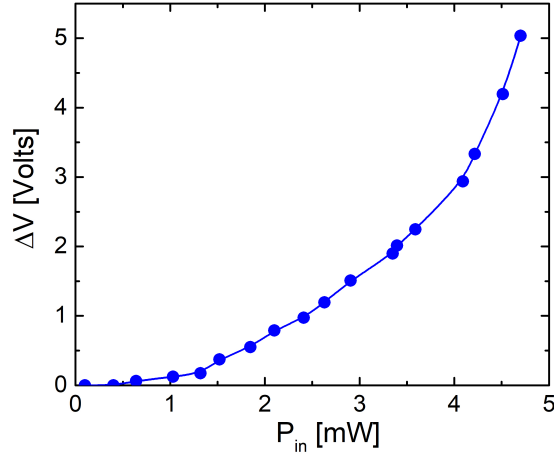


Figure 6.19: Voltage hysteresis width (ΔV) obtained experimentally with respect to the input optical power (P_{in}) launched inside the MRR.

Fig. 6.16. The hysteresis curves are plotted as a function of the bias voltage between the microheater contact pads. We observed clearly opened hysteresis curves for $P_{in} \geq 0.6$ mW. Wider hysteresis curves are observed as the input power increases. Fig. 6.19 shows the parabolic increase in the hysteresis width with the input optical power.

6.3 Summary

In this chapter we have presented the transient analysis of the silicon MRR integrated titanium metal microheater. We have studied the transient response for complete ON-OFF switching as well as switching within the resonance bandwidth of the MRR. Further, the transient response in the presence of bistability is studied. All the simulation results have been supported with experimental results. Temperature pulse in the simulation has been considered equivalent to the modulation voltage used in the experiments. Finally we have proposed optical memory using the bistable switching via thermo-optic detuning when operating at a fixed input laser power level in its nonlinear regime ($P_{in} \geq 0.6$ mW). Typical bistable switching time of the proposed device depends on the power launched into the device.

For the silicon MRR device integrated with a metal microheater we demonstrated that the rise time reduces to ~ 250 ns but the fall time increases to ~ 20 μ s when operated for complete ON-OFF switching. We have attributed this phenomenon similar

to the use of overdrive voltage/pulse to obtain faster rise time. As the modulation voltage is not removed, it is reflected as a high fall time. Further for thermo-optic bistable switching, we have observed similar values of rise and fall time ($\tau_r \sim 600$ ns, $\tau_f \sim 7$ μ s) for all levels of optical power when the applied modulation voltage (temperature) is positive. On the other hand, when the applied modulation voltage (temperature) is negative we observe a significant increase in the fall time ($\tau_f \sim 45$ μ s for 1.15 mW optical power) with the level of launched power. This has been attributed to the optical bistability that is prominent at high input power. To completely explain this asymmetric transient behaviour we have demonstrated the thermo-optic hysteresis by using a ramp signal of 1 kHz frequency, thus reaffirming the electrically controlled optical bistability in silicon MRR.

CHAPTER 7

Conclusion

The major contribution of this thesis is proposing a method to electrically control the bistability in silicon microring resonators for non-linear photonics applications. The detailed design and demonstration of the same has been reported in the preceding six chapters. This chapter summarizes the complete work and provides an outlook for future work.

7.1 Thesis Summary

In summary, we have proposed a method to electrically control the optical bistability in silicon microring resonators. We have demonstrated two different applications such as improved four wave mixing and optical memory using the same. In the introduction chapter, we have given the motivation for the requirement to control the optical bistability electrically. Hence we have shown a detailed literature review of the different applications of silicon MRRs, followed by the methods to electrically reconfigure them (electro-optic and thermo-optic). The non-linear applications were discussed and the areas of improvement were projected which led us to define our research objective. Finally, the overview of each of the chapters were discussed.

The second chapter discusses the theory and design of single mode rib waveguide followed by silicon MRRs. It further discusses the origin of non-linearity in silicon and the different non-linear mechanisms. The origin of optical bistability in silicon MRRs is studied which takes into consideration the effects of Kerr nonlinearity, two-photon absorption and the TPA induced free carriers absorption and dispersion as well as the thermal phase modulation. Simulation studies were presented to establish a model to electrically control the optical bistability by using an integrated phase shifter.

The third chapter of the thesis deals with the design and simulation of the phase shifters. A fabrication technique of using diffusion doping to integrate p-n/p-i-n diodes

with silicon rib waveguides has been proposed. Simulation studies starting from the complete process flow along with the simulations of electrical and optical characteristics of the p-n/p-i-n diodes integrated rib waveguides have been presented. Next, the thermo-optic phase shifter design has been discussed. The method to incorporate a single type of dopant using diffusion to obtain a microheater is presented. Process flow simulation to estimate the doping concentration to the thermal simulation to estimate the temperature profile is presented for p-doped microheaters. Towards the end of the chapter, the metal microheaters have been discussed. The process flow and thermal simulation results of the same have been presented.

The fourth chapter of the thesis has been used to present the complete fabrications done for this work. It starts with the fabrication of p-i-n diodes on $2\ \mu\text{m}$ SOI. Variable optical attenuator and TOA based photodiode characteristics have been studied and presented. The experimental results of the attempt made to obtain p-i-n/p-n diodes for scalable silicon photonics devices have been presented. Diode I-V characteristics were obtained till $750\ \text{nm}$ device layer thickness while reducing it from $1.5\ \mu\text{m}$ after the diffusion processes. Possible reasons of failure beyond $750\ \text{nm}$ device layer thickness have also been discussed. The next part of the chapter deals with the fabrication and characterization of the thermo-optic phase shifters integrated with MRRs. Fabrication results and basic characterization results of both p-doped microheater integrated MRRs and Titanium metal microheater integrated MRRs have been presented. The MRRs exhibited a Q-value in the range of 45000. It has been observed that the doped microheaters exhibit more effective wavelength tunability than their metal counterparts. However, the transient response of both the kind of microheaters are nearly same ($\sim 3.5\ \mu\text{s}$) when operated in the linear region of the MRR resonance. A comparison of both the types of microheaters have also been included towards the end of the chapter.

The fifth chapter of the thesis deals with the demonstration of bistability in silicon MRRs when subjected to high input power. Using the Titanium microheater integrated MRRs demonstrated in Chapter-4, experimental demonstration of the phase controlled bistability was performed. As an application, four wave mixing was demonstrated and it was shown that higher power of idler was obtained when the pump wavelength was aligned with the MRR resonance by reducing the phase instead of increasing the phase

and aligning. A conversion efficiency of ~ 11.6 dB was obtained for a pump power of ~ 8.4 mW which matches very well with the simulation as well as the proposed model.

In the sixth chapter we have presented the transient analysis of the silicon MRR for different modulation voltages to the microheater as well as for different input optical power. We have presented a simulation study considering the non-linear effects (TPA, Kerr, TPM) in silicon. It was observed that the thermo-optic rise time reduces to sub- μ s and fall time increases to 10's of μ s when the ON-OFF switching is beyond the resonance bandwidth of MRR while operating in linear regime. For the non-linear regime, it has been observed that there is asymmetric behaviour in the response time when a negative modulation voltage is applied. This has been explained with the hysteresis curve obtained at high optical power levels. Using this we have also proposed optical memory application which can be controlled electrically by the external phase shifter.

7.2 Future scopes

The electrical control of optical bistability in silicon MRRs has paved a way to generate efficient photon pair sources by integrating microheaters with MRRs and controlling the temperature of the device locally instead of completely heating or cooling the sample. This will be of much advantage in complex quantum photonics circuits where the temperature of the photon source (MRR) can be controlled individually without affecting the operation of the other devices in the circuit.

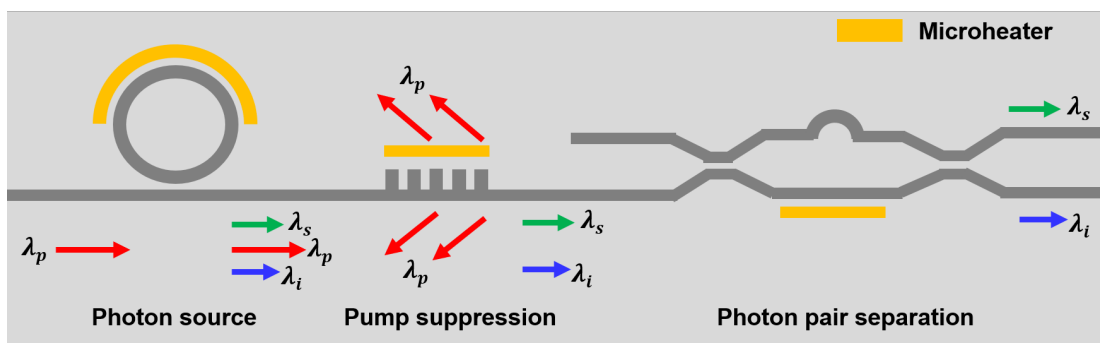


Figure 7.1: Schematic of a quantum photonic circuit used to separate the generated photon pairs.

Fig. 7.1 shows a integrated quantum circuit in silicon photonics platform where

a microring resonator integrated with a microheater can be used as a quantum photon source. A high pump laser (λ_p) is used to generate idler (λ_i) and signal (λ_s) photons as shown with the blue and green arrows in the figure. A high extinction filter is used to suppress the pump wavelength and the signal and idler is fed to an unbalanced Mach Zehnder Interferometer circuit to separate them. Using the proposed technique of electrically controlling the bistability of the MRR, the generation of the signal and idler photons can be enhanced.

The other part of the thesis aims in obtaining the response time of the microheater-rib waveguide system. The transient measurements mentioned in Chapter-6 will help to decide non-linear switching time. It can be used as optical memory which is already discussed. Instead of using two lasers as required in all-optical switching or all optical memory, this technique will help to obtain the similar function with thermo-optic tuning.

Considering all the work reported in this thesis, there is further scope of improving the MRR design to make it less dispersive, more compact and optimizing the doped microheater to increase the conversion efficiency as well as reducing the power requirement for the phase shifter.

APPENDIX A

Additional Information on Fabrication

A.1 SOI wafer specifications

Table A.1: Specifications of SOI wafers used

Device layer thickness	BOX thickness	Handle layer thickness	Dopant
2 μm	1 μm	500 μm	p-type
1.5 μm	3 μm	500 μm	p-type
250 nm	3 μm	500 μm	p-type
220 nm	2 μm	700 μm	p-type

A.2 Silicon Wafer Cleaning Steps

- TCE Cleaning:** To remove oil and grease
 - Ultrasonic agitation with TCE for 2 minutes
 - Boil at 60° for 2 minutes
- Acetone Cleaning:** To remove organic contaminants
 - Ultrasonic agitation with Acetone for 2 minutes
 - Boil at 60° for 2 minutes
 - Rinse in DI water and blow dry with Nitrogen
- HNO₃ Cleaning:** To form metal oxide
 - Boil at 80° for 3 minutes
 - Rinse in DI water and check for hydrophilic surface
 - Blow dry with Nitrogen
- Dil. HF Cleaning:** To remove metal oxide
 - Dip in dil. HF (HF : DI water :: 1 : 25) for 30 seconds
 - Rinse in DI water and check for hydrophobic surface
 - Blow dry with Nitrogen

A.3 Spin Coating Parameters

The spin coating parameters used for various steps of lithography is tabulated below

Table A.2: Spin coating parameters for S1805 (positive tone photoresist) to obtain ~ 500 nm thickness on SOI.

Spin coating parameters	Speed	Acceleration	Time	Thickness
Step-1 (Coat)	450 rpm	3000 rpm/s	45 s	-

Table A.3: Spin coating parameters for S1813 (positive tone photoresist) to obtain ~ 1200 nm thickness on SOI.

Spin coating parameters	Speed	Acceleration	Time	Thickness
Step-1 (Coat)	450 rpm	3000 rpm/s	45 s	-

Table A.4: Spin coating parameters for HSQ (negative tone resist) to obtain ~ 100 nm thickness on SOI.

Spin coating parameters	Speed	Acceleration	Time	Thickness
Step-1 (Spread)	100 rpm	100 rpm/s	10 s	-
Step-2 (Coat)	3000 rpm	1500 rpm/s	30 s	~100 nm

Table A.5: Spin coating parameters for PMMA (A4) (positive tone resist) to obtain ~ 250 nm thickness on SOI.

Spin coating parameters	Speed	Acceleration	Time	Thickness
Step-1 (Coat)	3000 rpm	600 rpm/s	45 s	~250 nm

A.4 Photolithography Parameters

1. Moisture removal for minimum 15 mins at ~200°C
2. Spin coating of photoresist (S1805/S1813)
3. Prebake/soft-bake for 15 mins at 80°C
4. Exposure (Vacuum contact)
5. Post-exposure bake at 120°C for 2 mins
6. Developing (using MF312/MF319)
7. Postbake/hard-bake at 80°C for 20 mins

Fig. A.1(a)-A.1(d) shows the SEM image of the photoresist profile obtained after i-line photolithography.

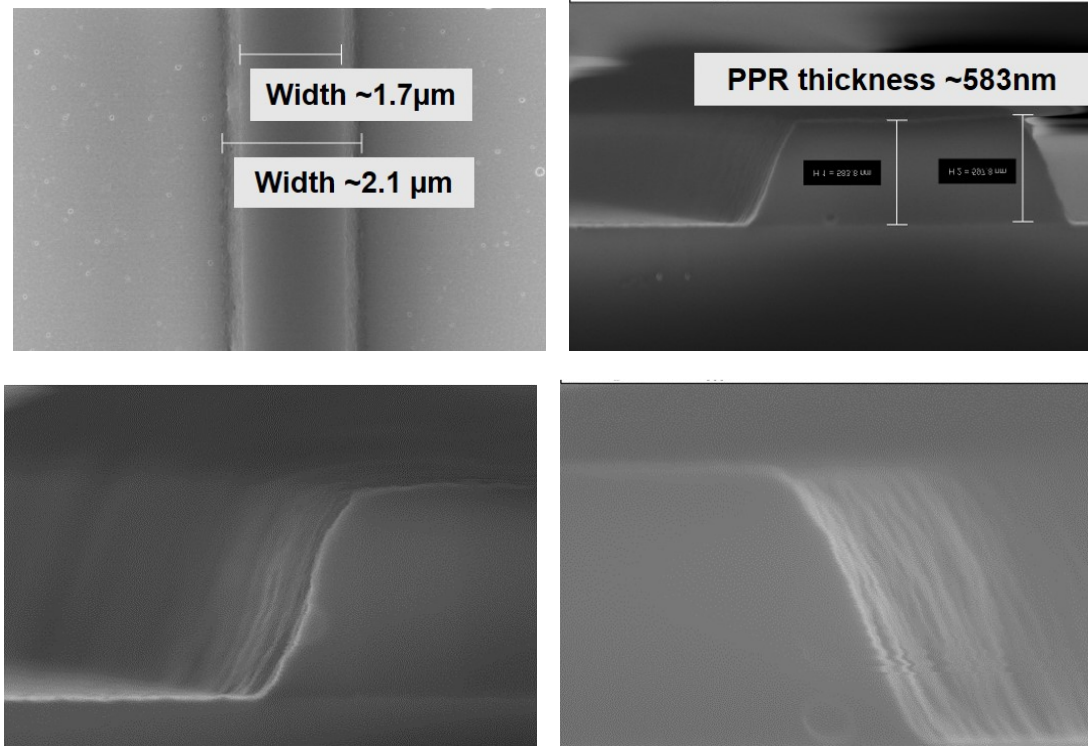


Figure A.1: SEM images of positive photoresist profile of (a) top view of a 2 μm rib waveguide, (b) cross-section view of the PPR, (c) and (d) zoom view of the PPR side wall roughness .

A.5 EBL Column Parameters

The column parameters for electron-beam lithography is tabulated as follows:

Table A.6: EBL (Raith 150 TWO) column parameters and patterning parameters used for conventional and FBMS patterning on HSQ resist.

Column parameters	Patterning parameters
Acceleration voltage : 20 kV	Area dose : 300 $\mu\text{C}/\text{cm}^2$
Aperture : 20 μm	FBMS dose : 400 $\mu\text{C}/\text{cm}^2$
Working distance : 10 mm	Area step size : 9.4 nm
Write field : 100 $\mu\text{m} \times 100 \mu\text{m}$	

A.6 Dry Etching Parameters

The ICPRIE etching recipes used for silicon and silicon-di-oxide etching is tabulated as follows:

Table A.7: Optimized recipe for dry etching of silicon using ICP-RIE

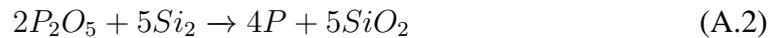
Parameter	Value
Gas flow rate	SF ₆ :CHF ₃ :: 5:18 sccm
RF power	30 W
ICP power	1000 W
Pressure	15 mTorr
Temperature	20°C

Table A.8: Optimized recipe for dry etching of silicon-di-oxide using ICP-RIE

Parameter	Value
Gas flow rate	Ar:CHF ₃ :: 25:25 sccm
RF power	100 W
ICP power	0 W
Pressure	15 mTorr
Temperature	0°C

A.7 Phosphorus Diffusion

Phosphorous diffusion was carried out using the liquid ($POCl_3$) source of diffusion. Oxygen and very low amount of nitrogen was bubbled through the $POCl_3$ kept in a glass-bubbler at 4°C. Nitrogen was used as the carrier gas for the diffusion process. $POCl_3$ while reacting with oxygen produces P_2O_5 and chlorine gas is released. The P_2O_5 on reacting with the silicon wafer produces phosphorous which gets diffused into the wafer and phosposilicate glass (PSG) is formed on the surface of the silicon wafer.



The above two equations explain the chemical reactions that go through during the phosphorus diffusion process. Fig. A.2 shows the data sheet for the sheet resistance obtained when the diffusion is performed at different temperature for various time duration.

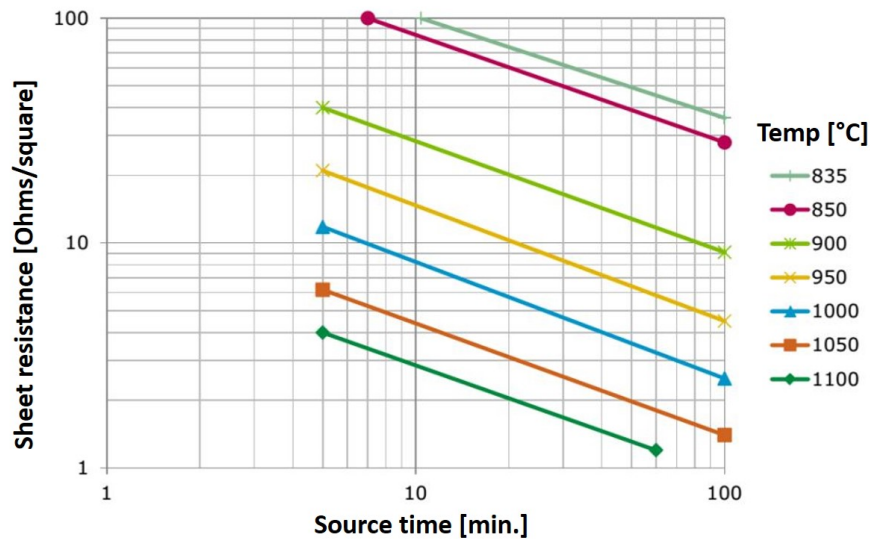


Figure A.2: Data sheet for sheet resistance of Phosphorous diffusion [85].

A.8 Boron Diffusion

For Boron diffusion Boron Nitride wafers were used as the solid source of diffusion. The BN wafers were cleaned in dilute HF solution (HF:DI water :: 2:3). After drying with nitrogen air gun, they were loaded and kept in the mouth of the furnace at 400°C for 2 hours. Nitrogen flow was maintained all these time. This ensured complete drying of the BN wafers. The temperature of the furnace was ramped up to 1000° for oxidising the wafers. The BN wafers were oxidised for 30 minutes in the presence of oxygen gas only. Then the wafers were unloaded and the furnace was ramped up to 1100°C. In the mean time the silicon samples were placed in between the BN wafers. Once the temperature of the furnace was stabilized, the BN wafers along with alternatively placed silicon wafers were loaded into the furnace for diffusion. During diffusion, Nitrogen was used as the carrier gas along with a very small flow of oxygen. The total temperature ramp up processes for processing the BN wafers is shown in Fig. A.3. Borosilicate glass (BSG) formation occurs on the silicon wafers as a result of the diffusion process.

The BSG is hard and needs to be softened using low temperature oxidation. Wet oxidation at 700°C was performed for 20 mins to soften the BSG. Finally the sample was cleaned using dilute HF solution to remove the BSG. The sheet resistance of the diffused sample can be estimated using Fig. A.4 by considering the temperature and

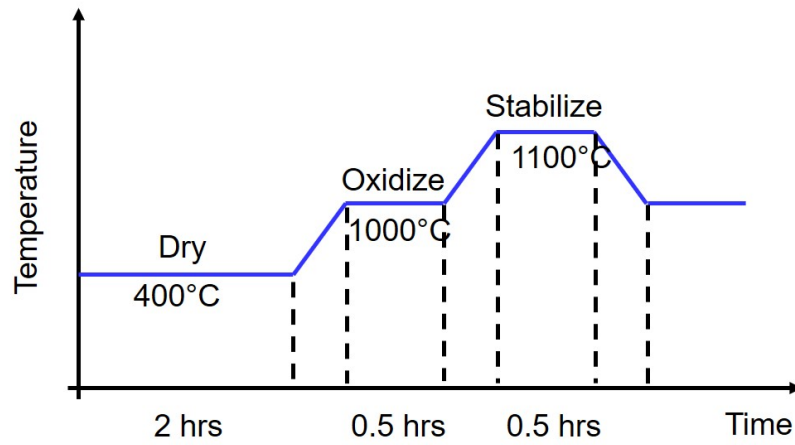


Figure A.3: Boron Nitride wafer preparation process for Boron diffusion.

duration of diffusion.

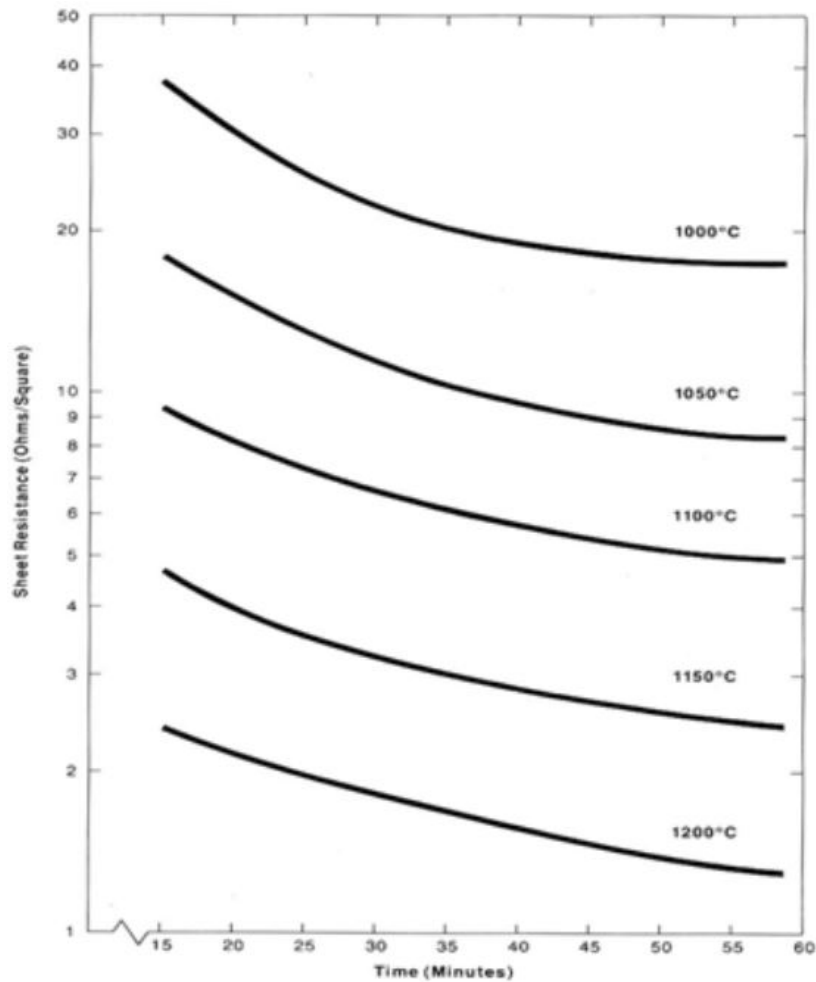


Figure A.4: Data sheet for sheet resistance vs time for Boron diffusion.

APPENDIX B

DOCTORAL COMMITTEE

CHAIR PERSON : Prof. Devendra Jalihal

Professor

Department of Electrical Engineering

Indian Institute of Technology, Madras

GUIDE : Prof. Bijoy Krishna Das

Professor

Department of Electrical Engineering

Indian Institute of Technology, Madras

MEMBERS : Prof. Shreepad Karmalkar

Professor

Department of Electrical Engineering

Indian Institute of Technology, Madras

: Dr. Deleep Nair

Associate Professor

Department of Electrical Engineering

Indian Institute of Technology, Madras

: Prof. Nilesh J Vasa

Professor

Department of Engineering Design

Indian Institute of Technology, Madras

APPENDIX C

List of Publications Based on Thesis

Journals

1. **Riddhi Nandi**, Arnab Goswami and Bijoy Krishna Das, "Phase Controlled Bistability in Silicon Microring Resonators for Nonlinear Photonics", IEEE Journal of Selected Topics in Quantum Electronics (2021), Vol. 27, No. 2, March/April 2021.
2. **Riddhi Nandi**, Arnab Goswami, Anushka Tiwari and Bijoy Krishna Das, "Thermo-Optic Switching Response of Silicon Microring Resonators in Presence of Two-Photon Absorption", Applied Optics, (manuscript under preparation).
3. B. K. Das, N. DasGupta, S. Chandran, S. Kurudi, P. Sah, **R. Nandi**, et. al, "Silicon Photonics Technology : Ten Years of Research at IIT Madras", Asian Journal of Physics, Vol. 25, No. 7, pp. 923 - 955, 2016.

Conference (Presentations / Proceedings/Symposium)

1. **Riddhi Nandi**, Arnab Goswami and Bijoy Krishna Das, "Electrically Controlled Bistability in Microring Resonator for Nonlinear Photonic Application", CLEO-Pacific Rim, 3-5 August 2020, Sydney, Australia (poster).
2. **Riddhi Nandi**, Anushka Tiwari, Ramesh K Gupta and Bijoy K Das, "Modelling Thermo-Optically Reconfigurable Silicon Photonics", International Conference on Optics and Electro-optics 2019, 19-22 October 2019, Dehradun, India (Invited talk).
3. **Riddhi Nandi**, Ramesh K Gupta and Bijoy K Das, "Thermo-optic Tuning of Microring Resonators using Diffusion Doped Microheaters in SOI." International Conference on Fibre Optics and Photonics, Optical Society of America, 12 - 15 December 2018, Delhi, India (poster).
4. **Riddhi Nandi** and Bijoy K Das, "Polarization Dependent Electro-Optic Effect in SOI Waveguides with Laterally Diffused P-N Junction", International Conference on Microwave and Photonics (ICMAP 2018), 9-11 February 2018, Dhanbad, India (oral).
5. Sreevatsa Kurudi, **Riddhi Nandi** and Bijoy K Das, "Scaling of Silicon PIN Waveguide Photodetector at 1550 nm Wavelength", International Workshop on Physics of Semiconductor Devices, 11-15 December 2017, Delhi, India (poster).

6. **Riddhi Nandi**, Sreevatsa Kurudi and Bijoy K Das, "Diffusion-doped p-i-n/p-n diodes for scalable silicon photonics devices", SPIE Microtechnologies 2017, 8-10 May 2017, Barcelona, Spain (poster).

REFERENCES

- [1] R. Soref, "Silicon photonics technology: past, present, and future," in *Optoelectronic Integration on Silicon II*, vol. 5730. International Society for Optics and Photonics, 2005, pp. 19–28.
- [2] M. Lipson, "Guiding, modulating, and emitting light on silicon-challenges and opportunities," *Journal of Lightwave Technology*, vol. 23, no. 12, p. 4222, 2005.
- [3] R. Soref, "The past, present, and future of silicon photonics," *IEEE Journal of Selected Topics in Quantum Electronics*, vol. 12, no. 6, pp. 1678–1687, 2006.
- [4] B. Jalali and S. Fathpour, "Silicon photonics," *Journal of Lightwave Technology*, vol. 24, no. 12, pp. 4600–4615, 2006.
- [5] N. Izhaky, M. T. Morse, S. Koehl, O. Cohen, D. Rubin, A. Barkai, G. Sarid, R. Cohen, and M. J. Paniccia, "Development of cmos-compatible integrated silicon photonics devices," *IEEE Journal of Selected Topics in Quantum Electronics*, vol. 12, no. 6, pp. 1688–1698, 2006.
- [6] T. Barwicz, H. Byun, F. Gan, C. Holzwarth, M. Popovic, P. Rakich, M. Watts, E. Ippen, F. Kärtner, H. Smith *et al.*, "Silicon photonics for compact, energy-efficient interconnects," *Journal of Optical Networking*, vol. 6, no. 1, pp. 63–73, 2007.
- [7] X. Chen, M. M. Milosevic, S. Stanković, S. Reynolds, T. D. Bucio, K. Li, D. J. Thomson, F. Gardes, and G. T. Reed, "The emergence of silicon photonics as a flexible technology platform," *Proceedings of the IEEE*, vol. 106, no. 12, pp. 2101–2116, 2018.
- [8] A. Rickman, G. Reed, and F. Namavar, "Silicon-on-insulator optical rib waveguide loss and mode characteristics," *Journal of Lightwave Technology*, vol. 12, no. 10, pp. 1771–1776, 1994.
- [9] O. Powell, "Single-mode condition for silicon rib waveguides," *Journal of Lightwave Technology*, vol. 20, no. 10, p. 1851, 2002.
- [10] L. Vivien, S. Laval, B. Dumont, S. Lardenois, A. Koster, and E. Cassan, "Polarization-independent single-mode rib waveguides on silicon-on-insulator for telecommunication wavelengths," *Optics Communications*, vol. 210, no. 1–2, pp. 43–49, 2002.
- [11] S. Janz, A. Balakrishnan, S. Charbonneau, P. Cheben, M. Cloutier, A. Delâge, K. Dossou, L. Erickson, M. Gao, P. Krug *et al.*, "Planar waveguide echelle gratings in silica-on-silicon," *IEEE Photonics Technology Letters*, vol. 16, no. 2, pp. 503–505, 2004.

- [12] S. Janz, P. Cheben, D. Dalacu, A. Delage, A. Densmore, B. Lamontagne, M.-J. Picard, E. Post, J. Schmid, P. Waldron *et al.*, “Microphotonic elements for integration on the silicon-on-insulator waveguide platform,” *IEEE Journal of Selected Topics in Quantum Electronics*, vol. 12, no. 6, pp. 1402–1415, 2006.
- [13] R. Sumi, R. K. Gupta, N. DasGupta, and B. K. Das, “Ultra-broadband add-drop filter/switch circuit using subwavelength grating waveguides,” *IEEE Journal of Selected Topics in Quantum Electronics*, vol. 25, no. 3, pp. 1–11, 2018.
- [14] P. Trinh, S. Yegnanarayanan, and B. Jalali, “Integrated optical directional couplers in silicon-on-insulator,” *Electronics Letters*, vol. 31, no. 24, pp. 2097–2098, 1995.
- [15] H. Yamada, T. Chu, S. Ishida, and Y. Arakawa, “Optical directional coupler based on si-wire waveguides,” *IEEE Photonics Technology Letters*, vol. 17, no. 3, pp. 585–587, 2005.
- [16] R. K. Gupta, S. Chandran, and B. K. Das, “Wavelength-independent directional couplers for integrated silicon photonics,” *Journal of Lightwave Technology*, vol. 35, no. 22, pp. 4916–4923, 2017.
- [17] K. Jinguji, N. Takato, A. Sugita, and M. Kawachi, “Mach-zehnder interferometer type optical waveguide coupler with wavelength-flattened coupling ratio,” *Electronics Letters*, vol. 26, no. 17, pp. 1326–1327, 1990.
- [18] D. Thomson, Y. Hu, G. Reed, and J.-M. Fedeli, “Low loss mmi couplers for high performance mzi modulators,” *IEEE Photonics Technology Letters*, vol. 22, no. 20, pp. 1485–1487, 2010.
- [19] D. Dai, Z. Wang, J. Peters, and J. E. Bowers, “Compact polarization beam splitter using an asymmetrical mach-zehnder interferometer based on silicon-on-insulator waveguides,” *IEEE Photonics Technology Letters*, vol. 24, no. 8, pp. 673–675, 2012.
- [20] A. Driessen, R. Dekker, M. B. Diemeer, D. H. Geuzebroek, H. J. Hoekstra, E. J. Klein, and A. Leinse, “Microresonators as promising building blocks for vlsi photonics,” in *Integrated Optics: Theory and Applications*, vol. 5956. International Society for Optics and Photonics, 2005, p. 59560Q.
- [21] P. Dumon, G. Roelkens, W. Bogaerts, D. Van Thourhout, J. Wouters, S. Beckx, P. Jaenen, and R. Baets, “Basic photonic wire components in silicon-on-insulator,” in *IEEE International Conference on Group IV Photonics, 2005. 2nd. IEEE*, 2005, pp. 189–191.
- [22] S. Chandran, M. Sundaram, S. Kurudi, and B. K. Das, “Design and fabrication of surface trimmed silicon-on-insulator waveguide with adiabatic spot-size converters,” *Applied Optics*, vol. 56, no. 6, pp. 1708–1716, 2017.
- [23] W. Bogaerts, S. K. Selvaraja, P. Dumon, J. Brouckaert, K. De Vos, D. Van Thourhout, and R. Baets, “Silicon-on-insulator spectral filters fabricated with cmos technology,” *IEEE Journal of Selected Topics in Quantum Electronics*, vol. 16, no. 1, pp. 33–44, 2010.

- [24] F. Horst, W. M. Green, S. Assefa, S. M. Shank, Y. A. Vlasov, and B. J. Ofreïn, “Cascaded mach-zehnder wavelength filters in silicon photonics for low loss and flat pass-band wdm (de-) multiplexing,” *Optics Express*, vol. 21, no. 10, pp. 11 652–11 658, 2013.
- [25] C. Nayak and G. Palai, “Realization of monochromatic filter using silicon grating structure: an application of silicon photonics,” *Optik*, vol. 127, no. 20, pp. 8264–8268, 2016.
- [26] C. Manganelli, P. Pintus, F. Gambini, D. Fowler, M. Fournier, S. Faralli, C. Kopp, and C. Oton, “Large-fsr thermally tunable double-ring filters for wdm applications in silicon photonics,” *IEEE Photonics Journal*, vol. 9, no. 1, pp. 1–10, 2017.
- [27] M. S. Nezami, B. Radi, A. Gour, Y. Xiong, M. Taherzadeh-Sani, M. Ménard, F. Nabki, and O. Liboiron-Ladouceur, “Integrated rf passive low-pass filters in silicon photonics,” *IEEE Photonics Technology Letters*, vol. 30, no. 23, pp. 2052–2055, 2018.
- [28] D. O. M. de Aguiar, M. Milanizadeh, E. Guglielmi, F. Zanetto, G. Ferrari, M. Sampietro, F. Morichetti, and A. Melloni, “Automatic tuning of silicon photonics microring filter array for hitless reconfigurable add-drop,” *Journal of Lightwave Technology*, vol. 37, no. 16, pp. 3939–3947, 2019.
- [29] Q. Fang, J. F. Song, T.-Y. Liow, H. Cai, M. B. Yu, G. Q. Lo, and D.-L. Kwong, “Ultralow power silicon photonics thermo-optic switch with suspended phase arms,” *IEEE Photonics Technology Letters*, vol. 23, no. 8, pp. 525–527, 2011.
- [30] D. Celo, D. J. Goodwill, J. Jiang, P. Dumais, C. Zhang, F. Zhao, X. Tu, C. Zhang, S. Yan, J. He, M. Li, W. Liu, Y. Wei, D. Geng, H. Mehrvar, and E. Bernier, “32 × 32 silicon photonic switch,” in *2016 21st OptoElectronics and Communications Conference (OECC) held jointly with 2016 International Conference on Photonics in Switching (PS)*. IEEE, 2016, pp. 1–3.
- [31] P. Dumais, D. J. Goodwill, D. Celo, J. Jiang, C. Zhang, F. Zhao, X. Tu, C. Zhang, S. Yan, J. He, Ming, W. Liu, Y. Wei, D. Geng, H. Mehrvar, and E. Bernier, “Silicon photonic switch subsystem with 900 monolithically integrated calibration photodiodes and 64-fiber package,” *Journal of Lightwave Technology*, vol. 36, no. 2, pp. 233–238, 2017.
- [32] K. Suzuki, K. Tanizawa, S. Suda, H. Matsuura, T. Inoue, K. Ikeda, S. Namiki, and H. Kawashima, “Broadband silicon photonics 8 × 8 switch based on double-mach-zehnder element switches,” *Optics Express*, vol. 25, no. 7, pp. 7538–7546, 2017.
- [33] R. Konoike, K. Suzuki, S. Namiki, H. Kawashima, and K. Ikeda, “Ultra-compact silicon photonics switch with high-density thermo-optic heaters,” *Optics Express*, vol. 27, no. 7, pp. 10 332–10 342, 2019.
- [34] K. Ikeda, K. Suzuki, R. Konoike, S. Namiki, and H. Kawashima, “Large-scale silicon photonics switch based on 45-nm cmos technology,” *Optics Communications*, p. 125677, 2020.

- [35] A. Melloni, A. Canciamilla, C. Ferrari, F. Morichetti, L. O’Faolain, T. Krauss, R. De La Rue, A. Samarelli, and M. Sorel, “Tunable delay lines in silicon photonics: coupled resonators and photonic crystals, a comparison,” *IEEE Photonics Journal*, vol. 2, no. 2, pp. 181–194, 2010.
- [36] S. Khan, M. A. Baghban, and S. Fathpour, “Electronically tunable silicon photonic delay lines,” *Optics Express*, vol. 19, no. 12, pp. 11 780–11 785, 2011.
- [37] S. Kaushal and B. Das, “Design of maximally flat delay lines using apodized crow structure in soi,” in *International Conference on Fibre Optics and Photonics*. Optical Society of America, 2014, pp. T4B–3.
- [38] H. Sun and L. R. Chen, “Discretely tunable optical delay lines using step-chirped subwavelength grating bragg gratings.”
- [39] Q. Xu, V. R. Almeida, and M. Lipson, “Micrometer-scale all-optical wavelength converter on silicon,” *Optics Letters*, vol. 30, no. 20, pp. 2733–2735, 2005.
- [40] L. Chen, K. Preston, S. Manipatruni, and M. Lipson, “Integrated ghz silicon photonic interconnect with micrometer-scale modulators and detectors,” *Optics Express*, vol. 17, no. 17, pp. 15 248–15 256, 2009.
- [41] A. Vorckel, M. Monster, W. Henschel, P. H. Bolivar, and H. Kurz, “Asymmetrically coupled silicon-on-insulator microring resonators for compact add-drop multiplexers,” *IEEE Photonics Technology Letters*, vol. 15, no. 7, pp. 921–923, 2003.
- [42] M. Geng, L. Jia, L. Zhang, L. Yang, P. Chen, T. Wang, and Y. Liu, “Four-channel reconfigurable optical add-drop multiplexer based on photonic wire waveguide,” *Optics Express*, vol. 17, no. 7, pp. 5502–5516, 2009.
- [43] M. S. Dahlem, C. W. Holzwarth, A. Khilo, F. X. Kärtner, H. I. Smith, and E. P. Ippen, “Reconfigurable multi-channel second-order silicon microring-resonator filterbanks for on-chip wdm systems,” *Optics Express*, vol. 19, no. 1, pp. 306–316, 2011.
- [44] S. Nakamura, S. Yanagimachi, H. Takeshita, A. Tajima, T. Hino, and K. Fukuchi, “Optical switches based on silicon photonics for roadm application,” *IEEE Journal of Selected Topics in Quantum Electronics*, vol. 22, no. 6, pp. 185–193, 2016.
- [45] S. Chen, Y. Shi, S. He, and D. Dai, “Compact eight-channel thermally reconfigurable optical add/drop multiplexers on silicon,” *IEEE Photonics Technology Letters*, vol. 28, no. 17, pp. 1874–1877, 2016.
- [46] S. Wang, H. Wu, H. K. Tsang, and D. Dai, “Monolithically integrated reconfigurable add-drop multiplexer for mode-division-multiplexing systems,” *Optics Letters*, vol. 41, no. 22, pp. 5298–5301, 2016.
- [47] B. Naghdi and L. R. Chen, “Silicon photonic four-channel optical add-drop multiplexer enabled by subwavelength grating waveguides,” *IEEE Photonics Journal*, vol. 10, no. 4, pp. 1–10, 2018.

- [48] S. Clemmen, K. P. Huy, W. Bogaerts, R. G. Baets, P. Emplit, and S. Massar, “Continuous wave photon pair generation in silicon-on-insulator waveguides and ring resonators,” *Optics Express*, vol. 17, no. 19, pp. 16 558–16 570, 2009.
- [49] E. Engin, D. Bonneau, C. M. Natarajan, A. S. Clark, M. G. Tanner, R. H. Hadfield, S. N. Dorenbos, V. Zwiller, K. Ohira, N. Suzuki, H. Yoshida, N. Iizuka, M. Ezaki, J. L. O’Brien, and M. G. Thompson, “Photon pair generation in a silicon micro-ring resonator with reverse bias enhancement,” *Optics Express*, vol. 21, no. 23, pp. 27 826–27 834, 2013.
- [50] K. Guo, L. Yang, X. Shi, X. Liu, Y. Cao, J. Zhang, X. Wang, J. Yang, H. Ou, and Y. Zhao, “Nonclassical optical bistability and resonance-locked regime of photon-pair sources using silicon microring resonator,” *Physical Review Applied*, vol. 11, no. 3, p. 034007, 2019.
- [51] S. Paesani, M. Borghi, S. Signorini, A. Mañnos, L. Pavesi, and A. Laing, “Near-ideal spontaneous photon sources in silicon quantum photonics,” *Nature Communications*, vol. 11, no. 1, pp. 1–6, 2020.
- [52] X. Zheng, I. Shubin, G. Li, T. Pinguet, A. Mekis, J. Yao, H. Thacker, Y. Luo, J. Costa, K. Raj, J. E. Cunningham, and A. V. Krishnamoorthy, “A tunable 1x4 silicon cmos photonic wavelength multiplexer/demultiplexer for dense optical interconnects,” *Optics Express*, vol. 18, no. 5, pp. 5151–5160, 2010.
- [53] B. A. Dorin and N. Y. Winnie, “Two-mode division multiplexing in a silicon-on-insulator ring resonator,” *Optics Express*, vol. 22, no. 4, pp. 4547–4558, 2014.
- [54] D. Tan, A. Grieco, and Y. Fainman, “Towards 100 channel dense wavelength division multiplexing with 100ghz spacing on silicon,” *Optics Express*, vol. 22, no. 9, pp. 10 408–10 415, 2014.
- [55] H. Guan, Z.-Y. Li, H.-H. Shen, and Y.-D. Yu, “Compact optical add-drop demultiplexers with cascaded micro-ring resonators on soi,” *Chinese Physics Letters*, vol. 34, no. 6, p. 064201, 2017.
- [56] J. K. Poon, J. Scheuer, Y. Xu, and A. Yariv, “Designing coupled-resonator optical waveguide delay lines,” *JOSA B*, vol. 21, no. 9, pp. 1665–1673, 2004.
- [57] J. Cardenas, M. A. Foster, N. Sherwood-Droz, C. B. Poitras, H. L. Lira, B. Zhang, A. L. Gaeta, J. B. Khurgin, P. Morton, and M. Lipson, “Wide-bandwidth continuously tunable optical delay line using silicon microring resonators,” *Optics Express*, vol. 18, no. 25, pp. 26 525–26 534, 2010.
- [58] J. Xie, L. Zhou, Z. Zou, J. Wang, X. Li, and J. Chen, “Continuously tunable reflective-type optical delay lines using microring resonators,” *Optics Express*, vol. 22, no. 1, pp. 817–823, 2014.
- [59] S. J. Emelett and R. Soref, “Design and simulation of silicon microring optical routing switches,” *Journal of Lightwave Technology*, vol. 23, no. 4, pp. 1800–1807, 2005.

- [60] S. Xiao, M. H. Khan, H. Shen, and M. Qi, "Silicon-on-insulator microring add-drop filters with free spectral ranges over 30 nm," *Journal of Lightwave Technology*, vol. 26, no. 2, pp. 228–236, 2008.
- [61] B. G. Lee, A. Biberman, P. Dong, M. Lipson, and K. Bergman, "All-optical comb switch for multiwavelength message routing in silicon photonic networks," *IEEE Photonics Technology Letters*, vol. 20, no. 10, pp. 767–769, 2008.
- [62] P. Dong, W. Qian, H. Liang, R. Shafiiha, N.-N. Feng, D. Feng, X. Zheng, A. V. Krishnamoorthy, and M. Asghari, "Low power and compact reconfigurable multiplexing devices based on silicon microring resonators," *Optics Express*, vol. 18, no. 10, pp. 9852–9858, 2010.
- [63] Z. Guo, L. Lu, L. Zhou, L. Shen, and J. Chen, "16× 16 silicon optical switch based on dual-ring-assisted mach–zehnder interferometers," *Journal of Lightwave Technology*, vol. 36, no. 2, pp. 225–232, 2017.
- [64] S. Palermo, P. Chiang, C. Li, C.-H. Chen, M. Fiorentino, R. Beausoleil, H. Li, K. Yu, B. Wang, R. Bai *et al.*, "Silicon photonic microring resonator-based transceivers for compact wdm optical interconnects," in *2015 IEEE Compound Semiconductor Integrated Circuit Symposium (CSICS)*. IEEE, 2015, pp. 1–4.
- [65] M. Rakowski, M. Pantouvaki, P. De Heyn, P. Verheyen, M. Ingels, H. Chen, J. De Coster, G. Lepage, B. Snyder, K. De Meyer, M. Steyaert, N. Pavarelli, J. Su Lee, P. O'Brien, P. Absil, and J. Van Campenhout, "22.5 a 4× 20gb/s wdm ring-based hybrid cmos silicon photonics transceiver," in *2015 IEEE International Solid-State Circuits Conference-(ISSCC) Digest of Technical Papers*. IEEE, 2015, pp. 1–3.
- [66] M. S. Rasras, K.-Y. Tu, D. M. Gill, Y.-K. Chen, A. E. White, S. S. Patel, A. Pomerene, D. Carothers, J. Beattie, M. Beals *et al.*, "Demonstration of a tunable microwave-photonic notch filter using low-loss silicon ring resonators," *Journal of Lightwave Technology*, vol. 27, no. 12, pp. 2105–2110, 2009.
- [67] W. Yang, X. Yi, S. Song, S. X. Chew, L. Li, and L. Nguyen, "Tunable single bandpass microwave photonic filter based on phase compensated silicon-on-insulator microring resonator," in *2016 21st OptoElectronics and Communications Conference (OECC) held jointly with 2016 International Conference on Photonics in Switching (PS)*. IEEE, 2016, pp. 1–3.
- [68] Y. Long and J. Wang, "All-optical tuning of a nonlinear silicon microring assisted microwave photonic filter: theory and experiment," *Optics Express*, vol. 23, no. 14, pp. 17 758–17 771, 2015.
- [69] M. Borghi, C. Castellan, S. Signorini, A. Trenti, and L. Pavesi, "Nonlinear silicon photonics," *Journal of Optics*, vol. 19, no. 9, p. 093002, 2017.
- [70] J. W. Silverstone, J. Wang, D. Bonneau, P. Sibson, R. Santagati, C. Erven, J. O'Brien, and M. Thompson, "Silicon quantum photonics," in *2016 International Conference on Optical MEMS and Nanophotonics (OMN)*. IEEE, 2016, pp. 1–2.

- [71] X. Qiang, X. Zhou, J. Wang, C. M. Wilkes, T. Loke, S. O’Gara, L. Kling, G. D. Marshall, R. Santagati, T. C. Ralph *et al.*, “Large-scale silicon quantum photonics implementing arbitrary two-qubit processing,” *Nature Photonics*, vol. 12, no. 9, pp. 534–539, 2018.
- [72] S. T. Fard, S. M. Grist, V. Donzella, S. A. Schmidt, J. Flueckiger, X. Wang, W. Shi, A. Millspaugh, M. Webb, D. M. Ratner *et al.*, “Label-free silicon photonic biosensors for use in clinical diagnostics,” in *Silicon Photonics VIII*, vol. 8629. International Society for Optics and Photonics, 2013, p. 862909.
- [73] M. Iqbal, M. A. Gleeson, B. Spaugh, F. Tybor, W. G. Gunn, M. Hochberg, T. Baehr-Jones, R. C. Bailey, and L. C. Gunn, “Label-free biosensor arrays based on silicon ring resonators and high-speed optical scanning instrumentation,” *IEEE Journal of Selected Topics in Quantum Electronics*, vol. 16, no. 3, pp. 654–661, 2010.
- [74] D.-X. Xu, M. Vachon, A. Densmore, R. Ma, A. Del age, S. Janz, J. Lapointe, Y. Li, G. Lopinski, D. Zhang *et al.*, “Label-free biosensor array based on silicon-on-insulator ring resonators addressed using a wdm approach,” *Optics Letters*, vol. 35, no. 16, pp. 2771–2773, 2010.
- [75] Q. Xu, B. Schmidt, S. Pradhan, and M. Lipson, “Micrometre-scale silicon electro-optic modulator,” *nature*, vol. 435, no. 7040, pp. 325–327, 2005.
- [76] R. Soref and B. Bennett, “Electro-optical effects in silicon,” *IEEE Journal of Quantum Electronics*, vol. 23, no. 1, pp. 123–129, 1987.
- [77] G. Cocorullo, F. Della Corte, and I. Rendina, “Temperature dependence of the thermo-optic coefficient in crystalline silicon between room temperature and 550 k at the wavelength of 1523 nm,” *Applied Physics Letters*, vol. 74, no. 22, pp. 3338–3340, 1999.
- [78] H. Yu *et al.*, “Performance trade-off between lateral and interdigitated doping patterns for high speed carrier-depletion based silicon modulators,” *Optics Express*, vol. 20, no. 12, pp. 12 926–12 938, 2012.
- [79] A. Atabaki, E. S. Hosseini, A. Eftekhar, S. Yegnanarayanan, and A. Adibi, “Optimization of metallic microheaters for high-speed reconfigurable silicon photonics,” *Optics Express*, vol. 18, no. 17, pp. 18 312–18 323, 2010.
- [80] F. Testa, C. J. Oton, C. Kopp, J.-M. Lee, R. Ortu no, R. Enne, S. Tondini, G. Chiaretti, A. Bianchi, P. Pintus *et al.*, “Design and implementation of an integrated reconfigurable silicon photonics switch matrix in iris project,” *IEEE Journal of Selected Topics in Quantum Electronics*, vol. 22, no. 6, pp. 155–168, 2016.
- [81] B. Guha, B. B. Kyotoku, and M. Lipson, “Cmos-compatible athermal silicon microring resonators,” *Optics Express*, vol. 18, no. 4, pp. 3487–3493, 2010.
- [82] B. Guha, J. Cardenas, and M. Lipson, “Athermal silicon microring resonators with titanium oxide cladding,” *Optics Express*, vol. 21, no. 22, pp. 26 557–26 563, 2013.

- [83] K. Padmaraju, D. F. Logan, T. Shiraishi, J. J. Ackert, A. P. Knights, and K. Bergman, “Wavelength locking and thermally stabilizing microring resonators using dithering signals,” *Journal of Lightwave Technology*, vol. 32, no. 3, pp. 505–512, 2013.
- [84] H. Jayatilleka, K. Murray, M. Á. Guillén-Torres, M. Caverley, R. Hu, N. A. Jaeger, L. Chrostowski, and S. Shekhar, “Wavelength tuning and stabilization of microring-based filters using silicon in-resonator photoconductive heaters,” *Optics Express*, vol. 23, no. 19, pp. 25 084–25 097, 2015.
- [85] D. Llewellyn, Y. Ding, I. I. Faruque, S. Paesani, D. Bacco, R. Santagati, Y.-J. Qian, Y. Li, Y.-F. Xiao, M. Huber *et al.*, “Chip-to-chip quantum teleportation and multi-photon entanglement in silicon,” *Nature Physics*, vol. 16, no. 2, pp. 148–153, 2020.
- [86] J. Wang, S. Paesani, Y. Ding, R. Santagati, P. Skrzypczyk, A. Salavrakos, J. Tura, R. Augusiak, L. Mančinska, D. Bacco *et al.*, “Multidimensional quantum entanglement with large-scale integrated optics,” *Science*, vol. 360, no. 6386, pp. 285–291, 2018.
- [87] J. W. Silverstone, D. Bonneau, K. Ohira, N. Suzuki, H. Yoshida, N. Iizuka, M. Ezaki, C. M. Natarajan, M. G. Tanner, R. H. Hadfield *et al.*, “On-chip quantum interference between silicon photon-pair sources,” *Nature Photonics*, vol. 8, no. 2, p. 104, 2014.
- [88] M. Kues, C. Reimer, P. Roztocki, L. R. Cortés, S. Sciara, B. Wetzel, Y. Zhang, A. Cino, S. T. Chu, B. E. Little *et al.*, “On-chip generation of high-dimensional entangled quantum states and their coherent control,” *Nature*, vol. 546, no. 7660, pp. 622–626, 2017.
- [89] A. C. Turner, M. A. Foster, A. L. Gaeta, and M. Lipson, “Ultra-low power parametric frequency conversion in a silicon microring resonator,” *Optics Express*, vol. 16, no. 7, pp. 4881–4887, 2008.
- [90] J. R. Ong, R. Kumar, R. Aguinaldo, and S. Mookherjea, “Efficient cw four-wave mixing in silicon-on-insulator micro-rings with active carrier removal,” *IEEE Photonics Technology Letters*, vol. 25, no. 17, pp. 1699–1702, 2013.
- [91] L. G. Helt, M. Liscidini, and J. E. Sipe, “How does it scale? comparing quantum and classical nonlinear optical processes in integrated devices,” *JOSA B*, vol. 29, no. 8, pp. 2199–2212, 2012.
- [92] V. R. Almeida and M. Lipson, “Optical bistability on a silicon chip,” *Optics Letters*, vol. 29, no. 20, pp. 2387–2389, 2004.
- [93] P. Dong, W. Qian, H. Liang, R. Shafiqi, D. Feng, G. Li, J. E. Cunningham, A. V. Krishnamoorthy, and M. Asghari, “Thermally tunable silicon racetrack resonators with ultralow tuning power,” *Optics Express*, vol. 18, no. 19, pp. 20 298–20 304, 2010.

- [94] D. Celo, D. J. Goodwill, J. Jiang, P. Dumais, M. Li, and E. Bernier, “Thermo-optic silicon photonics with low power and extreme resilience to over-drive,” in *2016 IEEE Optical Interconnects Conference (OI)*. IEEE, 2016, pp. 26–27.
- [95] R. K. Gupta and B. K. Das, “Performance analysis of metal-microheater integrated silicon waveguide phase-shifters,” *OSA Continuum*, vol. 1, no. 2, pp. 703–714, 2018.
- [96] J. W. Silverstone, R. Santagati, D. Bonneau, M. J. Strain, M. Sorel, J. L. O’Brien, and M. G. Thompson, “Qubit entanglement between ring-resonator photon-pair sources on a silicon chip,” *Nature Communications*, vol. 6, p. 7948, 2015.
- [97] Q. Xu and M. Lipson, “Carrier-induced optical bistability in silicon ring resonators,” *Optics Letters*, vol. 31, no. 3, pp. 341–343, 2006.
- [98] T. Carmon, L. Yang, and K. J. Vahala, “Dynamical thermal behavior and thermal self-stability of microcavities,” *Optics Express*, vol. 12, no. 20, pp. 4742–4750, 2004.
- [99] S. Chandran, “Integrated optical microring resonator in soi for wide range refractive index sensing,” Ph.D. dissertation, IIT Madras, 2017.
- [100] R. K. Gupta, “Broadband silicon photonics devices with wavelength independent directional couplers,” Ph.D. dissertation, IIT Madras, 2019.
- [101] C. Ma and S. Mookherjea, “Simultaneous dual-band entangled photon pair generation using a silicon photonic microring resonator,” *Quantum Science and Technology*, vol. 3, no. 3, p. 034001, 2018.
- [102] W. Bogaerts, P. De Heyn, T. Van Vaerenbergh, K. De Vos, S. Kumar Selvaraja, T. Claes, P. Dumon, P. Bienstman, D. Van Thourhout, and R. Baets, “Silicon microring resonators,” *Laser & Photonics Reviews*, vol. 6, no. 1, pp. 47–73, 2012.
- [103] R. L. Espinola, J. I. Dadap, R. M. Osgood, S. J. McNab, and Y. A. Vlasov, “C-band wavelength conversion in silicon photonic wire waveguides,” *Optics Express*, vol. 13, no. 11, pp. 4341–4349, 2005.
- [104] Q. Lin, J. Zhang, P. M. Fauchet, and G. P. Agrawal, “Ultrabroadband parametric generation and wavelength conversion in silicon waveguides,” *Optics Express*, vol. 14, no. 11, pp. 4786–4799, 2006.
- [105] M. A. Foster, A. C. Turner, J. E. Sharping, B. S. Schmidt, M. Lipson, and A. L. Gaeta, “Broad-band optical parametric gain on a silicon photonic chip,” *Nature*, vol. 441, no. 7096, pp. 960–963, 2006.
- [106] A. G. Griffith, R. K. Lau, J. Cardenas, Y. Okawachi, A. Mohanty, R. Fain, Y. H. D. Lee, M. Yu, C. T. Phare, C. B. Poitras *et al.*, “Silicon-chip mid-infrared frequency comb generation,” *Nature Communications*, vol. 6, p. 6299, 2015.
- [107] V. Van, *Optical microring resonators: theory, techniques, and applications*. CRC Press, 2016.

- [108] C. Ma and S. Mookherjea, “Prospects for photon-pair generation using silicon microring resonators with two photon absorption and free carrier absorption,” *OSA Continuum*, vol. 3, no. 5, pp. 1138–1153, 2020.
- [109] H. K. Tsang, C. Wong, T. Liang, I. Day, S. Roberts, A. Harpin, J. Drake, and M. Asghari, “Optical dispersion, two-photon absorption and self-phase modulation in silicon waveguides at 1.5 μ m wavelength,” *Applied Physics Letters*, vol. 80, no. 3, pp. 416–418, 2002.
- [110] T.-K. Liang and H.-K. Tsang, “Nonlinear absorption and raman scattering in silicon-on-insulator optical waveguides,” *IEEE Journal of Selected Topics in Quantum Electronics*, vol. 10, no. 5, pp. 1149–1153, 2004.
- [111] T. Liang, H. Tsang, I. Day, J. Drake, A. Knights, and M. Asghari, “Silicon waveguide two-photon absorption detector at 1.5 μ m wavelength for autocorrelation measurements,” *Applied Physics Letters*, vol. 81, no. 7, pp. 1323–1325, 2002.
- [112] H. Rong, R. Jones, A. Liu, O. Cohen, D. Hak, A. Fang, and M. Paniccia, “A continuous-wave Raman silicon laser,” *Nature*, vol. 433, no. 7027, pp. 725–728, 2005.
- [113] Z. Wang, H. Liu, Q. Sun, N. Huang, S. Li, and J. Han, “The influence of thermal and free carrier dispersion effects on all-optical wavelength conversion in a silicon racetrack-shaped microring resonator,” *Laser Physics*, vol. 26, no. 7, p. 075403, 2016.
- [114] C. M. Gentry, J. M. Shainline, M. T. Wade, M. J. Stevens, S. D. Dyer, X. Zeng, F. Pavanello, T. Gerrits, S. W. Nam, R. P. Mirin *et al.*, “Quantum-correlated photon pairs generated in a commercial 45 nm complementary metal-oxide semiconductor microelectronic chip,” *Optica*, vol. 2, no. 12, pp. 1065–1071, 2015.
- [115] L. Helt, Z. Yang, M. Liscidini, and J. Sipe, “Spontaneous four-wave mixing in microring resonators,” *Optics Letters*, vol. 35, no. 18, pp. 3006–3008, 2010.
- [116] P. Absil, J. Hryniewicz, B. Little, P. Cho, R. Wilson, L. Joneckis, and P.-T. Ho, “Wavelength conversion in gaas micro-ring resonators,” *Optics Letters*, vol. 25, no. 8, pp. 554–556, 2000.
- [117] Q. Lin, O. J. Painter, and G. P. Agrawal, “Nonlinear optical phenomena in silicon waveguides: modeling and applications,” *Optics Express*, vol. 15, no. 25, pp. 16 604–16 644, 2007.
- [118] I. D. Rukhlenko, M. Premaratne, and G. P. Agrawal, “Analytical study of optical bistability in silicon ring resonators,” *Optics Letters*, vol. 35, no. 1, pp. 55–57, 2010.
- [119] S. Abdollahi and V. Van, “Free-carrier-induced high-order instability in an optical microcavity,” *JOSA B*, vol. 34, no. 7, pp. 1489–1496, 2017.
- [120] Y. Guo, W. Zhang, N. Lv, Q. Zhou, Y. Huang, and J. Peng, “The impact of nonlinear losses in the silicon micro-ring cavities on cw pumping correlated photon pair generation,” *Optics Express*, vol. 22, no. 3, pp. 2620–2631, 2014.

- [121] D. Zheng, B. Smith, and M. Asghari, “Improved efficiency Si-photonic attenuator,” *Optics Express*, vol. 16, no. 21, pp. 16 754–16 765, 2008.
- [122] S. Fathpour, K. K. Tsia, and B. Jalali, “Two-photon photovoltaic effect in silicon,” *IEEE Journal of Quantum Electronics*, vol. 43, no. 12, pp. 1211–1217, 2007.
- [123] M. Chagnon, M. Morsy-Osman, M. Poulin, C. Paquet, S. Lessard, and D. V. Plant, “Experimental parametric study of a silicon photonic modulator enabled 112-gb/s PAM transmission system with a DAC and ADC,” *Journal of Lightwave Technology*, vol. 33, no. 7, pp. 1380–1387, 2015.
- [124] Q. Xu, S. Manipatruni, B. Schmidt, J. Shakya, and M. Lipson, “12.5 Gbit/s carrier-injection-based silicon micro-ring silicon modulators,” *Optics Express*, vol. 15, no. 2, pp. 430–436, 2007.
- [125] M. Asghari and A. V. Krishnamoorthy, “Silicon photonics: Energy-efficient communication,” *Nature Photonics*, vol. 5, no. 5, pp. 268–270, 2011.
- [126] H. Yu, W. Bogaerts, and A. De Keersgieter, “Optimization of ion implantation condition for depletion-type silicon optical modulators,” *IEEE Journal of Quantum Electronics*, vol. 46, no. 12, pp. 1763–1768, 2010.
- [127] Y. Liu, S. Dunham, T. Baehr-Jones, A. E.-J. Lim, G.-Q. Lo, and M. Hochberg, “Ultra-responsive phase shifters for depletion mode silicon modulators,” *Journal of Lightwave Technology*, vol. 31, no. 23, pp. 3787–3793, 2013.
- [128] Z. Yong, W. D. Sacher, Y. Huang, J. C. Mikkelsen, Y. Yang, X. Luo, P. Dumais, D. Goodwill, H. Bahrami, P. G.-Q. Lo *et al.*, “U-shaped PN junctions for efficient silicon Mach-Zehnder and microring modulators in the O-band,” *Optics Express*, vol. 25, no. 7, pp. 8425–8439, 2017.
- [129] T. Cao, Y. Fei, L. Zhang, Y. Cao, and S. Chen, “Design of a silicon Mach-Zehnder modulator with a U-type PN junction,” *Applied Optics*, vol. 52, no. 24, pp. 5941–5948, 2013.
- [130] D.-X. Xu, J. H. Schmid, G. T. Reed, G. Z. Mashanovich, D. J. Thomson, M. Nedeljkovic, X. Chen, D. Van Thourhout, S. Keyvaninia, and S. K. Selvaraja, “Silicon photonic integration platform: Have we found the sweet spot?” *IEEE Journal of Selected Topics in Quantum Electronics*, vol. 20, no. 4, pp. 189–205, 2014.
- [131] R. K. Gupta and B. K. Das, “Multi-input and multi-output soi (MIMO-SOI) platform for silicon photonics,” *CSI Transactions on ICT*, vol. (Special Issue Visvesvaraya), pp. 1–5, 2016.
- [132] Synopsys, “TSUPREM-4,” <https://www.synopsys.com/silicon/tcad/process-simulation/taurus-tsuprem-4.html>, (Accessed: 19 April 2017).
- [133] Lumerical, “MODE,” <https://www.lumerical.com/tcad-products/mode/>, (Accessed: 19 April 2017).

- [134] Lumerical, “DEVICE,” <https://www.lumerical.com/tcad-products/device/>, (Accessed: 19 April 2017).
- [135] A. Yariv and P. Yeh, *Photonics: Optical Electronics in Modern Communications*. Oxford University Press, 2007.
- [136] S. Kaushal and B. K. Das, “Modeling and experimental investigation of an integrated optical microheater in silicon-on-insulator,” *Applied Optics*, vol. 55, no. 11, pp. 2837–2842, 2016.
- [137] S. Kurudi, “Experimental studies of diffusion doped pin waveguides for integrated silicon photonics circuits,” MS dissertation, IIT Madras, 2017.
- [138] S. Pavadai, “Design and fabrication of diffusion doped pin waveguides for silicon photonics,” MS dissertation, IIT Madras, 2015.
- [139] S. Chandran, R. K. Gupta, and B. K. Das, “Dispersion enhanced critically coupled ring resonator for wide range refractive index sensing,” *IEEE Journal of Selected Topics in Quantum Electronics*, vol. 23, no. 2, pp. 424–432, 2016.
- [140] M. Bahadori, A. Gazman, N. Janosik, S. Rumley, Z. Zhu, R. Polster, Q. Cheng, and K. Bergman, “Thermal rectification of integrated microheaters for microring resonators in silicon photonics platform,” *Journal of Lightwave Technology*, vol. 36, no. 3, pp. 773–788, 2017.
- [141] M. W. Pruessner, T. H. Stievater, M. S. Ferraro, and W. S. Rabinovich, “Thermo-optic tuning and switching in soi waveguide fabry-perot microcavities,” *Optics Express*, vol. 15, no. 12, pp. 7557–7563, 2007.